Performance qualification of the DIRICH readout system and development of a novel electron reconstruction scheme for the CBM experiment

Dissertation

zur Erlangung des akademischen Grades eines

Doktors der Naturwissenschaften (Dr. rer. nat.)

der Fakultät Mathematik und Naturwissenschaften

Fachgruppe Physik

der Bergischen Universität Wuppertal

vorgelegt von

Pavish Subramani

subramani@uni-wuppertal.de

Wuppertal, 14. February 2025

Verteidigt

Wuppertal, 27. March 2025

1. Gutachter:
Prof. Dr. Karl-Heinz Kampert
Bergische Universität Wuppertal

2. Gutachter
Prof. Dr. Anton Andronic
Universität Münster

Betreuer
Dr. Christian Pauly
Bergische Universität Wuppertal

Abstract

The Compressed Baryonic Matter (CBM) experiment is an upcoming fixed-target experiment being constructed at the Facility for Antiproton and Ion Research (FAIR) at GSI, Darmstadt. The CBM experiment is designed to characterize the QCD medium at high net-baryon densities and moderate temperatures. Di-electrons interact electromagnetically and are unaffected by the strong medium. They are therefore used as a penetrating probe for understanding the QCD medium produced in the initial stages of heavy-ion collisions. Efficient identification of the electrons with minimum pion contamination is paramount for the di-electron analysis. The CBM experiment uses a Ring Imaging Cherenkov detector (RICH) as the primary electron identification detector. The focus of this thesis is to improve the identification performance of the RICH by characterizing its readout electronics and restructuring its software reconstruction scheme for electrons. The first part of the thesis describes the dedicated lab setup characterizing the DIRICH front-end electronics of the RICH. This study aims to evaluate the performance of the DIRICH electronics at high photon rate and high simultaneous photon occupancy in the sensor. Furthermore, supplementary measurements including the neighboring channel charge sharing crosstalk, the timing precision of the DIRICH front-end board, and the electronic noise-emitting characteristics of the power module are described. In the second part of this thesis, the development of a novel reconstruction scheme for electrons is described in detail. Conventionally, an artificial neural network based on a single-layer perceptron is used for electron identification in RICH. This thesis discusses the replacement of the conventional ANN with tree-based ensemble models. Furthermore, the performance of the upgraded model is further improved by exploiting the tracking capability of the transition radiation detector (TRD) situated downstream of the RICH. One major reason for pion misidentification in the RICH is Cherenkov rings from untracked electrons stemming from photon conversion in the detector material after the tracking stations. The latter sections of this thesis describe a robust method for reducing the contribution of these conversion electrons in the reconstruction algorithm. In the concluding section of this thesis, the reconstruction of the omega mesons via its di-electron decay channel, using the enhanced electron identification scheme developed during this thesis, is presented.

Kurzfassung

Das Compressed Baryonic Matter (CBM)-Experiment ist ein geplantes Fixed-Target-Experiment, das derzeit an der Facility for Antiproton and Ion Research (FAIR) der GSI in Darmstadt aufgebaut wird. Das CBM-Experiment dient dazu, das QCD-Medium bei hohen Netto-Baryonendichten und moderaten Temperaturen zu charakterisieren. Di-Elektronen interagieren elektromagnetisch und werden vom starken Medium nicht beeinflusst. Sie werden daher als durchdringende Sonde verwendet, um das QCD-Medium zu verstehen, das in den Anfangsphasen von Schwerionenkollisionen entsteht. Eine effiziente Identifizierung der Elektronen mit minimaler Pionkontamination ist für die Di-Elektronen-Analyse von größter Bedeutung. Das CBM-Experiment verwendet einen Ring Imaging Cherenkov Detektor (RICH) als primären Elektronidentifikationsdetektor. Der Schwerpunkt dieser Arbeit liegt auf der Verbesserung der Identifikationsleistung des RICH durch die Charakterisierung seiner Ausleseelektronik und Umstrukturierung des Software-Rekonstruktionsschemas für Elektronen. Der erste Teil der Arbeit beschreibt einen speziellen Laboraufbau zur Charakterisierung der DIRICH-Frontend-Elektronik des RICH. Diese Studie zielt darauf ab, die Leistung der DIRICH-Elektronik bei hoher Photonenrate und hoher gleichzeitiger Photonenlast im Sensor zu bewerten. Weiterhin werden ergänzende Messungen beschrieben, darunter die Vermessung des Übersprechens durch Ladungsaufteilung zwischen benachbarten Kanälen, die Bestimmung der Zeitgenauigkeit des DIRICH-Frontend-Moduls und das, durch das Power-Modul induzierte, zusätzliche elektronische Rauschen. Im zweiten Teil dieser Arbeit wird die Entwicklung eines neuartigen Rekonstruktionsschemas für Elektronen detailliert beschrieben. Herkömmlicherweise wird für die Elektronenidentifizierung im RICH ein künstliches neuronales Netzwerk auf Basis eines einfaches Perzeptrons verwendet. In dieser Arbeit wird der Ersatz des herkömmlichen ANN durch tree-based Ensemble-Modelle diskutiert. Darüber hinaus wird die Leistung des verbesserten Modells durch die Nutzung der Tracking-Fähigkeit des Transition Radiation Detectors (TRD) weiter verbessert, der sich strahlabwärts vom RICH befindet. Ein Hauptgrund für die Fehlidentifizierung von Pionen im RICH sind Cherenkov-Ringe von Elektronen die nicht in der Spurrekonstruktion erfasst wurden. Diese Elektronen stammen hauptsächlich aus der Photonenumwandlung im Detektormaterial nach den Spurrekonstruktions-Stationen. Die letzten Abschnitte dieser Arbeit beschreiben eine robuste Methode zur Reduzierung des Beitrags dieser Umwandlungselektronen im Rekonstruktionsalgorithmus. Im abschließenden Abschnitt dieser Arbeit wird die Rekonstruktion der Omega-Mesonen über ihren Di-Elektronen-Zerfallskanal unter Verwendung des in dieser Arbeit entwickelten, verbesserten Elektronidentifizierungsschemas vorgestellt.

Contents

1

Introduction

Ancient civilizations across the globe understood the importance of the forces of nature for their everyday use. The understanding of the fundamental forces of the universe has since evolved. The Gravitational force is the first known force to be theorized. Sir. Isaac Newton conceptualized his ideas of gravity in his book "Principia Mathematica" to explain the moon's trajectory around the Earth in 1687. During the 19th century, scientists progressed in understanding the hidden nature of magnets and electricity, fuelled by Michael Faraday. He proposed that the alternating current induced a change in the magnetic field and vice versa. Prof. James Clarke Maxwell proposed his theory of electromagnetic fields (1864-65), unifying electric fields and magnetic fields. The Maxwell equations indicated that light is an electromagnetic wave. Richard Feynman, Sin-Itiro Tomonaga, and Julian Schwinger formulated a Quantum Field Theory called Quantum Electro Dynamics (QED) to generalize the electromagnetic interactions with photons as the exchange particles of electromagnetic force. In the 20th century, the strong nuclear force which holds the protons and neutrons inside the nucleus was discovered. The fundamental charge carriers involved in the strong force are called quarks, and the exchange particles are called gluons. A field theory approach to formulate the strong interaction is called Quantum Chromo Dynamics (QCD). Around the same time, the weak nuclear force that facilitates radioactive decays was discovered. The exchange particles in weak nuclear decays are Z and $W^{\pm}$. Unifying the weak nuclear force with the electromagnetic force was postulated independently by Sheldon Lee Glashow, Abdus Salam, and Steven Weinberg during the 1960s. The puzzle of unifying the strong interactions with the electroweak theory resulted in the standard model of particle physics we know today.

This thesis focuses on the QCD interactions. The QCD predicts two important characteristics for the underlying charges – asymptotic freedom and confinement. At smaller distances or high momentum transfer (both being correlated by the uncertainty principle, $\Delta x \Delta p \geq \frac{\hbar}{2}$) the interaction strength of the partons reduces. This phenomenon is called asymptotic freedom. Conversely, at larger distances or low momentum transfer, the interaction strength increases and the partons confine themselves into hadrons (a system of quarks and gluons). The transition between the hadronic degrees of freedom and quark degrees of freedom can be controlled by the energy of the underlying system either by varying the temperature, the baryonic density, or both. The conditions required for such transitions can be found in the initial stages of the Big Bang, at the core of neutron stars and their mergers, and in the initial stages of collisions of heavy ions (HIC) at various accelerator facilities. The Relativistic Heavy-Ion Collider (RHIC) and Large Hadron Collider (LHC) facilities extensively probe the QCD phase diagram at low

baryonic chemical potentials μ_B (a proxy for net baryon density). It was found experimentally that at low net baryonic densities, there is a smooth crossover between the phases. The crossover in the temperature scale is around 156 MeV (T_c) for near-zero baryonic chemical potential, and these results could be explained theoretically using Lattice QCD methods. A first-order phase transition is predicted to occur between hadron degrees of freedom and quark-gluon degrees of freedom at moderate to high net baryon densities. This implies the existence of a critical point at which the first-order transition ceases. Multiple experimental facilities, including STAR and NICA are probing the phase diagram at moderate baryonic potential in the QCD phase diagram. The CBM experiment at the SIS100 accelerator is proposed to probe the phase diagram at high baryonic density and moderate temperatures.

The accessing of the QCD medium directly, which is produced only for a few femtometers in HIC, is impossible. Hence, the medium has to be probed by using its signatures. One such signature is the in-medium modification of the spectral function of Low Mass Vector Mesons (LMVM) (quark-anti quark particles with integral spin). We are interested in the leptonic decay, especially the electron decay of LMVMs, because electrons are not affected by the strong medium effects. The electron decay of LMVMs ($\rho, \omega, \phi \ \rightarrow e^+e^-$) is very rare, with a decay branching ratio (fraction of particles that decay into an individual decay mode with respect to the total number of particles that decay) in the order of 10^{-5}. Hence, a clean sample of electrons is required. This can only be achieved in an experiment with excellent electron / pion discrimination, due to the overwhelming background of pions (as compared to electrons) in heavy ion collisions. Pion suppression factor (inverse fraction of pions misidentified as electrons) in the order of 10^4 is necessary for reconstruction of the rare LMVM decays, which in CBM is achieved by using multiple electron identification detectors. The key detector for identifying electrons in CBM is the Ring Imaging Cherenkov Detector (RICH), which is employed in conjunction with the Transition Radiation Detector (TRD) and a Time of Flight (TOF) detector.

The RICH electron identification is based on the Cherenkov effect, which occurs when a particle with a velocity greater than the speed of light in a medium produces Cherenkov photon radiation. The Cherenkov photons emitted by the particles are captured by the photon sensors based on Hamamatsu MAPMTs. The signals from the MAPMTs are measured by an FPGA-based readout chain named as DIRICH readout chain (developed jointly for CBM RICH and PANDA DIRC detectors). Here, the readout electronics of RICH are crucial to fully exploit its capability. The CBM experiment is designed to eventually collect data at an unprecedented high collision rate of up to 10 MHz. This high collision rate results in a high single photon hit rate per pixel in the RICH detector, which is in the order of few 100 kHz. To understand the effect of these high hit rates on the performance of the readout chain and to benchmark the MAPMT-DIRICH readout (photon sensor and readout board) a high-rate test was performed in a controlled environment at the University of Wuppertal. The Cherenkov photons produced by the particle reach the photon detector quasi-simultaneously ($\delta T \leq 60$ ps). At CBM RICH, the expected average simultaneous hits are approximately nine hits per MAPMT, which translates into 15% of total occupancy of the MAPMT. Another laboratory measurement was commissioned to measure the operating effectiveness of the MAPMT-DIRICH readout chain under such high simultaneous

occupancies. Furthermore, dedicated measurements were conducted to evaluate the time measurement capability of the DIRICH readout chain. In addition to real photon hits, crosstalk hits are produced in MAPMT due to either charge leakage into adjacent channels or parasitic conduction in the common dynode system. A measurement was systematically conducted to estimate crosstalk hits. Moreover, the latest variant of the power modules, which features an onboard DCDC converter that regulates the low-voltage supply to various components of the backplane, was tested for its noise-emitting characteristics.

The second part of the puzzle is improving the electron identification capabilities of the RICH in the CBM software simulation framework (CBMROOT). The electron reconstruction algorithms of the RICH are studied in detail using the CBMROOT framework. A significantly longer lifetime and consequently a sharp spectral function are characteristic of the omega meson, as opposed to the rho meson, which has a sufficiently short lifetime to decay still within the medium. This renders the omega meson a suitable candidate for evaluating reconstruction algorithms. In the electron reconstruction algorithms, inefficiencies are observed in the track propagation from the tracker to the RICH. Data-driven methods are implemented to counter these inefficiencies, and their effectiveness is studied with electrons from the decay of omega mesons as the reference.

The differentiation between electrons and pions within the RICH detector was previously done using a single-layer perceptron with different ring and track variables as features. This scheme has now been modified to use the advanced gradient-boosted decision trees. A new concept of "Backtracking" in CBM is introduced to more efficiently include the information from the downstream detectors into an overall electron reconstruction framework, in addition to the RICH standalone reconstruction of the electrons. Furthermore, a method based on the backtracking concept is developed in order to assign the RICH rings with a probability that they might stem from electrons produced via photon conversion in the detector materials. This allows us to further reduce the hadron contamination in the electron sample. Ultimately, the novel electron reconstruction scheme, which incorporates all the improvements, is utilized to reconstruct the invariant mass spectrum of the omega mesons.

1.1 Aim of the thesis

The aim of this thesis is twofold: The first part is more hardware related, aiming to perform benchmark measurements of the MAPMT-DIRICH read-out chain for the CBM RICH detector. This includes the measurement of crosstalk in MAPMT, high rate, and high occupancy measurements. The second part of the thesis is focused on new reconstruction methods in data analysis, it proposes and optimizes the reconstruction algorithms to improve the electron identification performance of the CBM experiment using the RICH detector as basis.

1.2 Thesis overview

This thesis is organized into 8 chapters as is depicted in the following flowchart.

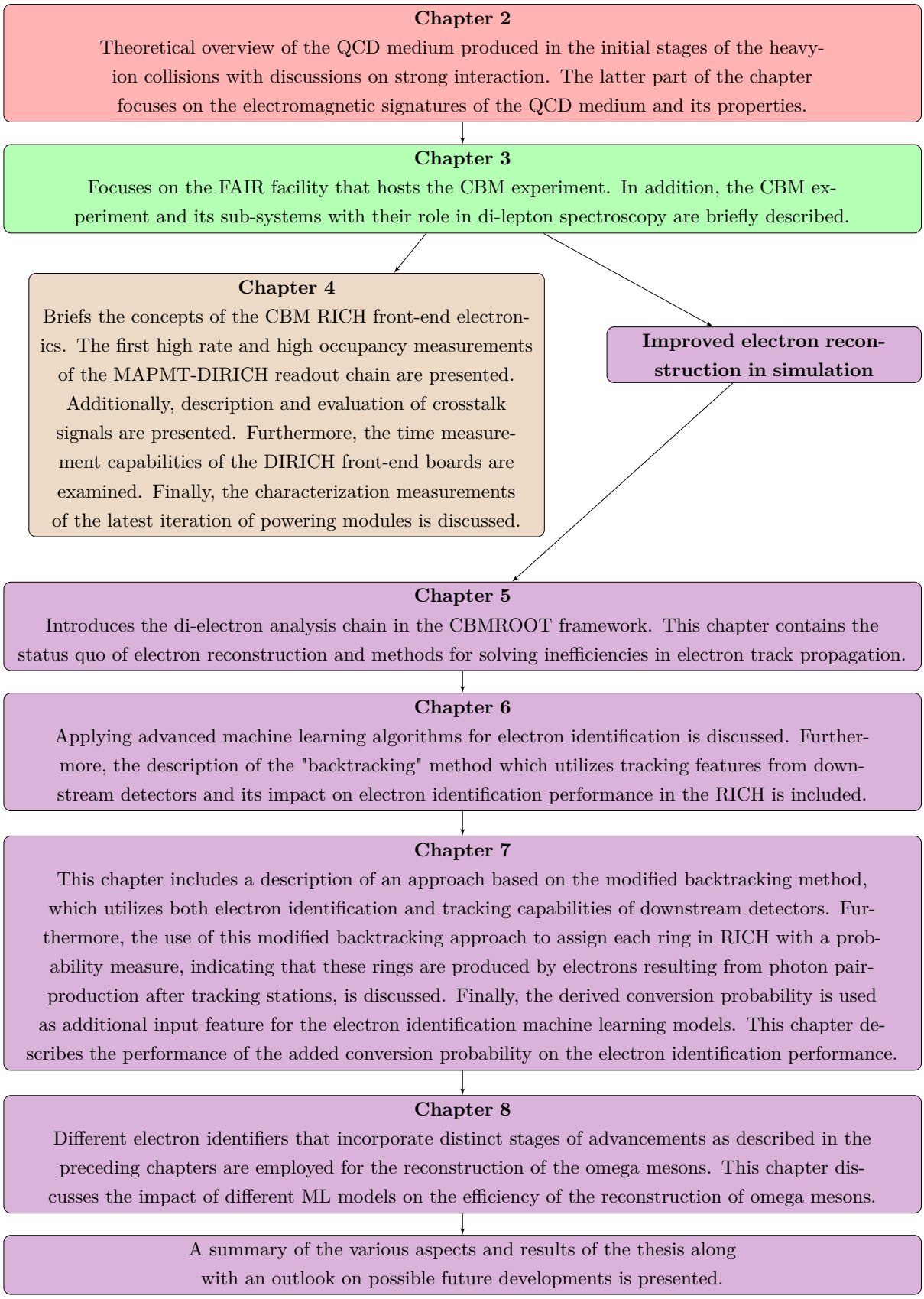

2

Electromagnetic probes

This chapter provides a brief overview of the theoretical framework of Quantum Chromo Dynamics (QCD) with the possibility of forming a deconfined state of quarks and gluons. The formation of hot and dense matter (henceforth referred to as Fireball) in heavy-ion collisions is discussed, as well as the distinct signatures of such a fireball in a heavy-ion experiment. In particular, the di-lepton production stemming from the decay of virtual photons as the probe to understand the fireball properties is highlighted in the latter sections of this chapter. Furthermore, the di-lepton emission during the evolution of the fireball in heavy-ion collision experiments is discussed.

2.1 Standard model

The description of the standard model is given in [1, 2] and references therein. The standard model is a successful quantum field theoretical approach that aims to achieve a unified description of strong, weak, and electromagnetic forces. All elementary particles in the standard models are classified into half-integral spin particles called fermions and integral spin particles called bosons. Quarks and leptons are fermions, which are particles that interact with one another. Their interactions are mediated by so-called gauge particles, which are bosons. The pictorial representation of the standard model is shown in figure 2.1.

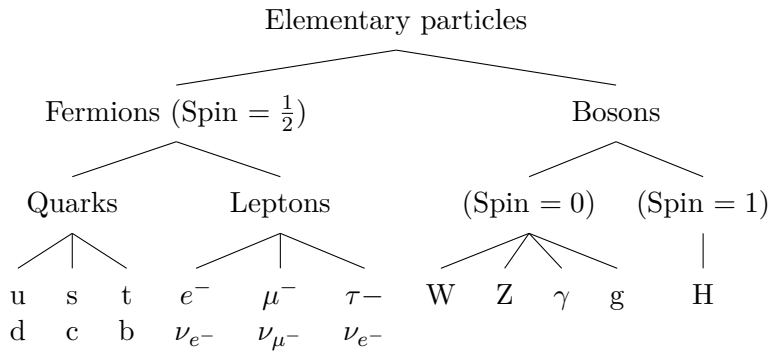

Figure 2.1: A flowchart that depicts the elementary particles within the standard model.

There are three generations of quarks, namely {up, down}, {strange, charm}, and {top, bottom} and three generations of leptons, which are {e, ν_e}, {μ, ν_μ}, and {τ, ν_τ} which are described in the standard model. Each fermion in the standard model has an anti-fermion with the same mass and non-identical intrinsic quantum numbers (like charge and strangeness). The generations of fermions are characterized by a hierarchy of masses.

Field theories are governed by their Lagrangian density $\mathcal{L}$, from which action, $S = \int_t dt \int_V \mathcal{L} dV$ can be derived. The equation of motion that explains the dynamics of the particles is described as the consequence of the principle of least action $\delta S = 0$. It is inferred from the particles in the standard model 2.1, the Lagrangian density $\mathcal{L}_{SM}$ is composed of multiple parts,

$$\mathcal{L}_{SM} = \mathcal{L}_{QCD} + \mathcal{L}_{EW} + \mathcal{L}_{Higgs} \tag{2.1}$$

The Higgs sector of the standard model addresses the interaction of the Higgs boson with all the charges and gauge particles. The electroweak part describes the electromagnetic and weak interactions. In this thesis, we focus on the QCD part of the standard model.

2.2 Quantum Chromo Dynamics (QCD)

The theory that explains the interaction of quarks and gluons is called Quantum Chromo Dynamics (QCD). The Lagrangian density of the QCD is given by [3, 4],

$$\mathcal{L}_{QCD} = \bar{q}(i\gamma^{\mu}D_{\mu} - M)q - \frac{1}{4}F_a^{\mu\nu}F^a_{\mu\nu} \tag{2.2}$$

Here, $q = column(q_R,\ q_B,\ q_G)$, $\bar{q} = row(\bar{q_R}\ , \bar{q_B},\ \bar{q_G})$ is the color quark field. Each component of the quark field q is a 4-element Dirac spinor. The summation over flavors ($N_f = 6$) in the equation 2.2 is implicit. Thus, the mass term M corresponds to $diag(m_u, m_d, .., m_{N_f})$ with m_i being the mass of an individual flavor. The QCD Lagrangian is invariant under the local color transformation symmetry group SU(3), i.e., the Lagrangian is invariant under $q \rightarrow e^{-i\alpha_a T_a}q$ transformation, where $T^a = \frac{\lambda_a}{2}$ are generators of SU(3) rotation, α_a are infinitesimal rotational angles, and λ_a are Gell-Mann matrices [5]. The index a runs from 1 to $N_c^2 - 1$ (for SU(3) gauge symmetry) which implies there are eight kinds of gluons. $D_{\mu} = \partial_{\mu} - igT_aA^a_{\mu}$ is the gauge covariant derivative that introduces a coupling between the quark field with the gluon field A^a_{μ}. The term $\frac{1}{4}F_a^{\mu\nu}F^a_{\mu\nu}$ encapsulates both kinetic and gluon-gluon interactions, where $F^a_{\mu\nu} = \partial_{\mu}A^a_{\mu} - \partial_{\nu}A^a_{\nu} - igf^{abc}A^b_{\mu}A^c_{\nu}$ is the gluon field strength tensor and f_{abc} is the structure constant for the SU(3).

It is apparent that in both interaction terms in the $\mathcal{L}_{QCD}$ the coupling strength g appears. For the completely renormalizable QCD theory [6], the coupling strength (usually referenced $\alpha_s = \frac{g^2}{4\pi}$) should depend on the 4-momentum transfer Q of the interaction. In leading order, it is parameterized as follows,

$$\alpha_s(Q) = \frac{\alpha_s(\Lambda)}{1 + \alpha_s(\Lambda)\beta_0 \ln(\frac{Q^2}{\Lambda^2})}. \tag{2.3}$$

Where $\beta_0 = \frac{33-2N_f}{12\pi}$ and Λ is the energy scale up to which the perturbative expansion of QCD Lagrangian holds (simply termed as "renormalization scale", usually referenced as the mass of W boson). The equation 2.3 implies that an inverse logarithmic dependence of the coupling strength α_s on momentum transfer Q^2 of the interaction. The momentum transfer can be related to the spatial separation of the quarks using the uncertainty principle as $r_q = \frac{\hbar}{\sqrt{Q^2}}$. For the smaller Q^2 (in the order of few GeV) or large values of the r_q (order of 1 fm), the coupling is stronger. This implies that a system of quarks is always confined as hadrons (i.e., a bare quark cannot be observed in nature). This phenomenon is usually referred to as confinement [7]. Therefore, the QCD processes at low energies that involve low momentum transfer interactions are typically characterized by the hadron degrees of freedom. However, at the higher Q^2 ($Q^2 \gg 1\,\mathrm{GeV}^2/\mathrm{c}^2$) the coupling strength reduces asymptotically, hence referred to as asymptotic freedom [8]. This leads to the possibility of observing a deconfined system of quarks and gluons, where the degrees of freedom are essentially quarks. Understanding the transition between the phases is a cornerstone of QCD research because it sheds light on the physical properties of the hadrons. The best example is the famous "mass deficit" problem [9], that the mass of hadrons is significantly higher than the sum of masses of the constituent quarks. For instance, in the case of protons

$m_{proton}(938\,\mathrm{MeV/c^2}) \gg\ 2 \times m_u + m_\mathrm{d}\ (9\,\mathrm{MeV/c^2})$.

2.3 "Recipes for the fireball"

The QCD fireball can be produced in the system having either high Q^2 ($> 1\,\mathrm{GeV^2/c^2}$) interactions or having a smaller inter-particle distance r ($\ll 1\,\mathrm{fm}$) or a combination of both. The high Q^2 can be achieved by increasing the system's temperature, whereas the small r is achieved by increasing the baryon chemical potential of the system at constant volume [10]. Within a few microseconds following the Big Bang, the high-temperature conditions were present to produce the fireball. The high baryonic density environment can be found in the cores of neutron stars and in neutron star mergers.

Similar conditions can be created by controlled collisions between relativistic hadrons and heavy-ions or a combination thereof at different particle accelerator facilities around the world. See for example, ALICE at LHC [11], STAR at RHIC [12], NA61 at SPS [13], and HADES at SIS18 [14]. The difference between the LHC (largest energy, $\sim$ TeV range) and the CBM (moderate energy, $\sim$ GeV range) energies manifests in the collision dynamics. At LHC energies ($\sim$ TeV), the overlap phase space essentially has vanishing baryon density and extremely high temperatures, reflecting the conditions of the early universe. However, at CBM energies ($\sim$ GeV) there is a high net baryon density environment and moderate temperature that resembles the conditions found in the core of neutron stars.

The deconfined quark-gluon phase is commonly referred to as the Quark-Gluon Plasma (QGP). The expansion of QGP is usually modeled as a low viscous fluid [15] (at LHC energies, the viscosity is estimated to be $\frac{\eta}{s} < 0.2$, where η is the shear viscosity and s is the entropy density [16, 17]). The deconfined phase of quarks and gluons can be achieved by collisions with few GeV center of mass energy (CM). The nature of a phase transition from the hadron to QGP is still unclear, particularly, the order of phase transition and ultimately the critical point(s) (depending on its order).

At vanishing net baryon chemical potential (μ_B) the phase transition is a crossover type. It is well understood theoretically by state-of-the-art lattice QCD calculations [18]. Experimentally, ALICE at LHC probes the $\mu_\mathrm{B} \approx 0$ regimes exhaustively for all temperatures, where the crossover temperature is measured for different systems. However, at higher μ_B, the lattice QCD suffers from its famous "sign problem" [19], making it hard to impossible to obtain firm predictions from the lattice calculations in this regime of the phase diagram. Although, extensive work in this field is carried out by different groups across the world [20]. At these regimes, we have only very few experiments, for instance STAR at RHIC and the CBM at FAIR. Hence, there exist limited avenues to probe the high μ_B region, both theoretically and experimentally.

After the initial collision phase, the fireball expands, and as the fireball expands, it cools down. Consequently, the mean free path of constituents becomes larger. The increased inter-particle distance forces the quarks to recombine to form different hadrons (confinement). Hence, a

transition from a deconfined phase to a confined phase of quarks and gluons is achieved. The production of different flavors of particles ceases after a certain temperature, called chemical freezeout temperature [21]. The statistical hadronization model predicts the yield of different particles for orders of magnitude in the energy of the system [22]. By calculating the ratios of different particle yields (which cancels the volume effect) one can estimate the temperature of the system at chemical freezeout equilibrium (T_c). After chemical freezeout, the particles continue to do elastic scattering, but this scattering ceases after a characteristic kinetic freezeout temperature [21, 23]. The freezeout system is better described by the blast wave approach based on hydrodynamics. The particles at the kinetic freezeout after decays of resonances (if any) will reach the detectors as final state long-lived hadrons (pions, kaons, and protons) and leptons (electrons and muons). The entire fireball evolution is in the order of a few Fermi length scales. Hence, the fireball produced in the initial stages of the collision is probed using its signatures on the final state particle spectrum. Many observables are proposed over time to probe the dense fireball and to establish the equation of the state of the matter. In the next section, a few of the signatures relevant to CBM are discussed.

2.4 Signatures of QGP

The pressure gradient in the collision zone drives the expansion of the fireball. Non-central collisions typically have elliptically formed overlap regions, resulting in azimuthal angle dependent particle production, referred to as particle flow. Understanding the equation of the state of QGP is possible by characterization of such flow [24].

At CBM, for larger center-of-mass energies of about 5 GeV per nucleon, charm production sets in, allowing for production of $c\bar{c}$ pairs in the initial, hard collisions. Due to the presence of deconfined quarks and gluons, the produced charm quarks undergo a color screening. Color screening leads to a separation of c and $\bar{c}$ quarks, and hence to an enhancement of open charm production (D-Mesons), on the other hand, production of J/ψ particle (hidden charm, $c\bar{c}$ meson) is suppressed. Thus, an enhancement of open charm production and suppression of the $c\bar{c}$ meson production in heavy-ion collisions compared to the elementary proton-proton collisions (absence of QGP) acts as the signature of the QGP [25].

The conserved quantities of the system fluctuate near the critical point(s). For heavy-ion collisions, these conserved quantities include the charge, baryon number, and strangeness. Therefore, estimating the fluctuations of these conserved quantities as a function of the center of mass energy of the collisions may provide clues regarding the location of the critical point [26].

During all stages of the evolution of the fireball, both real and virtual photons are produced. The latter decays into di-leptons. The produced di-leptons undergo electromagnetic interactions only and are least affected by the strong interactions in the medium and subsequent hadron phase, and hence it is a relatively pure signature to probe the QGP. The virtual photons and their subsequent decay to di-leptons will be the focus of this thesis.

2.5 Di-lepton production in a thermal medium

The di-lepton production in thermal medium is extensively explored in [27, 28, 29, 30, 31, 32, 33] and references therein. Consider a system with N initial quarks and gluons interacting to produce M final state quarks and gluons plus a di-lepton pair[1].

$$\underset{\text{Initial state quarks and gluons}}{(p_1^\mu, p_2^\mu, ...p_N^\mu)} \rightarrow \underset{\text{Final state quarks and gluons}}{(p_1'^\mu, p_2'^\mu, ...p_M'^\mu)} + \underset{\text{dileptons}}{(\bar{p}_1^\mu, \bar{p}_2^\mu)} \tag{2.4}$$

The number of di-leptons produced per unit volume can be written as [28, 34],

$$\begin{aligned}\frac{\mathrm{d}N^{l^+l^-}}{\mathrm{d}^4x} = e^4 \int \left(\prod_{i=1}^{N} \frac{\mathrm{d}^3p_i}{(2\pi)^3 2E_i}\right)\left(\prod_{j=1}^{M} \frac{\mathrm{d}^3p'_j}{(2\pi)^3 2E'_j}\right) \frac{\mathrm{d}^3\bar{p}_1}{(2\pi)^3 2\bar{E}'_1}\frac{\mathrm{d}^3\bar{p}_2}{(2\pi)^3 2\bar{E}'_2} \times \\ (2\pi)^4\delta\left(\sum_{i=1}^{N} p_i - \sum_{j=1}^{M} p'_j - \bar{p}_1 - \bar{p}_2\right) < p_{1..N}|j^\mu_{em}|p'_{1..M} >< p'_{1..M}|j^\nu_{em}|p_{1..N} > \times \\ \prod_{i=1}^{N} f_i \prod_{j=1}^{M}(1+f_j)\bar{u}(\bar{p}_1)\gamma^\mu v(\bar{p}_2)\frac{1}{q^4}\bar{v}(\bar{p}_2)\gamma^\nu u(\bar{p}_1)\end{aligned} \tag{2.5}$$

Where $q^\mu(q_0, q) = \bar{p^\mu}_1 + \bar{p^\mu}_2$ is the four-momentum of the virtual photons that decay into di-leptons. The function f is either the thermal Fermi-Dirac distribution for quarks or the Bose-Einstein distribution for gluons, assuming that di-leptons arise from a thermalized medium with temperature T and baryon chemical potential μ_B. The di-leptons however do not thermalize with the medium because they leave the medium faster and effectively undisturbed compared to the time for the system to thermalize [28].

According to McLerran-Toimela [28], by further simplifying the equation 2.5, the di-lepton emission per volume and 4-momentum of the virtual photons is expressed as,

$$\frac{\mathrm{d}^8N^{l^+l^-}}{\mathrm{d}^4x d^4q} = -\frac{\alpha_{em}^2}{\pi^3}\frac{L(q)}{q^2} f^b(q_0, T)\frac{g_{\mu\nu}}{3}\mathrm{im}(\Pi^{\mu\nu}_{\mathrm{em}}(q^2, q; T, \mu_\mathrm{B})). \tag{2.6}$$

where. $L(q)$ is the lepton phase factor [28], this quantity is essentially unity for the larger momentum of the virtual photons or vanishing lepton mass. Also note, $q^2 = q_\mu q^\mu = q_0^2 - \mathbf{q}^2 = M^2$, where M^2 is the invariant mass of the di-leptons. Hence, the equation 2.6 can be written in terms of invariant mass as [33],

$$\frac{\mathrm{d}N^{l^+l^-}}{\mathrm{d}M} = \int d^4x \frac{M\mathrm{d}^3\mathbf{q}}{q_0}\frac{\mathrm{d}^8N^{l^+l^-}}{\mathrm{d}^4x d^4q} \tag{2.7}$$

It is clear from equations 2.6 and 2.7 that by measuring the invariant mass of the di-lepton pairs in the experiment, we can access the imaginary part of the spectral function $\Pi^{\mu\nu}$ of the virtual photons.

[1] Each 4 momentum has Energy (E) and the momentum vector (p). The vector sign is dropped for simplicity.

On a similar footing to equation 2.6, one can write the "real" photon emission from the thermalized medium as [33],

$$q_0 \frac{\mathrm{d}^7 N^{l^+l^-}}{\mathrm{d}^4 x d^3\mathbf{q}} = \frac{\alpha_{em}}{\pi^2} f^b(q_0, T) \frac{g_{\mu\nu}}{2} \mathrm{im}(\Pi^{\mu\nu}_{\mathrm{em}}(M = 0, q; T, \mu_{\mathrm{B}})) \tag{2.8}$$

The photons have zero invariant mass, and hence it can be experimentally described only by its momentum distribution. Consequently, it is challenging to distinguish between distinct sources generating photons purely based on the momentum distribution. Therefore, the virtual photons are preferred over the real photons for understanding the QGP phase. Compared to the production of hadrons, the photon production is suppressed by the leading order factor of $\alpha_{em} \approx \frac{1}{137}$, while di-lepton production is further suppressed by the factor of $\alpha^2_{em} \sim 10^{-4}$ ($\gamma^* \rightarrow l^+l^-$ vertex) [35], and hence they are rare probes to understand the QCD medium.

Let us review the importance of the spectral functions to understand the phase transition. The spectral function of the virtual photons is expressed in terms of the electromagnetic currents as [23],

$$\Pi^{\mu\nu} = -i \int \mathrm{d}^4 x e^{-i\mathrm{q.x}} < [\mathrm{J}^{\mu}_{\mathrm{em}}(x), \mathrm{J}^{\nu}_{\mathrm{em}}(0)] > . \tag{2.9}$$

Here, $< .. >$ represents the thermal expectation value. The equation 2.9 is often referred to as the current-current correlation function. The electromagnetic current is defined as,

$$\mathrm{J}^{\mu}_{\mathrm{em}} = \sum_f \mathrm{q}_f \bar{f} \gamma^{\mu} f. \tag{2.10}$$

Where $f = (u, d, s)$ is the relevant quark flavors at lower CBM energies (which is below charm threshold $\mathrm{M_{ee}} < 2\ \mathrm{m}_c \approx 3\,\mathrm{GeV/c^2}$), q_f is the electric charge of the quark flavor f. In the relevant quark basis, the equation 2.10 can be expanded as follows,

$$\mathrm{J}^{\mu}_{\mathrm{em}} = \frac{2}{3}\bar{\mathrm{u}}\gamma^{\mu}\mathrm{u} - \frac{1}{3}\bar{\mathrm{d}}\gamma^{\mu}\mathrm{d} - \frac{1}{3}\bar{\mathrm{s}}\gamma^{\mu}\mathrm{s}. \tag{2.11}$$

The virtual photons have a spin of 1 and odd parity $J^P = 1^-$, similar to that of vector mesons. Thus, in the hadron degrees of freedom, i.e., at low-temperature the virtual photons couple to the low mass vector mesons. At the low invariant mass regime, $M_{ee} < M_{dual}$ where $M_{dual} \approx$ 1 GeV/c^2-1.5 GeV/c^2 one can rearrange the equation 2.11 in the hadron basis as, [2]

$$\mathrm{J}^{\mu}_{\mathrm{em}} = \frac{1}{2}(u\gamma^{\mu}\bar{u} - d\gamma^{\mu}\bar{d}) + \frac{1}{6}(u\gamma^{\mu}\bar{u} + d\gamma^{\mu}\bar{d}) - \frac{1}{3}\bar{\mathrm{s}}\gamma^{\mu}\mathrm{s} = \frac{1}{\sqrt{2}}\mathrm{J}^{\mu}_{\rho} + \frac{1}{3\sqrt{2}}\mathrm{J}^{\mu}_{\omega} - \frac{1}{3}\mathrm{J}^{\mu}_{\phi} \tag{2.12}$$

Where $\mathrm{J}^{\mu}_{\rho} = \frac{1}{\sqrt{2}}(u\gamma^{\mu}\bar{u} - d\gamma^{\mu}\bar{d})$, $\mathrm{J}^{\mu}_{\omega} = \frac{1}{\sqrt{2}}(u\gamma^{\mu}\bar{u} + d\gamma^{\mu}\bar{d})$, $\mathrm{J}^{\mu}_{\phi} = \bar{s}\gamma^{\mu}s$ are the respective representations of currents of LMVM in their constituent quark basis. The equation 2.12 enters quadratically into the Π_{em}, thus giving rise to relative contributions from vector mesons as $\rho : \omega : \phi =$ 9: 1: 2. Hence, the ρ is the dominating contribution in the lower invariant mass spectrum. However, at the high invariant mass/ high-temperature regime $M_{ee} > M_{dual}$, due to the dominance of quark degrees of freedom the virtual photon production can be attributed to

[2] The term "dual" arises from the Parton-Hadron duality described in [36] and references therein, description of which is beyond the scope of this thesis.

the annihilation of $q\bar{q}$, leading to a perturbative $q\bar{q}$ continuum. These processes are illustrated by the Feynman diagrams 2.2.

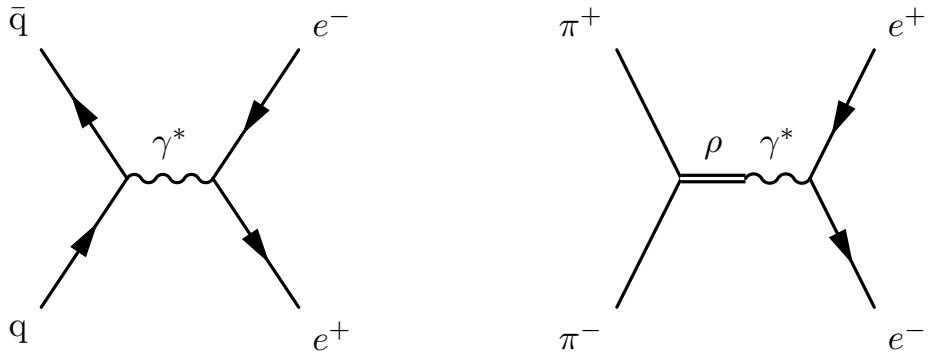

Figure 2.2: QCD Feynman diagrams of leading order virtual photon production in hot dense medium which further decays into di-electrons. Left panel: Quark-antiquark annihilation in QGP. Right panel : Pion annihilation in hadronic medium, producing a virtual photon coupled to a ρ meson.

2.6 Theoretical estimation of di-lepton production in medium and vacuum

The production of di-lepton in medium and vacuum is described in [37, 38, 31, 30, 39, 40] and references therein. The vector meson dominance model [37] states that hadronic currents are saturated by the light vector mesons. VMD directs to further rewrite the spectral function 2.9 in terms of the meson propagators at hadron degrees of freedom as,

$$\mathrm{im}\Pi = \sum_{V=\rho,\omega,\phi} (\frac{m_V^2}{g_V})^2 \mathrm{im}D_V. \tag{2.13}$$

Here g is the relative contribution factor and D_V is the propagator function of the vector meson V. We will focus on ρ, since it has the dominating contribution to the spectral function. In vacuum, a simple modelling is introducing the ρ meson as a gauge boson into the $\pi + \rho$ Lagrangian [38], giving rise to a propagator that has contribution from only its self energy term $\Sigma_{\rho\pi\pi}$,

$$\mathrm{D}_\rho(\mu_B = 0) = \frac{1}{M^2 - (m_\rho^0)^2 - \Sigma_{\rho\pi\pi}(M)}, \tag{2.14}$$

where m_ρ^0 denotes the bare mass of the ρ meson. This scenario is best recreated in the QCD vacuum, for example in the $\mathrm{e^+e^-}$ annihilation, where the relative production of hadrons are measured with respect to muons for various collision energies as depicted in figure 2.3. The quantity R is a ratio of cross-sections of $\mathrm{e^+e^-}$ into hadrons and muons, which is related to the vacuum EM spectral function as,

$$R = \frac{\sigma_{ee\to hadrons}}{\sigma_{ee\to\mu\mu}} \propto \frac{\mathrm{im}\Pi^{\mu\nu}_{\mathrm{vaccuum}}}{M^2}. \tag{2.15}$$

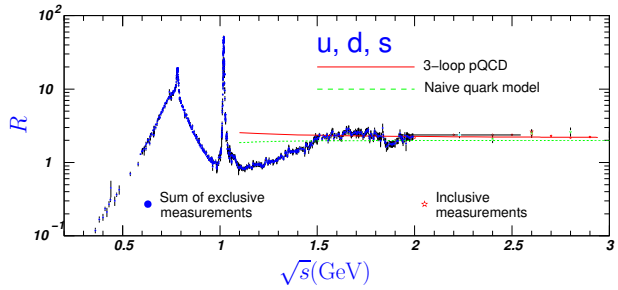

Figure 2.3: Ratio of cross-sections, R (Equation 2.15) as a function of center of mass energy $\sqrt{s}$ of e^+e^- collisions (Blue). The data depicts the abundance of the low mass vector mesons ρ, ω, and ϕ up to $\sqrt{s} \approx 1.1\,\text{GeV}$ transitioning into perturbative regime $\sqrt{s} \gtrsim 1.5\,\text{GeV}$ described by pQCD (Red) with light quark flavors (u, d, and s) [41].

In vacuum the di-electron annihilation is precisely explained by combination of hadron resonance production at lower collision energies ($< 1\,\text{GeV}$) and perturbative $q\bar{q}$ continuum of light quarks at higher energies ($> 1.5\,\text{GeV}$).

To comprehend the dynamics of the in medium ρ meson, we introduce them into the hadronic medium. According to the hadronic many body theory [29], the ρ propagator modifies as follows,

$$\mathrm{D}_\rho(\mu_B) = \frac{1}{M^2 - (m_\rho^0)^2 - \Sigma_{\rho\pi\pi}(M, \mu_\mathrm{B}) - \Sigma_{\rho B} - \Sigma_{\rho M}}. \tag{2.16}$$

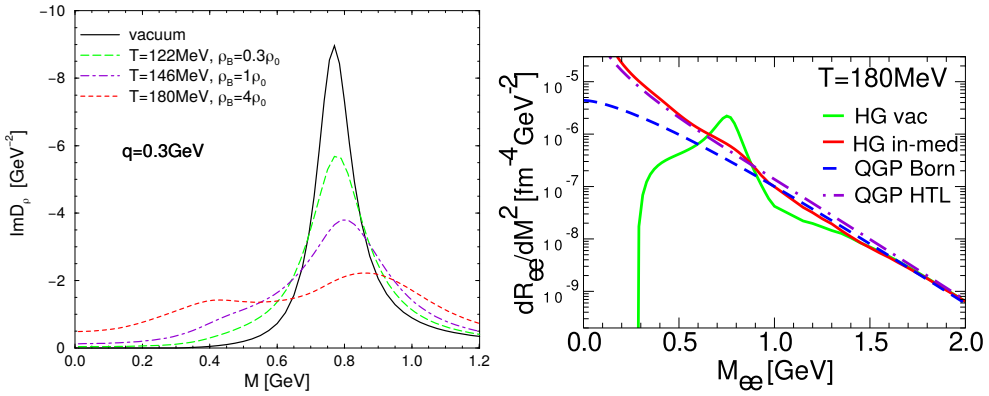

Figure 2.4: Left panel: Imaginary part of the ρ spectral function calculated in hadron many body theory for mediums with different temperature and baryon density, including vacuum. The resonance width increases at higher temperature and baryon density [30]. Right panel: Di-electron emission rate calculated using hadron gas model at vacuum (Green) and in-medium (Red) compared to the pQCD calculations with free non-interacting quarks (Blue) and with medium interactions (Violet).

In this scenario, the self energy of ρ is modified by the in-medium pion cloud [39], and direct interactions with mesons and baryons [40, 31]. The relative contributions of various components indicated in equation 2.16 are discussed in [29], wherein the modifications to the ρ self energy are predominantly attributed to baryons. The key point here is that at high temperatures or at

high baryon densities, the abundant hadrons interact strongly with the ρ mesons. Consequently, an extreme collision broadening occurs, where the width of the resonance equals its free mass. This phenomenon is loosely termed as the "melting of ρ", it is depicted in the figure 2.4 (Left). The bottom-up pQCD calculations of the thermal di-electron emission from QGP agree with the hadron many body theory, as depicted in the figure 2.4 (right). The spectral function of ρ merges into the quark-gluon description by pQCD at high invariant mass. This indicates the transition from the hadronic to the quark-gluon degrees of freedom. We now comprehend that the ρ meson is the primary contributor to the dilepton spectrum in the low invariant mass regime, whereas at high invariant mass, the emission of di-leptons results from in-medium $q\bar{q}$ annihilation.

2.7 Di-electron productions from heavy-ion collisions

The different stages of a heavy-ion collision are shown in the figure 2.5 (left). Di-electrons are emitted at all stages of a heavy-ion collision. Initially, we have so-called first chance inter-

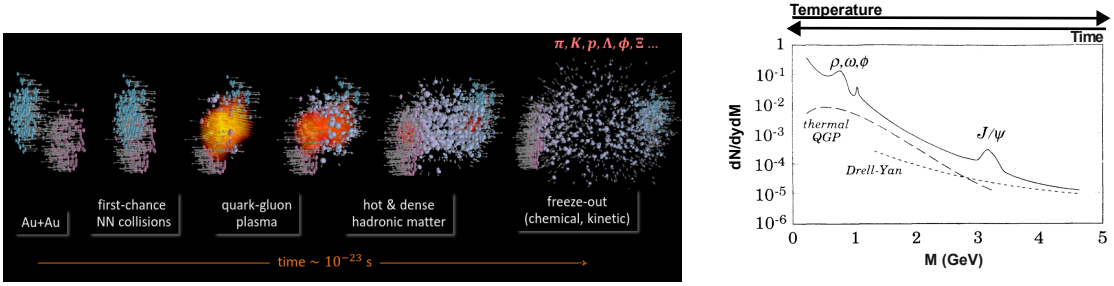

Figure 2.5: Left panel: Different stages of evolution heavy-ion collision [42] (Credits: Florian Seck) generated using UrQMD for Au-Au system. Right panel: Pictorial representation of different components of the di-electron invariant mass spectrum, with time and temperature ordering (adopted from Kampert, et. al. [32]).

actions, where the primordial $q\bar{q}$ annihilation takes place via nucleon Drell-Yan type process, $NN \rightarrow e^+e^-X$. The resultant di-electron pair typically has a large invariant mass. This portion cannot be experimentally isolated because it has a broad spectrum (due to missing mass of X), hence their contribution is simulated accordingly in theory estimations. The interesting part is the thermal radiation of the di-electrons, this includes the radiation from QGP ($q\bar{q} \rightarrow e^+e^-$) and from the hot and dense hadron medium. As explained in the previous section, the ρ mesons are the dominant hadronic component. Although non-dominant, the contribution from ω and ϕ still exists, since their lifetime is significantly longer than that of a typical fireball, such that their contributions should be calculated and carefully subtracted. In the same manner, the contribution from other long-lived hadron decays, including Dalitz decays of $\pi^0 \rightarrow e^+e^-\gamma$, $\eta \rightarrow e^+e^-\gamma$, and $\omega \rightarrow e^+e^-\pi^0$ should be subtracted. As a result, the background subtracted spectrum has the contribution only from thermal di-electrons. This exercise has been performed in several experiments [44, 45, 43]. The figure 2.6 depicts the di-electron spectroscopy from HADES at 2.42 GeV Au-Au collisions. After subtracting the background contributions, the excess invariant mass spectrum can be obtained. According to equations 2.6 and 2.7, if $\frac{\mathrm{im}\Pi_{em}}{M^2}$ is constant, then

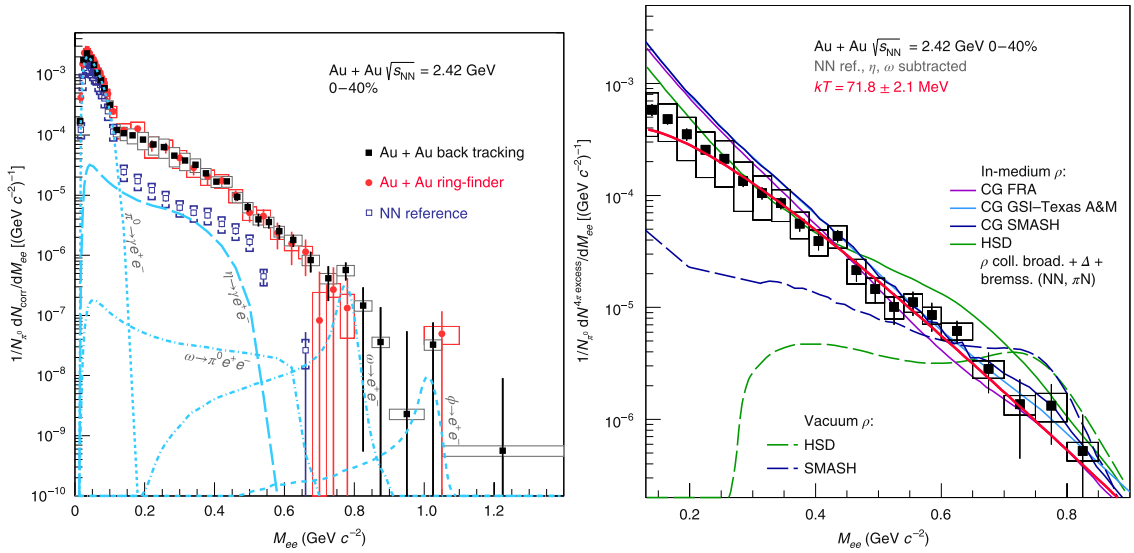

Figure 2.6: Di-electron spectroscopy at HADES for the Au-Au system at $\sqrt{s_{NN}}$ = 2.42 GeV [43]. Left panel: Di-electron invariant mass spectrum, with various contributions described in the text. Right panel: Excess di-electrons after subtracting background components. The vacuum and in-medium theoretical predictions for the excess spectrum are included, indicating that the in-medium ρ calculations describe the excess data reasonably well.

the excess spectrum $\frac{dN_{ee}}{dM}$ can be completely explained by the Boltzmann thermal distribution. Hence, the resultant excess spectrum can be fitted with a Boltzmann type distribution to obtain the source temperature. The temperature obtained from HADES data in the example is 71.8 MeV, indicated in figure 2.5 (right).

2.8 Challenges in di-electron reconstruction

In general, the detectors measure electron-positron tracks. From each track, the information on momentum ($\vec{p}$), and charge and its identity (mass m) can be derived using the tracking stations and particle ID detectors. Using $\vec{p}$ and m the energy of the particle $E = \sqrt{m^2 + \vec{p}^2}$ can be calculated. Finally, the invariant mass of the pair of leptons, from the electron track (E_1, $\vec{p_1}$) and from the positron track (E_2, $\vec{p_2}$) as $M_{e^+e^-} = \sqrt{(E_1 + E_2)^2 + (\vec{p_1} + \vec{p_2})^2}$ is derived. Forming all possible combinations from all identified e^- and all identified e^+ tracks within the same event leads to a large / certain combinatorial background due to mismatched pairs, which in theory can be estimated by event mixing techniques [46]. In heavy-ion collisions, pions are an abundant final state particle besides proton. The protons are heavy and hence can be eliminated by measuring their velocity (using time of flight detector in CBM). Whereas pions usually have a velocity close to the speed of light, similar to electrons. Hence, it is highly probable that pions may be mistakenly identified as electrons. The presence of pions in the electron sample further increases the combinatorial background. Increased misidentification leads to forming a distinct fake resonance also possibly extending towards the signal region of invariant mass. Hence, in order to efficiently reconstruct the rare di-electrons, a significant suppression of misidentification of pions as electrons is required.

3

CBM experiment

This chapter provides an overview of the FAIR facility, which hosts the CBM experiment and other major nuclear and particle physics experiments. The second part of the chapter emphasizes the CBM experiment itself, particularly it's different sub-detectors with their role in di-electron spectroscopy and the data acquisition infrastructure. A dedicated section of this chapter describes the working principle and technical construction of the RICH detector. The latter section provides an overview of the simulation and analysis framework of the CBM experiment, and in particular of the RICH. *Throughout this thesis, the beam traverses along the +Z direction.*

3.1 FAIR

The **F**acility for **A**nti-proton and **I**on **R**esearch is one of the world's largest accelerator complexes, which is being built in Darmstadt, Germany. FAIR will have the unique ability to produce beams of ions of all known elements, and in the medium term possibly also anti-protons [47]. The already existing facilities at GSI will be complemented by the FAIR facility. The UNIversal Linear ACcelerator (UNILAC) and SIS18 (beam rigidity, $B \times r = 18\,\mathrm{Tm}$) accelerator at GSI will act as the beam injector and booster for the FAIR. The injected beams are accelerated to relativistic speed (up to 99% speed of light for the heavy ions) by the superconducting ring accelerator (SIS100) of circumference 1100 m. The SIS100 (beam rigidity, $B \times r = 100\,\mathrm{Tm}$) ring accelerator is located 17 m below the ground. A combination of multipole superconducting

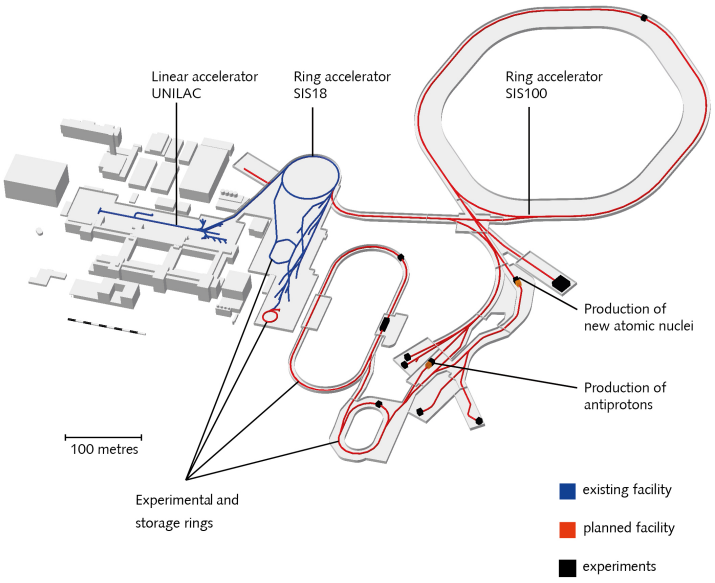

Figure 3.1: FAIR laboratory at the GSI complex, Darmstadt, Germany.

magnets accelerate and guide the beam. Liquid helium cools the superconducting magnets to $-269\,^{\circ}\mathrm{C}$. The available kinetic energy per nucleon (E/A) in the dipole field is given by the equation [23],

$$E/A = \sqrt{(0.3 \times B \times r \times Z/A)^2 + m^2} - m \tag{3.1}$$

where Z and A are the mass number and atomic number of the nuclei being accelerated, m is the mass of the accelerated nucleon, and $B \times r$ is the beam rigidity. In the SIS100 synchrotron the protons ($Z/A = 1$) can be accelerated up to kinetic energies of 29 GeV and Au beams ($Z/A \approx 0.4$) up to 11 AGeV. The accelerated beams can be used for experiments either directly or for the production of other secondary particles that are themselves then used as projectiles.

The four major pillars of the FAIR facility are:

NUSTAR: The **Nu**clear **ST**ructure, **A**strophysics and nuclear **R**eactions collaboration is tasked to study the structure of exotic atomic nuclei and to investigate reactions of these nuclei. The study results are relevant to understanding the element abundance in the universe. The

NUSTAR collaboration will use the **Super**conducting **Fr**agment **S**eparator (Super-FRS) which enables the production of secondary exotic isotopes and in-flight separation of the same [48]. Multiple sub-experiments will use these beams in different energy regimes within the collaboration. The low-energy branch uses the ions of energy between $0 - 300\,\mathrm{MeV/u}$, to probe excited nuclear states after the collision of radioactive isotopes with the target. It will be possible for high-precision mass measurements of exotic nuclei. Four collaborations, namely HISPEC/DESPEC, LASPEC, and MATS, are part of the low-energy branch [49]. The R3B collaboration is part of the high-energy branch with energies greater than 300 MeV/u [50] and it is tasked to study the reactions of rare isotopes, focusing on nuclear structure and dynamics. The Ring branch will use the beams in the storage ring to study ground and isomeric states of exotic nuclei being limited to radionuclides with a half-life above $10\,\mu\mathrm{s}$ and to perform electron scattering off short-lived radionuclides. Major experiments in the ring branch include the ILIMA, EXL, ELISe, and AIC [51].

APPA: APPA is an ensemble of several collaborations working with **A**tomic **P**hysics, **P**lasma, and **A**pplied sciences [52]. The Atomic Physics branch has two large sub-collaborations. One of them is the **S**tored **P**article **A**tomic physics **R**esearch (SPARC) which will use the beam from the **H**igh **E**nergy **S**torage **R**ing (HESR) to probe QED at different mean distances of the electrons from the nucleus [53]. However, the realization of the HESR is not yet fully established. The other is the **F**acility for **L**ow-energy **A**ntiproton and **I**on **R**esearch (FLAIR) is being designed to study the anti-hydrogen beam by using charged particle traps [54]. Plasma physics is planned to be conducted by the HED and WDM collaborations, whose program includes characterizing the warm, high-density matter usually found in the core of compact stars [55]. The Materials Research and Biomedical group is aiming to create new frontiers in radiotherapy with high-energy beams. The program also includes the study and synthesis of new radiation-hard materials for deep-space applications [55].

PANDA: The anti**P**roton **AN**nhilation at **Da**rmstadt is a proposed future fixed-target proton-anti-proton experiment with anti-proton beam momentum ranging from 1.5 GeV to 15 GeV that translates to the CM energy range from 2.2 GeV to 5.5 GeV [56]. The PANDA experiment is planned to be placed inside the HESR (if constructed), where the anti-proton beams are collected and collided with a hydrogen cluster jet or hydrogen pellet target (for open charm physics) [57]. The $p\bar{p}$ annihilation will provide the theoretical conditions of net zero-baryon density, which enables a wide physics program including the search for exotic particles, investigating the properties of hadrons, probing the nuclear structure, measurement of hypernuclei, and measuring strong medium effects on hadrons [58].[1]

CBM: The **C**ompressed **B**aryonic **M**atter experiment is a general-purpose experiment designed to systematically explore the QCD phase diagram at high baryon density and moderate temperature. A detailed explanation of the different sub-detectors of CBM is given in the next section.

[1] The synergy between the PANDA and CBM experiments is overwhelming, particularly concerning the proton program. Because of this the workshop "Physics Opportunities with Proton Beams at SIS100" was held at the University of Wuppertal [59].

3.2 CBM detector

The CBM experiment is a future fixed-target experiment operating at beam kinetic energies of up to 11 AGeV for heavy ions and up to 29 GeV for proton-ion and proton-proton collisions. At these collision energies, in heavy ion collisions, baryonic densities up to five times the normal nuclear density ($\rho_0 = 0.17$ nucleons / $(\mathrm{fm})^3$) [60] become accessible, which is sufficient to observe quark degrees of freedom. The CBM experiment has broad physics objectives summarized in the CBM physics book [23] each defined to study the fireball (QCD medium) produced in the collisions.

A few main physics objectives of the CBM experiment include:

1. **Criticality:** The event-by-event measurement of the fluctuations of conserved charges (baryon number, charge, and strangeness) can be used to locate the critical point and the order of phase transition.

2. **Vorticity:** It is understood that the angular momentum of the off-central collisions manifests as fluid vorticity. The spin coupling to the angular momentum results in the global polarization of the system. This was studied extensively across the HADES [61] and RHIC [62] experiments at different energies. The CBM data of Λ and other hyperons with high statistics enables the precise study of the vorticity at energies less than 5 AGeV.

3. **Emissivity:** High-precision di-lepton measurements can probe the QCD medium at all stages throughout the fireball evolution. Observables like di-lepton flow, polarization, and its excess production will shed light on the properties of the produced QCD medium.

4. **Hypernuclei:** The measurement of multi-strange hyperons and hypernuclei (Nucleus with bound hyperons, especially lambda hyperon) that might be formed in the dense core of neutron stars [63]. The measurement of the excitation function of hyperons and hypernuclei can provide valuable input into the equation of state of nuclear matter found in the core of neutron stars. Furthermore, it allows studying the hyperon-nucleon interaction, or, in the case of double hypernuclei, even the hyperon-hyperon interaction, which is again an important ingredient for the study of the equation of state of baryon-dense matter.

Being a fixed target experiment, the particles produced in the collision are boosted in the forward direction (direction of beam). CBM covers a hemisphere with an aperture of 2.5° to 25° in the laboratory frame for maximum acceptance for CM energies between 2 AGeV to 5 AGeV. The lower cut of 2.5° is due to the beam pipe tunnel. The probes for the QCD phases are often very rare, for instance, the $\rho \to e^+e^-$ decay channel has a branching ratio of 4.72×10^{-5} only. Even these rare probes can be studied with high statistical significance in the CBM experiment. This is achieved by engaging the detector at a high interaction rate of up to 10 MHz heavy-ion collisions, which is much higher than ALICE3 (~ 10 kHz), and STAR (~ 1 kHz) [64]. This large rate can be achieved at FAIR using high-intensity beams with up to 1×10^9 beam particles/sec $\times$ 0.01 interaction probability at the target. The high interaction rate leads to a high particle

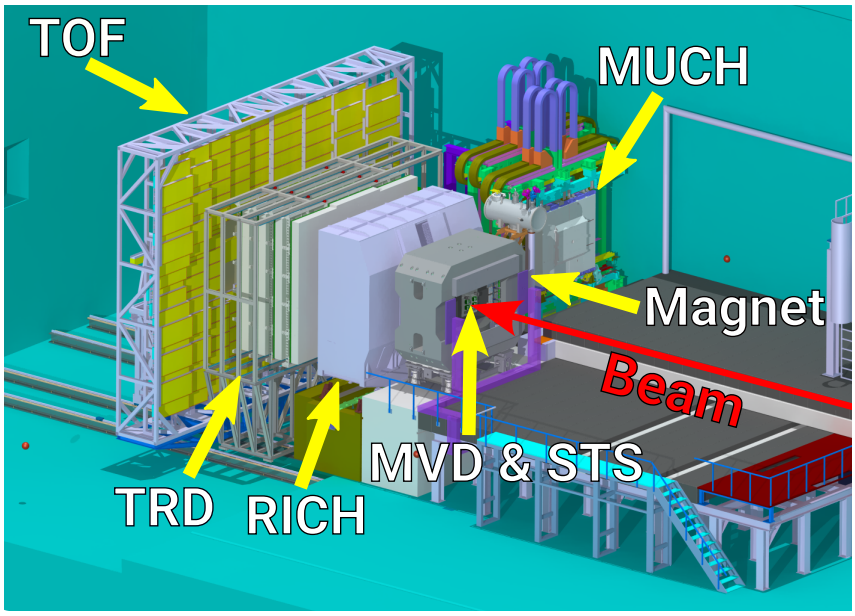

Figure 3.2: CAD rendering of the CBM detector in the SIS100 cave. Different sub-detectors and the direction of the beam (red) are indicated by the arrows. The forward spectator detector is located behind the time-of-flight detector (not depicted explicitly here).

flux of up to 1000 particles/event (central Au-Au collision) through the detector, hence all the sub-detectors are designed to be radiation-hard. The high collision rate requires the detectors to be fast to reduce the pile-up of hits from subsequent events. Some sub-detectors have several thousands of channels for the signal measurement. Since storing the data of each channel becomes challenging at high rates, a concept of free-streaming readout will be used in CBM, where each digitized signal is time-stamped and temporarily stored. A simple hardware or semi-hardware level data selection triggering scheme (like those used in ATLAS and CMS, which run at up to 1 GHz interaction rate) is not available for the CBM physics cases. Instead, an online real-time event reconstruction will be performed on the time-stamped data on a compute cluster. Based only on physics-based software triggers (for example, off-vertex decay of Λ), an event filtering scheme will be employed. The events of interest will depend on the physics goals of different beam campaigns. The figure 3.2, displays the setup of the CBM experiment. The description of different sub-detectors is given in the following section.

3.2.1 Beam Monitor (BMON)

The Time of Flight measurement to determine the velocity of the particle is made possible with the combination of stop time from the dedicated Time-of-Flight detector and start time from the T0 detector. This is crucial in reducing the misidentification of hadrons as electrons. The T0 system is housed as a station in the BMON system in addition to the beam halo station [65] with a complimentary arrangement. The BMON system is placed before the CBM target system. A polycrystal chemical vapour deposition diamond technology will be used for the T0 system, with a sensor size of 1 cm $\times$ 1 cm and 16 strips on both sides. The T0 measurement is foreseen

to have a timing precision of 50 ps [66]. Even at the highest interaction rates, corresponding to up to 10^7 beam particles/s, the BMON system is foreseen to work with an efficiency close to 100% [66].

3.2.2 CBM Magnet

Inside a superconducting (SC) dipole magnet, the target system, vertexing detector, and tracking stations will be placed. The magnet is of length 1.5 m and will provide a sufficient field integral of 1 T m to bend the charged tracks [67]. The magnetic field is not homogeneous, being higher along the vertical YZ plane. Assuming the particle boost direction along $+Z$, the track will experience maximum bending along the XZ plane and negligible bending along the YZ plane. The path of the charged track is traced by the tracking stations, thus allowing us to calculate the momentum-over-charge ratio of the particle.

3.2.3 Micro-Vertex Detector (MVD)

The **M**icro-**V**ertex **D**etector (MVD) consists of four planar stations with large-area monolithic active pixel sensors placed inside the superconducting magnet [68]. The MVD is designed to measure the displaced decay vertices of open charm, and weak decays of charged hyperons. The MVD is used in two configurations: vertexing and tracking. In the vertexing configuration, the first layer is set at 5 cm from the target and the subsequent stations are 5 cm apart, where a vertex reconstruction precision of $\sigma_{PvZ} = 4.1$ µm is achieved. In the tracking configuration, the first layer is at 8 cm and subsequent stations are 4 cm apart. As for di-electron measurement, the MVD is used as a tracker with four stations. This setup is to reconstruct and thereby reduce the background from electrons stemming from photon pair production (in the target material) that do not reach STS tracking system or electron identification detectors downstream (so-called "track segments"). Additionally, the MVD is used to apply "topological cuts" in dilepton reconstruction. A track pair where one of the legs is only seen in the MVD, not in STS, is both discarded because of probably conversion processes. Due to the proximity of the MVD to the target, the probability of reconstruction for such track segments is higher. The e^+e^- pair candidates are selected by charged track separation in the magnetic field. Since the conversion pair has a low opening angle, the close distance of these tracks in the first layer of MVD will provide the necessary rejection criteria. This is possible because of the excellent single-hit spatial precision of 5 µm.

3.2.4 Silicon Tracking System (STS)

The STS is a 3 + 5 stations modular tracking system for the CBM. All stations of STS are placed inside the SC magnet between 0.3 m to 1 m downstream of the target. The STS uses 876 double-sided silicon strips with a pitch of 58 µm, enabling a spatial resolution for a hit of about

25 µm [69]. Double-sided strips are used for two-dimensional tracking XY plane. The charged particles that traverse the sensor generate electron-hole pairs, resulting in the loss of energy. Electrodes capture the charge that is produced. The signals from the electrodes are captured by the self-triggering front-end readout electronics with a shaping time of 20 ns. Double-sided strips (XY coordinates), a modular multi-station design (Z coordinate), and time stamping precision (T coordinate) allow for the 4D reconstruction of tracks (X, Y, Z, T). With these settings, a momentum resolution $\frac{\mathrm{d}P}{P}$ of about 1% can be achieved for maximum magnetic field operation. The multiple scattering of charged tracks in the detector material is the bottleneck for the momentum resolution. Hence, the sensors and other components are made lightweight with a limited material budget within the acceptance. Energy loss in the STS can be used as an additional particle identification feature. Since the energy loss is proportional to the squared charge, the STS can separate the same momenta-different charge number particles, for example He_3^{2+} vs deutron vs proton. Good electron-pion separation cannot be efficiently achieved within the current STS design.

3.2.5 Muon Chamber (MUCH)

The MUCH detector is placed next to STS in the muon setup for dedicated measurements of muons from the decays of low mass vector mesons (ρ, ω, ϕ) and J/ψ [70]. As muons are penetrating particles, in order for their pure identification, the hadrons produced from the collision need to be absorbed. To prevent the absorption of low-momentum muons, the hadron absorbers are split into four stations, where each station is equipped with three layers of gaseous detectors. This setup will enable a momentum-dependent measurement of muons. The latest optimized design of the MUCH detector [65] foresees the first station with 28 cm low-density graphite and 30 cm concrete, and subsequent stations will be equipped with iron absorbers of 20 cm, 20 cm, and 30 cm thickness. Gas Electron Multiplier (GEM) based detectors will be used for the first two stations because they are high-rate capable and can withstand a large flux of particles ($\sim 1\,\mathrm{MHz/cm^2}$, $\sim 0.1\,\mathrm{MHz/cm^2}$ respectively). Because of the absorbers, the third and fourth stations will see only $\sim 15\,\mathrm{kHz/cm^2}$ and $\sim 5.6\,\mathrm{kHz/cm^2}$ respectively [71]. Hence, the use of Resistive Plate Chambers (RPCs) is foreseen for the last two stations, providing better timing precision as compared to the GEM detectors in the first layers. The MUCH enables the exploration of di-lepton spectroscopy in the muon channel, which is complementary to the electron channel.

3.2.6 Transition Radiation Detector (TRD)

The transition radiation detector has a single station composed of four detector layers positioned behind the RICH [72]. The TRD is based on the principle that fast particles traversing between two media with different dielectric constants produce transition radiation (TR) [73]. The energy deposited by the particle and the TR are the basis for particle identification. In this scheme, the CBM TRD will use foam as the radiator. Relativistic electrons produce TR while pions and

heavier particles which are slower will not produce TR, enabling the electron/pion separation. The particle and the TR will then reach the ionizing gas chamber composed of Xe/CO_2 mixture (85%:15%) [72]. This gas mixture is chosen since for typical TR with energies less than 10 keV the Xe has an absorption length of 10 mm. The electrons from the ionization process drift into a Multi-Wire Proportional Counter (MWPC) producing a signal which is then shaped by the readout electronics. PID is performed using the combination of energy losses in the layers (see chapter 5). In the di-electron setup, the TRD is used to identify electrons with momenta above 1 GeV/c with an efficiency of 80% at a pion suppression factor of about 20. The TRD geometry has two types of modules, TRD-1D and TRD-2D pads. The TRD-1D pads are rectangular and have a good spatial resolution in one dimension while the TRD-2D modules which will populate the low p_T region around the beam pipe, have a good spatial resolution in both dimensions ($\sigma_x \approx 100\,\mu m$, $\sigma_y \approx 800\,\mu m$) [74]. This excellent spatial resolution enables us to use the TRD as an intermediate tracker (see chapter 6).

3.2.7 Time of Flight detector (TOF)

The TOF uses Multi-gap timing Resistive Plate Chambers (MRPC) for particle detection. The principle of the MRPC is similar to that of a silicon sensor (section 3.2.4), except the electrodes are placed around a gas chamber. A charged particle passing through the gas chamber will cause ionization along the track within the gas. When the voltage is applied to the electrodes, these free charges accelerate and further ionize the gas, thus resulting in an avalanche of electrons and holes. These charges then move towards the electrodes, producing a signal. The TOF detector in CBM is made up of six different kinds of modules with varying sizes of multiple MRPC strips. The thickness of the gas layer determines the timing resolution of the TOF. MRPCs have an overall timing precision of 60 ps [75]. The TOF will be placed at about 6 m to 10 m downstream from the target. For the maximum acceptance at 10 m from the target, the TOF has an active area of 120 m^2. Using the length of the track from the origin to TOF and the time information, the velocity of the track can be calculated. This can be used for particle identification (Chapter 5).

3.2.8 Forward Spectator Detector (FSD)

The previously conceived forward wall Projectile Spectator Detector (PSD) is re-conceptualized into the Forward Spectator Detector (FSD) [65]. The FSD is planned as a plastic scintillator detector where the high-energy particles produce scintillation light. MAPMTs are used to capture the scintillation light [76]. The DIRICH+TRB readout chain (the same as the RICH) will be used to process the signals from PMTs. FSD will measure the centrality of the collision and its event plane [77], hence will play a role in the centrality differential analysis of the di-electron spectrum. A proposal under consideration is to add a neutron calorimeter (NCAL) in addition to FSD for reconstruction of neutrons under small scattering angles.

3.2.9 Data acquisition (DAQ) infrastructure

The DAQ infrastructure collects the outputs from each sub-detector and bunches them into micro-time slices. The HTG-Z920 common readout interface (CRI) boards, housing a Xilinx Kintex FPGA will collect all the time-stamped data from the FEBs connected to Common Readout Boards (CROBs) via GBT links and TRB links (for RICH). Sub-nanosecond synchronization is required for the free streaming readout setup. A Timing and Fast Control (TFC) provides synchronization triggers to the FEE via CRI boards [78]. All data from the CRI is passed to the First-Level Event Selection (FLES) input nodes via a PCIe connection. Thus, the CRI connects the hardware parts of the readout and the software architecture of the event building and selection. On the FLES input nodes, the data container from the CRI is bunched into micro-time slices. The FLES input nodes are dedicated compute nodes for the operation of CBM and will be present along the DAQ in the CBM cave [79]. The micro slice data is then passed via InfiniBand (a high-speed optical connection) to the FLES computing nodes. The FLES combines the time-stamped data of about 100 ms into a large data format. This data is then used for online event/track reconstruction and selection. Together with the data packaging, the FLES input nodes provide a connection to the Experimental Control System (ECS) via Ethernet. The ECS is a high-level control system that interfaces with the front-end boards, online systems, and monitoring systems of each detector [80].

3.2.10 Compute Cluster

The data from the experiments and the simulations are processed using the high-performance computing (HPC) facility at GSI. The CBM users use the Virgo compute cluster. Virgo nodes allow the user to run applications on Linux containers, separating the host and user nodes. The cluster is housed inside the “Green IT Cube”. The water cooling concept allows for the IT cube to be dubbed Green and highly power efficient.

3.2.11 Ring Imaging CHerenkov detector (RICH)

The RICH detector is the prime electron identification detector for CBM. The electron identification in RICH is based on the principle of the Wawilov-Cherenkov effect. The effect describes photon radiation that is emitted when a charged particle traverses a medium at velocities larger than the speed of light in that medium. Cherenkov proposed the effect in a paper [81], where he pointed out that when fast electrons traverse through pure liquids, they produce visible radiation.

A pictorial representation of the Cherenkov effect is shown in figure 3.3. Assuming the charged particle travels through a dielectric medium that has a refractive index $n(\lambda)$ (for the photons of wavelength λ), the electric field of the charged particle induces momentary dipoles around the particle trajectory. Given the velocity of the particle v_p smaller than the speed of light

in the medium $\frac{c}{n(\lambda)}$, this polarization is globally symmetric, meaning the net field at a large distance is zero, and hence no radiation is observed. Conversely, if the velocity of the particle, $v_p > \frac{c}{n(\lambda)}$, then an asymmetry in polarization along the particle trajectory is produced. This results in the production of coherent radiation at an angle θ with respect to the velocity vector of the particle [82]. At the Cherenkov threshold, the velocity becomes $v_{pc} = \frac{c}{n(\lambda)}$, therefore $\beta_c = \frac{v_{pc}}{c} = \frac{1}{n(\lambda)}$. From the figure 3.3 we see,

$$\cos(\theta_c(\lambda)) = \frac{c\delta t}{n(\lambda)v_{pc}(\lambda)\delta t} = \frac{c}{n(\lambda)v_{pc}} = \frac{1}{\beta_c n(\lambda)}. \tag{3.2}$$

The Lorentz factor for a relativistic particle is given by the equation,

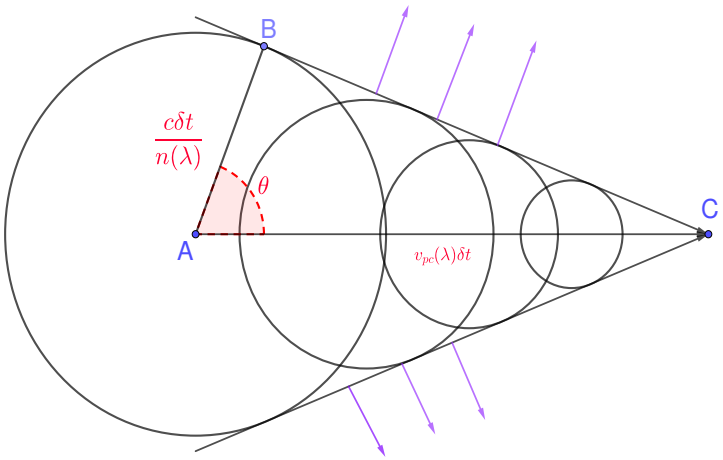

Figure 3.3: Pictorial representation of the Cherenkov radiation. The particle enters the medium at point A and reaches point C at time δt. The Cherenkov photons that were originating at A reach point B at time δt. The outward arrow (Violet) indicates the trajectory of the Cherenkov photons.

$$\gamma = \sqrt{1 + (\frac{p}{mc})^2}. \tag{3.3}$$

Therefore, the threshold Lorentz factor for the particle to produce Cherenkov radiation is given by,

$$\gamma_c = \sqrt{\frac{1}{1-\beta_c^2}}. \tag{3.4}$$

Using the above equations, one can find the threshold momentum (p_c) for a particle of mass m to produce Cherenkov radiation as,

$$\sqrt{1 + (\frac{p_c}{mc})^2} = \sqrt{\frac{1}{1-\beta_c^2}} \implies p_c = mc\sqrt{\frac{1}{n(\lambda)^2 - 1}}\ . \tag{3.5}$$

From equation 3.5, one can infer that by carefully choosing the radiator medium, i.e., by controlling $n(\lambda)$, the Cherenkov threshold for different particle species can be controlled, which enables particle species identification. The CBM RICH will use CO_2 gas with a refractive index, $n(600\,\text{nm}) \approx 1.00045$ as the radiator. This close-to-unity refractive index provides a momentum threshold p_c of 4.65 GeV/c for charged pions (m=135 MeV/c^2) while for the electrons

($m = 0.5\,\mathrm{MeV/c^2}$) it is $16\,\mathrm{MeV}/c$ thus allowing pion-electron separation.[2] Cherenkov photons are produced over a wide wavelength range from far UV to infrared, but CO_2 absorbs light at wavelengths below 180 nm. CO_2 also has a lower probability for fluorescence compared to other gases with similar refractive index (traversing charged particles produce scintillation). The CO_2 at 2 mbar over-pressure will be housed inside a hermetically sealed gas vessel (RICH box) made of steel and aluminium, with thin entry- and exit windows made of composite materials with a low material budget. The optimization of material composition and thickness of the entrance and exit windows for the RICH box is yet to be performed.

Frank and Tamm who jointly shared the Nobel Prize with Cherenkov, derived the equation for the Cherenkov photon multiplicity [83] produced per unit length (x) and wavelength (λ) (equation 3.6).

$$\frac{d^2N}{dxd\lambda} = \frac{2\pi\alpha Z^2}{\lambda^2}\left(1 - \frac{1}{\beta^2 n^2(\lambda)}\right), \tag{3.6}$$

here α is the fine structure constant and Z is the atomic number of the radiator. Assuming a constant refractive index $n(\lambda = \text{constant})$, the photon multiplicity falls quadratically with respect to λ. One can do a simple transformation from wavelength to energy ($E = \frac{hc}{\lambda}$) to find the multiplicity is constant over the energy. Integrating the equation 3.6 for the radiator length of 2 m and wavelength above 180 nm we get a photon multiplicity of ~ 100. The Cherenkov photons are produced at an angle θ with respect to the direction of the charged particle through the medium. In order to capture the Cherenkov photons with maximum efficiency, a spherical focusing mirror system is used. The mirror system consists of an upper- and lower half, both halves are slightly tilted outside (12 degrees) in order to reflect the photons outside the CBM acceptance, where they are captured by the photon cameras. This scheme helps to avoid the presence of the photon sensors and read-out electronics within the detector acceptance. A similar concept of the RICH optical system is also used in other experiments [84, 85].

The two halves of the spherical mirror system are each made of 40 (5×8) glass mirror tiles coated with Al + MgF_2. Each mirror tile is trapezoidal-shaped with an 40 cm edge length and a radius of curvature of 3 m, hence the focal length is 1.5 m ($f = \frac{R}{2}$ for the spherical mirror). The mirrors have a reflection efficiency of about 85% for the expected wavelengths of Cherenkov photons [86].

The spherical mirror has a spherical focal plane, hence to cover all photons ideally one needs to build a spherical camera. Since building such a camera is unfeasible, a compromise using a cylindrical design with a tilt with respect to the X axis is made [87]. Using such a setup, the radius of the rings formed by the electrons originating from the target is nearly constant. The camera is a 2D array of Multi-Anode Photon Multiplier Tubes (MAPMT) made by Hamamatsu (see Chapter 4). A box made up of Iron houses the camera, this is to shield the MAPMTs from the magnetic stray field of the SC magnet. The placement of the RICH camera, the size of the mirror, and the selection of the photon sensor ensure a geometrical acceptance of 90% for electrons with momenta above $1\,\mathrm{GeV}/c$ emitted within the acceptance of CBM (2.5° to 25°).

[2] The temperature and pressure dependence of the refractive index are not considered.

3.3 CBM simulation and reconstruction framework

The detector simulation is necessary for understanding the capabilities of the detector, further optimization of the detector design, and physics performance evaluation. CBMROOT is C++ based simulation and analysis software based on the ROOT data analysis framework. In the first generation, CBMROOT encapsulated all the necessary packages for the complete detector simulation. Since multiple FAIR experiments had similar requirements, the software framework was split into FAIRSOFT, FAIRROOT, and other detector-specific software frameworks (CBMROOT, PANDAROOT, R3BROOT, etc.). FAIRSOFT includes the backbone packages like GEANT, Pythia, ROOT, Boost, and Virtual Monte Carlo (VMC) [88]. FAIRROOT [89] uses all FAIRSOFT packages and builds a framework of base classes on top that the detector groups can use. This includes the GEANT transport, track classes, and visualization of events.

The components of the simulation are depicted in the flowchart 3.4.

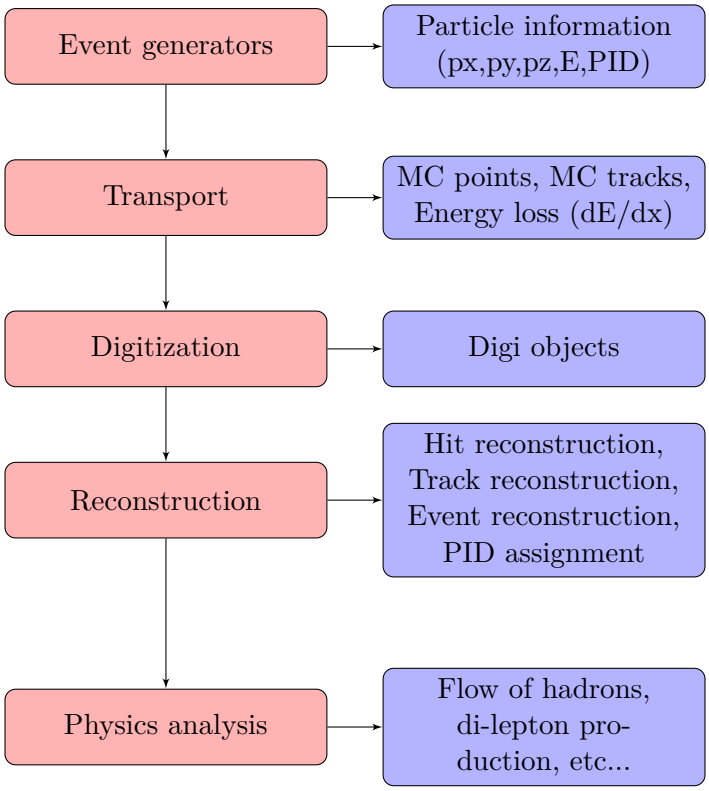

Figure 3.4: The flowchart of the CBMROOT analysis framework shows each stage of simulation (Red) and the information from each stage (Blue).

Event generation: Monte Carlo event generators are used to simulate events at a given energy and collision system. The event generators, which are based on physics models, provide us with a list of particles with their phase space parameters (vertex, momentum vector, energy, and type (PID)). The event generators used in this thesis are UrQMD, PLUTO, and FAIRBox generators.

Ultra-relativistic Quantum Molecular Dynamics (UrQMD): UrQMD is a microscopic transport

model that treats the nuclei collisions as multiple nucleon collisions [90]. In the context of this thesis, the UrQMD generator is used to generate complete events from which the background contributions, mainly the production of pions from the collisions and hadron decays, are derived. While the other generators are used to produce the electrons or decays of LMVM.

PLUTO: The decay of ω, ϕ, ρ into di-leptons is rare. To generate sufficient numbers of these decays, one therefore needs to either simulate more collision events or artificially enhance decays in every collision. The PLUTO event generator is used to produce rare decays in the boosted frame. Embedding the decay into the UrQMD simulated collision event allows enriching the data samples with particle decays of interest [91].

FAIRBox generator: The FAIRBox generator is used to generate a specific particle species within a given kinematic parameter range. In this thesis, the FAIRBox generator is used to generate electrons within the acceptance, either standalone or in combination with UrQMD-generated collision events. Pure FAIRBox-generated electron samples are used to derive the geometrical acceptance for the different PID detectors.

Transport: The particles generated by the event generators are transported through the detectors using the GEANT engine [92, 93]. For each detector and its sub-volumes, the transport class uses the geometry objects created using TGeoManager. These geometry objects can be made from active and passive materials (software definitions, no physical difference). The tracks propagated through materials interact with it. The interaction in the active material, which is usually characterized by its energy deposit, is stored as so-called MCPoints. A single track can produce multiple MCPoints in each active- or passive material element. By combining the MCPoints from all detectors, one can form an MCTrack. The MCTrack object encapsulates the track parameters, including its PID and MCPoints.

Digitization: This step encapsulates the detector response for the MCTracks including the responses of the sensors and connected readout electronics (transfer function of the sensors, the efficiency of pixels, etc.). The digitized output is the raw file corresponding to the data readout from the real experimental setup. The output of the digitization stage (usually referred to as "Digi") contains the time information of the signal generation, the pixel/sensor address, and signal characteristics.

Reconstruction: The raw data from the digitization is reconstructed to produce hits and tracks. One or more digis are combined to form hits. The hit reconstruction involves mapping the pixel address to spatial coordinates and time from the digitized hit with the associated uncertainties $(\vec{r}, \vec{\delta r},\ t,\ \delta t)$. The container of hits is then used for the reconstruction of tracks. The track finder is based on a Cellular Automaton algorithm. First, the hits are clustered in time, corresponding to a single event. CA then finds tracks using clustered hits by separating them into discrete Z blocks corresponding to different tracking stations. A few consecutive stations of MVD and STS are used as the seed for the CA tracker. The found tracks are then fitted separately in XZ and YZ (because of the inhomogeneous magnetic field), and the momentum and charge information of the tracks is derived. These fitted tracks (which will be referred to

as “reconstructed tracks” or just “tracks”) are then extrapolated to the downstream detectors. At the downstream detectors, apart from the reconstruction of hits and local tracks (usually referred to as “tracklets”), the reconstruction of energy loss, rings, and the PID assignment are done.

Analysis: The tracks reconstructed are used for different physics analyses like di-electron reconstruction, flow measurement, fluctuation measurements, etc. . .

3.4 CBM RICH reconstruction

A flowchart depicting the various stages of the RICH reconstruction algorithm is shown in the figure 3.5. The GEANT-transported MCPoints in the RICH are the Cherenkov photons entering the active regions of the camera. In the RICH camera, the active region is a group of pixels that mimics the MAPMT pixel structure. For different wavelengths of light, the MAPMT has different quantum efficiency (QE). One can define the QE as the fraction of the photons that produce the signal in the MAPMT cathode. This includes the photo-electric efficiency and cathode collection efficiency. This combined efficiency is applied to each MCPoints, rejecting the reconstruction of a corresponding amount of MCPoints. All the surviving MCPoints are

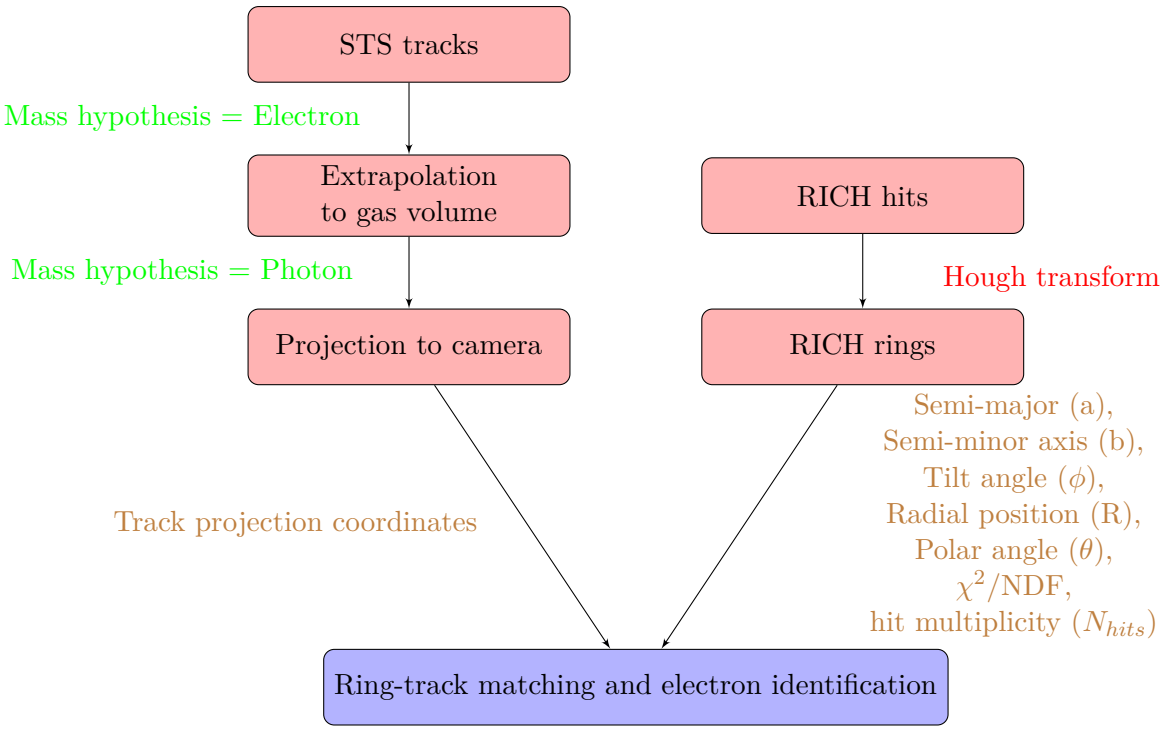

Figure 3.5: The flowchart of the RICH reconstruction algorithm (Green: Assumptions, Brown: Outputs, Red: Algorithms).

considered to be the output from the MAPMT and digitized. The digis carry information about the arrival time of the MCPoints (which is Gaussian smeared to a timing precision of 1 ns in order to reflect the detector's time resolution) and the pixel address of the incident hit. Currently, the RICH hit digitizer only delivers photon time-of-arrival. A realistic signal-width (Time-

over-threshold) reproduction is currently not implemented. ToT plays an important role in the analysis of real data for separation of real photon signals from the capacitive crosstalk signals produced in the MAPMT. This kind of cross talk can be effectively eliminated by requiring a minimum ToT of the registered pulses (see Chapter 4). Meanwhile, a second type of crosstalk, namely charge sharing crosstalk, was already implemented in the reconstruction chain, based on the quantitative results from this thesis (see Chapter 4). Every pixel address is mapped to the XYZ position. The "Hit" is created from the information of arrival time from the digi and its mapped spatial position, taking into account the corresponding precisions. Now for an event, we have a container of hits. These hits are then used to find the rings.

Ring-finding is based on a localized Hough transform. The Hough transform is implemented as a circle ring finder with three parameters: radius and two-dimensional ring center (x, y). This ring finder implementation does local searches using the knowledge that the rings must have an upper radius limit because of the limited Cherenkov angle. The found rings with N_{hits} are fitted using a multi-parameter Taubin fit as an ellipse fitter $F(x) = Ax^2 + Bxy + cy^2 + Dx + Ey + F$. Combinations of these parameters are then used to derive the semi-major axis (a), semi-minor axis (b), and ring tilt angle (ϕ). The fit provides a χ^2/NDF. Each ring is quality-checked using an ANN, which is a Single Layer Perceptron (SLP) with the ring parameters as the features : a, b, ϕ, number of hits (N_{hits}), and absolute ring center in polar coordinates (radial position (R) and angle (θ)).

All the tracks fitted in STS are extrapolated to the RICH gas volume assuming an electron mass hypothesis. This mass hypothesis accounts for the effect of multiple scattering and track bending in the magnetic field. The position in Z to which the tracks are extrapolated, assuming an electron mass hypothesis, is called the "extrapolation layer". The Cherenkov photons themselves are not scattered and are unaffected by the magnetic field. Hence, after the extrapolation layer, the tracks are analytically projected to the RICH camera by a straight line. The ring-track distance, Δd is calculated as the distance of the closest ring to a track projection. Finally, the electron identification is done by a separate ANN, which is a single-layer perceptron (SLP) for the ring-track pair with the ring-track distance and the ring quality parameters. The SLP distinguishes electrons from pions and is trained on FAIRBox-generated electrons and UrQMD-generated pions.

4

Performance and quality testing of CBM RICH front-end electronics

This chapter describes the laboratory setup at the University of Wuppertal and its use to measure charge-sharing crosstalk, perform high rate and high occupancy tests of MAPMT-DIRICH readout electronics using a realistic detector setup. Furthermore, the time measurement capabilities of the DIRICH front-end boards are presented. The latter part of the chapter includes the analysis of induced electronic noise characteristics of a new iteration of the DIRICH power module to be used in the CBM RICH readout chain. Sections of this chapter have been published in the following papers/reports:

1. M. Becker, et al., corresponding author: P. Subramani, *"Qualification of DIRICH readout chain"*, Nuclear Instruments and Methods in Physics Research Section A (2024) [94].

2. M. Becker, et al., *"Status of the development of the RICH detector for CBM including a mRICH prototype in mCBM"*, Nuclear Instruments and Methods in Physics Research Section A (2024) [95].

3. P.Subramani, et al., *A new lab setup for studying DIRICH and PMT properties*, CBM Progress report 2020 [96].

4. P.Subramani, et al., *Testing of new DIRICH power modules for their noise bandwidth*, CBM Progress report 2021 [97].

5. P. Subramani, et al., *"Performance and quality testing of CBM RICH front-end electronics"*, CBM Technical Note.

4.1 Ring Imaging Cherenkov detector front-end electronics

The CBM RICH uses H12700 multi-anode photo multiplier tubes(MAPMT) manufactured by Hamamatsu as spatially resolved photon sensors. Each H12700 MAPMT has 64 pixels (8×8) of size 6 mm × 6 mm and has a peak quantum efficiency of 33% and a large effective area of 87%. The gain per photoelectron is in the order of $\sim 10^6$, with the dark count rate of < 100 Hz per pixel. Each set of six photon sensors is connected to a backplane, which also hosts all necessary front-end readout components. Furthermore, the backplane also provides a light- and gas-tight seal of the radiator volume and incorporates all connections to power and signal lines.

Signals from the MAPMTs are read out via the DIRICH front-end board (FEB). Each channel of the DIRICH FEB incorporates a single-stage transistor-based inverter amplifier with a gain of $\sim$ 10 to 20 in order to provide sufficient amplification to the input signal. The native PMT single photon signal is a short, negative pulse of 3 ns to 5 ns width and an amplitude in the range of 10 mV per photon (depending on the individual PMT gain). After analog pre-amplification, the signal is directly fed to one of the two inputs of a differential line receiver port of the onboard ECP5 FPGA, where it is compared to a channel-individual threshold voltage (connected to the second input), generated via pulse-width modulation (PWM) using two Mach XO3 FPGAs on the same DIRICH FEB. In this approach, the differential line receivers onboard the ECP5 FPGA are used as signal discriminators, minimizing the need for additional components.

Both threshold crossings (leading- and trailing edges of the signal) are subsequently measured in a high-precision FPGA-TDC implemented onboard the ECP5 FPGA. The data flow in the TDC is explained in section 4.7.1. Each DIRICH FEB has 32 analog input channels. A single backplane can host up to six MAPMTs and twelve DIRICH FEBs (two DIRICH FEBs per PMT).

The data from all individual DIRICH FEBs on a given backplane are transferred via individual 2 Gbps digital links to the DIRICH combiner/concentrator module hosted on the same backplane. The DIRICH Combiner acts as a simple data hub, combining the data stream of the 12 input links to a single 2 Gbps optical output link. The data protocol on all these data links is defined by the TRBnet specifications [98]. The combiner module can also receive external trigger signals, which are distributed simultaneously via the backplane to each DIRICH module. An additional, special TDC channel on each DIRICH assigns timestamps to the incoming trigger signal, needed for later hit assignment and event building across multiple DIRICH backplanes.

The DIRICH-Power module (one per backplane) provides all low-voltage power supply lines (1.1 V, 1.2 V, 2.5 V, and 3.3 V) generated from a single input (18 V to 36 V) using DC/DC converters. Special attention is paid to minimizing the amount of electronic noise (EMC) induced on the analog components on the backplane. In addition, the DIRICH-Power module also transfers a single HV input supply line (~ -1 kV, Lemo-01 input connector) via the backplane to all 6 MAPMTs. A picture of the backplane with readout components is shown in figure 4.1.

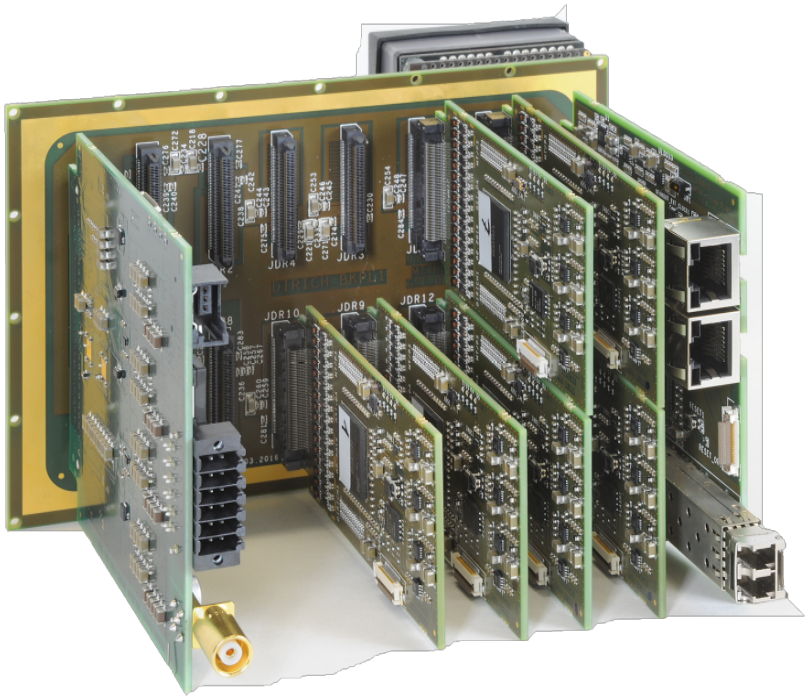

Figure 4.1: Backplane with MAPMT and readout components. Picture Courtesy: G. Otto (GSI)

4.2 Motivation

Both the upgraded HADES RICH and the mini-CBM (mCBM) setups at GSI SIS18 use the same DIRICH front-end electronics, which are also planned for the CBM RICH readout, along with the already acquired H12700 MAPMTs. Initial testing and detailed characterization of all MAPMTs has already been completed; the obtained series data are used for gain matching sets of six MAPMTs on one backplane sharing the same HV supply channel [99]. The DIRICH FEBs have already been successfully tested for average input hit rates up to 100 kHz per channel [98]. In the CBM RICH, when running at maximum heavy ion interaction rates of up to 10 MHz and at highest operational energies, one expects maximum hit rates in the order of a few 100 kHz per pixel (6 mm × 6 mm) in the "hottest" regions of the photon detector.

Emission of Cherenkov photons is a quasi-instantaneous process, emitted photons travel basically with the same speed as the emitting electron (i.e., the speed of light in the radiator medium), and the track length of all photons emitted from the same lepton is quasi-identical. As a consequence, all Cherenkov photons belonging to the same Cherenkov ring are arriving at the MAPMT simultaneously, resulting in larger hit multiplicity ("occupancy" if normalized to the total number of MAPMT pixels) during a very short time duration (typically < 100 ps) [100]. The dimension of the active area of an H12700 MAPMT is 48.5 mm × 48.5 mm. Based on the average number of photons per ring (~ 30) and the expected ring radius ($R \sim 50$ mm) the number of simultaneous photon hits per MAPMT (i.e., PMT occupancy) is estimated to be 6 – 9 simultaneously incident photons per MAPMT. Incident light on one MAPMT channel can induce

signals in other channels, a phenomenon known as crosstalk. Crosstalk can be of two types, neighboring channel charge sharing crosstalk and capacitive crosstalk. The neighboring channel crosstalk is caused by parts of the electron avalanche leaking into neighboring pixels, producing a signal above the threshold. While the capacitive crosstalk is the result of the parasitic conduction between the channels due to large signals at the common photocathode [1]. These crosstalk signals are typically short and can be removed by imposing a Time over Threshold cut (discussed in sec 4.5). Larger occupancies may increase the probability of crosstalk, hence the characterization of the MAPMT as a function of photon occupancy is paramount.

The large maximum expected hit rate also implies a large data rate at the readout- and combiner boards. All 12 DIRICH FEBs on a given backplane transmit data to a single combiner, which forwards it over a single data link to subsequent DAQ readout stages. Therefore, this combiner upstream link is one of the current bottlenecks for the data flow. In order to maximize the data performance of the existing hardware chain, individual channel- and event buffer sizes on DIRICH- and Combiner modules can be optimized (in software). In a second step, also the uplink speed of the existing combiner modules might be further increased (currently 2 Gbps, FPGA limit is 10 Gbps) using the existing hardware. Ultimately, a new version of the combiner module, possibly with more than one output link, might follow. However, the analog part of the DIRICH front-end modules (2500 modules in total) is fixed already and could possibly pose a hard limit to the achievable maximum hit rates for many years to follow. So a detailed study of the hardware limitations in terms of hit rate and data quality is of utmost importance and had to be done before the start of series production. Since HADES and mCBM, in general, both do not provide the environment for such tests, a laboratory setup was made to study the high-rate behavior of the DIRICH readout chain and also to define the optimal readout parameters. The results of these studies are summarized in the subsequent sections.

4.3 Laboratory setup

The setup basically consists of a single readout module equipped with a single MAPMT, two DIRICH modules for readout, and two different light sources (a pulsed laser source and a DC source), enclosed in a light-tight box (originally built for a beam test at the COSY accelerator in FZ Jülich see [101]). The main goal is to operate MAPMT and DIRICH readout under realistic high-rate conditions, as similar to the final CBM RICH high-rate operation as possible. The schematic and photograph of the setup are shown in figure 4.2.

Readout of the data is done using a TRB3 (Trigger Readout Board: V3), connected to the upstream optical link of the DIRICH combiner module on the backplane. In this setup, the TRB3 board, in addition to the pure data transport, is also incorporating a Central Trigger System (CTS), generating regular readout triggers fed to each individual DIRICH in the setup. Later in CBM, this part of the readout will be replaced with a CRI-based readout of the CBM DAQ concept, which will not be studied here. Data is sent via a single GBit Ethernet connection

[1] The H12700 MAPMT is designed with common dynode grids in combination with a segmented anode

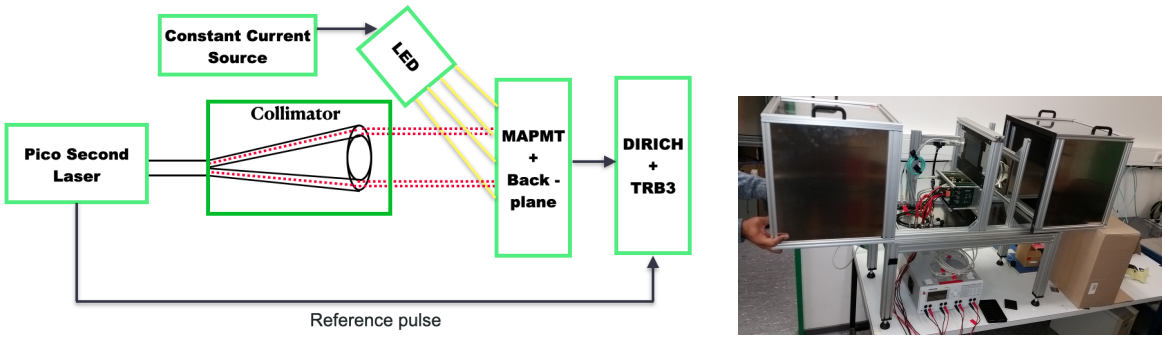

Figure 4.2: Left panel: Schematic showing components of the laboratory setup. The MAPMT is illuminated by a LED and a picosecond laser source. The signal from MAPMT is processed by the DIRICH-TRB3 readout chain. Right panel: Photograph of the laboratory setup.

from the TRB3 to a DAQ PC for disk storage. A pulsed laser light source produces ultra-short picosecond pulses (width $< 50\,\text{ps}$ in Violet, $\lambda \approx 400\,\text{nm}$) which are passed through an optical cable into a collimator with a conically opening slit structure. At the input of the collimator, the incoming light is diffused by using a white glass diffuser and homogeneously illuminates the collimator slit. Light from the collimator is then projected onto the MAPMT, generating a ring-like image of numerous simultaneous photons, mimicking a Cherenkov ring in the real detector. A pulse-synchronous reference signal, generated by the laser pulser, is measured additionally using a dedicated TDC on the TRB3, which allows isolating PMT signals generated by the pulse laser (so-called "signal" hits) from hits by other sources ("background"). The photon yield per pulse of the laser can be adjusted (0–30 photons/pulse) in order to vary the MAPMT occupancy. In general, the large interaction rate at the future CBM experiment, and possibly also fluorescence effects, will produce a large photon background that is not time-correlated to signal photons in a given event, and which must be incorporated into the setup. This is achieved by implementing a second light source into the setup: A LED driven by a DC constant current source, causing an uncorrelated, statistically distributed photon background. Combining both light sources, the setup provides a controlled signal photon rate together with a controlled stochastic background noise, which is not possible in normal test beam operation.

4.4 Charge sharing crosstalk measurement

In the first commissioning measurement, this setup was used to re-evaluate the neighboring-channel charge-sharing crosstalk of the H12700 MAPMTs in comparison to its predecessor H8500. A similar study has been done [102] using CERN test beam data but using different (nXYter-based) readout electronics and slow signal shaping. The new results presented here are based on the DIRICH readout to be used in the later CBM RICH detector. The measurement aims to quantify the amount of crosstalk (to be included in Monte Carlo simulations) and to study the influence of the noise reduction threshold voltage on crosstalk.

4.4.1 Measurement principle

The measurement presented here is based on the illumination of the MAPMT with low-intensity short laser pulses ($\sim 5\,\text{ps}$). A reference signal from the pulse generator is fed into the data and used to select "signal" hits based on a time cut around the prompt peak. In the setup figure 4.2, no collimator is used, and also the LED is switched off. The charge-sharing crosstalk into a neighboring channel is then estimated as follows:

- Only events with two simultaneous "signal" hits on the MAPMT are selected (characterized by a relative time difference between reference pulse and PMT signal of less than $\geq 10\,\text{ns}$, and a ToT (Time over Threshold) $\geq 3\,\text{ns}$).
- The distance between the positions of the two hits (counted in the number of pixels) is histogrammed.
- The obtained 1D distance distribution is compared to a simple Monte Carlo simulation where two hits are randomly thrown on the MAPMT (8×8 pixels).
- Non-uniform illumination of MAPMTs and efficiency variations of the pixels might distort the statistical distribution of the measured distances. In order to account for it in simulation, an efficiency matrix was derived for MAPMT based on the normalized absolute number of hits in each pixel,

$$\text{efficiency} = \frac{\text{Hit multiplicity in a pixel}}{\text{Total number of events}}. \tag{4.1}$$

  This is then applied to each pair of hits as a correction factor.
- The simulated distance distribution is scaled to the measurement such that optimal agreement for all distances $d \geq 2$ is achieved. Any excess yield of measured distances $d = 1$ can now be attributed to the charge-sharing crosstalk.
- Finally, the relative crosstalk contribution is quantified using the following formula:

$$F_{cross\,talk} = \frac{N_{data,d=1} - N_{sim,d=1}}{N_{sim,all}} \times 100\% \tag{4.2}$$

  where $N_{data,d=1}$ and $N_{sim,d=1}$ are the number of entries in data and simulation histograms corresponding to distance $d = 1$. $N_{sim,all}$ is the total number of simulated pair events.
- The procedure is repeated for four different PMTs and five different threshold values.

4.4.2 Results and Discussions

The measurement results are shown in figure 4.3. The measured distance distribution matches very well with the simulation results, with the only sizable difference being observed in the first

bin, corresponding to the crosstalk into neighboring channels. The H8500 MAPMT (figure 4.3 (left)) shows a sizable amount of crosstalk, which is much reduced in the case of the H12700 MAPMT (figure 4.3 (right)).

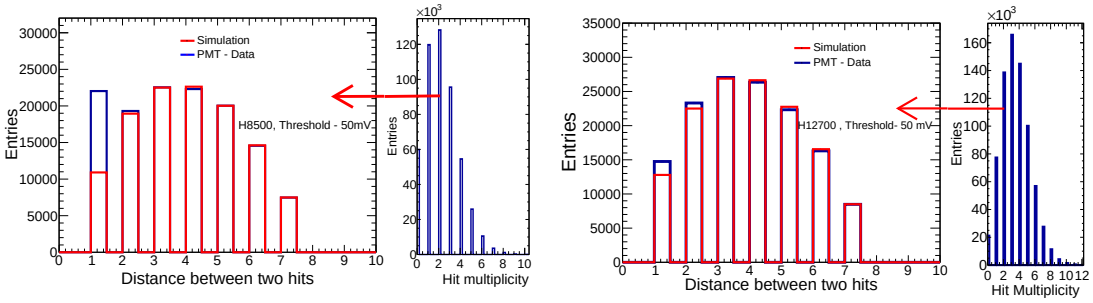

Figure 4.3: Measured distance between two hits for data (blue) and simulation (red) and the hit multiplicity of detected photons per event. Left: H8500 MAPMT, Right: H12700 MAPMT. Threshold: 50 mV (after pre-amplification).

Results for measurements on four different MAPMTs (2× H8500 and 2× H12700) are summarized in figure 4.4, with relative crosstalk being plotted as a function of applied noise reduction threshold value (threshold after pre-amplification).

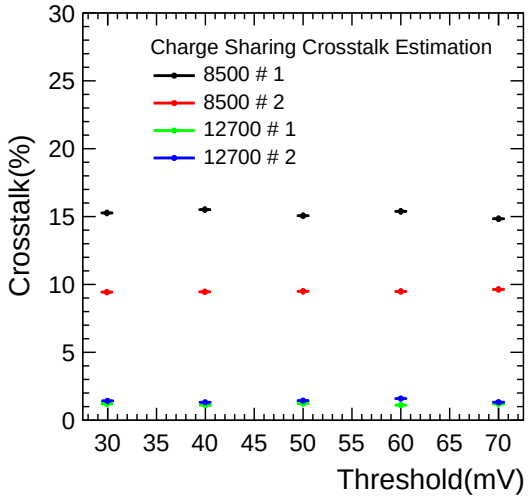

Figure 4.4: Neighboring channel charge sharing crosstalk is plotted against noise rejection threshold voltage. Different colors indicate different MAPMTs used for measurement. H12700 MAPMTs have significantly lower neighboring channel crosstalk compared to the H8500 variant.

The observed crosstalk for H8500 MAPMTs is in the order of 10-15%, which is in good agreement with the earlier measurements. In contrast, the crosstalk for both H12700 MAPMTs is only in the order of 1-2%. This is expected based on the MAPMT series testing results, but could now be confirmed with the full DIRICH readout chain.

As a second interesting result, the crosstalk contribution does not depend on the applied noise threshold. This comes as a bit of a surprise, since the total amount of charge generated by a photon is fixed, and sharing this charge over two channels should result in reduced signal amplitude and thus reduced charge-sharing contribution at higher threshold values. However,

the range of threshold values covered in this study resembles realistic threshold values as would be used in the real experiment. All studied thresholds are still well below the average single photon signal, in the order of 10% to 20% of the typical single photon charge. The expected reduction of charge sharing would probably be observed at much higher threshold values only.

4.5 High occupancy analysis

A good understanding of possible capacitive crosstalk and time over threshold (ToT) spectra at high occupancy (as described in sec. 4.2) is required for implementing it properly in the detector simulation and optimal selection of ToT threshold for the operation of MAPMT-DIRICH readout. It is stipulated that the charge-sharing crosstalk between neighboring channels, as discussed in the preceding section, is independent of occupancy in MAPMT, as it persists whenever there is at least a single hit in a pixel. In this section, the measurement principles and results of the high occupancy test of MAPMTs are presented. The capabilities of the readout chain to handle possible crosstalk resulting from these higher occupancies are discussed.

4.5.1 Measurement principle

A picosecond laser is used to produce high photon occupancy. To separate the signal from the background, a reference pulse is used as described in the previous sections. The hits that are correlated in time ($\leq$ 10 ns) are selected. The schematic of the setup used for the study is depicted in figure 4.5. Photon emission from a laser is a stochastic process. It is quite challenging to accurately measure the photon flux from the laser (on a few photon level) with a basic laboratory setup. Hence, in order to have a measurable control over the photon yields, a set of neutral density (ND) filters (with well-known attenuation factors) are used as a calibration device. Using this setup, instead of quantifying the number of photons per single pulse, the measurement is reduced to counting the number of detected single photons in a large given number of pulses, with well less than one photon per pulse. Difficult quantification is reduced to simple binary counting.

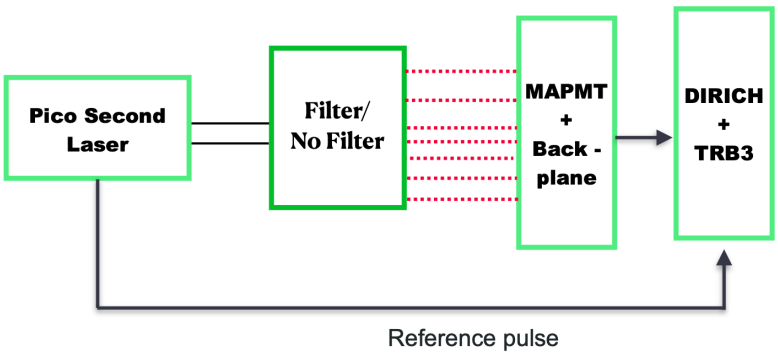

Figure 4.5: Schematic of setup for high occupancy measurement. No LED is used for the measurement. A set of neutral density filters is used for attenuating photon intensity from the laser.

The measurement principle for this analysis is as follows:

1. The neutral density filters to be used are calibrated, i.e., the transmittance T of the ND filter is calculated .
2. An ND filter is placed in between the laser and MAPMT, thereby attenuating the laser yield.
3. With the measured transmittance of the filter, the expected hit multiplicity without the filter is calculated.
4. The measurement is repeated by removing the filter while maintaining the same intensity of laser.
5. The observed hit multiplicity is compared with the expected result; any excess measured is attributed to crosstalk resulting from the high occupancy setting.
6. The intensity-dependent crosstalk contribution is estimated by repeating steps 2 to 5 for different intensities of the laser.

An explanation of the measurement principle is provided in the subsequent sections.

4.5.2 Calibration of filters

In order to calibrate the ND filters, the intensity of the laser pulses is reduced to produce low hit multiplicity in MAPMT (hits < 3). In this setting the capacitive crosstalk contribution is assumed to be minimal. The hit multiplicity per event without filter ($N_{without-filter}$) is measured and plotted in the X $axis$. Further, the neutral density filter is placed between the laser and MAPMT. The resulting reduced hit multiplicity is measured and plotted on the Y $axis$ ($N_{with-filter}$). Both the values are subtracted by dark hits ($N_{dark-hits}$), which is the number of hits measured when the laser is off (because of stray light and/or other sources). The procedure is repeated for 10 different laser intensities. The resultant graph (shown in the figure 4.6) is fitted with a straight line,

$$N_{without-filter} = N_{with-filter} \times T + N(0), \tag{4.3}$$

where $N(0)$ is the Y intercept and T is the slope. The slope derived by line fit is considered as the transmission probability (T) of the ND filter. To reduce bias, the measurement is repeated using two different filters with different transmittance, and the results are tabulated in 4.1. A similar procedure is repeated by imposing a ToT cut (ToT > 3 ns) on the hit selection (appendix A.1.1).

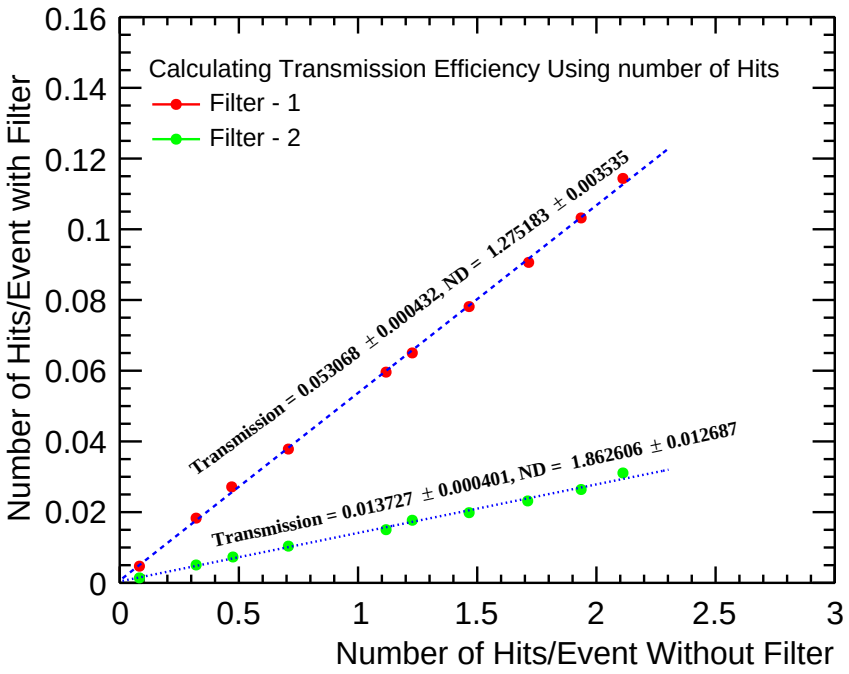

Figure 4.6: Hit multiplicity with filter is plotted against hit multiplicity without filter. The resultant graph is fitted with a line, and the extracted slope is considered as the transmittance of the filter.

Table 4.1: Transmission probability and neutral density are calculated for the two different filters and compared with their nominal value (taken from [103]). The measured neutral density is in agreement with the nominal value .

Filter Number	**Transmission probability (T)**	**Neutral density (ND = $\log_{10}\frac{1}{T}$)**	**Nominal ND**
1	0.0531 ± 0.0004	1.2751 ± 0.0035	1.3 ± 0.02
2	0.0137 ± 0.0004	1.8626 ± 0.0126	2 ± 0.2

4.5.3 Estimation of crosstalk at high occupancy conditions

The calibrated filters are placed in between the laser and MAPMT. The hit multiplicity with filter ($N_{with-filter}$) is measured, and the intensity of the laser is adjusted such that multiplicity does not exceed 2 hits (crosstalk is assumed to be minimal).

The expected hit multiplicity without filter (adjusted for the dark hits) is calculated as,

$$N_{Expected} = N_{with-filter} \times \frac{1}{T} - N_{dark-hits} - N_{double-photons}. \tag{4.4}$$

An additional correction is applied to correct for the increased probability of double photon hits (two real single photons reaching the same channel) within the same pixel at increasing occupancy. Such contribution from double photon ($N_{double-photon}$) is simulated (appendix A.1.2) and subtracted accordingly. Calculated expected hits are plotted in figure 4.7. The expected hit multiplicity without ToT cut is slightly higher than the same with filter in figure 4.7, this is caused by the estimation of transmittance T with and without ToT cut (appendix A.1.1). The

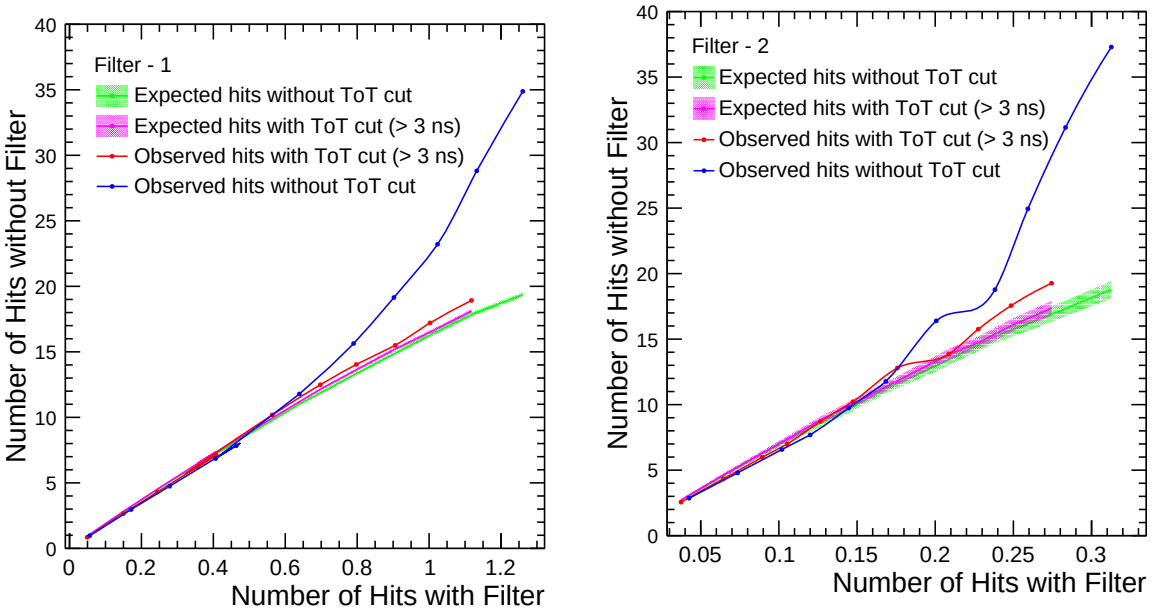

Figure 4.7: Expected number of hits vs. observed hits for filter 1 (Left) and filter 2 (Right). Without any ToT cut, the observed hits increases with increasing hit multiplicities. However, the observed hits with the ToT cut are in agreement with the expected hits. Since the filter 2 has transmission efficiency close 1%, the error in estimation of hits in higher multiplicities is higher compared to filter 1 which is about 5% transmittance.

difference in the estimation of the T might be due to the negligible crosstalk associated with low hit multiplicities, which is assumed to be zero in these studies.

The filter is removed, and hit multiplicity $N_{without-filter}$ is measured. Measured hit multiplicities are adjusted for dark hits as,

$$N_{Observed} = N_{without-filter} - N_{dark-hits}. \tag{4.5}$$

The measurement procedure is repeated for 12 different laser intensities; the results are plotted in figure 4.7. Each data point in the analysis is averaged over 10^6 regular readout trigger events (readout trigger—10 kHz, laser frequency—10 kHz). In the expected range of hit multiplicities of 6–9 hits/event/MAPMT (8–14% occupancy), the additional hits due to crosstalk are minimal (less than 1), as shown in figure 4.7. Significant crosstalk hits are observed for the expected hit multiplicities greater than 10 hits. Similar results were observed for both the filters under test. As anticipated, the contribution of capacitive crosstalk hits increases with an increase in hit multiplicity. However, once the ToT cut of 3 ns is employed on the hits, the observed hit multiplicities follow the trend of expected hit multiplicities. This indicates that the ToT cut plays a vital role in eliminating capacitive crosstalk signals.

Choosing the optimal ToT cut depends on its capacity to eliminate crosstalk hits as well as preserve true photon hits. Quantifying the impact of the ToT cut on selecting the true photon hits is quite intricate. As a general rule, a lower ToT is better for the efficiency of selecting true photon hits. Hence, a minimal ToT cut for maximum rejection of capacitive crosstalk is

employed as a compromise strategy. In order to test the impact of different ToT cuts on the effect of the capacitive crosstalk, an extended version of the analysis presented in figure 4.7 is performed. Here, the expected and observed hit multiplicities are calculated for different ToT cuts. Figure 4.8 displays the excess hits, which are calculated by subtracting observed hits and expected hits, as a function of expected hits for different ToT cuts. The performance of lower ToT cuts (less than 3 ns) is worse in higher occupancies. More than 30% additional hits are produced as compared to expected hits for the ToT cut of 1.5 ns. For CBM RICH safety occupancy of 18 hits (9 (maximum) $\times 2$) which translates to $\sim 28\%$ pixels, a ToT cut of 3 ns is optimal.

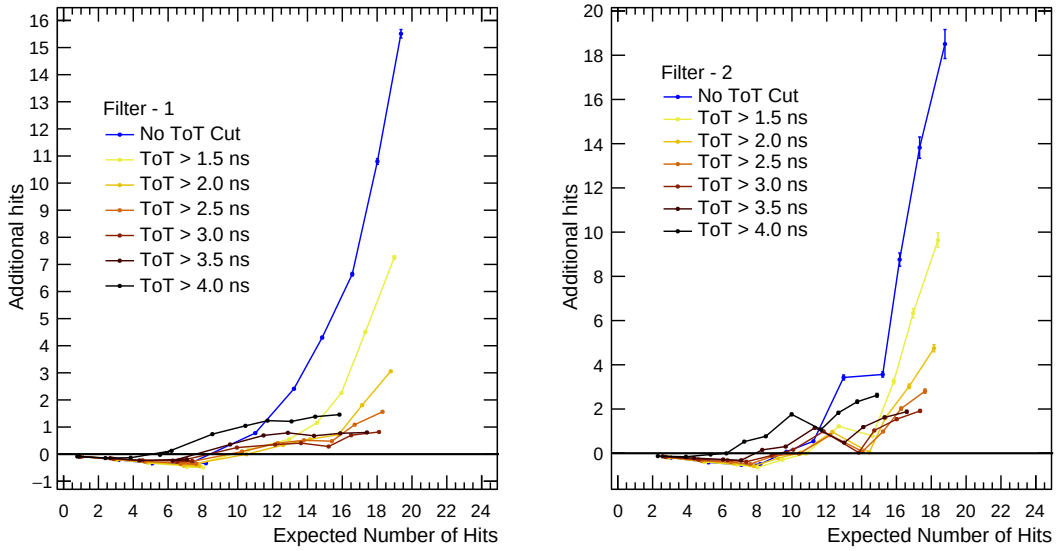

Figure 4.8: Excess hits (observed-expected) as a function of the expected hit multiplicity for different ToT cuts for the filter 1 (left panel) and filter 2 (right panel).

The time over threshold (ToT) spectra for different multiplicities are plotted in figure 4.9. One can observe a rise in the low ToT peak as the hit multiplicity increases, indicating additional crosstalk. Furthermore, the valley between the lower ToT and higher ToT peaks shifts gradually towards the higher ToT region and tends to get sharper with the increase in multiplicity, indicating that the ToT usage for crosstalk signal suppression has certain limitations.

The histogrammed ToT spectra in figure 4.9 are shown in three different variants, using different choices of scaling factors of the individual curves of increasing illumination. The first plot uses no additional scaling, i.e., the number of entries in each curve increases simply with increasing hit multiplicity. The second plot is scaled such that all individual ToT distributions have the same area of the signal peak for ToT > 3 ns. This is done to visualize the proportional increase in the left peak (crosstalk). The third iteration of this ToT plot is scaled in order to better express the single photon contribution. A scaling factor, defined as,

$$\text{Scaling factor} = N_{expected} - N_{double-photons} = N_{with-filter} \times \frac{1}{T} - N_{dark-hits} - 2 \times N_{double-photons} \tag{4.6}$$

is used to scale the ToT spectra in the region above ToT > 3 ns.

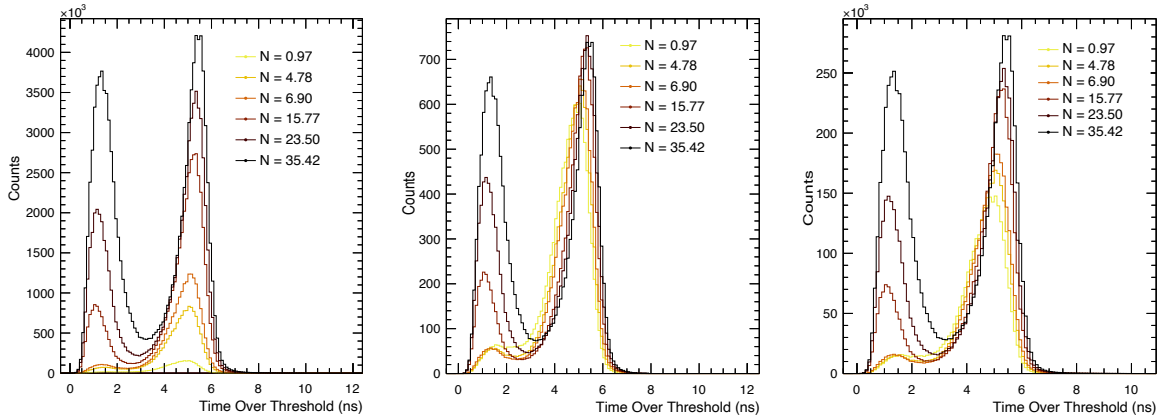

Figure 4.9: ToT spectra for different hit multiplicities (N), left panel - No scaling, middle panel - Scaled to integral of spectra for ToT > 3 ns, right panel - Scaled to single photon contribution.

The effective charge deposited on the photocathode due to the incidence of two photons is twice as large as the single photons. Thus, it is expected that the double photon hits will have a larger ToT. At high occupancies, which are facilitated by the high intensity of laser pulses, the likelihood of encountering double photons in a pixel is higher. Hence, at higher hit multiplicities, one would expect distinct peaks of ToT spectra for single photon and double photon hits. On contrary, figure 4.9 (right) indicates that the separation is weak for discrimination of single and double photon hits. On comparing the lowest hit multiplicity ($N \approx 0.97$) and highest hit multiplicity ($N \approx 35$), the most probable value of the ToT spectra (> 3 ns) is about 1 ns. Thus, the DIRICH front-end board is not very well suited to separate single- and double photon hits within the same channel only based on ToT information.

4.6 Leading edge- and Time-over-Threshold timing characteristics of the DIRICH FEB

In the CBM experiment, due to the high interaction rate and large track multiplicity, multiple electron/positron tracks (mostly stemming from photon conversion in the detector materials) might enter the RICH detector at close vicinity in space and time. Since the emission of Cherenkov photons is a rather instantaneous physical process, this can result in multiple simultaneous single-photon hits into the same readout pixel. The probability of multi-photon hits might be further enhanced due to additional scintillation light caused by the large charged track multiplicity for a given event inside the RICH gas radiator and surroundings.

In this section, we discuss the capability of the DIRICH readout chain to differentiate simultaneous multi-hits (which result in larger PMT pulse charge compared to single photon hits) only based on the measured leading-edge time and ToT information. The evaluation is based on a systematic study of the DIRICH FEB response to input pulses generated by a pulse generator, systematically varying both the amplitude and width of the input pulses. Since the DIRICH

FEB does not provide a direct measurement of the input pulse charge, its time response is the only criterion available to distinguish photon multiplicity.

4.6.1 ToT response from DIRICH FEB

Already from figure 4.9, it is evident that the separation of double and single photon hits using ToT information is rather weak. A detailed characterization of the leading-edge and ToT response to well-controlled input pulse shapes can help to better understand this behavior.

A pulse generator was used to generate distinct negative pulses with 1 ns rise time (RT) and 1 ns fall time (FT), similar to PMT pulses. The signal from the pulse generator is fanned out into 16 DIRICH input channels in parallel using a resistor divider. The DIRICH threshold (after the pre-amplification stage) is set to 100 mV. Two measurements were conducted, one involving the variation of the amplitude of the signal at the input of DIRICH FEB at a constant pulse width, and the other involving the variation of the width of the signal while fixing the amplitude of the signal. Each data point is analyzed for 10^6 regular readout triggers.

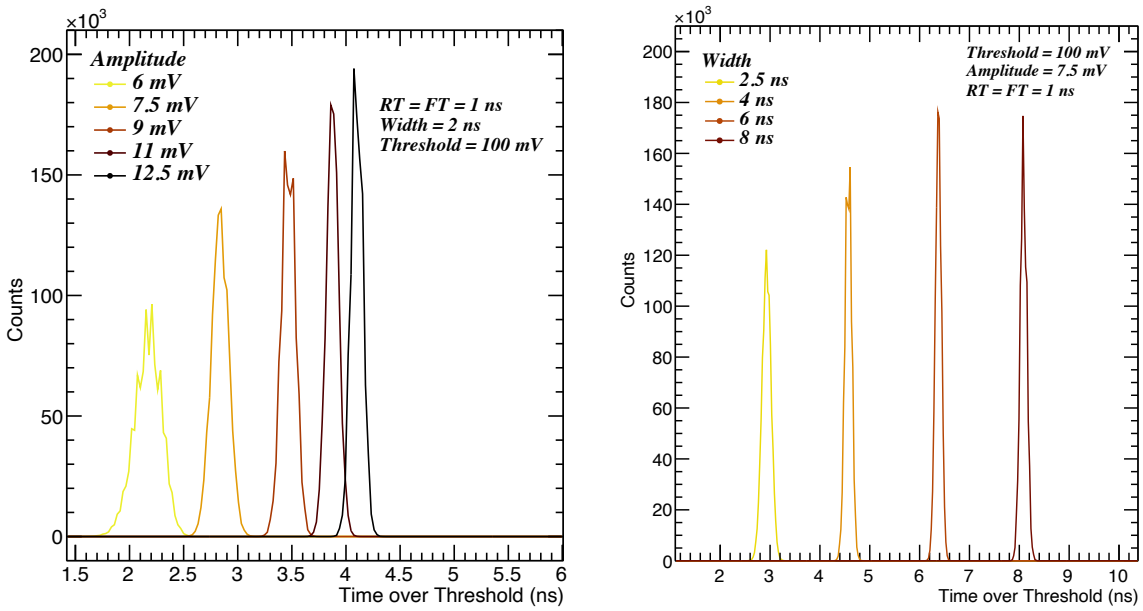

Figure 4.10: Left panel: Time over threshold (ToT) distribution measured for different amplitudes of input signal by maintaining a constant width. Right panel: Same for different widths of input signal at constant amplitude.

In the first measurement, the input pulse amplitude is systematically incremented in steps of 6 mV, keeping the width of the input signal constant at 2 ns. The result of this measurement is plotted in the figure 4.10 (left): Increasing amplitude of the input signal translates to higher ToT values. However, a clear saturation effect is observed for signal amplitudes beyond 10 mV. In addition, larger amplitude input signals exhibit a narrower peak in the ToT distribution in comparison to low amplitude signals. These observations are to be expected given the fact that the DIRICH time measurement is based on a simple leading / trailing edge discrimination at a

given threshold. For low threshold (relative to the pulse height), discrimination happens early in the signal rise-, and late in the signal tail, with low timing jitter due to steep signal rise / fall. For relatively large thresholds / low pulse amplitudes, discrimination happens in the less steep top part of the signal waveform, resulting in larger timing jitter and broader ToT peaks.

For the second measurement, the amplitude of the input signals was fixed at 7.5 mV while their width was varied; the result is plotted in figure 4.10 (right). Here, a nice linear dependence of measured ToT on the input pulse width can be observed, proving the good pulse-width measurement capability of the DIRICH. The analog DIRICH input stage comprises an inductive signal transformer for galvanic isolation of the input, which is known to cause a bipolar signal shaping prior to discrimination. However, for the covered range of pulse widths, this clearly does not hinder the pulse width measurement.

These results suggest that the PMT pulse itself already exhibits only a weak correlation between pulse charge (photon multiplicity) and signal width. Combined with the saturation effects in the amplitude-to-ToT correlation as observed in the first measurement, this can explain the limited capability to distinguish photon multiplicity based on measured ToT alone.

4.6.2 Leading edge timing precision from DIRICH FEB

Another measurement is performed to understand the DIRICH FEB response to distinguish quasi-simultaneous hits in time. To understand the Leading edge (LE) precision of the DIRICH FEB, a measurement was made using the same setup as described in the previous subsection. For a comparative study, two active channels in the same and different DIRICH FEBs are used. The LE time difference between two hits is calculated to eliminate any path length effects of the fan-out module on the signal.

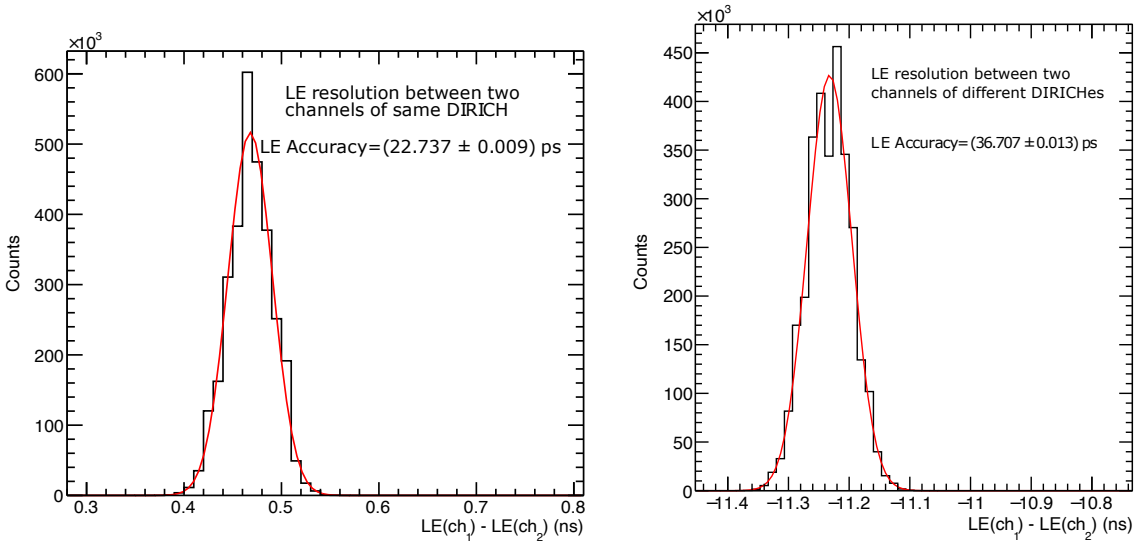

Figure 4.11: Leading edge accuracy measured with two active channels of the same DIRICH (left) and two active channels of two different DIRICHes (right).

The difference in the LE time between the hits of the two active channels in the same DIRICH FEB is plotted in the figure 4.11 (left). The resulting distribution is fitted with a Gaussian profile, and the width of the profile is the LE spread and a measure of time measurement precision of the DIRICH. Similarly, the LE time difference between hits in two active channels in two different DIRICH FEBs is histogrammed and fitted with a Gaussian profile, and the LE spread is calculated.

For two channels in the same DIRICH FEB,

$$\sigma_{\mathrm{LE}} = (22.7377 \pm 0.009)\ \mathrm{ps}. \tag{4.7}$$

For two channels in different DIRICH FEBs,

$$\sigma_{\mathrm{LE}} = (36.7071 \pm 0.013)\ \mathrm{ps}. \tag{4.8}$$

If the registered time of two hits of the same DIRICH (different channels) are measured and compared, then both time measurements are derived from the same clock signal and can be directly compared. The time difference δt and the uncertainty (σ) in measuring time for two hits (t_1, t_2) in different channels of the same DIRICH can be expressed as,

$$\delta t = t_1 - t_2, \tag{4.9}$$

$$\sigma_{same-DIRICH} = \sqrt{\sigma_{t_1}^2 + \sigma_{t_2}^2}. \tag{4.10}$$

However, if two hits in two different DIRICH modules are compared to each other, then the time measurement in both DIRICH modules is based on two individual clocks, running asynchronously. In order to derive an absolute time difference, first, both measurements have to be synchronized. This is achieved by measuring the arrival time of the readout trigger signal (distributed to both DIRICH modules) using a dedicated extra TDC channel (channel 0) on each of the DIRICH modules. Since each DIRICH measures the time of the hit relative to the measured trigger arrival time, the absolute trigger arrival time cancels out. Let t_0 be the absolute time in channel 0, the time difference δt and the uncertainty (σ) in measuring time for two hits (t_1, t_2) in two channels of the different DIRICH can be expressed as,

$$\delta t = (t_1 - t_0) - (t_2 - t_0) = t_1 - t_2, \tag{4.11}$$

$$\sigma_{different-DIRICH} = \sqrt{\sigma_{t_1}^2 + \sigma_{t_2}^2 + \sigma_{t_0}^2 + \sigma_{t_0}^2}. \tag{4.12}$$

As is shown, the absolute value of the t_0 measurement cancels out; however, the measurement uncertainty of the reference channel 0 on each DIRICH adds to the overall uncertainty. Opposite, if both hits were measured on the same DIRICH, there is no additional penalty for the t_0 measurement. This explains the lower precision in time difference measurement, if the two hits are spread over different modules (see figure 4.11). The results (equations 4.7, 4.8), indicate that the LE timing precision of the DIRICH FEB is an order of magnitude better than the transit time

spread (TTS) from the MAPMTs (the TTS for the H12700A Hamamatsu MAPMTs is about ∼350 ps FWHM), indicating that the DIRICH FEB is not the limiting factor in measuring / comparing photon arrival time of different hits.

4.7 Test of DIRICH maximum hit rate capability

The maximum hit rate capability of the DIRICH module, and understanding its limiting factors, is another important aspect of the DIRICH readout chain qualification. This section describes the measurement principle and results of a high rate test of the complete MAPMT-DIRICH readout chain. Inside the DIRICH FEB, incoming analog input signals are first amplified and then fed into differential line receivers of the FPGA for signal discrimination (sec. 4.1). Inside the FPGA, individual scaler entities are implemented and connected to the output of each comparator, directly counting the number of detected edges in each channel. These scaler values can be read out via slow control data stream and allow counting hits and measuring input rates, completely independent of all further data digitization and transfer. The slow control path is logically separated from the main data stream, and as such, not affected by loss of data or data quality due to data overload, buffer overflows, or high rate conditions in general. This feature allows for a sensitive test of high rate stability of the DIRICH by comparing the number of detected hits per channel as obtained from the slow-control scalers to the number of hits found in the output data stream written to the file.

4.7.1 Data flow in the TRB-based lab setup compared to later (m)CBM operation

Data measured by the DIRICH TDC is organized in hit messages containing several data words of 32 bits each. Usually, a single hit consists of a maximum of 3 data words: the leading edge time, the trailing edge time, and an additional occasional epoch message containing the absolute time information. For a given readout trigger, each channel can produce several such hit messages, depending on the number of hits registered since the last readout, and depending on a possible readout window, which can be defined relative to the trigger time. Different buffers in the data flow provide the capability of a quasi-free streaming data-taking operation, despite a fixed-period readout initiated by the regular readout trigger. The first stage of the data storage happens at individual DIRICH FEB channel buffers which (in the present DIRICH firmware) can store a maximum of up to 123 words. Upon receiving a readout trigger, the data from all 32+1 channel buffers are sequentially shifted into the DIRICH FEB main readout buffer, starting with channel 1. This common readout buffer can store up to 499 words, limiting the maximum number of individual hits that can be read out by a single readout trigger. The data from each DIRICH on a single backplane module (containing up to 12 FEBs) are streamed to the DIRICH combiner module, which is acting as a data hub, combining the individual sub-events from each FEB into a single output event. The combiner output link is a standard TRBnet optical link of 2 Gbps (2.4 Gbps) in case of the CRI readout used in mCBM and later CBM

operation).

The further data transfer from the combiner onwards is different for the lab setup and the future CBM experiment. In the lab setup, a "Trigger and readout board V3", TRB3 is used

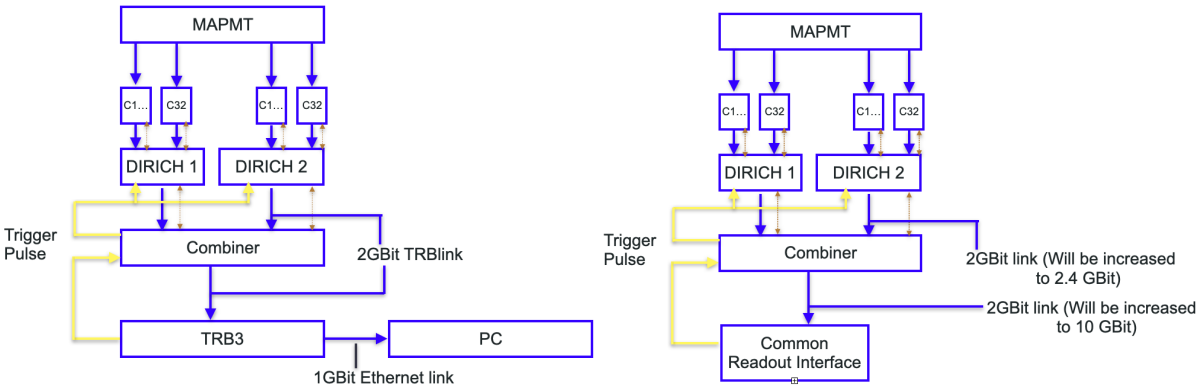

Figure 4.12: Schematic showing data flow in the lab (left) and future CBM (right). The blue arrow indicates the direction of the data stream and the dotted brown indicates the slow control link. Yellow lines indicate the flow of the trigger signal.

as the DAQ master. Its task is to collect data from up to $4 \times 7 = 28$ combiner modules, and to send these data via its single GBit Ethernet interface to a DAQ PC for data storage and analysis. The TRB3 in addition facilitates the Central Trigger System "CTS", generating and sending out the regular readout trigger, which is then distributed via the Combiner modules to all DIRICH frontend FEBs. It is obvious that the Ethernet link is the slowest bottleneck in this setup, followed by the optical link between individual combiners and the TRB3. These bottlenecks in the lab setup make it challenging to operate the system at large data rates for evaluating data rate capabilities of the DIRICH frontend. In the future CBM DAQ setup, as well as in mCBM already today, a modified data transport scheme is implemented. Here the single TRB3 DAQ master is replaced by several "Common Readout Interface" (CRI) boards. Each CRI board provides up to 47 serial data links of up to 10 Gbps each and sends collected data via its multi-lane PCI-express interface to its corresponding high-performance DAQ PC and further via InfiniBand network to the GreenCube compute cluster. This CRI-based readout chain is currently further developed and tested in the mCBM detector setup at GSI. Details can be found in [104].

However, all test measurements described in this chapter were conducted using the TRB3-based laboratory readout. Overall schematics of both data transport variants are sketched in figure 4.12.

4.7.2 Analysis method

The measurement described below uses a single H12700 MAPMT connected to two DIRICH FEBs. In order to produce a large hit rate at the DIRICH FEB, the MAPMT is illuminated by an LED (enclosed in a light-tight box) that is powered by a constant current source (figure 4.13). The DIRICH threshold was set at standard 50 mV (unless mentioned otherwise), providing good

single-photon detection efficiency. The variation of hit multiplicity in the MAPMT is achieved by changing the intensity of the LED controlled by the current source. In figure 4.13 (middle), the LED driving current is plotted versus the average photon hit rate as measured by the scaler counters on each DIRICH channel. No data acquisition is required to obtain this plot, only slow control communication is used to periodically read out the scaler values. A quadratic relation between output rate and current is observed, and the position of the LED in the box is adjusted to produce a nearly homogeneous illumination of the MAPMT (see figure 4.13 (right)). For testing the rate capability of the DIRICH digitization chain, this scaler rate is now compared to the number of fully digitized hits per time in the DAQ data file, after activating the DIRICH digitization. Each data point in the scaler rate is averaged over 10 seconds, and each data point in DAQ data is averaged over 10^6 regular readout trigger events.

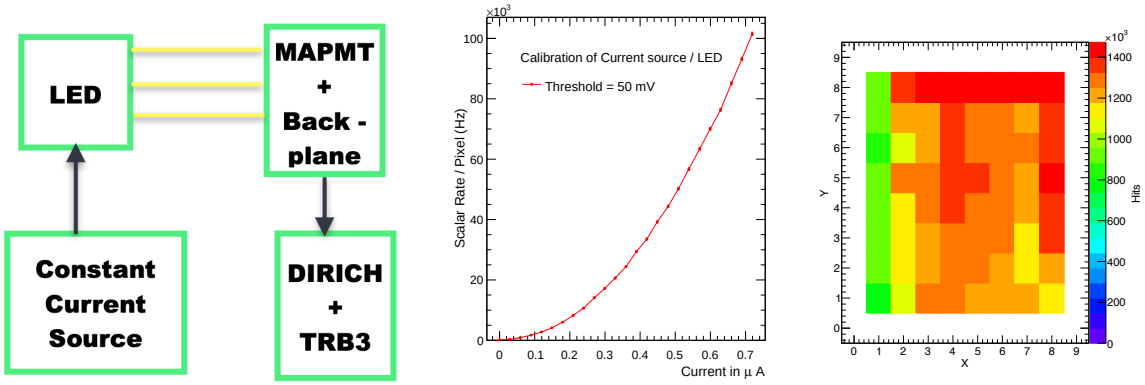

Figure 4.13: Left panel: Schematic depicting laboratory setup for performing the high rate capability test on DIRICH readout electronics. Middle panel: Relationship between scaler hit multiplicity and operating current for LED. Right panel: Distribution of hits on MAPMT (each bin of this 2D histogram corresponds to a pixel of MAPMT).

4.7.3 DIRICH performance at high rate

To perform the high rate test, the DIRICH FEB channel buffer size is fixed at 120 words and the main ring buffer size at 499 words. In the first measurement, this test was carried out using two DIRICH FEBs at 10 kHz regular readout trigger frequency (shown in the figure 4.14 (yellow)). A linear relationship between the scaler rate and the rate of DAQ per pixel is seen, as is expected because they are identical. However, after a break-even point in the recorded scaler rate, the rate measured at DAQ saturates, indicating data loss (see figure 4.14).

In order to understand the reason for saturation, the measurement is repeated using only one active DIRICH FEB. Both measured curves overlap (yellow and orange curves in figure 4.14), indicating that the combiner output link or the TRB3 Ethernet link is not the limiting factor. If the combiner or Ethernet link would be overloaded by the data from 2 DIRICH modules / 64 pixels, one would expect the saturation to shift to a higher rate when the number of channels is reduced by half. Since measured data overlaps, indicating that the combiner link is not the limiting factor. Hence, the DIRICH FEB channel buffer or the DIRICH FEB main buffer must

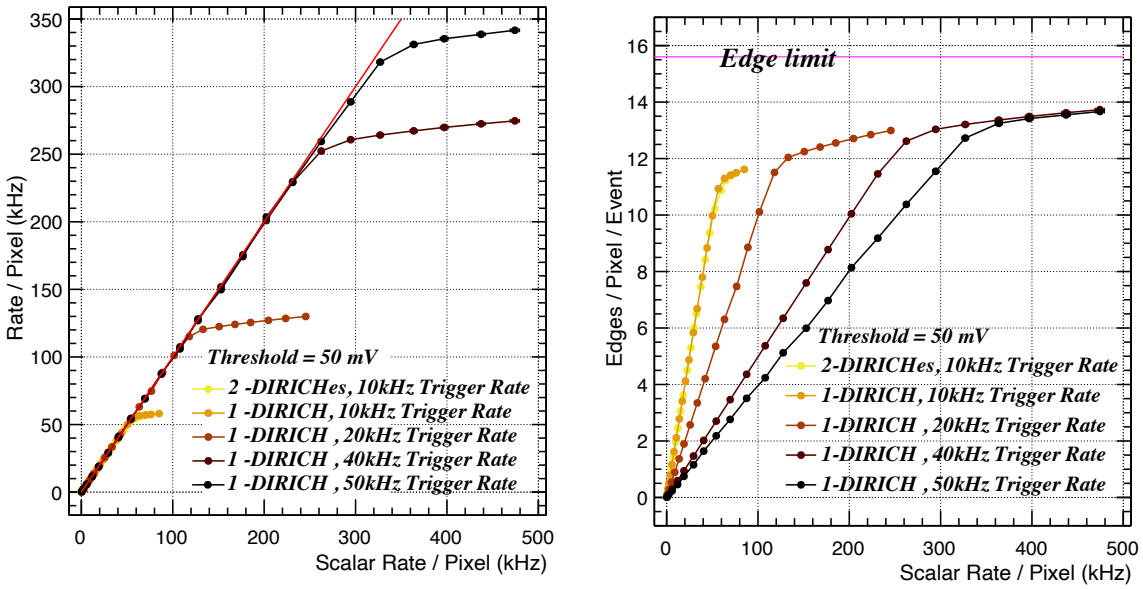

Figure 4.14: Left panel: Hit rate recorded at DAQ is plotted against the scaler rate per pixel for measurements carried out with different numbers of active DIRICH FEBs and different readout frequencies. Right panel: For the same measurement setup, the number of recorded edges (only LE and TE) in DAQ is plotted against scaler rate (edge limit—maximum number of edges that can be recorded per pixel when there is overflow at the DIRICH FEB main buffer).

be the limiting factors in these measurements.

To identify which buffer on the DIRICH (channel- or ring buffer) is limiting the data rate, the number of recorded edges (only leading edge and trailing edge) per trigger is plotted in figure 4.14 (right). If the DIRICH channel buffer is the limitation, then the saturation of the edge multiplicity must be near the maximum buffer size set for the channel, which is 120 words. This is not observed here; the edge multiplicity saturates close to 12 edges per channel per trigger (at 10 kHz readout frequency, yellow and orange curves in figure 4.14). This indicates the rate saturation is due to the size of the DIRICH main ring buffer.

In order to increase the dynamic range of the measurement, the readout trigger frequency is increased up to 50 kHz in steps, the results are plotted in the figure 4.14 (red, brown, black). This increase in readout frequency reduces the hit multiplicity in the queue at the buffer, thereby increasing the bandwidth. As the readout frequency increases, the saturation rate at the DAQ increases, this is reflected in the number of edges measured. A single-channel hit rate of up to 320 kHz per pixel is observed in the DAQ data stream if only a single DIRICH FEB with all 32 channels active is read out. Further increase of the readout frequency (beyond 50 kHz) and measurement of even higher rates caused an overload of the Ethernet link from the TRB3 to the DAQ PC.

The largest data rate possibly produced by a single DIRICH-FEB is the product of the maximum hit rate per channel (320 kHz), the number of channels in the DIRICH-FEB (32), and the maximum size of a single hit (12 bytes = 4 bytes × (2 edges + 1 epoch)), resulting in 1.144 Gbps

(assuming 8b/10b encoding). This data size is below the saturation limit of the DIRICH-combiner link (TRB link) which is at 2 Gbps. Therefore, the DIRICH-combiner link is not a limitation for the data transmission at such high rates on a single DIRICH-FEB.

Now that the maximum attainable per-channel rate from a fully active DIRICH FEB (32 channels) using the lab setup is established (for a maximum readout rate of 50 kHz), further tests are done to test the rate capability of an individual channel. This is achieved by reducing the number of active channels, also fixing the readout frequency at 40 kHz in order to prevent the Ethernet bottleneck. The measurement mentioned above is repeated for the reduced number of active channels, and the results are shown in figure 4.15. Here, a saturation rate of up to 2.2 MHz per pixel is achieved for the 1, 2, and 4 active channels. This higher saturation rate up to 4 channels is due to individual channel buffer size. Since individual channel buffer size is set at 120 words, for up to 4 channels the DIRICH FEB buffer will not be maxed out (4 channels $\times$ 120 words per channel = 480 $<$ 499 words per DIRICH FEB). When the number of active channels is increased to 6 and 8, a proportional drop in the overall saturation rate is observed, here the limitation is in the DIRICH FEB main buffer (6 channels $\times$ 120 words per channel $>$ 499 words per DIRICH FEB). This is reflected in the number of leading and trailing edges derived, as shown in the figure 4.15 (right), where the edge multiplicity saturates close to the channel buffer size limit.

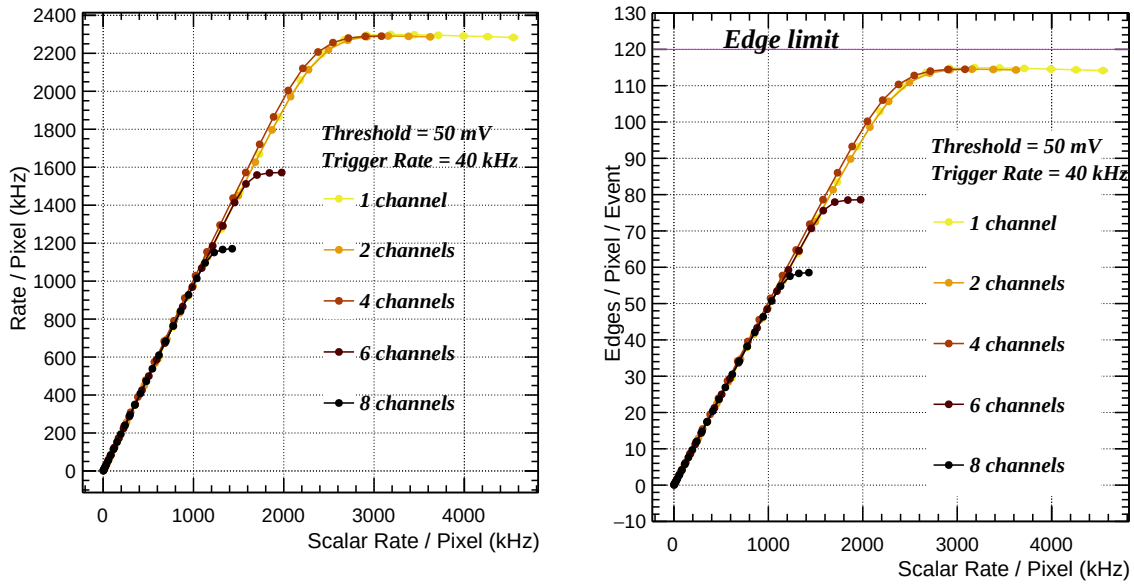

Figure 4.15: Left panel: Hit rate recorded at DAQ is plotted against the scaler rate per pixel, for measurements carried out with reduced number of active channels of a DIRICH FEB at 40 kHz readout frequency. Right panel: For the same measurement setup, the number of recorded edges (only LE and TE) in DAQ is plotted against scaler rate (Edge limit - Maximum number of edges that can be recorded per pixel when there is overflow at the DIRICH channel buffer).

Sharp saturation effects are not observed in either 64, 32, 8, or even only 6 active channels, in contrast to 1, 2, and 4 active channels, because of the inhomogeneity of the hit distribution in the different channels (individual channel rate is defined by inhomogeneity of illumination and variation in PMT efficiency). For 64, 32 channels the edge multiplicity does not saturate at the

maximum DIRICH ring buffer size (edge limit), which is $\frac{499\ \text{(DIRICH ring buffer size)}}{32\ \text{(number of channels)}} = 15.6$ edges / trigger / channel (see figure 4.14 (right)). Similarly, for 1,2, and 4 channels the saturation is not at the maximum channel DIRICH buffer size of 120 words (see edge limit in figure 4.15). This is due to the addition of epoch messages along with the LE and TE messages. All DIRICH and combiner on one backplane share a common 100 MHz clock onboard. For approximately 100 µs, each channel sends out its epoch signal which contains the absolute time of the onboard clock. The edges recorded in between two epochs are assigned time relative to the epoch, thereby reducing the data overhead of sending absolute time for each edge. This is also why the saturation limit of edges per readout is higher at a higher readout rate in the figure 4.14 (right). Because the probability of receiving multiple edges in between the epoch markers is higher at high hit rates, the edges/epoch ratio per readout is higher compared to lower hit rates.

Apart from the buffer limitations in DIRICH FEB, there are no severe limitations in the analog signal processing and subsequent digital processing of the signals. With the current setup, a single channel of the DIRICH can handle hit rates of at least 2.2 MHz. This is a much higher rate than the expected photon rate at hot regions of the CBM RICH, and is limited by the maximum tested readout trigger rate of 50 kHz. For even larger readout rates (which could not be implemented in the TRB lab setup) even higher rates/channel seem feasible.

4.7.4 Data quality test

After evaluation of the readout chain performance in terms of data loss under high rate conditions, a natural next step is to check the quality of data transmitted at these rates. The setup shown in figure 4.2 is used for this measurement. The measurement procedure is structured as follows,

- Using the circular collimator, a ring like contour of hits is produced on the MAPMT plane. Since the opening width of the collimator slit is about 1 mm, in order to avoid the divergence of light, the distance to MAPMT is adjusted such that the ring width is one pixel.
- A 20 ns selection window relative to the laser sync signal is applied to separate laser hits from uncorrelated background. Even within the correlation window, there are hits due to stray light, although they are minimal. Therefore, in order to trace the ring contour, a minimum hit multiplicity per pixel condition is used.
- The hit multiplicity in the pixels of the ring contour without any background illumination and dark hits, $N(0)$ is measured. The dark hits are detected in the absence of laser and LED, primarily due to stray light and these are subtracted for all measurements.
- The MAPMT is now homogeneously illuminated additionally to the laser reference pulse using an LED (in DC mode) as background source. Hence, the LED acts as the uncorrelated background source and the laser as the correlated signal source.

- The hit multiplicity in the ring for different background illumination is measured, $N(r)$ where r is the overall rate in Hz.
- The ratio of hit multiplicities with and without LED background is measured, $\frac{N(r)}{N(0)}$. In the absence of loss of any data due to high rate, the ratio should be equal to one.

One DIRICH FEB is used for this analysis, the measurement setup is depicted in figure 4.16.

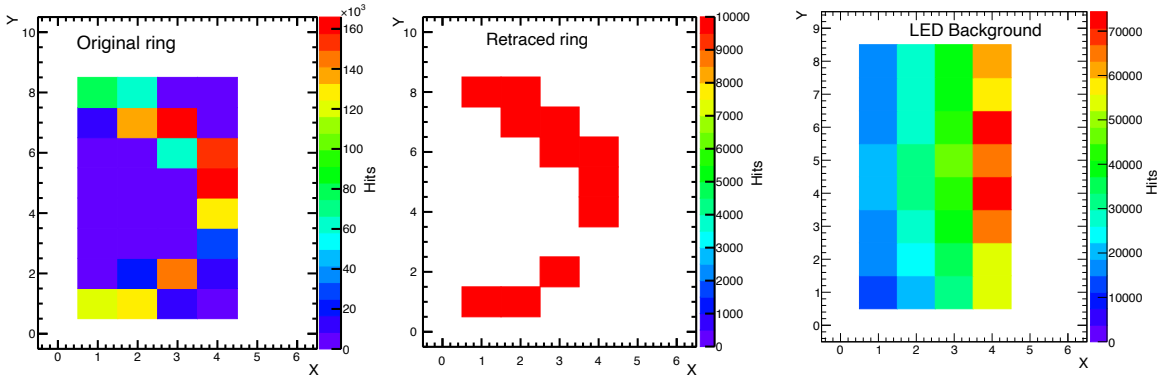

Figure 4.16: Left panel: The hits correlated to the laser signal are shown, where the arc of the ring on MAPMT is visible. Middle panel: The ring contour is retraced by specifying a minimum hit per pixel criteria on the histogram from left panel. Right panel: The uncorrelated hits showing the background illumination by the LED (applying an exclusion window for the laser reference signals).

4.7.5 Results and discussions

The average signal hit multiplicity per laser event within the correlation window is varied up to 6 hits. During the test, the total hit rate (coming from the LED background hits) was gradually increased from 3 Hz to 300 kHz. A regular readout trigger rate of 40 kHz, together with a laser pulse frequency of 10 kHz was used during these tests. A total of 3×10^6 readout trigger events are analyzed for each data point. A snapshot of the ring image as reconstructed at different overall hit rates in the DAQ stream is shown in figure 4.17, this is the image of laser-correlated hits after applying the 20 ns coincidence time cut. No data loss is observed up to an average photon hit rate of $\sim$ 240 kHz/channel. Above these rates, data loss is expected (section 4.7.3). The DIRICH FEB main buffer overflow due to background LED hits results in a complete data loss for a few channels including the channels where the ring is projected. The channels sequentially transmit the data to the main ring buffer. Upon reaching its full capacity, the buffer discards data from a few channels first in the queue. This explains the complete loss of data for some channels. Even when some data from a few channels is lost, the data in the remainder of the channels remains identical for all hit rates. This indicates there is no deterioration in the quality of the data transmitted.

As a quantitative measure of the quality of the ring, the normalized number of hits per ring is

calculated as $N(r)/N(0)$, with

$$N(r) = \sum_{Ring} (N_{hits} - N_{hits-uncorrelated} - N_{dark-hits})$$

being the number of laser-induced signal hits per ring for different values of the background rate r, and

$$N(0) = \sum_{Ring} (N_{hits-LED-off} - N_{dark-hits})$$

being the number of signal hits without background rate, with the LED being switched off. Since LED hits are spread uniformly in the event trigger window, an uncorrelated contribution from the LED is estimated assuming a 20 ns wide readout window ($N_{hits-uncorrelated}$), and subtracted from $N(r)$ to correct for the contribution from trans-incidence of LED hits onto the ring. The results are plotted in the figure 4.18. Nearly no loss of hits is observed in the ring up to the afore determined buffer overflow limit, where the ratio drops drastically. Using a readout rate of 40 kHz this indicates good data quality for background rates up to at least 240 kHz. The response is the same for different hit multiplicities in the ring. In another iteration of the analysis, in order to reduce any additional hits that might be caused by crosstalk due to the presence of LED hits with Laser hits, a ToT cut (> 2.5 ns) is imposed on all hits registered. Even with the ToT cut, there is still a sub-percent shift from ideal linear behavior before the saturation region. This shift increases with an increase in the overall hit rate, suggesting a direct correlation between them. The cause of the shift can be understood as additional neighboring channel crosstalk which has the ToT almost similar to that of a real photon hit.

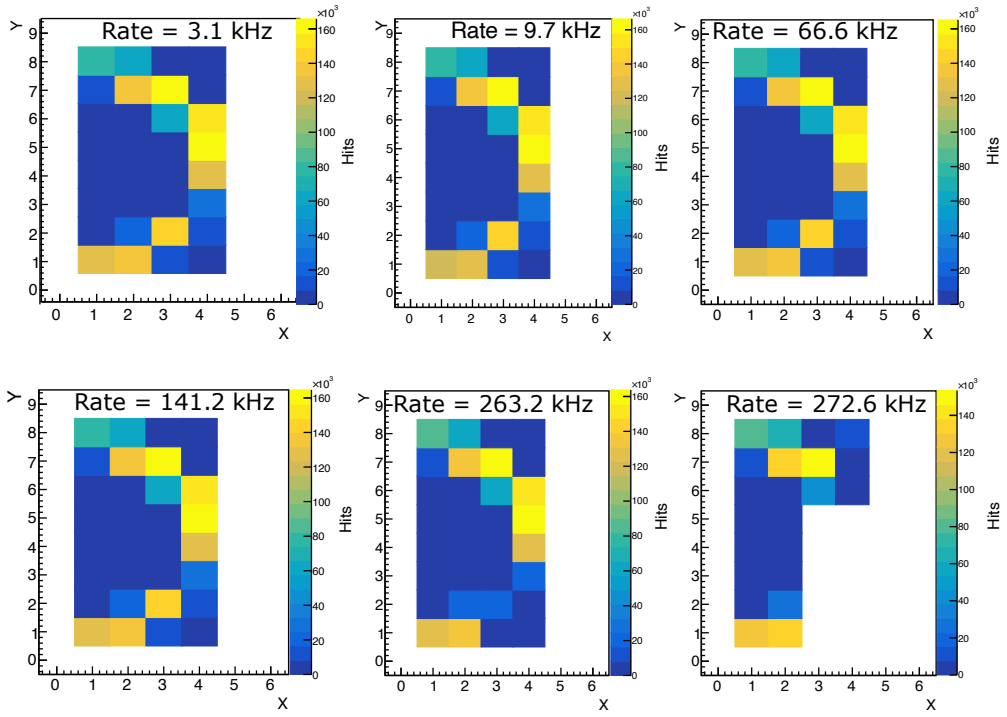

Figure 4.17: Snapshot of the reconstructed ring image for different overall hit rates as observed in the DAQ data stream. Laser correlated hit multiplicity per event = 5.94 hits.

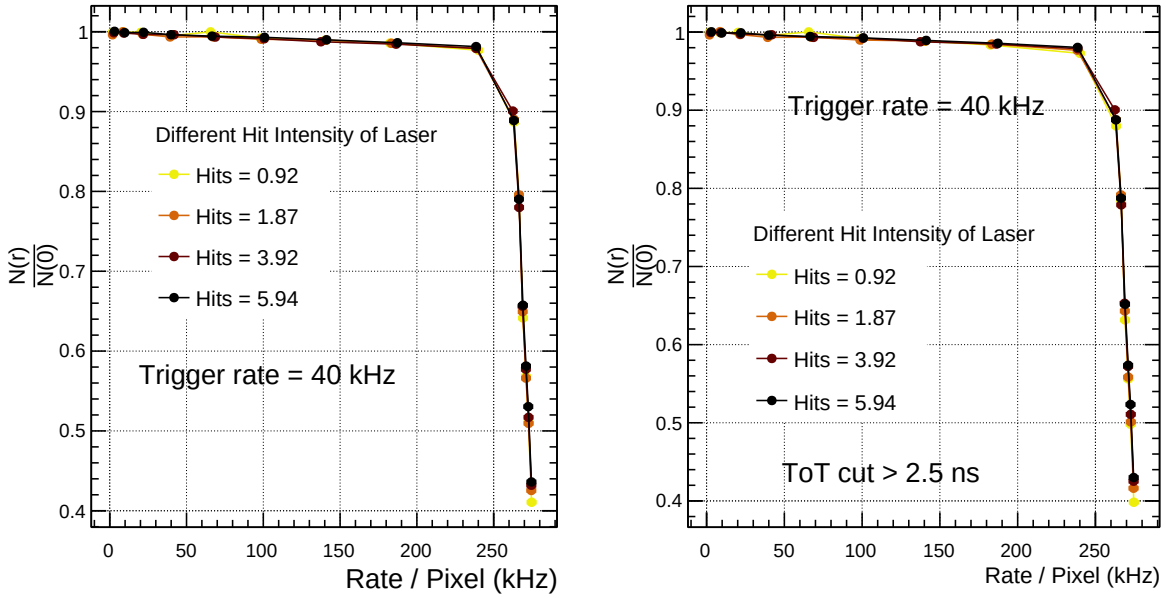

Figure 4.18: $\frac{N(r)}{N(0)}$ as a function of rate/pixel for different hit multiplicity in the ring. Left panel: Without ToT cut. Right panel: With ToT cut (ToT > 2.5 ns).

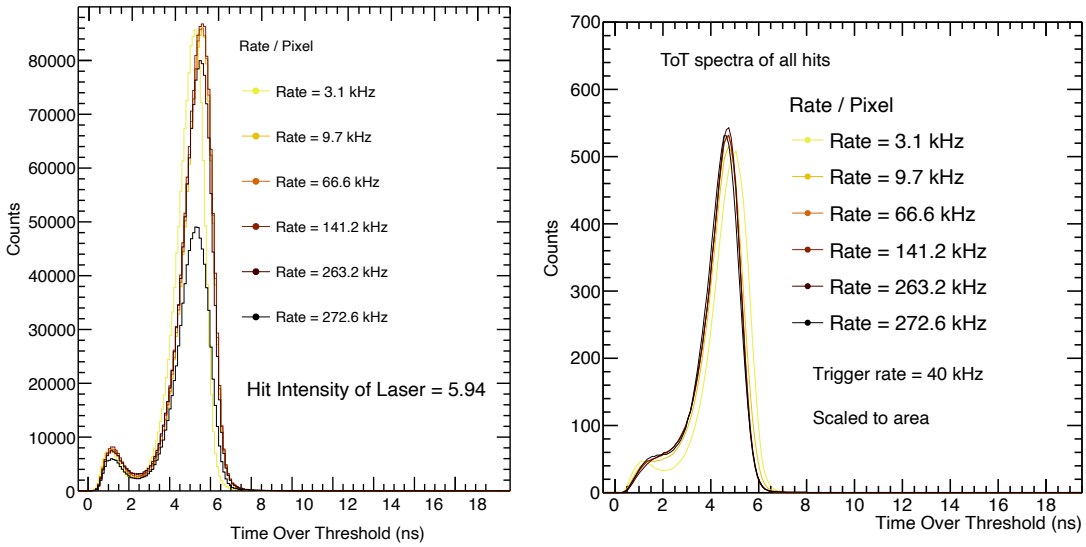

Figure 4.19: Left panel: ToT spectra of correlated laser hits in the ring. Right panel: ToT spectra of integrated hits from all pixels, scaled to area.

Another dedicated analysis was carried out in order to assess the possible effect of the high hit rate on the timing performance of the DIRICH by analyzing the ToT spectra of laser-correlated hits in the ring and integrated hits in all pixels of the MAPMT. The results are plotted in figure 4.19. The ToT spectra of the laser-correlated hits resemble a typical ToT spectra of six simultaneous hits in the MAPMT which was derived earlier in the previous section 4.5. The ToT spectra of the laser-correlated hits (figure 4.19 (left)) exhibit no significant qualitative difference for different hit rates. However, the ToT spectra of integrated hits from all pixels resemble single-hit ToT spectra for higher hit rates (> 60 kHz). This is to be expected because the hits are mostly dominated by uncorrelated LED hits, which are isolated hits spread over time. For

the lower hit rates ($< 10\,\text{kHz}$), the hits are dominated by the laser-correlated hits (since the pulse rate of the laser is 10 kHz). This is reflected in the ToT spectra (figure 4.19 (right, yellow legend)), which bear resemblance to the ToT spectra of the correlated laser hits (figure 4.19 (left)). In conclusion, the shape of ToT spectra did not change with the increase in the hit rate, indicating that large hit rates have no effect on the DIRICH timing performance.

4.8 Investigation of noise induced by DC/DC converters in a new DIRICH Power module

The MAPMT signal amplitude for single photons is rather small, in the order of a few mV only. In the DIRICH FEB, these signals are first amplified in the frontend amplifier (roughly factor 20) and subsequently discriminated (threshold in the range of 30 mV to 100 mV after amplification) to measure individual photons. Preserving a good signal-to-noise ratio throughout the analog part of the digitization chain is important in order not to trigger on noise, and to obtain clean digitized signals despite small amplitudes. A major source of noise and S/B degradation had been observed earlier to be caused by the usage of DC/DC converters on the DIRICH Power module. DC/DC converters are notoriously known to be a source of EMC noise, both electrically radiated and magnetically radiated, due to the large switching currents with fast rise / fall times.

4.8.1 The DIRICH LV power supply scheme

Up to 12 DIRICH FEBs and the DIRICH Combiner module on a given backplane need to receive electrical power on several different voltage levels: 1.1 V and 2.5 V are needed for the FPGA core and I/O banks of the DIRICH FEB, and 1.1 V as well for powering the FEB analog stage. Another 1.2 V is needed in addition for powering the FPGA core on the DIRICH Combiner module, and 3.5 V are necessary for powering the SFP fiber interface on the Combiner. It is the task of the DIRICH power module (one per backplane) to provide and regulate these 4 different voltage levels, which are further distributed via the DIRICH backplane to all modules. In addition, the DIRICH power module also receives the HV for the PMTs and delivers this also via the common backplane. Two alternative powering concepts were initially implemented on the first iteration of the power module:

- All 4 individual LV supply levels can be either provided via a multi-pin connector using external LV power supplies to provide all different voltage levels. Here, the DIRICH power module only provides additional filtering and stabilization using linear Low-Dropout Voltage regulators (LDOs).
- All 4 individual LV supply voltages are generated on the power module itself using several individual DC/DC switching converters, fed by a single, common external supply line of up to 36 V.

The first variant was implemented in the HADES RICH detector. It offers a big advantage of exceptionally clean power supply lines, inducing no additional noise into the sensitive preamplifiers. However, the big disadvantage of this variant is the large supply currents at low voltage levels. In the case of HADES, supply currents of several 100 A had to be distributed, potentially causing shifts of ground levels and significant power loss and heat on the supply cables. A total of 10 individual LV power supplies is used for HADES in order to power the detector. The required complexity of the power distribution cabling is enormous.

Variant 2 is much more elegant in this sense, requiring only a single LV power source with moderate current due to the larger voltage. However, operating 4 different DC/DC converters on each DIRICH backplane / Power module in very close vicinity to the sensitive analog part of the front-end electronics is a major challenge for proper shielding and filtering.

A first iteration of the DIRICH Power module design allowed choosing between both powering variants by comprising DC/DC converters and an additional connector for external powering (with DC/DC converters being switched off). Initial tests of both schemes revealed major noise issues with the DC/DC variant, which is the reason why, for the HADES detector, the external powering scheme was implemented.

However, for the CBM RICH detector, due to the much more confined space constraints and much longer cable lengths, using a set of external LV power supplies for all required voltage levels is excluded. Consequently, a second iteration of the DIRICH Power module was developed, using new, recent state-of-the-art “silent-switcher” DC/DC converters (LT8648S from Analog Devices) combined with better filtering- and shielding design, accompanied by an external metal shielding to reduce EMC noise as much as possible.

The following chapter describes a comprehensive test of this new DIRICH power module and a direct comparison to the first variant in terms of induced noise into the readout chain. Aiming for a full qualification of this new variant of the power module for usage in the CBM RICH detector. Figure 4.20 shows the different variants of power modules that were tested: the version 1 module (with either internal DC/DC or external LV powering), the new, improved version 2 module, the new module including an external EMC shield, and the new module with an EMC shield plus additional ferrite EMC absorber foil on top. To reduce the contact conduction, the EMV foil is covered with insulating tape. All these variations were tested both in a dedicated lab setup as well as inside the mRICH detector setup in mCBM.

4.8.2 Measurement of Noise bandwidth

To compare the effect of different powering variants on the noise performance of the readout, the noise bandwidth of the DIRICH FEB is used as the measurement observable. Each DIRICH input stage is based on a comparator, comparing the actual input signal to an onboard-generated bias- or threshold voltage (see section 4.1). For measurement of the noise bandwidth, this threshold voltage is systematically varied from negative values, crossing zero, to positive

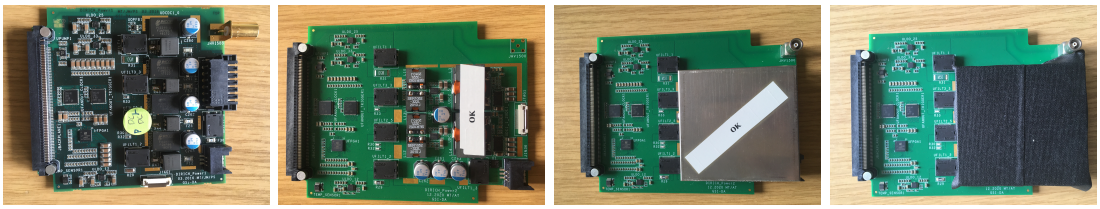

Figure 4.20: (From left) Picture 1: First iteration of power module with on-board DC / DC converter, which has both single voltage input (SVI) port and externally regulated LV input port. Picture 2: Second iteration of power module with DC/DC converter (having only the SVI port). Picture 3: Second iteration of power module with additional shielding box. Picture 4: Second iteration of power module with shielding box and EMV foil.

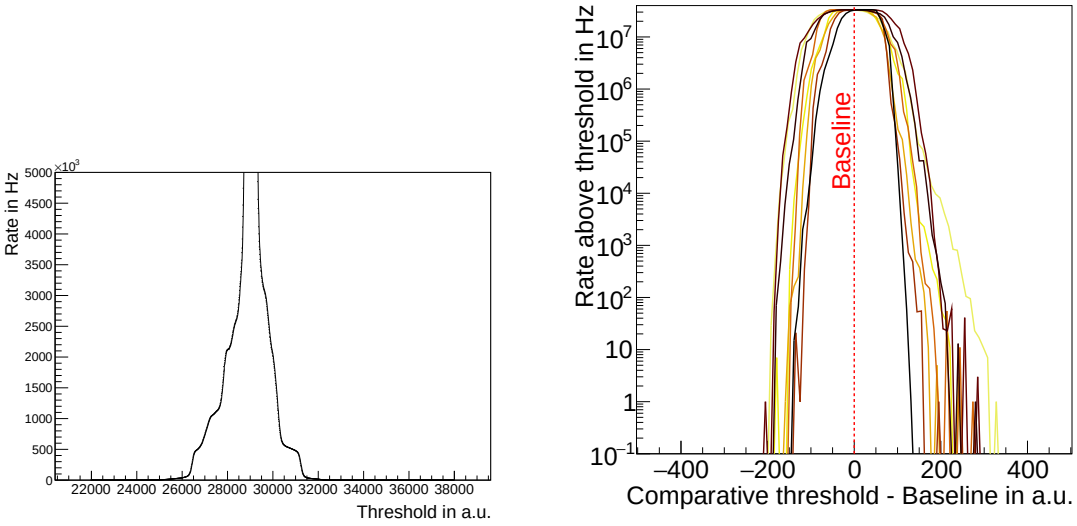

Figure 4.21: Left panel: Graph depicting the scaler rate for a single channel of DIRICH for different noise reduction threshold voltages. Right panel: Graph depicting scaler rate measured above the noise reduction threshold (adopted from [105]).

voltages, while measuring the rate of detected threshold crossings (i.e., "hit rate") as a function of threshold for each voltage using the scalers directly connected to the output of the comparators on the DIRICH. A depiction of the scaler rate versus threshold is shown in the figure 4.21. A very steep increase in hit rate by many orders of magnitude (i.e., "noise") is observed for absolute threshold voltage levels lower than the noise amplitude on the input signal. The bias voltage span for which such noise is observed is called "noise bandwidth". The center of this band is defined as "bias level", corresponding to threshold zero. For normal DIRICH operation, the threshold must be set well outside this noise band, of which the half-width defines the minimum-useable threshold value.

For comparison of the different power module variants, this noise bandwidth (both average and maximum over all channels of a given FEB) is used as a measure of the noise induced by the power module into this individual module.

4.8.3 Laboratory setup

A fully equipped backplane with 12 DIRICH FEBs, a power module, and a combiner is set up in the lab (see figure 4.22). The power drawn for different power modules at different input voltages is shown in table 4.2.

Table 4.2: The power drawn by various types of power modules is summarized in this table.

Power module variant	Voltage (V)	Current (mA)	Power drawn by backplane (W)
New (DC / DC)	32	768	24.57
New (DC / DC)	18	1242	22.46
Old (DC / DC)	32	796	25.47

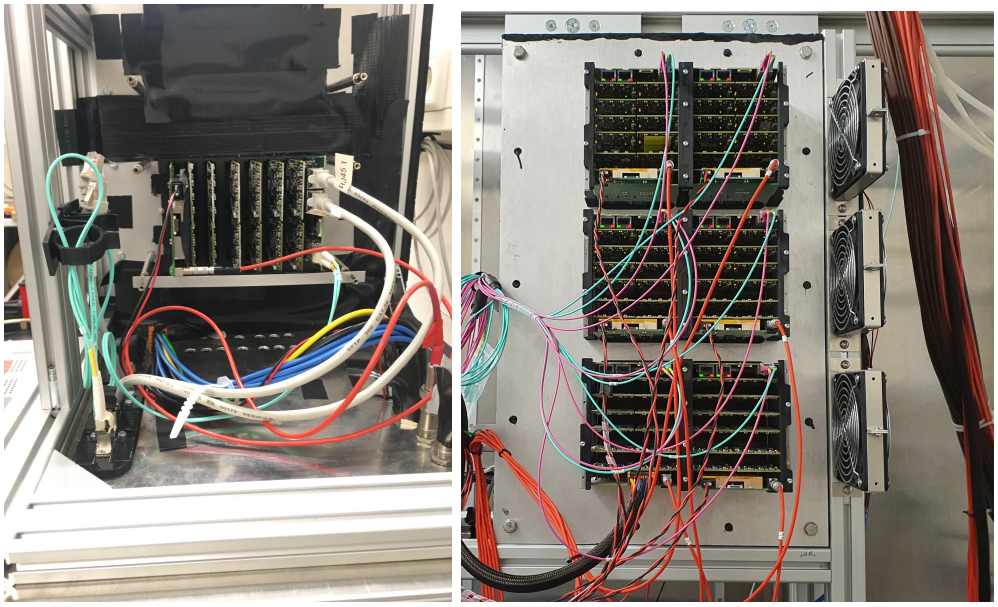

Figure 4.22: Left Photograph: The laboratory setup, where one backplane with 12 DIRICH FEBs and a power module. Right Photograph: The mRICH setup at mCBM, showing six backplanes with 72 DIRICH FEBs and six power modules.

Measurement principle:

- To understand the effect of distance from the power module on the emitted EM noise, the DIRICH FEB under tests are kept at different distances (positions relative) to the power module in a backplane.
- The backplane is fully loaded by filling vacant places with dummy DIRICH FEBs (having equivalent power consumption as ordinary FEBs).
- A noise bandwidth scan is performed.
- Average / Maximum half noise bandwidth over/of 32 channels of each DIRICH FEBs is obtained.

- To reduce the positional bias, the DIRICH FEB under test is shuffled to three different positions. The average of all three measurements is considered as the final noise bandwidth.
- The procedure is performed for the old power module with an external LV supply and using a supply voltage of 32 V.
- The procedure is performed for two new power modules, without and with using a shielding box and EMV foil.
- Since the new DC/DC-based converter can work from 18 V to 32 V supply voltage, the module is powered with both extreme voltages for comparison.

4.8.4 Measurement results and discussion

For calculation of the noise bandwidth, six DIRICH FEBs at different distances to the power module are considered. Figure 4.23 shows the comparison of average noise bandwidth measured for different power modules with different configurations. The noise bandwidth for a DIRICH FEB close to the power module is higher, and reduces as the distance from the power module increases. This distance dependence indicates that most of the induced noise is radiated via air, and not caused by noise or ripple on the low-voltage side and supply lines (thanks to the extensive filtering on the power module).

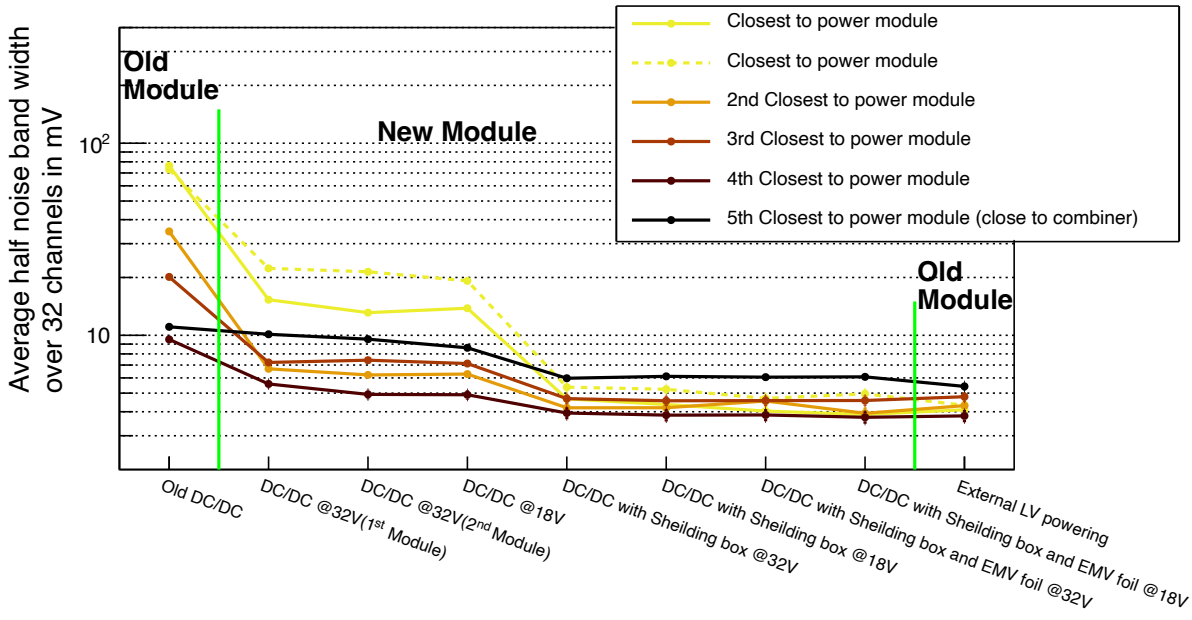

Figure 4.23: Average half noise bandwidth over 32 channels for different iterations of power modules with different configurations. The old module referenced here is the first iteration of a power module with an on-board DC / DC converter. The new module is the iteration with an advanced silent-switcher-based DC / DC converter. The green line helps to distinguish the responses from the old and new modules more clearly. The *X axis* shows different powering schemes.

The old power module using an external LV supply, with DC/DC converters being switched off, has the lowest-possible noise level (less than 10 mV half-bandwidth, roughly 0.5 mV at the amplifier input), and can be regarded as a reference for evaluation of the new, DC/DC-based power module. Using the DC/DC converters on the old power module results in much larger noise levels (10 mV to 100 mV depending on distance). It is evident from comparing the first two points in figure 4.23, that the new, DC/DC-based power module radiates much less noise (5 mV to 25 mV) compared to the old module using a DC/DC converter. The use of the shielding box further reduces the noise (less than 7 mV) for the new module, and adding additional EMV absorber foil on top of the shielding box does not have much effect. Two different new power modules produce similar results for noise bandwidth. The noise bandwidth is independent of applied input voltage (18 V to 32 V), as is the total power consumption (indicating constant DC/DC efficiency over a wide input voltage range).

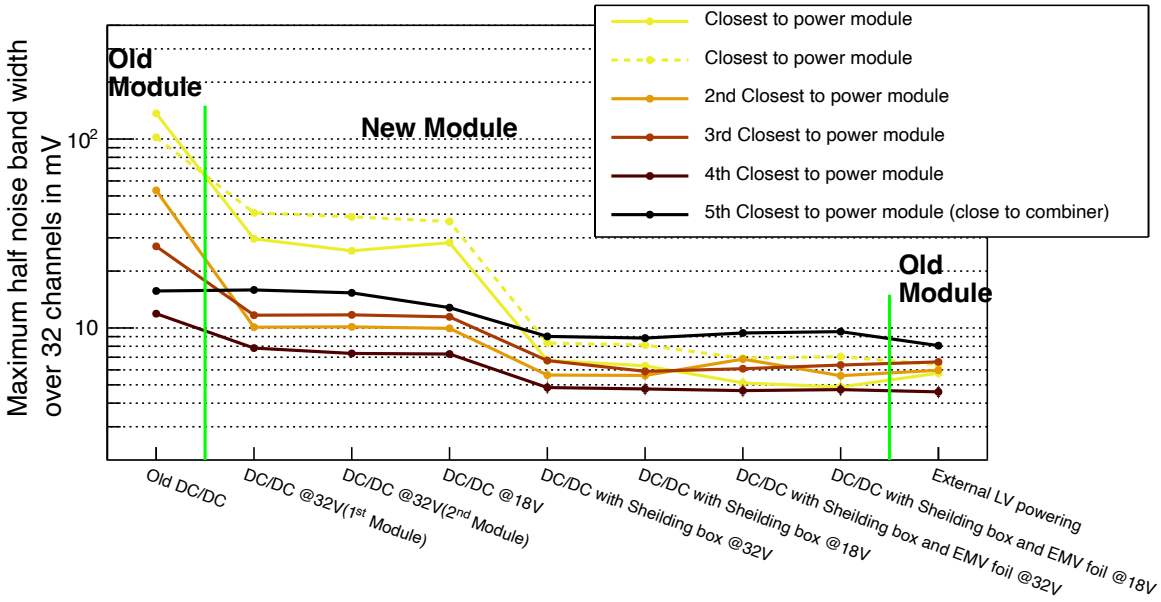

Figure 4.24: Maximum half noise bandwidth over 32 channels for different iterations of power modules with different configurations. Additional descriptions are provided in the figure 4.23.

With the new iteration of the DC/DC-based power module, and mounting the additional shielding cover plate, the overall noise half-bandwidth is less than 10 mV which is far less than the intended operating threshold of 50 mV to 100 mV and comparable to the noise observed using external LV powering with the old module.

4.8.5 mRICH Setup and Measurement Results

The lab measurements described above provide a solid, quantitative evaluation of the noise performance of the new DC/DC-based power module iteration; however, they were derived using a single backplane only and using several DIRICH power dummy modules due to an

insufficient number of DIRICH modules available at the time of measurements.

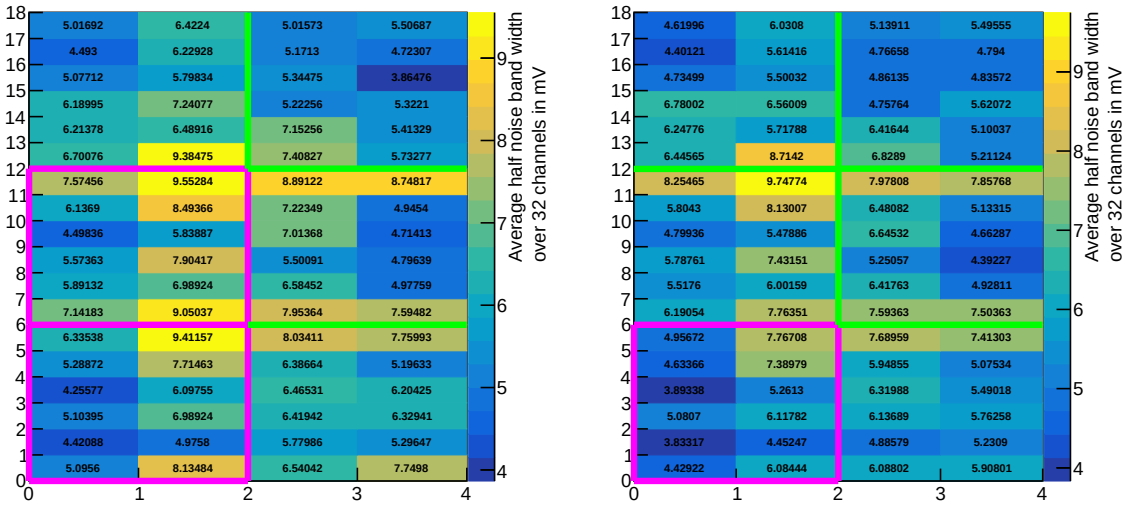

Figure 4.25: Left panel: Scan 1 with 4/6 backplanes with new power module. Right panel: Scan 2 with 5/6 backplanes with the new power module. The green lines indicate the border of each backplane with the new power module, and the purple line indicates the border of the backplane with the old power module. Each box represents a DIRICH FEB, and the values in each box are the average half noise bandwidth over 32 channels in mV.

In order to confirm these results under realistic conditions, an additional, conceptually similar measurement was carried out using the mRICH prototype detector setup, which is part of the mCBM installation at GSI. The mRICH setup (see figure 4.22) consists of six fully populated backplanes (with six power modules, six combiner modules, and 72 DIRICH FEBs). Five (four) of the power modules are of the new, DC/DC-based type; only a single (two) power module (lower left in figure 4.22) is of the old type and using the external LV supply scheme. Each of the new power modules was fitted with a shielding cage. Using this setup, the noise bandwidth of all 72 DIRICH FEBs on each of the 6 backplanes could be measured in parallel, thus providing a very comprehensive evaluation. Two scans were performed, where in the first scan four out of six backplanes were fitted with power modules of the new type, and the rest with power modules of the old type powered by an external LV supply. For the second scan, one more of the old-type modules was replaced with a module of the new type. Thus, one can analyze the noise bandwidth for more DIRICH FEBs at different distances, and also one can have a direct comparison of one particular backplane with two different power modules under identical conditions.

The results of the measurement are plotted in the figure 4.25. The following inferences can be drawn from the two scans:

- The average half noise bandwidth of all the DIRICH FEBs connected to the backplane with the new power module is less than 10 mV, and thus comparable to the old power module with external LV supply (the optimum reference standard).

- The measured noise bandwidth is far below the standard operating threshold values for standard operation ($\geq 50\,\mathrm{mV}$).
- The noise bandwidth in the DIRICH FEB closest to the power module is slightly increased, and quickly drops with increasing distance. Similar observations can be made on each of the backplanes.

5

Electron identification in CBM

Electron identification methods based in different subsystems are briefly described in this chapter. The performance metrics for electron identification are described, and the current status of the reconstruction is presented. Counter-measures are proposed and evaluated in the latter sections to address the inefficiency of track propagation from STS to RICH. Sections of this chapter have been published in the following papers/reports,

1. P.Subramani, et al., *Updated RICH geometry QA tests*, CBM Progress Report 2022 (p85-86) [65].

2. P.Subramani, et al., *STS - Magnet updated geometry and its impact on the RICH performance*, CBM Progress Report 2022 (p82-83) [65].

3. P.Subramani, et al., *Optimization of the extrapolation plane position for RICH ring-track matching*, CBM Progress Report 2023 [106].

4. P.Subramani, et al., *RICH reconstruction performance improvement*, CBM Progress Report 2022 (p87-88) [65].

5.1 Simulation setup

The CBMROOT simulation framework is under continuous development. During the course of this thesis, each sub-detector underwent many software changes. The shielding box component of RICH GEANT geometry has been included in version v22a. Quality tests have been conducted against both the old and new versions, and the results have been reported [65]. The GEANT geometry of STS was changed from 8 stations in version v22a to 3+5 modular stations in version v23a. RICH performance against the version change was quantified and incorporated into the report [65]. The simulation setup for this thesis is summarized in table 5.1. Since

Table 5.1: Table displaying simulation setup, which includes the choice of FAIRSOFT, FAIRROOT, and the current version of CBMROOT. The GEANT V3 is used for simulation; the geometry versions of different detectors used in this thesis are listed.

Software	**Version**	**Geometry**	**Version**
CBMROOT	Feb23	MVD	v20d_tr
FAIRROOT	v18.8.0	STS	v22c
FAIRSOFT	nov22p1	Magnet	v22a
GEANT	V3	RICH	v23a
		TRD	v20b_1e
		TOF	v21a_1e
		Beam pipe	v21d
		Platform	v22b
		Field map	v22c

the particles of interest are the electrons originating from Low-mass Vector mesons (LMVM) decaying inside the target, the proposed reconstruction algorithms are evaluated for electrons from $\omega \rightarrow e^+e^-$ decays implanted into UrQMD simulated data. However, for the development of the reconstruction algorithms (as discussed in this thesis), a single-electron sample is used, either standalone or in combination with UrQMD-generated events. Details of which are given in the table 5.2.

Table 5.2: Table detailing different MC simulation data samples, which includes the event generator, collision system, phase space, and number of events.

Name	**Event Generator**	**Collision system**	**Centrality/Phase-space**	**Event multiplicity**
Embedded omega sample	UrQMD with enriched $\omega \rightarrow e^+ + e^-$	Au-Au,8 AGeV/c beam momentum	central (0-40%)	1×10^6
Exclusive electron sample	FAIRBox generator	-	$2.5° < \theta_{lab} < 25°$	-
Embedded electron sample	UrQMD with enriched exclusive electrons	Au-Au,8 AGeV/c beam momentum	central (0-40%), $2.5° < \theta^e_{lab} < 25°$	-

5.2 Electron Identification methods

RICH: For the UrQMD MC sample with embedded $\omega \to e^+e^-$ decays (1 per event), the ideal response of the RICH is displayed in figure 5.1. For each true MCTrack, hits on the RICH detection plane are fitted using the Taubin elliptical fit function; the resultant radius is derived as $R = \frac{a+b}{2}$, where a and b are the semi-major and semi-minor axis of the ring. The derived radius is plotted as a function of the momentum in figure 5.1. From figure 5.1 we can infer that the RICH can be used for efficient identification of electrons up to momenta of 6 GeV/c. Above momenta of 6 GeV/c the Cherenkov rings originating from pions start to show similar characteristics as electron rings, and hence are no longer separable.

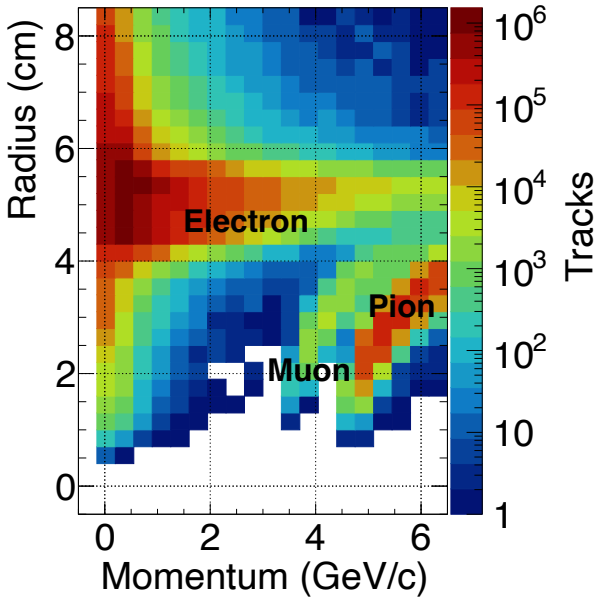

Figure 5.1: Ideal response of the RICH detector. Shown here is the radius of the fitted hits from MCTrack as a function of momentum. The Cherenkov threshold pions with momentum greater than 4.7 GeV/c produce rings in RICH, which is clearly visible in figure.

As described in section 3.4, the electron identification of ring-track pairs is based on an ANN. Distributions of the input parameters for the embedded omega data are shown in figure 5.2. A preliminary data selection criterion of ring-track distance < 10 cm is imposed before feeding data to the ANN.

Pions above the Cherenkov threshold of $\gamma_{thr} = 33.34$ at Normal Temperature and Pressure (henceforth called "threshold pions") i.e., above momenta of 4.7 GeV/c will also create Cherenkov rings in the RICH detector, albeit with smaller radius in the lower momentum range. From figure 5.1, it can be seen that threshold pion rings up to 6 GeV/c momenta are typically smaller $R < 4$ cm. This is associated with a lower number of hits per ring and reflected in higher χ^2/NDF of the ring fitter.

Due to their abundance, the sub-threshold pions can be falsely matched to uncorrelated electron

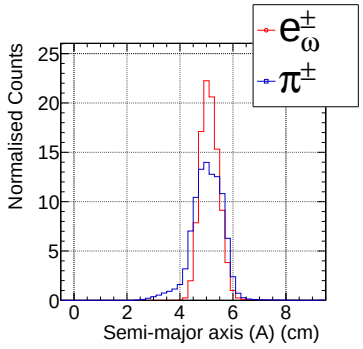

(a) Semi-major axis, a of the ring.

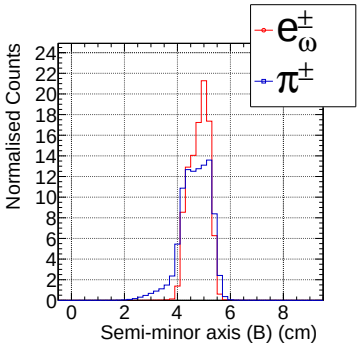

(b) Semi-minor axis, b of the ring.

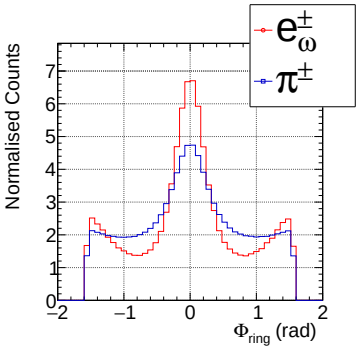

(c) Ring tilt angle, ϕ of the ring.

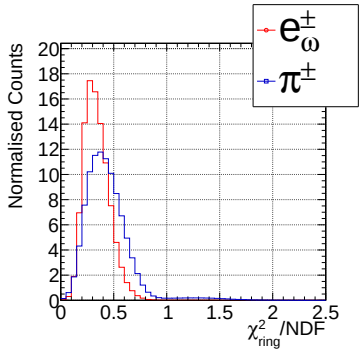

(d) Goodness of the elliptical ring fit: χ^2/NDF measure.

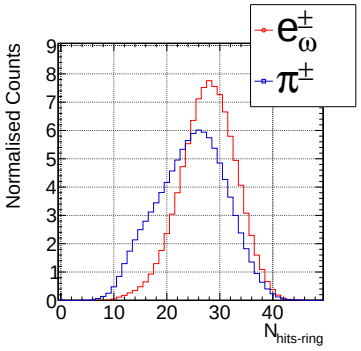

(e) Number of hits per ring.

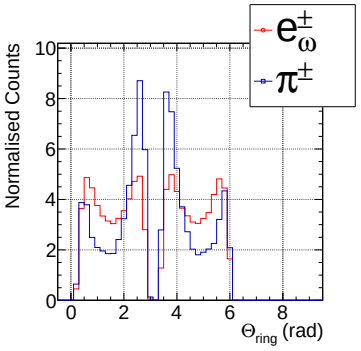

(f) Absolute position of the ring in the RICH camera in polar coordinates: Angle θ.

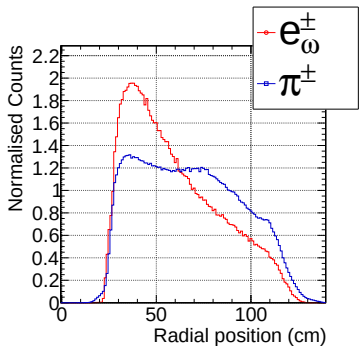

(g) Absolute position of the ring in the RICH camera in polar coordinates: radial position.

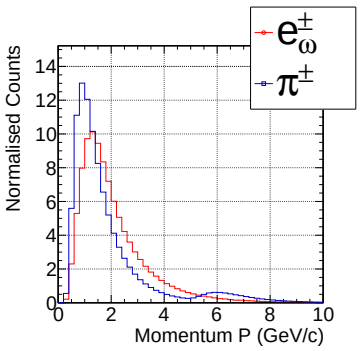

(h) Absolute momentum of the track matched to the ring.

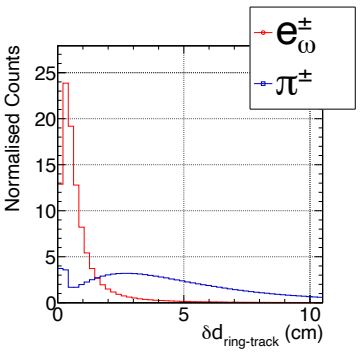

(i) Distance between track projection and closest ring center.

Figure 5.2: Input features to the ANN-based electron identifier with an initial cut on ring-track distance of 10 cm.

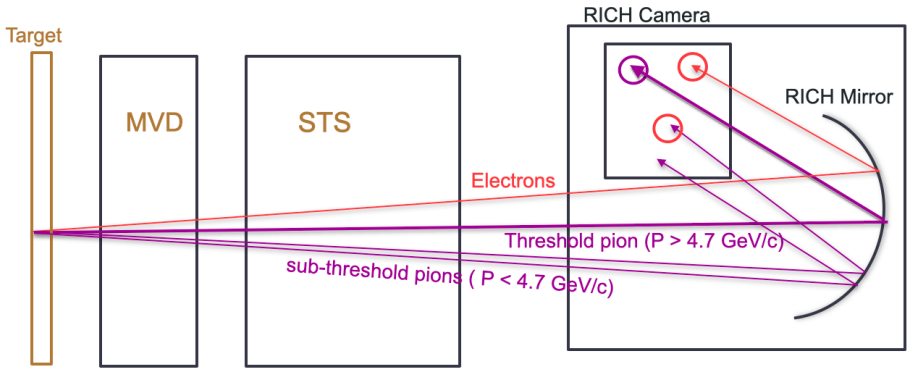

Figure 5.3: A schematic showing electrons and pions from the target forming rings in RICH and sub-threshold pions mismatching with electron rings.

rings at short distances, either stemming from primary electrons, or, much more probable, stemming from conversion electrons originating downstream of the target. A schematic visualization of the effect is presented in figure 5.3. This is reflected in the input features of the ANN, where the rings matched to the pion tracks exhibit both characteristics of pion rings and electron rings. The momentum distribution for ring-matched pion tracks has a second peak after the Cherenkov threshold (see figure 5.2h), which indicates that the tracks are matched to pion rings. It is also visible in the ring-track distance δd for pions (see figure 5.2i) where a peak close to zero is observed, indicating pion rings are matched to the pion tracks. However, the sub-threshold pions that do not have a ring candidate have a broad δd spectrum increasing with the distance. Because at a larger distance, the probability of finding an electron ring is higher. It can be inferred from the figure 5.2i that the ring-track distance, δd is the most important feature for distinguishing electrons from pions.

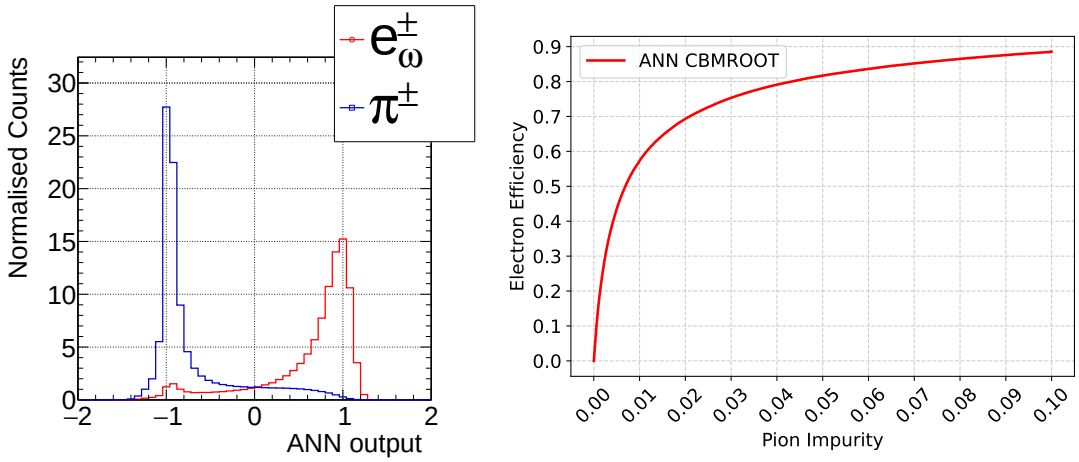

Figure 5.4: Left panel: Response from RICH ANN, showing clear separation between electrons and pions. Right panel: The receiver operating characteristic curve (or simply ROC) for applying different thresholds for the ANN response. Note that the pion impurity shown in the X axis is after the initial ring-track selection criteria ($\delta d < 10\,\text{cm}$).

The ANN output for the UrQMD sample with embedded $\omega \to e^+e^-$ decays is shown in figure 5.4. Electron candidate selection for di-electron analysis is done by setting a threshold on the ANN

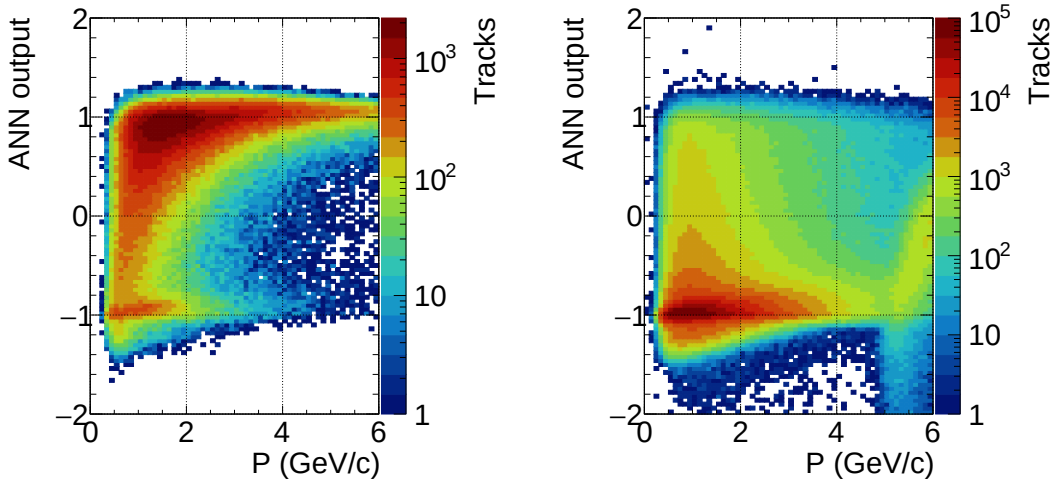

Figure 5.5: Response from RICH ANN as a function of absolute momentum, for $e^{\pm}_{\omega}$ (left) and $\pi^{\pm}$ (right) tracks.

output. In order to have control over the reconstruction efficiency of electrons over the broad phase-space, a momentum dependent cut can be employed. The momentum-dependent ANN response for electrons and pions is shown in figure 5.5.

TRD: The STS-fitted track is extrapolated to TRD by using the pion mass hypothesis. An extrapolated track is matched to the closest TRD hit in each of the layers. A TRD tracklet is formed by the matched hits. The energy deposit of the tracklet in each layer of the TRD is measured as E_i, where $i = 1, 2, 3, 4$ (layer index). Typical energy deposit from different identified particles are shown in figure 5.6 (left). Energy deposit from electrons consists of both ionizing energy loss (similar to pions) plus additional energy deposit due to a potential transition radiation photon. Using the measured energy deposit by a particle, a probability distribution for it to deposit energy in the layer i is derived, $p(s/E_i)$, where s ={Pion, Electron, Kaon, Proton}. Note that the energy deposit is independent of the charge polarity of a particle species. The likelihood that the given charged particle is an electron is given by a naive Bayes condition,

$$L_e = \prod_i \frac{p(s = e/E_i)p(E_i)}{p(s = e)} \tag{5.1}$$

The calculated electron likelihood for the embedded UrQMD data sample is shown in figure 5.6 (right). Similar to RICH ANN, the electron track selection is based on a threshold of electron likelihood. Because the TR production depends on the momenta of the track, the threshold for electron candidate selection is often done differentially as a function of momenta. The momentum dependence of the estimated electron likelihood is shown in figure 5.7. It can be inferred from the plot 5.7, that the low-momentum electrons, $P < 1\,\mathrm{GeV}/c$ have similar characteristics to the pions and hence are not differentiable. However, high-momentum electrons $P > 1\,\mathrm{GeV}/c$ are differentiable from pions. The likelihood estimation strongly depends on the number of hits (or layers) in the TRD tracklet. The lower the number of hits, the lower the classification efficiency.

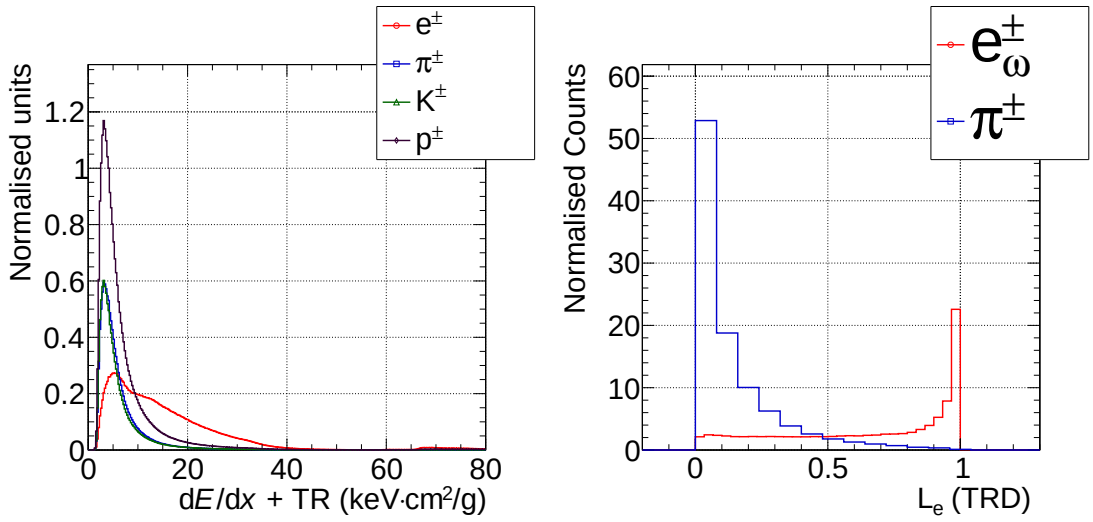

Figure 5.6: Left panel: Energy deposit by the particle and the TR for the different identified charged particle. Right panel: The calculated likelihood that the TRD tracklet is an electron.

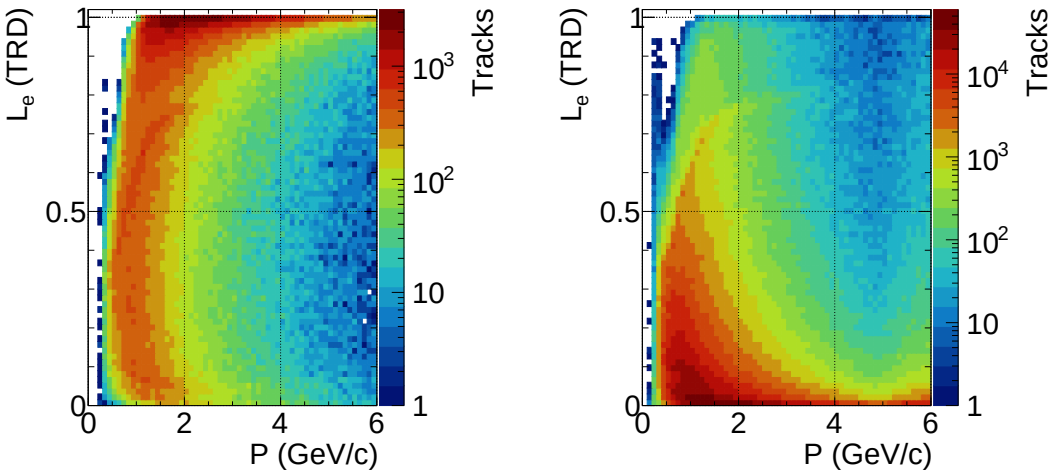

Figure 5.7: Electron likelihood as the function of momentum for $e^{\pm}_{\omega}$ (Left) and $\pi^{\pm}$ (Right) tracks. The figures indicates that, for lower momenta ($p < 1\,\mathrm{GeV}/c$), the separation between electrons and pions is weaker.

TOF: The tracks fitted in STS and matched to at least one hit in TRD are further extrapolated to TOF using a pion mass hypothesis in the track extrapolation algorithm. The closest hit in TOF to the extrapolated track is matched. Using the length of the track (L) and the difference in time between the event start time and the TOF hit time Δt (called Time-of-flight, TOF), the velocity β can be calculated as,

$$\beta = \frac{L}{c\Delta t}. \tag{5.2}$$

Furthermore, using β and momentum (p) of the track, the squared mass (m^2) of the particle can be calculated as follows,

$$m^2 = p^2\Big(\frac{1}{\beta^2} - 1\Big). \tag{5.3}$$

The dependency on quantum of charge (q) is omitted here, since we are mainly interested in

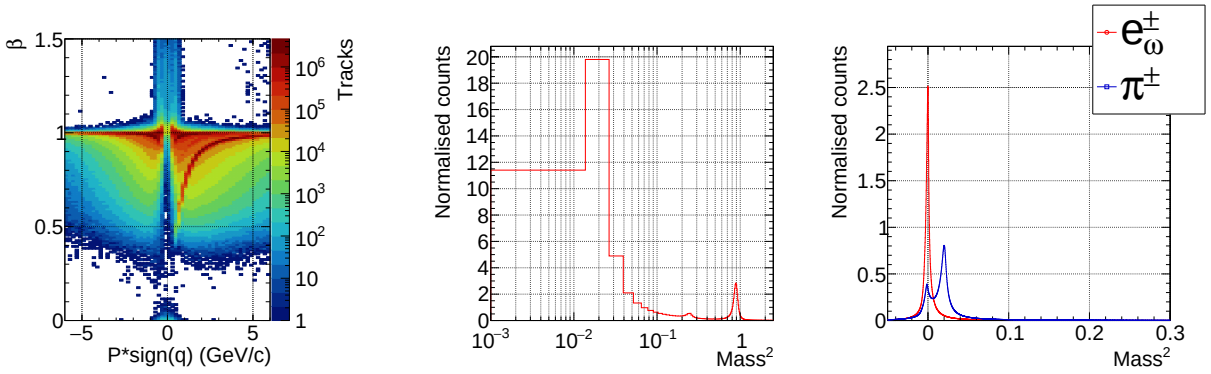

Figure 5.8: TOF response for the embedded omega sample. Left panel: Velocity of the particle as a function of the momentum is plotted, which indicates the possibility of strong high mass hadron suppression. Middle panel: Calculated squared mass for all particles. Right panel: Mass squared for $e^{\pm}_{\omega}$ and $\pi^{\pm}$, indicating the possibility of differentiating electrons from pions.

particles with $|q| = 1$. The velocity fraction β as a function of the momentum p for all charged particles in the embedded UrQMD data is shown in figure 5.8 (left). The proton band is visible for a momentum up to 5 GeV/c, which follows the $\beta = \frac{p}{\sqrt{p^2+m^2_{proton}}}$. Squared mass m^2 for the particles is shown in figure 5.8(middle). Similar to RICH, the TOF also suffers from mismatch of pion tracks to electron hits 5.8 (right). A double-peak structure for pions with one of the peaks under the electron mass regime indicates the mismatch phenomenon. The electron candidate selection is dependent on the quality cut based on m^2.

5.3 Figure of merit

The geometric acceptance for the electrons in RICH is defined as,

$$\text{Acceptance} = \frac{\text{Number of primary MC electrons with } N^{RICH}_{hits} \geq 7}{\text{Number of primary MC electrons with } 2.5° < \theta < 25°}. \tag{5.4}$$

The minimum number-of-hits criteria for better ring reconstruction efficiency is $N^{RICH}_{hits} \geq 7$. The denominator in the equation 5.4 is the global acceptance of CBM. An exclusive electron

sample (see table 5.2) is used to derive the geometric acceptance. The exclusive electron sample consists of 1×10^5 of e^+ and e^- generated within the global acceptance with $p_T \sim Uniform(0, 3)$ GeV/c. Figure 5.9 shows the geometrical acceptance of the RICH. For electrons/positrons with momenta $p > 1$ GeV/c, the acceptance is around 90%.

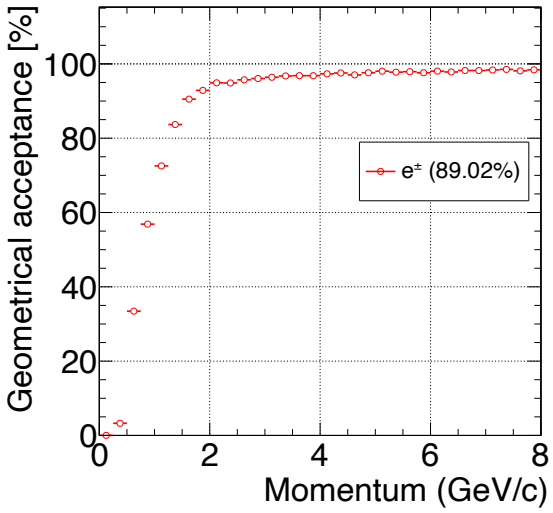

Figure 5.9: Geometrical acceptance of the RICH detector as a function of momentum for the electrons produced in the CBM global acceptance. The acceptance close to 90% reflects the active area (packing density) in a MAPMT [107].

The figure of merit for the quality of electron identification consists of two quantities: "Electron identification efficiency" (or simply Efficiency) and the inverse fraction of pions misidentified as electrons, which is called "pion suppression factor" (or simply pion suppression). Since RICH is the first electron ID detector downstream of the tracker, it is used as the basis for further definitions. The downstream detectors (TRD and TOF) may exhibit lower geometrical acceptance in comparison to RICH, particularly for tracks with low momentum. This reduction in geometrical acceptance is absorbed into the definition of the efficiency of those detectors. Hence, the standard efficiency and pion suppression are defined as,

$$\text{Efficiency} = \frac{\text{Number of primary electrons identified as electrons}}{\text{Number of primary electrons having acceptance in RICH}} \tag{5.5}$$

$$\Rightarrow \text{Efficiency} = \frac{\text{Number of primary electrons identified as electrons}}{\text{Number of tracks with } N_{hits}^{RICH} \geq 7}, \tag{5.6}$$

$$\text{Pion suppression} = \frac{\text{Total number of reconstructed pion tracks}}{\text{Pions mis-id as electrons}}. \tag{5.7}$$

The figure 5.10 shows the efficiency and the pion suppression for different detectors. A track is identified as an electron by the RICH if the ANN output is greater than 0.3. Electron identification within the TRD detector is based on the condition $L_e > 0.4$ and the TOF electrons are tracked with $m^2 < 0.01$. It can be observed from figure 5.10 that the RICH standalone pion suppression is about 230, at an electron efficiency of 81%. Inclusion of the TRD likelihood metric, with standalone efficiency $\times$ acceptance (considering RICH as basis) of 75%, enhances the pion suppression factor by about 10. This results in the overall RICH+TRD efficiency of

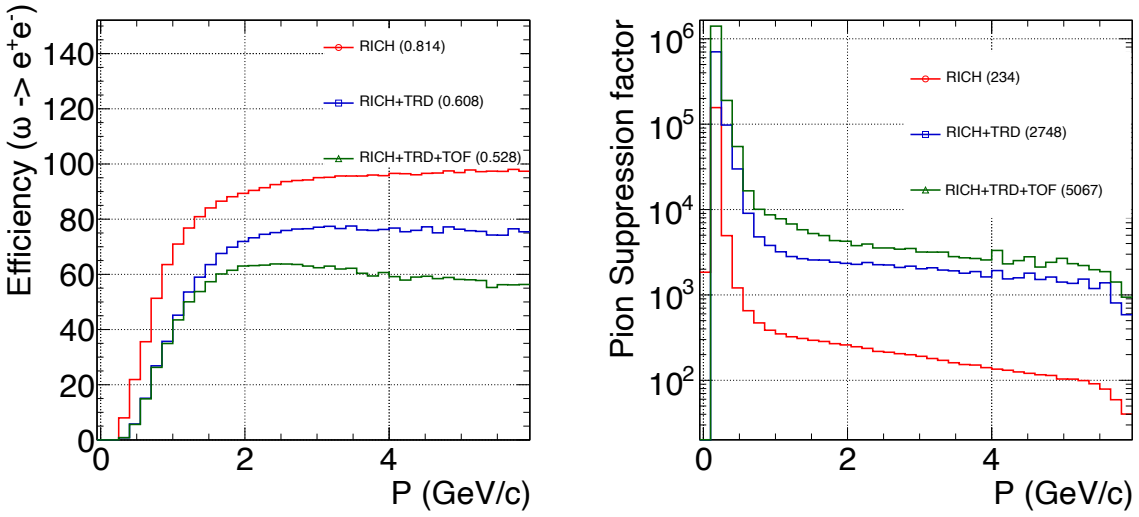

Figure 5.10: Figure of merit for the electron identification derived for the embedded omega sample for selected quality cut on electron identification metric from different detectors. Left panel: Identification efficiency of the primary electrons stemming from ω decays for different detectors. Right panel: Pion suppression factor from different detectors.

about 60% with a pion suppression factor of 2750. Similarly, imposing a TOF m^2 cut, with standalone efficiency $\times$ acceptance (considering RICH as the basis) of 65%, doubles the pion suppression factor compared to RICH+TRD. For an overall global efficiency of about 52%, the pion suppression of about 5000 is achieved with RICH+TRD+TOF.

5.4 Optimization of track extrapolation

The ring track matching procedure starts with the stepwise extrapolation of all STS tracklets to the extrapolation plane Z (described in section 3.4) taking into account the deflection in the magnetic stray field, assuming an electron mass hypothesis. The position of the extrapolation plane plays a crucial part in the performance of the ring track matching procedure. The further downstream the plane is placed, the more accurately the deflection in the magnetic stray field is accounted for, but also larger is the computational effort. In this section, an optimization procedure is discussed based on a minimum variance of ring-track distance as a criterion.

An exclusive electron dataset (see table 5.2) composed of 1×10^6 of e^+ and e^- each is used to derive the optimal extrapolation plane. The distance of the track projections to the nearest ring (dx/dy) is measured separately in dx and dy as function of electron momentum, assuming different extrapolation plane positions.

An example of dx distribution as a function of momentum and extrapolation plane is shown in figure 5.11, a similar distribution for dy is added in the appendix A.2.1. Each distribution of dx and dy is fitted with a Gaussian profile, and the mean (μ) and the standard deviation (σ) are

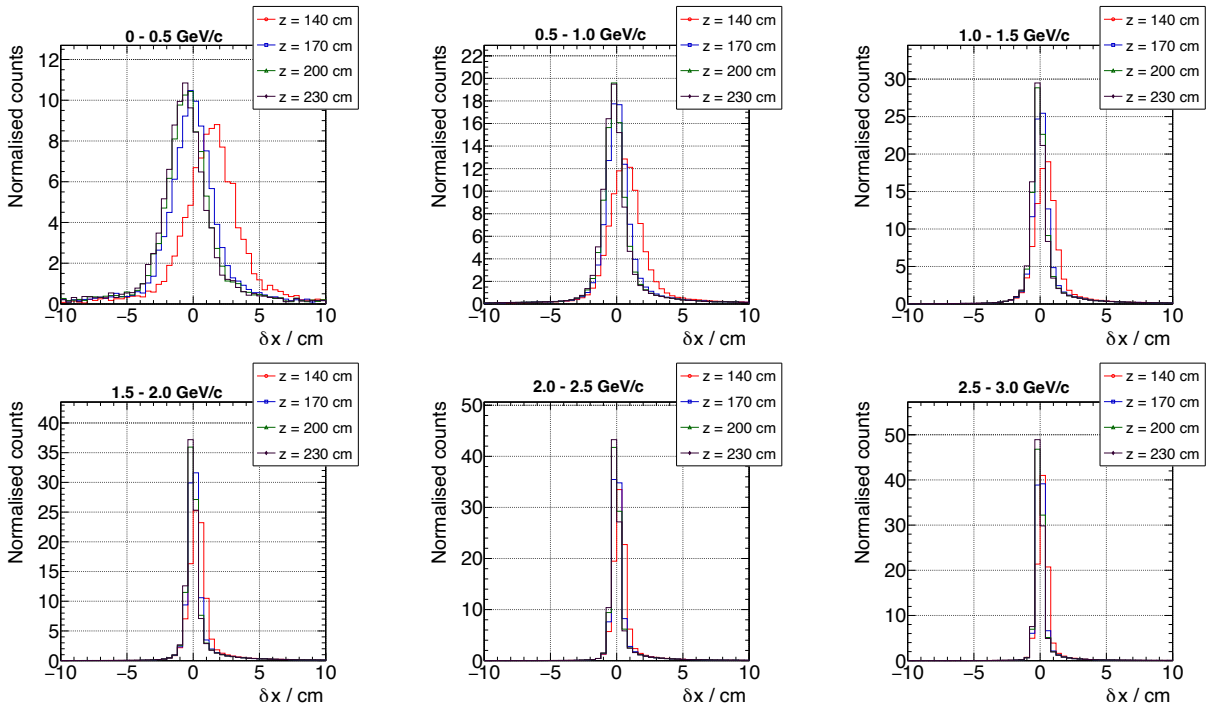

Figure 5.11: X component (δx) of the ring-track distance for different momenta of the electrons extrapolated to RICH at selected extrapolation layers.

extracted. Since a non-zero mean, i.e., a systematic ring-track offset, can always be corrected by applying simple correction maps (see section 5.5), the main focus is put on the extracted standard deviations $\sigma_{\mathrm{d}x}$ and $\sigma_{\mathrm{d}y}$ displayed in figure 5.12. In this figure, the standard deviation along x is higher compared to that in y. This is mainly due to the magnetic field inducing variances along the xz-plane. Similar results (with systematic shifts in the opposite direction) are observed for positrons (not shown here). To derive the optimal position of the extrapolation plane, $Z_{optimal}$, the standard deviations in both dx and dy are used as feature variables.

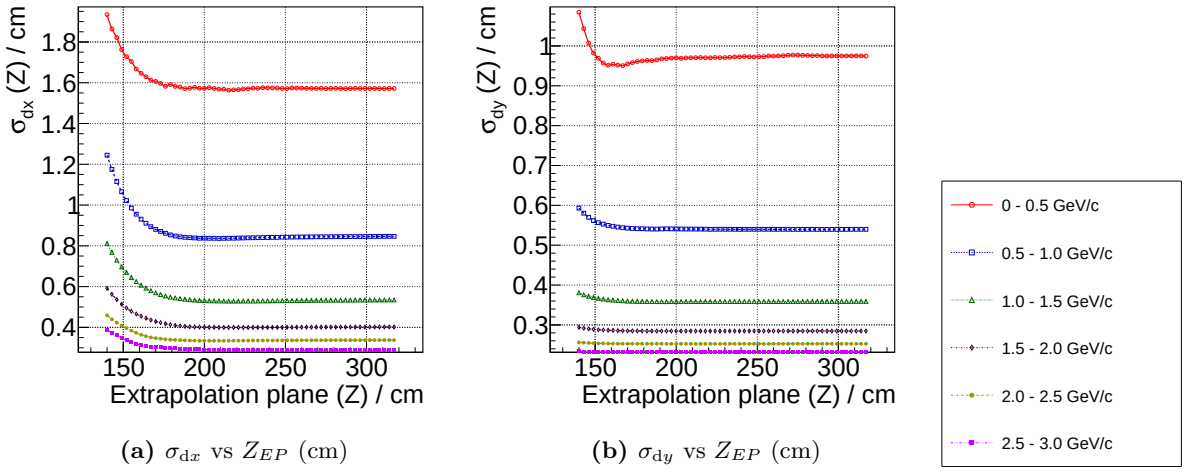

(a) $\sigma_{\mathrm{d}x}$ vs Z_{EP} (cm) **(b)** $\sigma_{\mathrm{d}y}$ vs Z_{EP} (cm)

Figure 5.12: Standard deviation σ of the ring-track dx and dy distributions for electrons of different momenta.

Since there is no correlation between dx and dy, both their variances can be minimized simultaneously, giving the objective function:

$$f(Z) = \sum_{\{momentum\}} \left\{ -\frac{|\sigma_{dx}(Z)|}{|\sigma_{dx}|_{max}} - \frac{|\sigma_{dy}(Z)|}{|\sigma_{dy}|_{max}} \right\}. \tag{5.8}$$

Where $Z_{optimal}$ is extracted to be the point where $f(Z)$ is largest:

$$Z_{optimal} = \underset{Z}{\text{argmax}}\ f(Z) \tag{5.9}$$

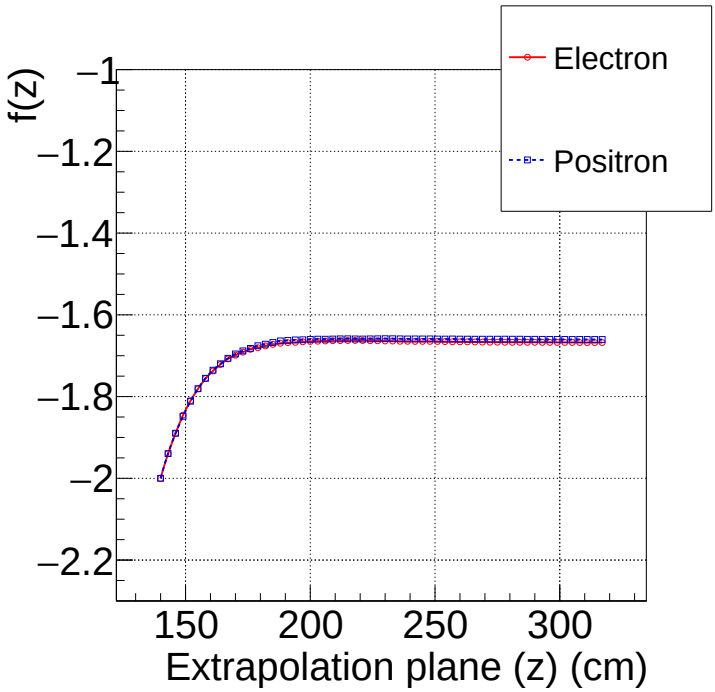

Figure 5.13: Objective function $f(Z)$ vs Z for an electron and positron sample.

The result of the optimization is shown in figure 5.13 for electrons and positrons. For both, electrons and positrons, the optimal extrapolation plane position Z is found to be $Z_{optimal} > 180\,\text{cm}$. This is consistent with the current position of the extrapolation plane of $Z = 220\,\text{cm}$.

5.5 Systematic correction for track projection

The STS tracks are extrapolated and projected to the RICH photon detection plane, searching for the closest ring candidate for the projected track. Due to the magnetic stray field and other effects, there could be a systematic shift between the projected track coordinate and its corresponding ring center. In this section, a data-driven correction for such systematic shifts is described, and its effectiveness with regard to improving the ring-track matching performance is evaluated. The following tests and results are based on a simulation of 10^5 embedded omega mesons.

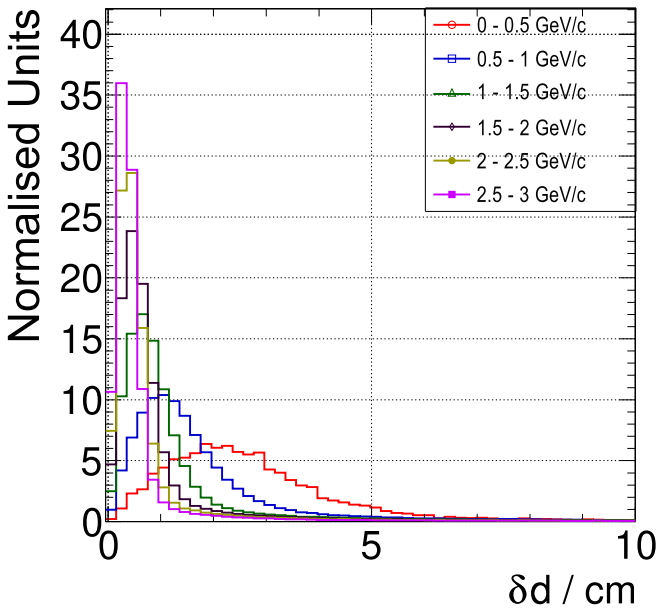

Figure 5.14: Absolute ring-track distance at the photo-detector plane for electrons of different momenta.

Figure 5.14 shows the absolute ring-track distance

$$\delta d = \sqrt{(x_{ring} - x_{track})^2 + (y_{ring} - y_{track})^2}$$

for primary e^- for different momenta; similarly, for positrons (e^+) are depicted in appendix A.2.2 and feature similar characteristics. Here, x_{track} and y_{track} refer to the projected position of either a true, or reconstructed STS track onto the RICH photodetector. Visibly, the δd distribution shifts and widens for lower momenta, which in parts can be explained by the effect of magnetic stray fields.

In order to correct for these systematic effects, correction maps are derived to be applied during normal reconstruction using simulations of a pure electron sample produced by the box generator. For this purpose, 10^6 events with three e^+ and three e^- are generated in the standard acceptance with momentum $p < 3$ GeV/c. The ring-track distances, δx ($x_{ring} - x_{track}$) and δy ($y_{ring} - y_{track}$) are calculated differentially in 15 momentum bins, 10×10 spatial bins in the RICH, and two charge bins. The procedure is repeated using three methods,

1. Using MC true momentum and MC true ring centre.
2. Using STS fitted momentum and MC true ring centre.
3. Using STS fitted momentum and found ring centre.

The idea behind methods two and three is to test and account for biases in the momentum reconstruction and ring finding.

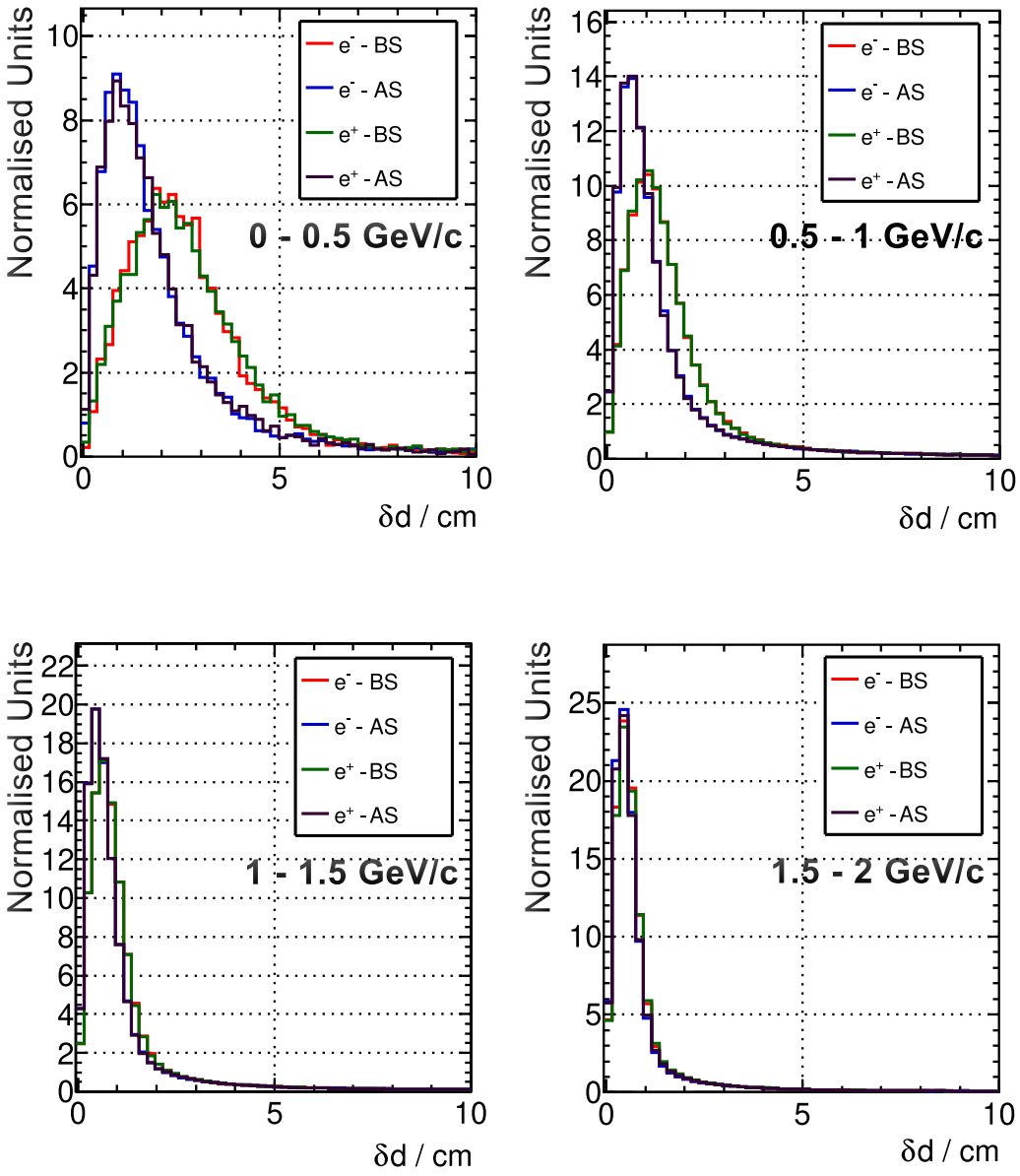

Figure 5.15: Absolute ring-track distance for electrons and positrons at different momenta before (BS) and after (AS) correction.

In a first test, the correction methods were analyzed based on the exclusive electrons that were used to derive the correction maps. Applying the correction derived on the basis of the true ring-track differences (method one) one observes an improvement in, δd especially for low electron momenta. This is shown in figure 5.15 where δd is depicted before and after correction for different momenta. The mean value of δx and δy (added in appendix A.2.3, A.2.4) are shifted towards zero and the result is reflected in δd distribution (see figure 5.15).

The three different correction maps were applied during the reconstruction process and the results are shown in figure 5.16. Similar outcomes have been observed for all three methods. Accordingly, one can state that the derived procedure should also work in the real experiment, where only reconstructed momenta and ring centers are available, and where the correction could even be derived from data directly (instead of Monte Carlo).

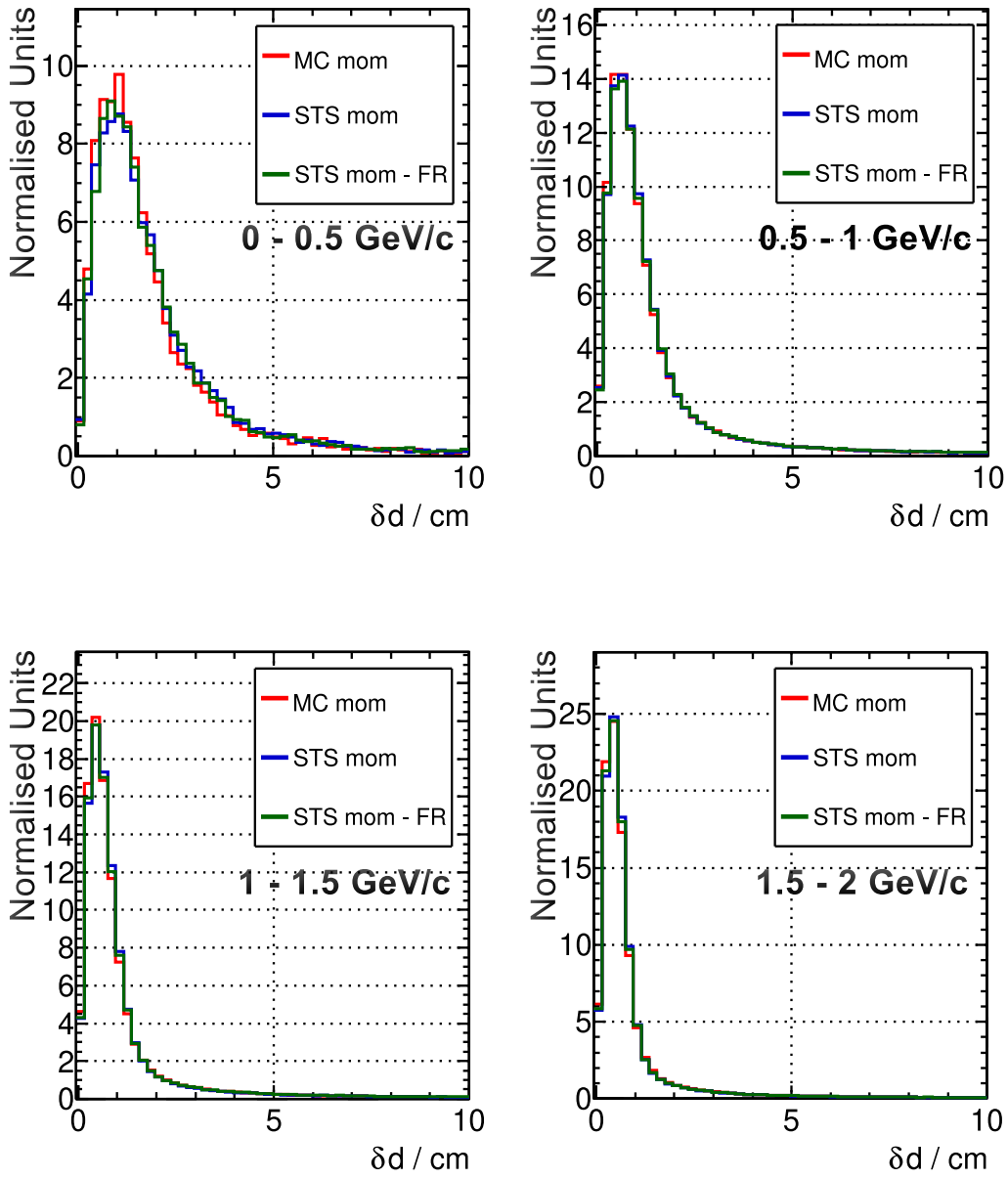

Figure 5.16: Absolute ring-track distance for electrons and positrons at different momenta after correcting using method one (red), method two (blue) and method three (green).

In a second step, the correction was tested on the UrQMD sample embedded with one $\omega \to e^+e^-$ decay per event (see table 5.2). In figure 5.17 the electron efficiency and the pion fraction are displayed as functions of the maximum ring-track distance allowed in the matching process. Efficiency hereby refers to the fraction of reconstructed electrons divided by the number of electrons with at least seven MC hits in the RICH detector, with the additional requirement that the reconstructed ring has a radius of $r > 4\,\text{cm}$. Pion fraction refers to the fraction of pions incorrectly matched to reconstructed rings, again featuring the same ring radius requirement. As expected, applying the correction improves the electron efficiency for a given ring-track maximum distance condition while having no major impact on the pion fraction. This improvement is mostly observed for strict ring-track distance conditions, as most correctable systematic shifts lie in this region.

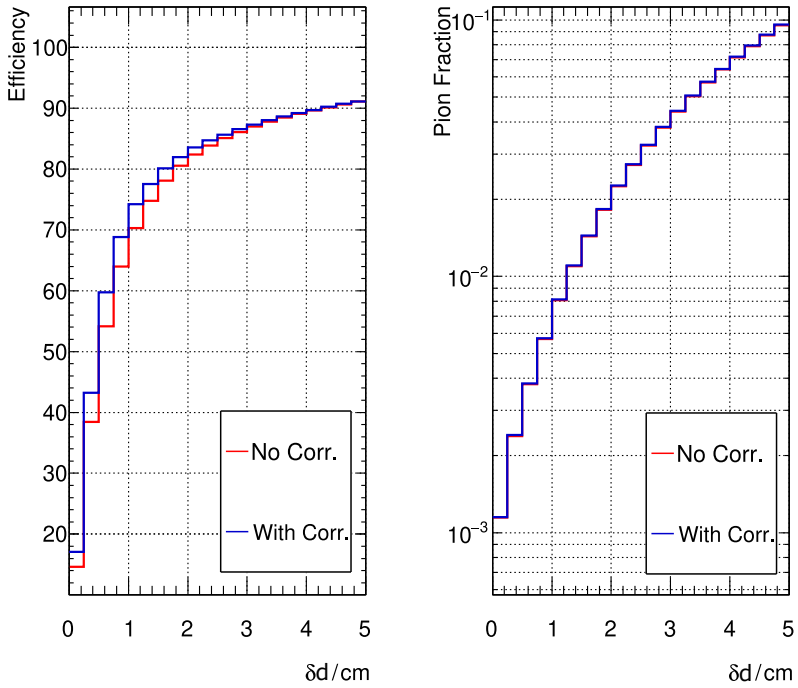

Figure 5.17: Electron detection efficiency and pion fraction as function of absolute electron ring-track distance.

6

Enhanced RICH ML model

The artificial neural network used for electron identification has been around for 15 years and was last optimized in 2017. With the advent of advanced ML models, it is important to revisit the electron identification network. This thesis discusses the potential application of the XGBoost model as a substitute for the conventional Artificial Neural Network (ANN). The decision to use XGBoost (in fact, any tree-based model) is motivated by its superiority over other deep-learning ensembles for tabular data [108], as available for the CBM RICH. Further, the inclusion of differential ring-track distances ($\delta x,\ \delta y$ instead of $\delta d = \sqrt{\delta x^2 + \delta y^2}$) as an additional input feature for the ML model is discussed. In the subsequent section of the chapter, a procedure for standalone tracking (track finding and fitting) in TRD (downstream to RICH) and extrapolating these tracks to RICH, termed as "backtracking" is presented. The TRD backtracks are used as additional ring-track references and included as additional parameters for the ML model. In the last section of this chapter, the results of the backtracking procedure are presented. The use of different ML models to replace ANN was discussed and partially tried in [109], indicating that the XGBoost model outperforms other tree-based ensemble models and multi-layered perceptrons. In this thesis, a new training strategy and adding new features to improve the performance of the XGBoost model further are discussed. [1] Sections of this chapter have been published in the following papers/reports:

- Pavish Subramani, *Machine learning application for electron identification in CBM*, FAIR next-generation scientists: 8th Edition Workshop, 2024 (Accepted for publication, Proceedings of Science) [110].
- P. Subramani, *"Global electron identifier for CBM using Machine Learning approach"*, XXXI International Conference on Ultra-relativistic Nucleus-Nucleus Collisions (Quark Matter 2025).
- P.Subramani, et al., *Using TRD-2D tracking for an improved ring-track matching*, CBM Progress Report 2023 [111].

[1] Comparison of different kinds of models for the same input features is not the focus of this thesis.

6.1 Fundamentals of the XGBoost model

In general, data consists of two components, namely features and labels. The feature refers to the descriptions that define the underlying data, such as ring radius and number of hits in the description of a ring. The label specifies the type or class of data that corresponds to a specific feature, such as electron ring or pion ring. Any prediction model will input features and output a value that is used to determine the label. A model can be trained with available data in order to have an informed prediction for unseen data derived from the same underlying distribution on which it was trained. This method is loosely defined as machine learning. According to the type of data the model learns and predicts, machine learning can be broadly classified into supervised and unsupervised learning[2]. If the model learns on the data in which the label is known for the feature, this is called supervised learning (e.g., electron identification in CBM experiment is trained on the simulated data). Whereas, if the label for the underlying data is unknown, the learning process is referred to as unsupervised learning (e.g., anomaly detection). Furthermore, in supervised learning, if the label is a continuous variable, then the problem is characterized as regression type and if the label is a discrete variable, then the problem is characterized as classification type (e.g., electron/pion discrimination in CBM experiment). This thesis further discusses the supervised learning of classification models as it pertains to electron identification in CBM experiment.

6.1.1 Supervised learning

Consider a set of n labeled data instances ($\vec{x_i}$,y_i), where $\vec{x_i}$ is a m dimensional set of input features ($\vec{x_i} \in \mathbb{R}^m$) and y_i is a one-dimensional target ($y_i \in \mathbb{R}^1$) or output label for the instance i. A supervised learning algorithm takes $\vec{x_i}$ as an input and provides a model output $\tilde{y}$. In general, $\hat{y}_i$ can be expressed as $\hat{y}_i = f(\vec{x}_i, \vec{\theta})$, where f is a function in the hypothesis space (consisting of all possible functions that map the input to output), which is intended to predict the target label y_i and $\vec{\theta}$ is the parameter of the model. The output of the chosen model should match that of the label, meaning $f(\vec{x_i}, \vec{\theta}) \approx y_i$. The approximation $f(\vec{x_i}, \vec{\theta}) \approx y_i$ is quantified by a function called the loss function $L(f(\vec{x_i}, \vec{\theta}), y_i)$. The loss function $L(f(\vec{x_i}, \vec{\theta}), y_i)$ is defined as the deviation of the output of the model to the expected output, should be minimum for the optimal parameters $\vec{\theta}$. The model is trained to find the optimal parameter $\vec{\theta}$ that fits the input $\vec{x_i}$ to the output y_i. Given a set of training data, the model has the capability to be arbitrarily complex, resulting in significant computation time and a higher possibility of overfitting. In order to prevent overfitting, a regularization term ($\Omega(\vec{\theta})$) is added to the loss function, which acts as a penalty for complexity. The final function that must be optimized to determine the optimal parameter for a given complexity is commonly referred to as the objective function, defined as,

$$O(\vec{\theta}) = \; L(f(\vec{x_i}, \vec{\theta}), y_i) \; + \; \Omega(\vec{\theta}). \tag{6.1}$$

[2] A combination of supervised and unsupervised learning is called semi-supervised learning. They are commonly used to improve the performance of unsupervised learning models when there is limited but incomplete information about labels in the training dataset.

The conventional artificial neural network (ANN) in CBMROOT, which is a single layer perceptron [112, 113], is one of the most commonly used supervised learning models.

6.1.2 Decision trees

Decision trees are an example of supervised learning models. A straightforward decision tree is constructed by posing affirmative or negative inquiries regarding the value of each of the input attributes. A simple example is in the set of {radius, number of hits}, then with two subsequent decisions: if $radius > 4\,\text{cm}$ and if $hits > 10$, one can predict the ring belongs to the class of electrons in the overall ring dataset. The decision trees are easy to interpret due to their simple structure.

The decision trees partition the input spaces into different regions (e.g., $radius < 4\,\text{cm}$). Consider, at any parent region R_p, then one can define a split function S_p, that divides R_p into R_1 (e.g., hits ≤ 10) and R_2 (e.g., hits > 10) based on a threshold t (in the case of this example, the threshold in number of hits is "10") applied to any input feature j (in the case of this example, number of hits is the feature). Mathematically, a split function is defined as,

$$S_p(j,t) = (\{\tilde{x}|\tilde{x}_j \leq t,\ \tilde{x} \in R_p\},\ \{\tilde{x}|\tilde{x}_j > t,\ \tilde{x} \in R_p\}).$$

The objective is to find the optimal threshold t and the input feature j for the best split, this is done by optimizing an objective function O_p defined as $O_p = \underset{j,t}{\text{argmax}}\,(L(R_p) - L(R_1) - L(R_2))$, where $L(R_p),\ L(R_1),\ L(R_2)$ are loss functions over the region R_p , R_1, R_2 respectively (note that the dependency of j, t is implicit in defining the region R_1, R_2). The intuitive idea is that, given the loss of the parent node (already determined), the sum of loss in the children nodes should be minimal, such that the difference between the loss of the parent node and loss in the children nodes should be maximum. This approach of deciding splits based on the current node is called the greedy heuristic [114]. Again, intuitively, it is apparent that the optimal decision for the split at any node should be influenced by all subsequent splits down the current node. This method has the potential to exhibit significant memory and time complexity. Hence, in the advanced implementation, a top-down approach (root to leaf) is used to build the decision trees, where each leaf is split using a greedy algorithm.

The loss function mostly used for classification (also in this thesis) is the binary logistic loss function (binary form of the cross-entropy loss [115]).[3] Considering the binary classification of {electrons, pions}, the binary logistic loss function is defined as $L = \log(\frac{p(electron)}{1-p(electron)})$, where p(electron) for any leaf is defined as $\frac{\text{number of electrons in that leaf}}{\text{total data points in that leaf}}$. The binary logistic function restricts the output between $(0, 1)$.

In general, a tree may be constructed with an arbitrary depth and number of leaves (an extreme example is when each leaf has only one training data point). This may result in overfitting

[3] Some of the other loss functions used in the decision trees are the Gini criteria.

and an increase in time complexity. Hence, for the construction of the tree, a stop criterion[4] is always required. The stop criteria may include: maximum depth (variable *max_depth* in the table 6.1), minimum number of samples in a leaf, maximum number of leaves, and misclassification/impurity (stop if impurity is less than the threshold, denoted as *min_split_loss* in the table 6.1). When necessary, the tree can also be pruned (removing branches) after its construction is complete. This can typically be accomplished by utilizing the validation dataset, which is a component of the training dataset used to validate the model. During validation, certain stop conditions mentioned previously can be utilized.

6.1.3 Gradient boosting

A single decision tree on its own is usually a weak classifier, meaning the performance of the decision tree can be approximated as slightly better than random selection. In order to improve the overall performance of classification, an ensemble of decision trees (generally true for any underlying model) can be used. The output of the ensemble of models is taken to be the weighted sum of the output of the individual models, $H(\vec{x}) = \sum_{t=1}^{T} \alpha_t h_t(\vec{x})$, here T is the number of learners (models) in the ensemble, α_t and h_t are the weights and output of the learner t. The ensemble of models can be constructed using two approaches. First, a set of different models that train on the same data set can be used (same data set, different types of models), for example, stacking method [116]. Second, the training data can be subsampled, and a common model can be used to train on each subsample of the data (same underlying model, different subsample of training data). Commonly used methods for the second type of ensemble construction are: bootstrap aggregate [117](or "bagging") and boosting [118]. In the process of bagging, the training data is randomly subsampled, and the underlying model is trained on each subsample of the data.[5].

The idea of boosting involves iteratively adding a new model to the ensemble, where the model learns from the data samples in which the previous models had poor performance [120]. A generalized loss function $l(H)$ for the ensemble can be defined as $l(H) = \frac{1}{N} \sum_{j=1}^{N} l(H(\vec{x_i}), y_i)$, here the y_i is the target label (true output) for N data points. Consider at any iteration $t+1$, the current ensemble is $H_t(\vec{x})$, then the best model h_{t+1} that has to be added to the ensemble is chosen from the space of all possible models $\mathcal{H}$(function space) such that it minimizes the loss function that arises from adding the new model [121],

$$h_{t+1}, \alpha_{t+1} = \underset{(h \in \mathcal{H}), \alpha}{argmin}\ l(H_t + \alpha h). \tag{6.2}$$

Then the ensemble at the end of the iteration will be $H_{t+1} = H_t + \alpha_{t+1} h_{t+1}$. If the minimization problem (defined in the equation 6.2) is solved by following its gradient direction, then those classes of boosting methods are generally called gradient boosting models. To solve the problem of minimizing the loss function (see equation 6.2) in the space of all functions (models) is

[4] Apart from the default stops which include the "no feature left" and "no instances left".

[5] Bagging of decision trees creates a forest of trees called random forests [119], which is another powerful model, increasingly used for classification of tabular data.

exceedingly difficult. Therefore, most algorithms use a Taylor approximation of the loss function defined in the equation 6.2. An example of an ensemble of decision trees is shown in the figure 6.1.

Data instance	Hits	P	label
1	14	1.1	e
2	16	2.1	e
3	20	4.9	e
4	11	5.0	π
5	12	5.6	π
6	21	3.4	e

(a) A example data sample.

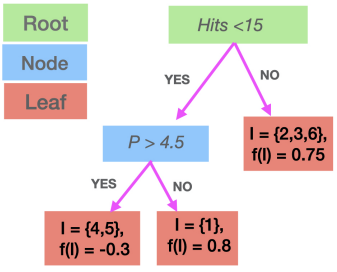

(b) Decision tree 1

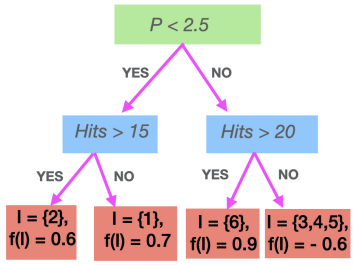

(c) Decision tree 2

Figure 6.1: An example for ensemble of fully constructed decision trees. The response of the tree t to any data instance k is given as $I_t(k)$ (shown in the leaf). The output of the decision tree for each instance is taken as the sum of the response of each tree for that instance (assuming no weights to each tree). Here, the response for the data instance 5 can be calculated as $I(5) = I_1(5) + I_2(5) = -0.3 - 0.6 = -0.9$, similarly, for the instance 2, $I(2) = I_1(2) + I_2(2) = 0.75 + 0.6 = 1.55$. Using the response of this ensemble, one can determine that if $I(k) > 0$, then it is an electron, and otherwise it is a pion.

6.1.4 XGBoost

The XGBoost ("Extreme Gradient Boosting") is a scalable implementation of gradient boosting with decision trees as the underlying model [122]. The complexity of any tree $f(x)$ can be defined as, $\omega(f) = \gamma L + \frac{1}{2}\lambda \sum_{l=1}^{L} w_l^2$, where L is a number of leaves, and w is a score function (not described here, but can be understood as a function describing the importance of a leaf). Here, λ (table 6.1) are called the regularization parameters (sometimes, a first order regularization term, $\alpha|w_l|$ is used in addition).

Adding the complexity term to the equation 6.2 for current iteration, the objective function similar to the equation 6.1 can be written as,

$$O_t = \sum_{i=1}^{n} l(f_t(x_i), y_i) + \gamma L + \frac{1}{2}\lambda \sum_{l=1}^{L} w_l^2. \tag{6.3}$$

The XGBoost model uses a second-order Taylor approximation of the objective function. Thus, the best objective function contains the first derivative (g for gradient) and second derivative (h for Hessian) of the defined loss function (binary logistic loss function) along with the complexity parameters. An approximated objective function is termed as a score function, which is a combination of a measure of impurity in a decision tree and a measure of model complexity (higher score is better). Similar to the vanilla decision tree (described earlier), the decision to

split is taken at leaf level. Expected gain from a split is calculated as,

$$\begin{aligned}\text{Gain} = \text{Score on left leaf} \; + \; \text{Score on right leaf} \; - \; \text{Score on parent node} \\ - \text{Threshold (for pruning)}.\end{aligned}$$

If the gain is less than γ, the tree is not split further (greedy algorithm). To find the best way to split a leaf for a feature, the XGBoost uses a histogram of data points instead of scanning all possible values (for example, searching for 6 bins of ring hits instead of single values from 10 to 22). This is called histogram-based optimization. The general gradient boosting method is serially processed, while the histogram method allows each bin to be calculated in parallel, increasing the speed of computation. Also, for each iteration, a subsample of data instances and columns can be used (controlled by the parameters *subsample*, *subsample_bytree* in table 6.1). The XGBoost algorithm uses optimized sparse matrices (many entries are zero) to increase the speed of processing large datasets. Furthermore, the XGBoost also incorporates processes to address the issue of missing values and analysis of the importance of features[6].

6.1.5 Output of XGBoost model

It should be noted that despite the discrete input label fed to the XGBoost model, the model's output is a continuous value ranging from 0 to 1. In the case of the electron/pion discrimination, the training input label value for electrons is set at 1 and for pions at 0. Therefore, the anticipated response (output) of the proficiently trained XGBoost model is expected to exhibit two distinct peaks, one of which is close to zero ($P_{XGBoost} \approx 0$) for pions and another one close to one ($P_{XGBoost} \approx 1$) for electrons. The final selection of the different classes (electrons or pions) can be achieved by setting different levels of threshold on output ($P_{XGBoost} \geq P_{thr}$ for electrons and $P_{XGBoost} < P_{thr}$ for pions). Depending on the threshold, the true positive rate (TPR) and false positive rate (FPR) can be calculated. They are defined (in terms of positive – electrons and negative – pions) as follows,

$$TPR = \frac{\text{Number of correctly classified true positive}}{\text{Total number of true positive}}, \tag{6.4}$$

$$FPR = \frac{\text{Number of negative misclassified as positive}}{\text{Total number of true negative}}. \tag{6.5}$$

As can be seen from the equation 6.4, in the case of electron identification, TPR is the efficiency of identifying electrons, and FPR is the fraction of total pion misidentified as electrons (inverse pion suppression). If the threshold (P_{thr}) is varied from 0 to 1, for each value of the threshold, the TPR and FPR can be calculated and plotted. The plot with TPR and FPR is often referred to as the Receiver Operating Characteristic (ROC) metric. This metric can be used to compare the performance of different models. On occasions, the area under the ROC metric (AUC) is also used to evaluate the performance of the model due to its simplicity (one value for a model).

[6]The XGBoost package uses the relative number of times the feature has split as the feature importance, which in many cases need not be the best feature that produces more gain.

6.1.6 Importance of input features

The proper explanation of the response of the model is imperative for evaluating the expected outcome of the model and comprehending the significance of the various input features on its performance. Furthermore, the enhanced interpretation of the model's prediction is necessary for further improvement of the model. Different interpretation methods for prediction of ML models are proposed in [123, 124, 125, 126, 127]. A widely used interpretation method is Shapley additive explanations, or simply SHAP as it attempts to include elements of other interpretation methods [127]. Deriving its root from game theory, the adaptation of the SHAP in machine learning is straightforward. In simple terms, the importance of the feature x_k (e.g., ring radius) on the model is assigned based on comparing the prediction value of the model with and without the feature x_k. Consider a subset of features $S \subseteq F$, where F is the set of all features. For a particular S (subset of all features), the model f_S is trained with all input features including x_k, and another model $F_{S\cup\{k\}}$ is trained with all features in S without feature k. The marginal contribution is given as [128],

$$\phi_k(S) = \left[f_{S\cup\{k\}}(x_{S\cup\{k\}}) - f_S(x_S) \right]. \tag{6.6}$$

The importance of the feature x_k is calculated by the weighted average of all possible configurations of S,

$$\Phi_k = \sum_{S\subseteq F\setminus\{k\}} \omega(S)\phi_k(S). \tag{6.7}$$

Here $\omega(S)$ is calculated as a fraction of all possible combinations of the input feature space. The process of calculating the model response by retraining with different subsets of input features is resource-intensive. In order to address this issue, the implementation of the SHAP value calculation frequently involves substituting the mean value of the feature of interest instead of completely removing it. In practice, including this thesis, the SHAP values are calculated using a partial data set, which is carefully selected as a representative data set that reflects the variance of the full data set.

6.2 Training strategy

A good training data set is important for any machine learning application. From the RICH perspective, the application of the ML algorithm is to distinguish electrons from pions. In order to prevent the bias of the model towards one class (either electrons or pions), a balanced data set comprising an equal number of electrons and pions is used as the training data set.

6.2.1 Training data selection

In a fixed target setup, all the particles produced during a collision are subject to a boost in the forward direction. Hence, the di-electrons from different sources, including LMVM, have differ-

ent momentum distributions in the laboratory frame depending upon their mass. Moreover, the boost depends on the collision energy. Hence, the di-electrons produced from the same particle at different collision energy and centrality will have different momentum distributions. The ML model is foreseen to work for all collision energy and collision systems. Thus, a momentum-independent training strategy is used. Accordingly, the training data set was chosen to ensure that electrons and pions have a uniform momentum distribution (see figure 6.3i). This training data set is derived by using an embedded electron sample (see table 5.2) wherein a combination of the FAIRBox generator and UrQMD generator are used. The signal is the primary electrons produced from the target; they are derived from the FAIRBox-generated particles. The kinematic range for production of electrons is given as follows,

1. $e^{\pm}$, multiplicity = 5, $p_T \sim U(0,\ 2.5)$ GeV/c $\rightarrow$ covers all momentum for electrons.
2. $e^{\pm}$, multiplicity = 2, $p \sim U(0,\ 1)$ GeV/c $\rightarrow$ enhances the electron sample size in low momentum.
3. $e^{\pm}$, multiplicity = 3, $p \sim U(0,\ 0.5)$ GeV/c $\rightarrow$ enhances the electron sample size in very low momentum.

The main background source in electron identification stems from pions misidentified as electrons (these originate at the target). They are generated inherently in the UrQMD input sample. The hard cut on the momentum at 7.5 GeV/c is imposed for selecting training samples because no significant change of characteristics can be observed for electrons and pions beyond these momenta. A balanced data set of 790×10^3 $e^{\pm}$ and 790×10^3 $\pi^{\pm}$ is used for training.

6.2.2 Optimization of hyperparameters

The XGBoost model for classification uses many internal configuration parameters, which are usually called "hyperparameters" [129]. In order to choose the optimal hyperparameters of a model for its maximum performance for a given dataset, the model has to be trained systematically with different configurations of hyperparameters. There are many methods for tuning hyperparameters of the model, including grid search, random search, and gradient-based optimization methods [130, 131]. The grid search is an exhaustive search technique that is generally considered the most efficient approach to identifying the optimal hyperparameters. But it is computationally expensive. Hence, in this thesis, a Bayesian approach to hyperparameter tuning is used [132]. The tuning of optimization is essentially maximizing a function (output of model) in hyperspace (of hyperparameters). The Bayesian approach involves constructing a posterior distribution of known Gaussian process functions that best fits the function that must be optimized. The details of the Gaussian process (GP) and its application for optimization can be found in [133, 134].

A comprehensive overview of the hyperparameter search ranges and training setup for the XGBoost model in this study is presented in the table 6.1. All training setups have the same default

settings for the XGBoost general settings, including the booster type and number of cores used to run the model. The tree construction method is based on histogram optimization for efficient runtime. The subsampling of the trees is enabled to avoid overfitting the data. Other tree parameters in the table 6.1 constitute the space of optimizable hyperparameters. The training and evaluation for each setting of hyperparameters is done by the cross-validation (CV) method [135]. In CV, the training dataset is divided into n subsets (called folds), for each i^{th} fold ($i = 1, ..., n$), the model is trained on other parts except the i^{th} fold and the error is calculated for the i^{th} fold. A 5-fold cross-validation (CV) is performed for the stratified training data set. To control the complexity and avoid overfitting the data, the maximum number of trees is capped at 100 for each iteration of CV. The area under the receiver operating characteristics (ROC) curve (called as AUC score) is used to evaluate the performance of the model under training. The model with optimal hyperparameters has the highest AUC score.

A Bayesian approach using a Gaussian process is used to find the point of maximum AUC in the hyperspace by a series of explorations. At any point, a GP is fitted to all previously explored points, thereby serving as a prior distribution for the subsequent iteration. Then a posterior distribution is derived based on the prior distribution and an exploration algorithm (called a utility function [133], analogous to the likelihood). The derived posterior is then used to find the next optimal point to explore. This systematic search is driven by many internal parameters of the Gaussian process. In this thesis, the default setting of the package [132] is used for all internal variables except for the number of search points. In order to avoid arriving at local maxima, the number of exploration points is set to a higher value (Exploration points = 150). However, in order to identify the global maxima, additional local search around the already explored points is necessary, and the maximum number of such exploitation searches is set externally for each training setup (Exploitation points = 100).

Table 6.1: Table showing all the hyperparameters of the XGBoost and training setup.

	Parameter name	Use/Definition	Range/Option	Reason
General parameters	booster	Configuring XGBoost mode	gbtree	Use XGBoost in gradient tree boosting mode
	nthread	Number of parallel threads	8	Hardware limit
Tree parameters - Fixed	tree_method	Tree construction method	hist	Faster, optimized using the same greedy algorithm
	subsample	Fraction of data for building tree	0.7	Avoids overfitting for every boosting iteration
	sampling_method	Method of sampling	uniform	Equal probability of selecting each training instance
Tree parameters - Scan	colsample_bytree	Subsampling columns for every tree constructed	(0,0.99)	Scan parameter
	max_depth	Maximum depth of tree	(2,10)	Avoid overfitting and reduce training time
	min_child_weight	Sum of weights in the leaves	(4,100)	Avoids underfitting
	eta	Learning rate	(0,1)	Stop condition for gradient boosting
	gamma	Sum of weights in the leaves	(2,100)	Complexity cost for new leaf
	alpha	L1 Regularization term	(2,20)	Avoids overfitting
	lambda	L2 Regularization term	(2,20)	Avoids overfitting
Cross validation parameters	num_boost_round	Maximum number of trees	100	Control model complexity
	early_stopping_rounds	Number of iterations to wait for early termination in case of no improvements in model performance	10	Avoids overfitting and shorter training time
	nfold	Number of groups the sample is split	5	Possible use of all data samples for training
	stratified	Choosing equal size for each class ($e^{\pm}$, $\pi^{\pm}$) per validation	true	Controlling cross validation error (ideally should reflect the error of whole training set)
	evaluation_metric	Metric for finding optimal hyperparameter	Area under test ROC curve	Measured for validation data set
Gaussian process parameters	Exploration points	Number of explorations in the hyperspace	100	Avoid local maxima
	Exploitation points	Number of exploitations in the hyperspace	150	Finding global maxima

6.3 Understanding input variables to the ML model

The input features for the XGBoost model are the same as those for the ANN (see chapter 5), which are $\{a_{ring},\ b_{ring},\ \phi_{ring}$, Absolute ring position in polar coordinates (R, θ), hits/ring, χ^2/NDF, $\delta d_{ring-track}$, Momentum$\}$. The model performance has to be optimized for the embedded omega data 5.2. Hence, before training, the input feature distributions of the embedded omega sample are revisited.

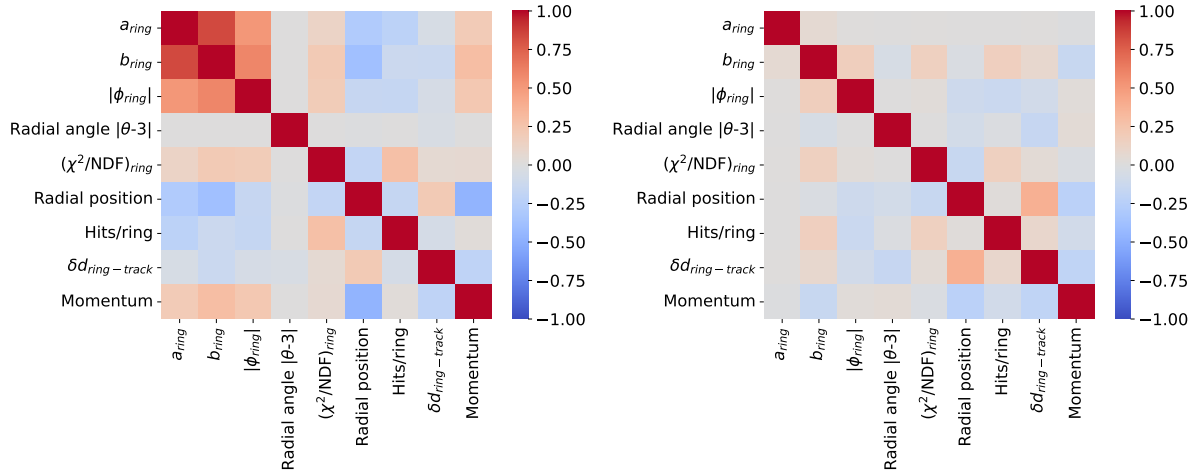

Figure 6.2: The Pearson correlation table depicts the linear correlation between various inputs to the ML model for both electrons (left panel) and pions (right panel) in the embedded omega meson data sample.

The linear Pearson correlation between a pair of features (x, y) is defined by its correlation value ρ as,

$$\rho_{x,y} = \frac{\mathrm{Covariance}(x, y)}{\sigma_x \sigma_y}, \tag{6.8}$$

whose value ranges between $(-1, 1)$. If any variable exhibits no linear correlation with all the other variables, i.e., $\rho_{x,all} = 0$, then those variables can be taken out of the model and can be used simply based on a cut value. If a pair of variables exhibits a significant correlation, i.e., $\rho_{x,y} = 1$, then one of the variables can be eliminated from the training process as all the information from the second variable is redundant and will not have a significant impact on the model's outcome.

The Pearson correlation, calculated for all pairs of input features for both electrons and pions in the embedded omega dataset, is given in the figure 6.2. All of the diagonal entries in the table represent the self-correlation of the features, with the value of ρ being 1. If the input feature has a symmetric distribution around zero with values ranging from positive to negative, then the contribution to the pair correlation value from the positive values will cancel the contributions from the negative values. In order to avoid that, the absolute value of the input features ϕ_{ring} and radial angle θ (subtracted by 3 to make the distribution symmetric about zero[7]) is used to

[7]The calculated radial angle was increased by three to ensure that all input variables had a value greater than zero during the training of the conventional ANN.

derive the correlation.

It can be observed that, for electrons, the major- and minor-axis of the ring have a strong positive correlation (averaged over the full XY plane). This is due to the fact that the electron rings, with the exception of those formed by extremely low momenta tracks, are less elliptical and more circular. The ring size variables a_{ring}, b_{ring} are negatively correlated with the absolute radial position of the ring in the camera (in polar coordinates). This is due to the low-momentum electron rings. The low-momentum primary electrons (small momentum), whose rings are typically elliptical and slightly smaller (small a_{ring}, b_{ring}), are strongly bent by the magnetic field at large angles to the outer parts of the mirror, which are then reflected to the outer parts of the camera (large R). The same explanation can be given for the negative correlation between the size of the rings and hits per ring. Conversely, the rings formed by high-momentum electrons are typically larger, explaining the modest positive correlations between momentum and the size variables. The high-momentum electron tracks have better ring-track fit resolution, which then translates to the negative correlation between ring-track distance and momentum. Conversely, the low-momentum primary electron tracks that populate the outer parts of the camera (large R) have lower ring-track fit resolution, which then results in large ring-track distances (large $\delta d_{ring-track}$). Hence, a positive correlation is observed for absolute radial position (R) with the ring-track distance. The radial angle (θ) however has the least correlation with other input features.

The pair correlations for pions are difficult to understand because the pion track projection (at maximum distance 10 cm to ring) has two contributions: the sub-threshold pions (with momenta $\leq 4.7\,\mathrm{GeV}/c$) that do not have a ring but are falsely matched to a ring and high-momentum pions which have rings in RICH. This combination might modify some pair correlations of input features. It is important to note that all variables have some form of correlation with other variables. Therefore, all variables can be used to train ML models without losing any information.

6.4 Electron identification using the XGBoost model

As discussed in section 3.4, the ANN is the status quo electron identification network, which has been replaced by an XGBoost model in this thesis. The training strategy outlined in the preceding section is used to train the XGBoost model with the same input features as for the ANN. Input feature distributions for both $e^{\pm}$ and $\pi^{\pm}$ used for training the XGBoost model are shown in the figure 6.3.

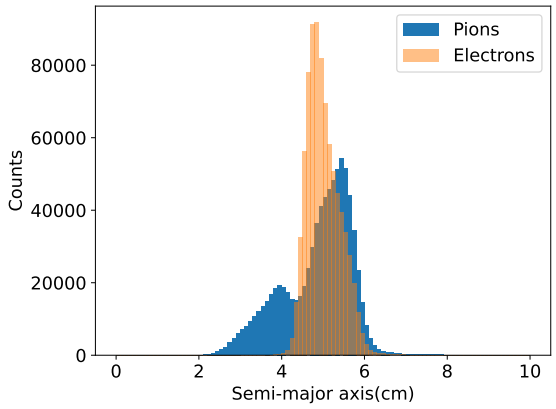

(a) Semi-major axis, a of the ring.

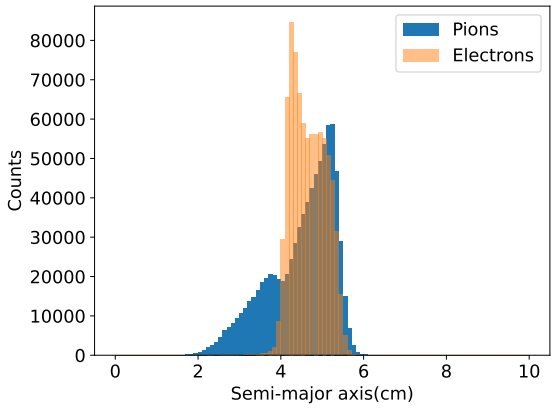

(b) Semi-minor axis, b of the ring.

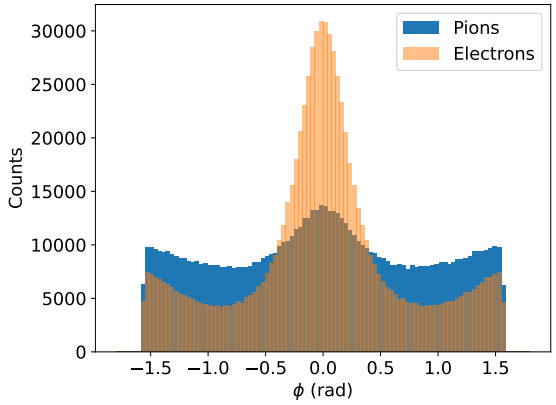

(c) Ring tilt angle, ϕ of the ring.

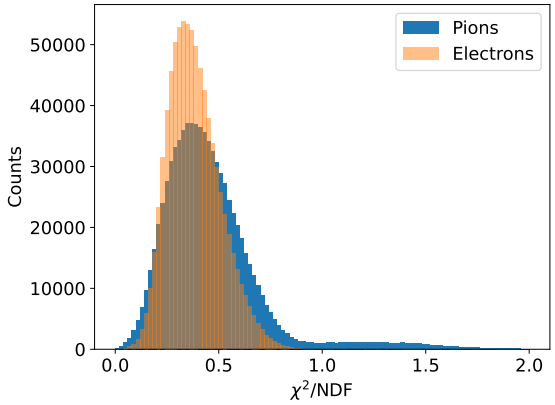

(d) Goodness of the elliptical ring fit: χ^2/NDF measure.

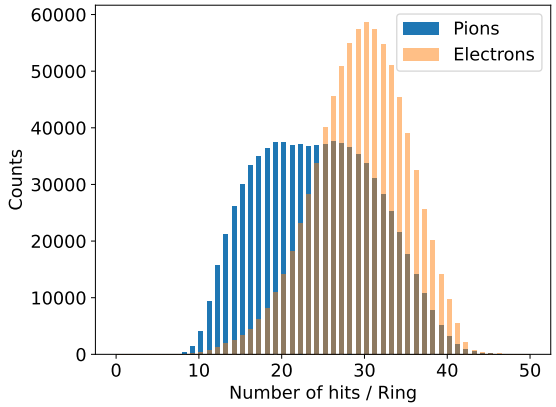

(e) Number of hits per ring.

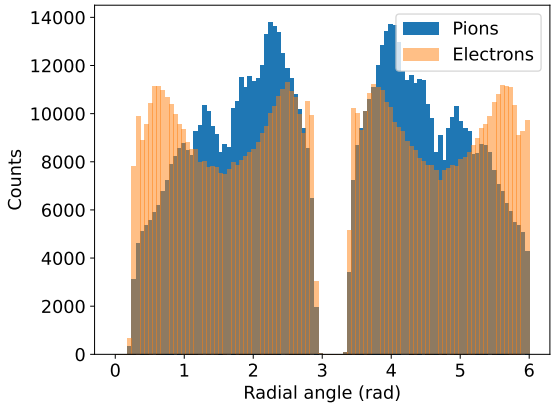

(f) Absolute position of the ring in the RICH camera in polar coordinates: Angle θ.

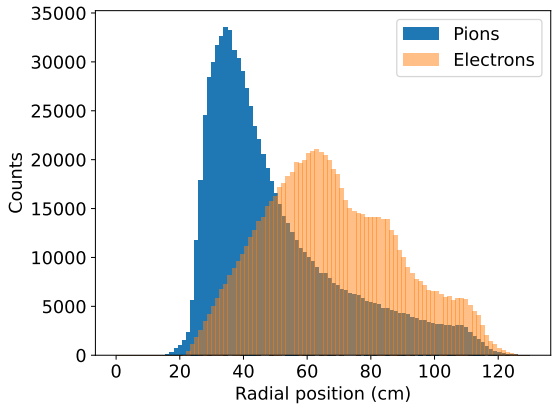

(g) Absolute position of the ring in the RICH camera in polar coordinates: Radial position.

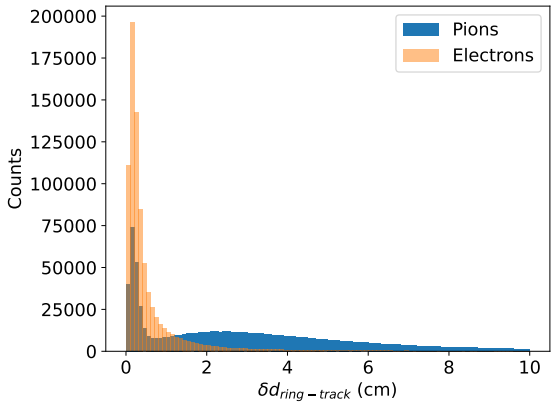

(h) Distance between track projection and closest ring center.

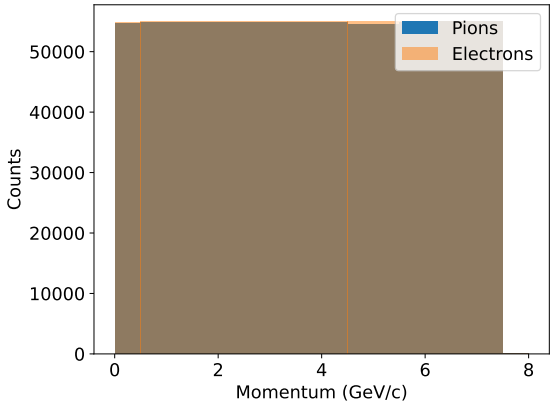

(i) Absolute momentum of the track matched to the ring.

Figure 6.3: Input feature distributions of the training dataset, which is used for the electron identification XGBoost model, with an initial cut on ring-track distance of 10 cm. Additional structures seen in the absolute ring positions for electrons (angle and radial position) are a consequence of using different kinematic regimes for the inputs (see section 6.2.1).

Deep learning models usually require input values to be "standardized", either by scaling or shifting or by combining both. This helps avoid bias when calculating residues, like finding the closest neighbors. But the standardization is not required for tree-based models, as the splitting of the leaf is based on comparing the absolute value stored in the leaf with a threshold. Although standardization is not a strict requirement, all input values are scaled in this work to ensure that the values of inputs do not exceed ±1 for ease of handling of the data. The hyperparameters of the model are optimized using the Bayesian approach.

6.4.1 Results for the training dataset

An ROC curve is derived for both the conventional ANN in CBMROOT and the XGBoost model evaluated for the training sample and plotted in the figure 6.4 (left). Since the training and evaluation set is fed to the model by cross-validation setup, the model is expected to perform

better with these data. An interesting aspect is that the ROC curves of ANN and XGBoost do not overlap even at the lowest impurities (< 0.01); consequently, the XGBoost approach outperforms the ANN in CBMROOT in all efficiency points. This ensures that, for any other input electron sample (LMVM or otherwise) with the identical pion background, the XGBoost model performance will be the same or superior to ANN in CBMROOT.

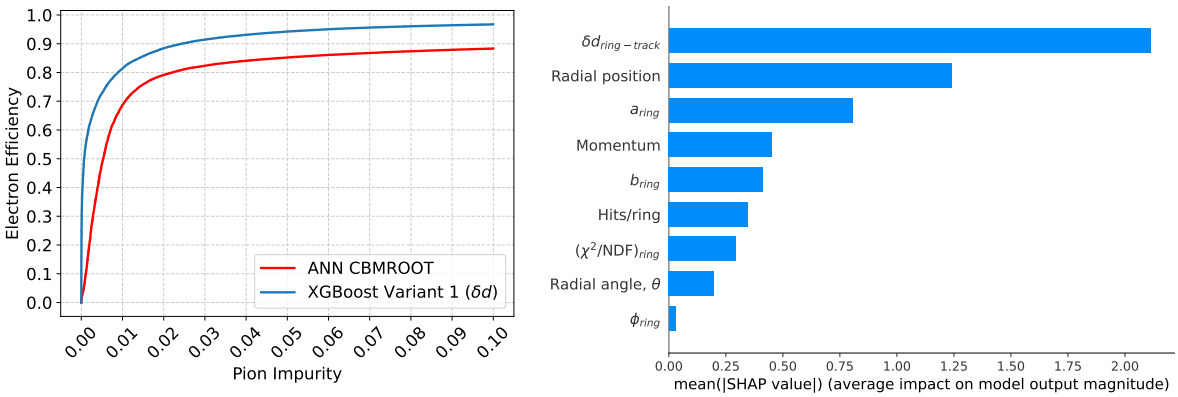

Figure 6.4: Response from the ML model to the training dataset with status quo input variables. Left panel: ROC curve depicting the reduced pion impurity for the same electron identification efficiency, resulting from changing the model from ANN (Red) to XGBoost (Blue). Right panel: Relative input variable importance chart measured by the SHAP metric.

The importance of different variables to the model performance calculated by the SHAP metric is plotted on the figure 6.4 (right). The ring-track distance variable holds the greatest significance for the performance of the model in comparison to other variables. The importance of the ring-radial position is partly influenced by the generation of an electron sample for the training, where different kinematic cuts for the FAIRBox generator influence the position of the track in the RICH camera. Since this dependency is momentum-driven, for the testing sample with omega decays, this dependency should be reduced (since the momentum range of most of the electrons (80%) from omega decay spans from 0.5 GeV/c to 2 GeV/c). The model prediction for the testing data might be affected by this reduced influence, but it is a small price to pay to make the model universally applicable. As per the training strategy used (see section 6.2), the performance of the model is less influenced by the momentum itself. Ideally, the momentum should have the lowest impact because of the identical uniform input distributions for the electrons and pions (see figure 6.3i). But the other input features are dependent on the momentum. This dependence is incorporated into the model's outcome; consequently, the momentum exerts an impact on the model. Other ring parameters have an almost identical impact on the model's outcome. The ring tilt angle ϕ_{ring} is the least important parameter; it is likely to be due to its strong correlations with a_{ring}, b_{ring}.

6.4.2 Results for the embedded omega dataset

The trained network is evaluated against the embedded omega data. Similar to the training step, the ROC of the response is calculated for both the ANN in CBMROOT and XGBoost, and the results are plotted in the figure 6.5 (left). The ROC for ANN and XGBoost overlaps at lower efficiencies of up to 15%. However, this is not the relevant range of efficiencies commonly used for the reconstruction of omega particles. Above this range, the XGBoost performs better at all efficiency points. At 70% efficiency for identification of the primary electrons, the pion impurities are reduced by a factor of 2 for the XGBoost model in comparison with the ANN in CBMROOT.

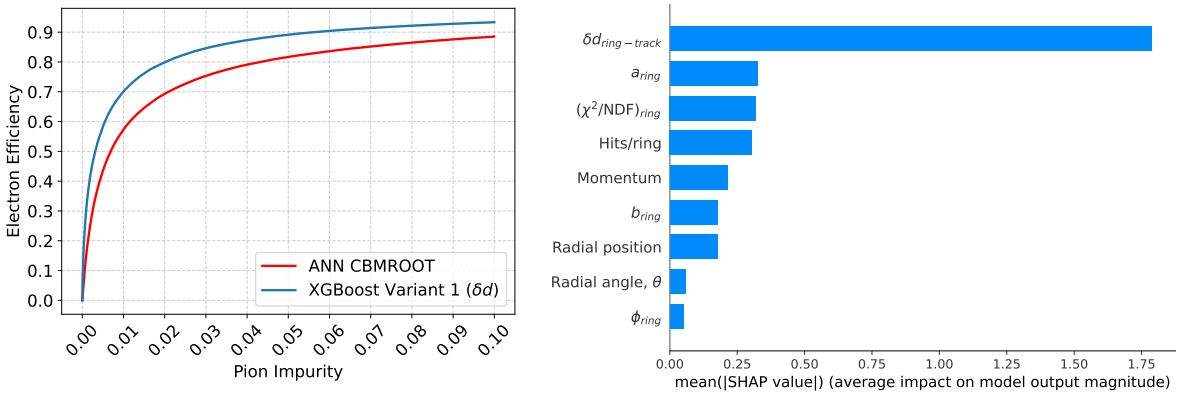

Figure 6.5: Response from the ML model for the embedded omega dataset (see table 5.2). Left panel: ROC curve depicting the reduced pion impurity for the same electron identification efficiency, resulting from upgrading the conventional ANN in CBMROOT (red) to the XGBoost model (blue) trained with the same input features. Right panel: Relative input variable importance chart measured by the SHAP metric for the XGBoost model trained with the status quo input features.

The importance of the different input variables to the performance of the XGBoost model is quantified using the SHAP metric and plotted in the figure 6.5 (right). As expected, the ring-track distance is the most influential variable for the XGBoost model's performance. The other parameters of the ring hold a similar range of significance in the performance of the model as they did for the training dataset. As anticipated, the absolute ring position in the RICH camera has lower significance for the embedded omega dataset as compared to the training dataset. The XGBoost model trained with the status quo input variables will from now on serve as the base model for evaluating future enhancements.

6.5 Inclusion of differential ring-track distance variable

As the ring-track distance is the most vital parameter for the classification (see figure 6.5 (right)), hence the possibility of deriving additional separation power using differential ring-track distances $\delta x_{ring-track}$, $\delta y_{ring-track}$ as inputs for the ML model is explored. In this regard, a simulation with the pure electron sample (see table 5.2) containing 100×10^3 $e^{\pm}$ is performed.

The differential ring-track distance as a function of momentum is histogrammed. The distance distribution is extracted from each momentum bin and fitted using a Gaussian profile. The

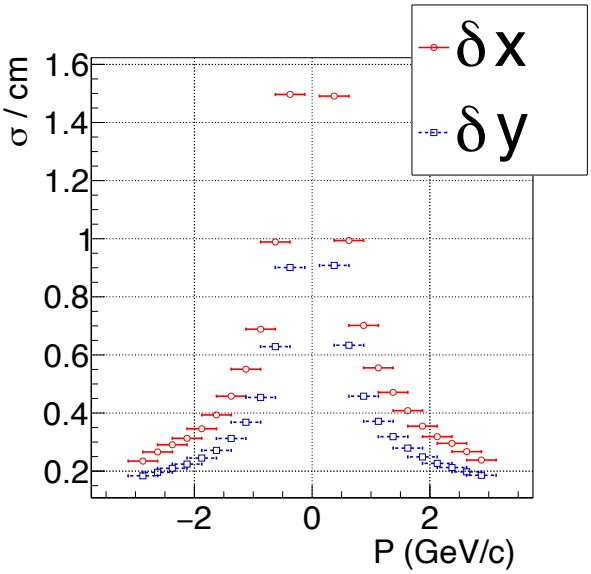

Figure 6.6: Figure showing the standard deviations for differential ring-track distances as a function of momentum for the FAIRBox-generated electron sample.

standard deviation of the Gaussian fits for both $\delta x_{ring-track}$ and $\delta y_{ring-track}$ distributions is plotted in the figure 6.6. From the figure 6.6, it can be observed that the widths of $\delta x_{ring-track}$ is larger than $\delta y_{ring-track}$ for all momentum ranges. This is because of the additional errors associated with track fitting and propagation in the presence of a magnetic field (which is along the XZ plane). The differential distances are used as input for the ML model in order to capture these differential widths and to avoid the false matching of pions at a large $\delta y_{ring-track}$ which is less likely for electrons.

Similar to the previous section (see section 6.2), the training is performed based on an embedded electron sample with a balanced number of electrons and pions. The hyperparameters of the model are optimized using the Bayesian approach (see section 6.2), and the results of the training are displayed in the appendix A.3.1. The trained modified model is tested with the embedded omega data set. The momentum-integrated differential ring-track distances for electrons and pions in the embedded omega data (additional input variables) are plotted in figure 6.7. As it can be seen, similar to the previous non-differential ring-track distance δd distribution, the differential ring-track distances for pions show two characteristics as well: a sharp peak close to zero deviation (similar to electrons) on top of a much broader distribution. The broad distribution is again attributed to false ring-track matches of sub-threshold pion tracks (random track projections into the RICH plane), which actually do not produce a Cherenkov ring at all. The sharp peak is caused by high-momentum pions with rings: high-momentum pions (momenta $\geq 4.7\,\mathrm{GeV}/c$) form rings, their tracks are least affected by the multiple scattering, and they have low track fitting and propagation errors due to bending in the magnetic field. Hence, the sharp peak close to zero for pions is identical in both $\delta x_{ring-track}$ and $\delta y_{ring-track}$. The differential ring-track distance distributions are sharper for electrons with a zero mean (after the systematic

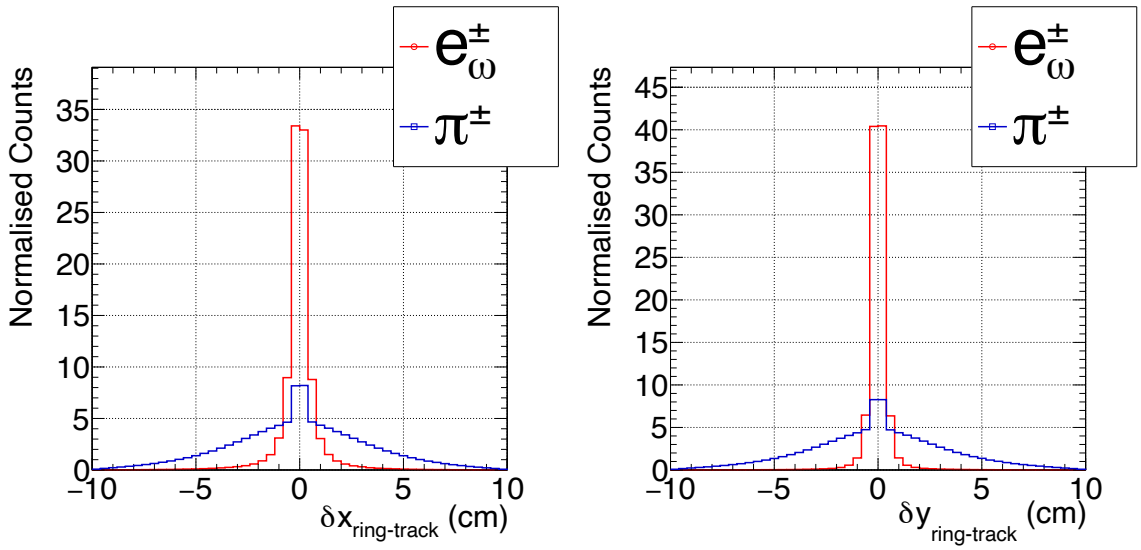

Figure 6.7: Plots depicting the momentum-integrated differential ring track distances derived for both primary electrons and pions in the embedded omega sample.

corrections (see sec. 5.5)), but with different widths for $\delta x_{ring-track}$ and $\delta y_{ring-track}$.

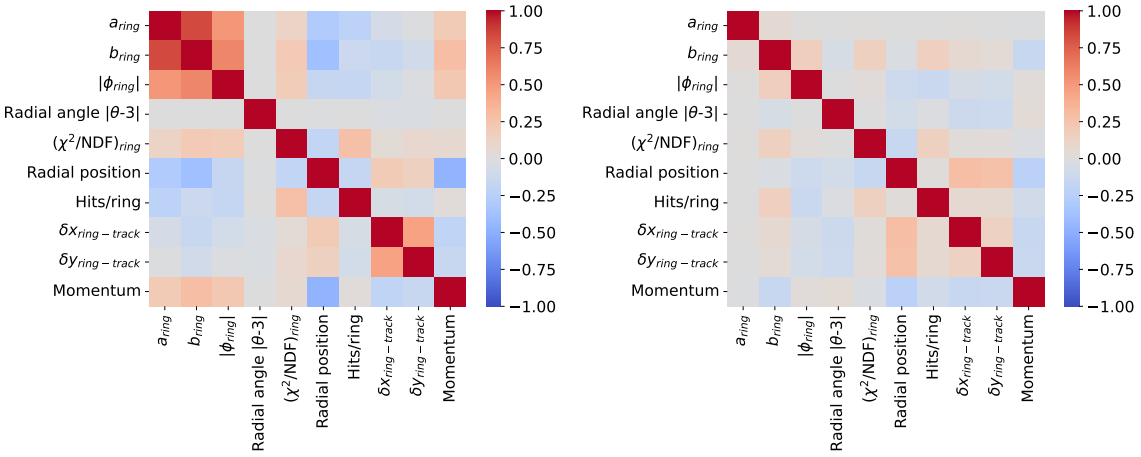

Figure 6.8: The Pearson correlation table depicts the linear correlation between various inputs to the ML model after inclusion of the differential distance variables for both electrons (left panel) and pions (right panel) in the embedded omega sample.

The Pearson linear correlation is calculated for the differential distances with other input features, and it is plotted in the figure 6.8. Here, $\delta x_{ring-track}$ and $\delta y_{ring-track}$ distributions are symmetric about zero for both electrons and pions. Only the absolute deviations are used for calculating the Pearson correlation in order to avoid cancellation effects for shifts in X and Y with opposite signs.

It is observed that the correlation between $\delta x_{ring-track}$ and $\delta y_{ring-track}$ is vanishing for pions due to dominating random projections at low momentum. However, for electrons, the correlation between $\delta x_{ring-track}$ and $\delta y_{ring-track}$ is positive, although not significantly close to one. Due to this difference from unity, both differential distance variables can be used as inputs for the ML model. As expected from the figure 6.6, both $\delta x_{ring-track}$ and $\delta y_{ring-track}$ are negatively

correlated with the momentum of the track, similar to $\delta d_{ring-track}$. Furthermore, the correlations between the differential distances ($\delta x_{ring-track}$, $\delta y_{ring-track}$) with other ring parameters are similar to one observed for the ring-track distance $\delta d_{ring-track}$.

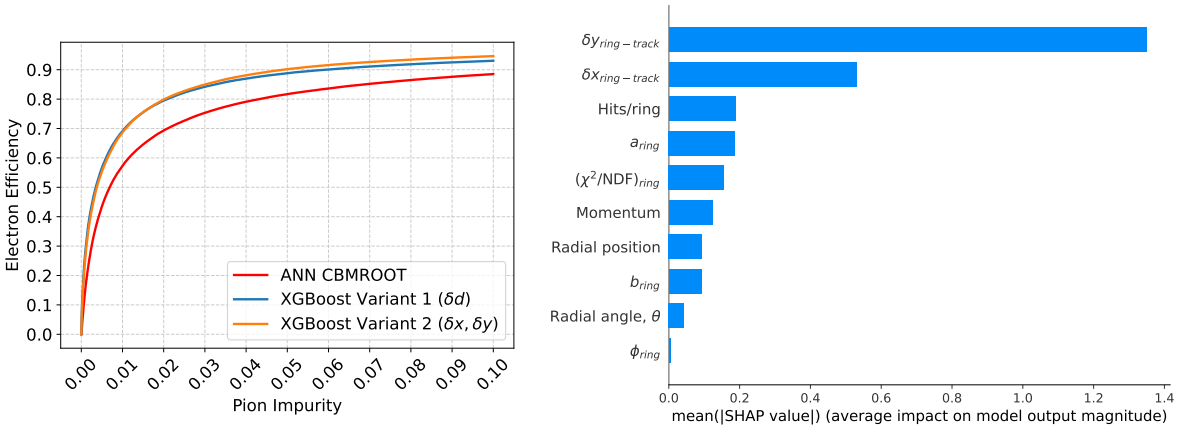

Figure 6.9: Response from the ML model for the embedded omega dataset (see table 5.2) after including the differential distance variables, compared with the ANN in CBMROOT (red) and the XGBoost model (variant 1) trained with $\delta d_{ring-track}$ (blue). Left panel: ROC curve depicting the reduced pion impurity for higher electron identification efficiency, resulting from inclusion of the differential distance variables. Right panel: Relative input variable importance chart measured by the SHAP metric for the improved model with differential distance variables.

The response of the new ML model to the embedded omega dataset is shown in the figure 6.9. For efficiencies up to 80% the fraction of pions in the data selection is identical for the model trained with $\delta d_{ring-track}$ and $\delta x_{ring-track}$, $\delta y_{ring-track}$. The high-momentum pion tracks ($> 4.7\,\mathrm{GeV}/c$) and the low-momentum pions forming random projections with both ring-track distances $\delta x_{ring-track}$, $\delta y_{ring-track}$ very close to zero still form small pion impurities, which have the XGBoost response similar to electrons. The inclusion of differential distances in the XGBoost model results in a noticeable enhancement in efficiency, particularly for higher pion impurities, in comparison to the XGBoost model without these parameters (additional information can be found in the appendix A.3.2).

The significance of the input variables in the performance of the advanced XGBoost model is again calculated using the SHAP metric and is plotted in figure 6.9 (right). It can be seen that the variables $\delta x_{ring-track}$, $\delta y_{ring-track}$ are the most influential variables for the model prediction, similar to $\delta d_{ring-track}$ (see figure 6.5 (right)). As expected, $\delta y_{ring-track}$ has more relative importance compared to $\delta x_{ring-track}$ because of the smaller width of the $\delta y_{ring-track}$ distribution as compared to $\delta x_{ring-track}$ distribution (see figure 6.6). The other input variables have relative importance similar to that of the model trained with $\delta d_{ring-track}$ as shown in the figure 6.5 (right).

6.6 Backtracking TRD fitted tracks to RICH

The ring-track distance has been proven to be the most effective parameter for separating electrons from pions. In this regard, an additional ring-track distance measure is introduced in this section. Here, the global track is re-fitted in the detectors downstream of RICH, especially TRD, and they are then back-propagated to RICH. This backpropagation will be referred to as "backtracking". A schematic of backtracking is given in the figure 6.10. This enables the introduction of an additional pointing vector, along with a forward track projection from STS to the same ring.

TRD-2D will be part of the standard TRD day-1 geometry. The triangular pads of TRD-2D will cover the inner region of acceptance where large track densities are expected. One of the advantages of the TRD-2D is its increased spatial resolution, which is expected to be $\sigma_x \approx 100\ \mu m$ and $\sigma_y \approx 800\ \mu m$. TRD-2D's better spatial resolution makes it better than TRD-1D for tracking applications.

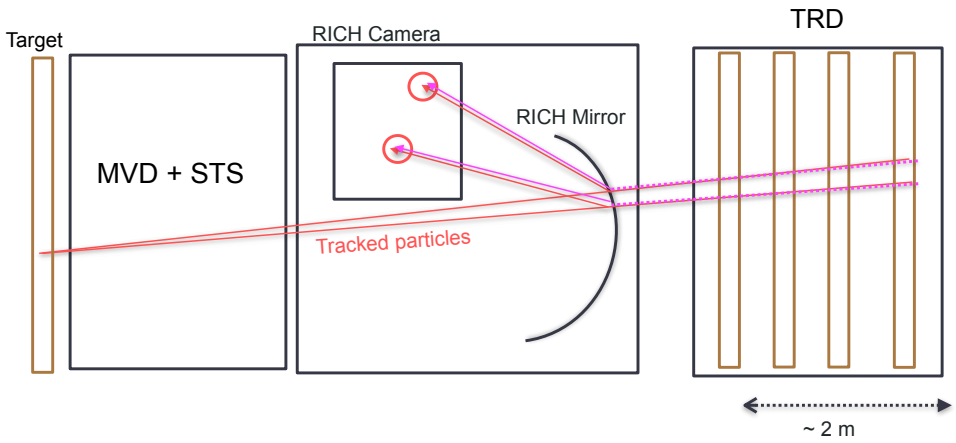

Figure 6.10: A schematic depicting the backtracking of TRD tracks to the RICH camera, providing an additional ring-track pointing reference.

6.6.1 Simulation of TRD-2D

At the time when these simulations were performed, the TRD-2D geometry was not yet available for standard simulations. Instead, in order to simulate the TRD-2D geometry, the standard TRD geometry was used, taking the MC-true hit positions of TRD hits subsequently smeared with the expected TRD-2D spatial resolution ($\sigma_x \approx 100\ \mu m$ and $\sigma_y \approx 800\ \mu m$) using Gaussian smearing. No modifications have been made to the timing information of the hit, as there is no anticipated disparity in the timing performance between TRD-1D and TRD-2D. This method of smearing on hit level preserves all digitizer effects on the MC points, hence is comparable to a true TRD-2D geometry simulation.

All tracks in TRD are straight since there is a minimal magnetic field downstream of the RICH.

Hits inside the TRD detector are fitted using a linear model using the least square fitter algorithm. As there is no correlation between the propagation of tracks along the XZ and YZ planes, the tracks can be fitted simultaneously in both planes. Consider if there are N_{hits} in the TRD track and each hit 'i' has spatial coordinates $\{x_i,\ y_i,\ z_i\}$ with corresponding resolution σ_i, where i=1,...,N_{hits}. The least square minimizer is used to find the optimal entry vector $\vec{r_0} = (x_0, y_0, z_0)$ and the exit vector $\vec{r_f} = (x_f, y_f, z_f)$ as follows,

$$\frac{\mathrm{d}\xi_x^2}{\mathrm{d}x_0} = 0,\ \frac{\mathrm{d}\xi_x^2}{\mathrm{d}x_f} = 0,\ \frac{\mathrm{d}\xi_y^2}{\mathrm{d}y_0} = 0,\ \frac{\mathrm{d}\xi_y^2}{\mathrm{d}y_f} = 0. \tag{6.9}$$

Where,

$$\xi_x^2 = \frac{1}{N_{\text{hits}}} \sum_{i=1}^{N_{\text{hits}}} \frac{(t_i(x_f - x_0) + x_0 - x_i)^2}{(\sigma_i^x)^2}, \tag{6.10}$$

$$\xi_y^2 = \frac{1}{N_{\text{hits}}} \sum_{i=1}^{N_{\text{hits}}} \frac{(t_i(y_f - y_0) + y_0 - y_i)^2}{(\sigma_i^y)^2}, \tag{6.11}$$

$$t_i = \frac{z_i - z_1}{z_f - z_1}. \tag{6.12}$$

Note that $z_0 = z_1$ and $z_f = z_{N_{\text{hits}}}$. Finally, the resultant vector $\vec{r_0} - \vec{r_f}$ which is the vector pointing towards RICH, is derived. Since the magnitude of the vector is of no importance, the direction vector towards RICH is calculated as $\vec{v} = \frac{\vec{r_0} - \vec{r_f}}{||\vec{r_0} - \vec{r_f}||}$. This unit vector is then extrapolated back to RICH.

6.6.2 Extrapolation of TRD tracks to RICH camera

The directional unit vector is extrapolated to the RICH camera in two steps: TRD to the mirror and mirror to the camera. The RICH mirror is modeled as a sphere with a parametric equation $||\vec{r} - \vec{c}||^2 = r_m^2$, where center $\vec{c}$ and radius r_m (same as the mirror). A vector can intersect the sphere at two points, except when it is a tangent (those tracks will be ignored because they cannot have rings in RICH). The distance from the TRD entry vector $\vec{r_0}$ to the closest point of intersection of the track with the RICH mirror sphere is calculated by solving the equation of line for the track $\vec{r} = \vec{r_o} + d\vec{v}$ and the sphere $||\vec{r} - \vec{c}||^2 = r_m^2$, which yields distance $d = -\vec{v}.(\vec{x_0} - \vec{c}) - \sqrt{|\vec{v}.(\vec{x_0} - \vec{c})|^2 - |\vec{x_0}|^2 - |\vec{c}|^2}$. The point of vector crossing the sphere at closest distance is then estimated as $\vec{r}_{mirror} = \vec{r_0} + d\vec{v}$. This vector is then reflected (with respect to the mirror normal vector) at the point of intersection and projected to the RICH camera as a straight line, similar to as it is done in the forward projection of STS tracks. In addition to the STS track projection, there is now a TRD track back-projection.

6.7 Ring-backtrack fit performance

In order to evaluate the ring matching performance of using the TRD-fitted tracks, a dedicated simulation was conducted by using pure electron samples (see table 5.2). All simulations are based on a sample of 1×10^6 electrons and positrons simulated with momentum up to 3 GeV/c, covering the full CBM acceptance. The differential distance (separated into δx and δy) between the track back-projection towards the RICH detection plane and the nearest ring found inside the RICH is histogrammed in multiple bins of the momentum of the corresponding electron track. Each momentum bin is 0.5 GeV/c wide. The restriction is limited up to 3 GeV/c because

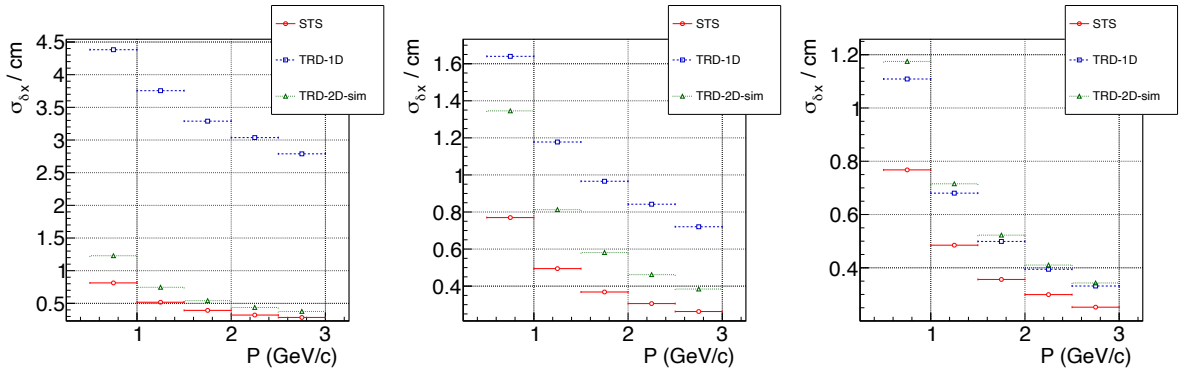

(a) 2 TRD hits **(b)** 3 TRD hits **(c)** 4 TRD hits

Figure 6.11: Standard deviation $\sigma_{\delta x}$ of distribution of x-differences between STS / TRD-1D / TRD-2D extrapolated electron track and corresponding RICH ring as a function of momentum. Furthermore, the figure shows the variation of derived standard deviation $\sigma_{\delta y}$ for tracks with 2, 3, and 4 TRD hits.

the only factor that affects the track-pointing performance is the multiple scattering, and its contribution is minimal at large momentum. The resulting δx and δy distributions are fitted using a Gaussian function, and finally the distribution mean and standard deviation (for each momentum bin) are extracted. This same procedure is carried out for all three cases: TRD, TRD-2D, and standard STS forward tracking. The mean deviations are not discussed here, since

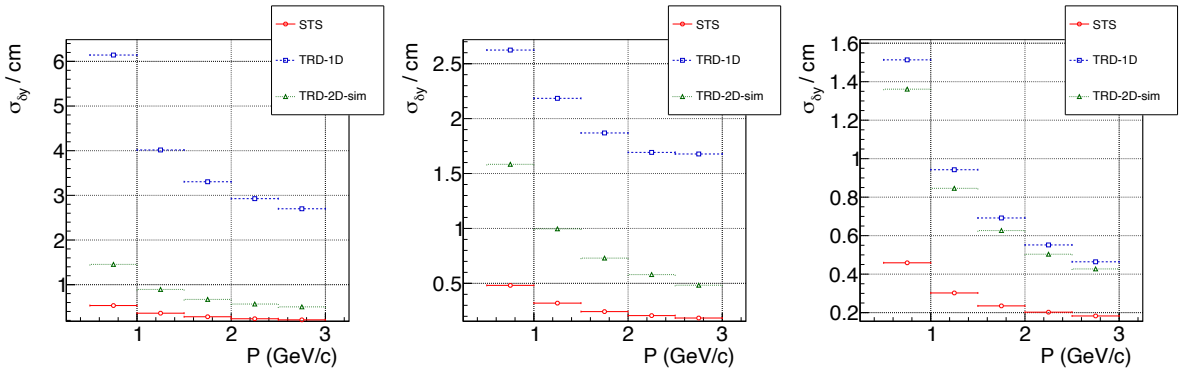

(a) 2 TRD hits **(b)** 3 TRD hits **(c)** 4 TRD hits

Figure 6.12: Standard deviation $\sigma_{\delta y}$ of distribution of y-differences between STS / TRD / TRD-2D extrapolated electron track and corresponding RICH ring as a function of momentum. Furthermore, the figure shows the variation of derived standard deviation $\sigma_{\delta y}$ for tracks with 2, 3, and 4 TRD hits.

systematic mean deviations observed in the ring track matching (if any) can always be corrected for in the camera plane (see section 5.5). Of larger importance is the standard deviation of the fits (see figures 6.11, 6.12), which is a measure of the statistical (back)tracking accuracy, and as such cannot be corrected for using tables. On comparing TRD-1D and TRD-2D, the TRD-2D geometry shows better overall resolution in the fit both in δx and δy if compared to TRD-1D tracklets with less than 4 hits (hit layers). This is because the TRD-1D has four layers: the first and third layers have better spatial resolution along X, while the second and fourth layers have better spatial resolution along Y. Therefore, if the number of hits in TRD-1D is N, then the effective number of hits with a better resolution comparable to TRD-2D is $N/2$. Only for TRD-1D tracks, including all 4 layers, does the TRD-1D tracking accuracy reach comparable accuracy to TRD-2D with at least 2 hit layers. Hence, the extrapolated ring-track matching resolution is also comparable. For TRD-2D tracking, the further benefit in tracking resolution when having 3 or 4 hit layers included is minimal compared to two hit layers. The STS forward track extrapolation is still slightly better in comparison with TRD-2D (roughly $\sim 80\%$ in δx), which is not surprising given the position resolution of STS being 25 µm.

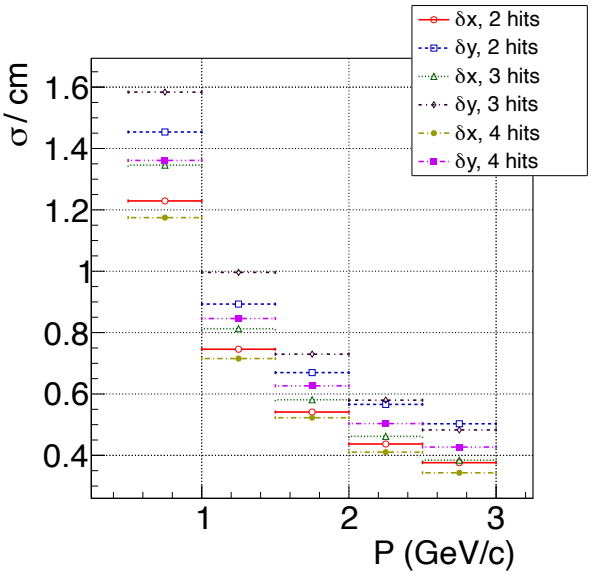

Figure 6.13: The performance of the ring track matching using TRD-2D for electrons. (Re-derived from figures 6.11, 6.12 displaying only TRD-2D performance)

The TRD-2D tracking resolution is improved with additional hit layers by at least 10% with each additional layer for δx in all momentum bins (shown in the figure 6.13). For δy the TRD-2D matching resolution is worse than for δx (by roughly $\sim 35\%$). This is expected since the hit position resolution along Y is worse than along X for TRD-2D. Similar results are obtained for positrons of the same momenta, which are not shown here (see appendix A.3.3).

6.8 Inclusion of TRD backtrack-ring distance parameter into forward ML model

The derived ring-backtrack distance is used as an additional parameter for the forward ML model for electron/pion separation. Because of the different widths of the fits for δx and δy, the differential distances $(\delta x, \delta y)$ are used instead of the squared distance $\delta d = \sqrt{(\delta x)^2 + (\delta y)^2}$. Since the width of δx and δy also depends on the number of hit layers (see figure 6.13), the number of hits in TRD (N_{TRD}) of the track is included as the parameter. As a minimum of two

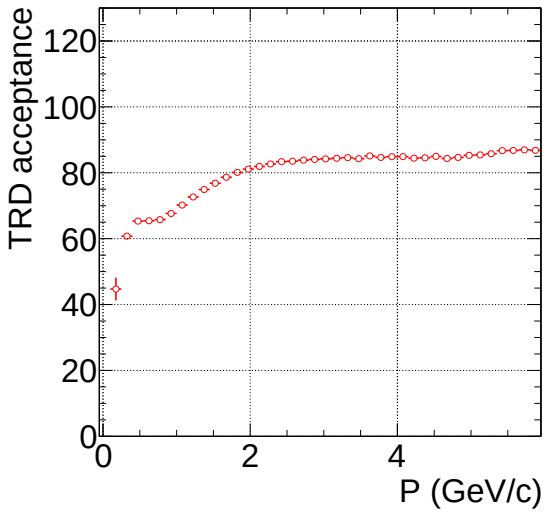

Figure 6.14: The acceptance for the tracks in TRD defined by equation 6.13 is plotted as a function of its momentum.

hits are required for the formation and fitting of the track in TRD, the range of TRD hits input is between 2-4. As TRD is situated further downstream from RICH, it is possible that certain tracks that are within the acceptance of RICH may not have the same geometric acceptance in TRD. In order for the TRD track to be accepted, it must have at least two hits registered. For the electrons and pions within RICH acceptance, the TRD acceptance is defined as,

$$\text{TRD acceptance} = \frac{(e^{\pm} + \pi^{\pm}) \text{ tracks with } N_{\mathrm{hits}}^{\mathrm{TRD}} \geq 2}{(e^{\pm} + \pi^{\pm}) \text{ tracks within RICH acceptance}}. \tag{6.13}$$

For the embedded omega sample (see table 5.2), the geometric acceptance for $e^{\pm}$ and $\pi^{\pm}$ in TRD is derived as a function of momentum and plotted in the figure 6.14. There is a lower acceptance for tracks with low momentum ($p < 1.5\,\mathrm{GeV}/c$). This is likely due to the residual magnetic field after STS, which bends the low-momentum tracks strongly outside the acceptance. For the tracks with momenta above $1.8\,\mathrm{GeV}/c$, the acceptance is above 80%. The reduced acceptance of high momenta tracks is due to the non-active region of the TRD sensors, which is about 9% [72].

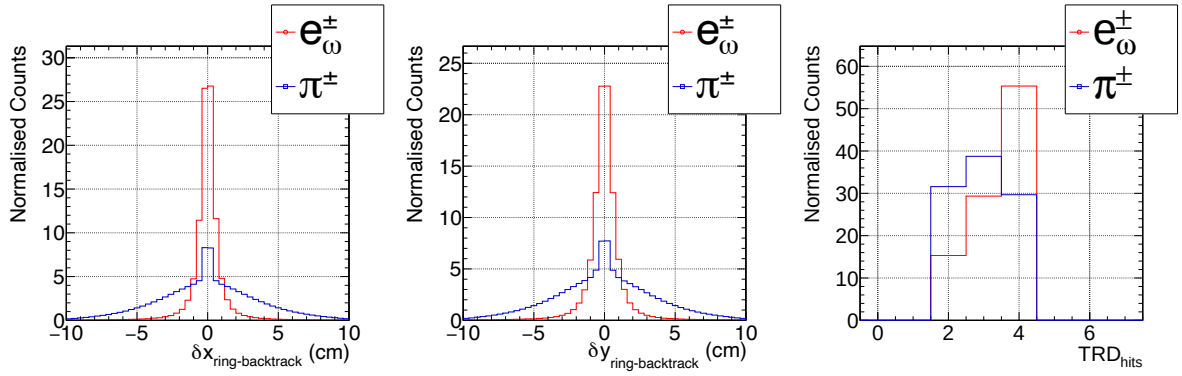

Figure 6.15: Left and middle panel: Momentum integrated differential ring-backtrack distances introduced in the forward ML model. Right panel: Number of TRD hits per track for primary electrons and pions.

For the embedded omega dataset, the additional input features from TRD backtracking for the ML model are shown in the figure 6.15. Similar to the forward ring-track distance, the backtracked distances for primary electrons yield sharp spectra with width ≈1 cm and a mean of zero. Furthermore, the pion spectra have two components similar to the forward ring-track distance. One from high-momentum pions above the Cherenkov threshold (which form rings in RICH), with the visible peak contribution close to zero (see figure 6.15 (left and middle)). There are also sub-threshold pions without rings in RICH, and therefore their track projections in the RICH are uncorrelated to any ring, which translates to a broad ring-backtrack distance spectra due to false matches. The linear Pearson correlation between the TRD backtracking variables

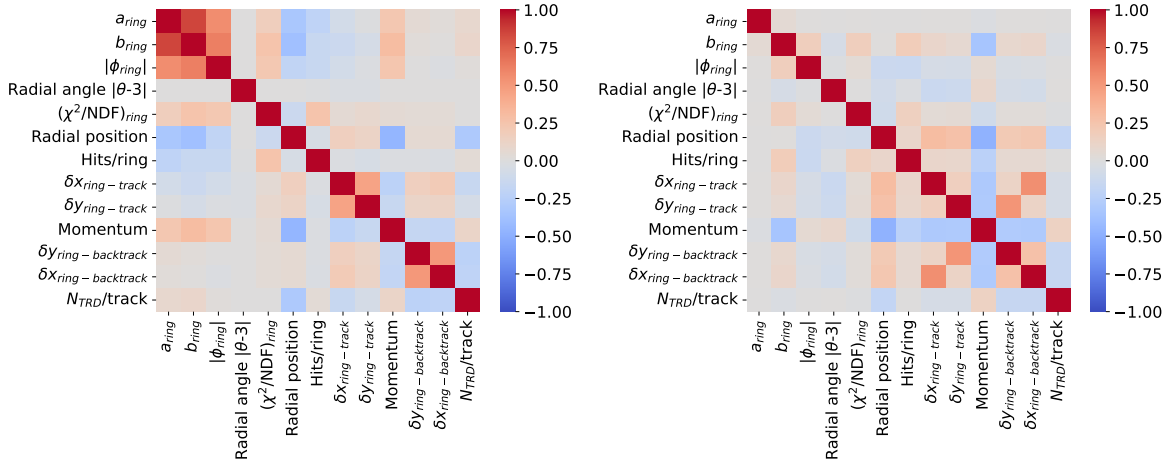

Figure 6.16: The Pearson correlation table depicts the linear correlation between various inputs to the ML model after inclusion of the TRD backtracking variables for both electrons (left panel) and pions (right panel) in the embedded omega sample.

and all the other features of the ML model is calculated and plotted in the figure 6.16. The ring-backtrack distances for electrons have a negative correlation with both the momentum and number of TRD hits/track (figure 6.16 (left)), as expected because the low-momentum tracks and/or lower number of TRD hits have a larger spread of the ring backtrack distance (compare spread in fit in the figure 6.13). A positive correlation is observed between the forward ring-track distances and ring-backtrack distances. But most importantly, the correlation is not strong (<

1), this makes it possible to use the ring-backtrack distances as an additional input variable for the forward ML model. Analogous to the forward ring-track distances, the ring-backtrack distances do not have significant correlations with other ring parameters. The pions exhibit a similar characteristic for the ring-backtracking distances and the number of TRD hits per track as electrons.

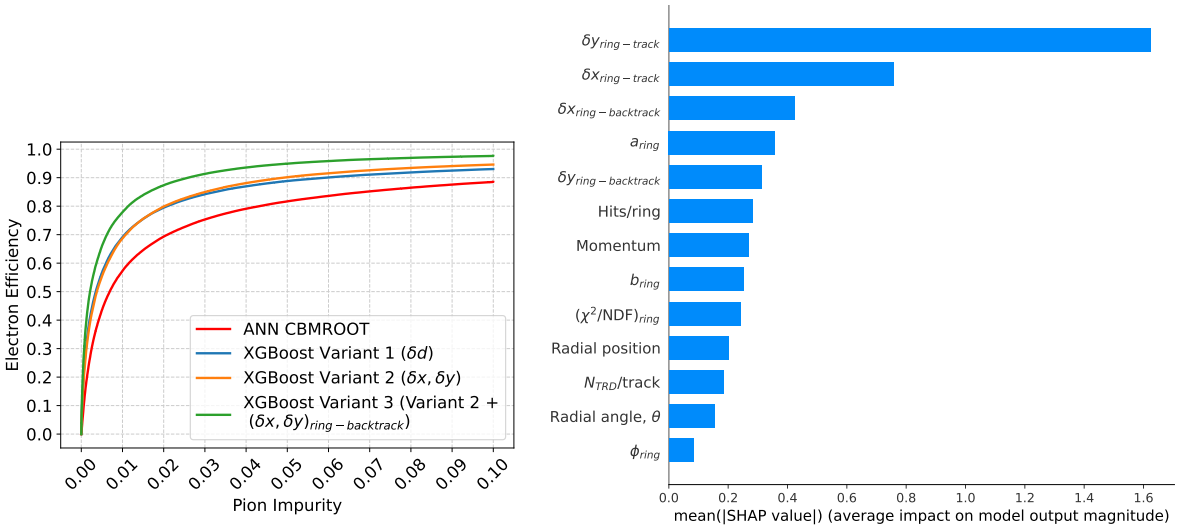

Figure 6.17: Response from the ML model after including the TRD backtracked parameters. Left panel: ROC curve depicting the reduced pion impurity for the same electron identification efficiency, resulting from inclusion of the TRD backtracked parameters. Right panel: Relative input variable importance chart measured by the SHAP metric for the improved model with backtracking variables.

Similar to the previous sections (see section 6.2), the training strategy is based on selecting a uniform distribution of momentum for electrons and pions, using the embedded FAIRBox-generated electrons with UrQMD-generated pions. Furthermore, the aforementioned Bayesian optimization methodology is employed to identify the optimal hyperparameters. The performance of the model for the training data set is displayed in the appendix A.3.4. The trained model is evaluated against the embedded omega sample. The results of the evaluation are presented in the figure 6.17.

It can be observed that the new model, including TRD-2D backtracking, outperforms the previous settings with only forward ring-track distances (see figure 6.17, Green). Upon comparing the ANN in CBMROOT with the XGBoost model with backtracking variables, it has been observed that the improved model has better efficiency at all points with the same proportion of pion impurities. For efficiency values below 50%, the XGBoost model with and without backtracking variables shows the same amount of pion impurities. However, at higher efficiencies (above 50%), the achievable pion impurity decreases for the model additionally using backtracking variables in comparison to the one without. At about 80% efficiency, the XGBoost model with backtracking variables performs twice as good at rejecting pions as compared to the XGBoost model without backtracking variables and almost 10 times better than the original ANN in CBMROOT.

The relative importance of the different input variables on the model with TRD backtracking variables performance is given in the figure 6.17. The forward ring-matching distances have the highest impact compared to the ring-backtracking distances. This is anticipated because the forward tracks have better resolution for the ring-track matching compared to the TRD-fitted tracks (see figures 6.11 6.12). Interestingly, the ring-backtrack distance $\delta x_{ring-backtrack}$ is the third most influential variable. The ring-backtrack distance along Y ($\delta y_{ring-backtrack}$) has less influence compared to the distance along X ($\delta x_{ring-backtrack}$), this is because the ring-backtrack fit resolution is better along X compared to Y (see figure 6.13). As per the training strategy, the model did not use the momentum as a major distinguishing factor.

The updated model can only be used on tracks with TRD acceptance (see figure 6.14), which accounts for about 80% of all electrons and pions in embedded omega data. Thus, there are two possible solutions for this scenario, one of which involves filling the missing data for tracks without TRD acceptance with nonphysical values, and the other involves employing two distinct models for tracks with and without TRD acceptance. In this thesis, the viable option of using two different models for two scenarios involving acceptance of the TRD tracks is used (additional information can be found in the appendix A.3.5).

The summary of the different XGBoost models developed in this chapter is shown in the table 6.2.

Table 6.2: Table displaying different variants of XGBoost developed in this chapter, with the input features used to train these models. The following input features are common for all models : $\{a_{ring},\ b_{ring},\ \phi_{ring}$, absolute ring position in polar coordinates (R, θ), hits/ring, ring-fit quality metric χ^2/NDF, Momentum$\}$ labeled "common input features". Note: δq represent the ring-track distance measure q, where $q = \{x,\ y,\ d\ (d = \sqrt{x^2 + y^2})\}$.

XGBoost model	Label	Input features			
		Common	δd (STS)	$\delta x, \delta y$ (STS)	$\delta x, \delta y, N_{hits}$ (TRD)
Variant 1	δd	✓	✓		
Variant 2	$\{\delta x, \delta y\}$	✓		✓	
Variant 3	$\{\delta x, \delta y\}$ $+\{\delta x_{BT}, \delta y_{BT}\}$	✓		✓	✓

7

Backtracking conversion electrons

In addition to the electrons and pions with Cherenkov threshold ($p_{thr,CO_2} \geq 4.7\,\mathrm{GeV}/c$) originating from the collision vertex, numerous Cherenkov rings in the RICH camera are formed by the electron tracks stemming from photon pair production (usually referred to as photon conversion) in the detector material. Furthermore, the majority of these conversion electrons originate in the last few stations of the STS and exit window of the STS. Hence, they cannot be reconstructed as tracks in the STS+MVD tracker. The abundance of these conversion rings, together with the abundance of pions stemming from the target, makes it more likely that these (electron) rings will be mismatched to pions from the target. In this chapter, a framework based on backtracking is described to identify the rings from the conversion electrons in the RICH detector. Furthermore, the results of the procedure are discussed, in which the rings are tagged with a probability that the ring might originate from a conversion electron (hereafter known as conversion probability). The conversion probability is added as an additional feature to the final ML model, and the results of the modified model are included in the last section. All the analysis in this chapter is based on the simulated UrQMD with omega mesons (see table 5.2). The decay of omega mesons into e^+e^- which is explicitly embedded as a reference signal for evaluation of the reconstruction performance. Sections of this chapter have been published in the following papers/reports:

- Pavish Subramani, *Machine learning application for electron identification in CBM*, FAIR next-generation scientists: 8th Edition Workshop, 2024 (Accepted for publication, Proceedings of Science) [110].
- P. Subramani, *"Global electron identifier for CBM using Machine Learning approach"*, XXXI International Conference on Ultra-relativistic Nucleus-Nucleus Collisions (Quark matter 2025).
- P.Subramani, et al., *Proof of concept for the TRD backtracking approach*, CBM Progress Report 2023 [111].
- P.Subramani, et al., *RICH timing precision and its possible applications*, CBM Progress Report 2023 [136].

7.1 Understanding the origin of Cherenkov rings in the RICH detector

The electrons are the primary source for producing Cherenkov rings in the RICH. In addition to electrons, pions above the Cherenkov threshold ($p > 4.7\,\mathrm{GeV}/c$) and muons (with a negligible contribution) form rings in the RICH. Due to the presence of electronic noise and fake hits, it is

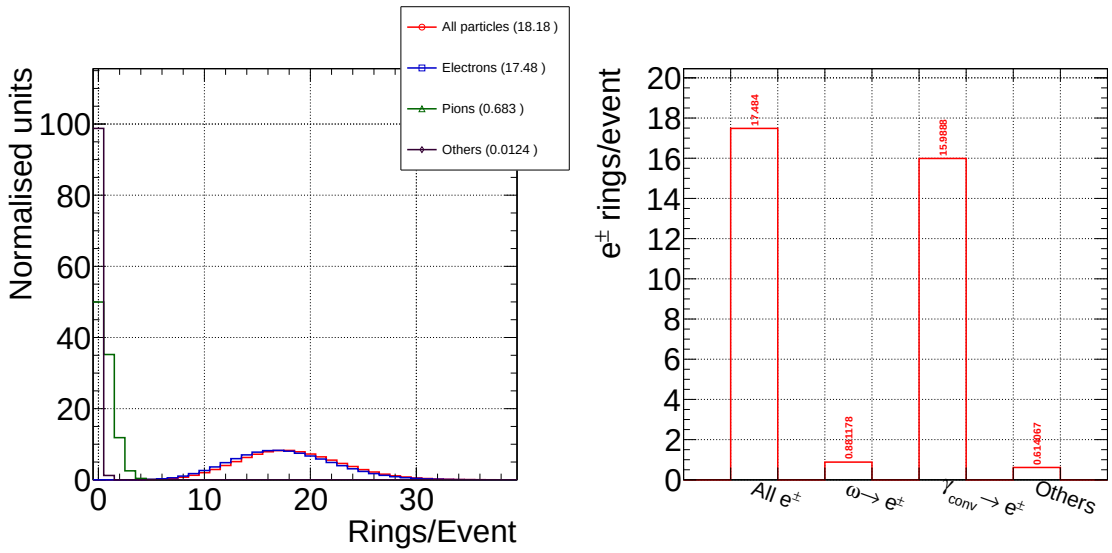

Figure 7.1: Left panel: Number of reconstructed rings per event produced by different particles. Right panel: Different processes producing the electron rings, indicating a substantial number of rings originate from conversion electrons.

possible that fake rings may be reconstructed by utilizing those fake hits and partially sharing hits from other rings. In figure 7.1 (left), contributions from the different sources to the total number of reconstructed rings for the Monte Carlo sample with embedded omega mesons are plotted. Almost 96% of all rings per event stem from electrons. Further investigation of the sources of the electron rings reveals that more than 90% of the electron rings originate from tracks produced by photon conversion in the detector material (see figure 7.1 (right)). Besides conversion electrons, there are also primary electrons stemming from the embedded $\omega \to e^+e^-$ decays (5%), and other contributions ($< 4\%$) – primarily from Dalitz decays of η and π^0 .

The impact of these conversion electron rings on pion suppression is contingent upon the possibility of reconstructing a track for the corresponding conversion electron. In this regard, the multiplicity of conversion rings with and without track candidates per event is estimated and depicted in figure 7.2. It is evident from the figure 7.2 that approximately 80% of the conversion rings are without a corresponding track candidate, whereas only 20% of the conversion rings have a track candidate in the STS+MVD tracking system. The number of MC points produced by these conversion electron tracks in the STS + MVD tracker system are plotted in the figure 7.2 (right). The tracked conversion electrons generated more than four MC points, whereas the untracked electrons generated fewer than four MC hit points, and their majority even produced no MC points. The CA tracker algorithm requires a hit in three consecutive stations as a track

seed and a minimum of one hit attachment to form a complete track. Therefore, conversion electrons with fewer than four consecutive hits are not registered as reconstructed tracks. The

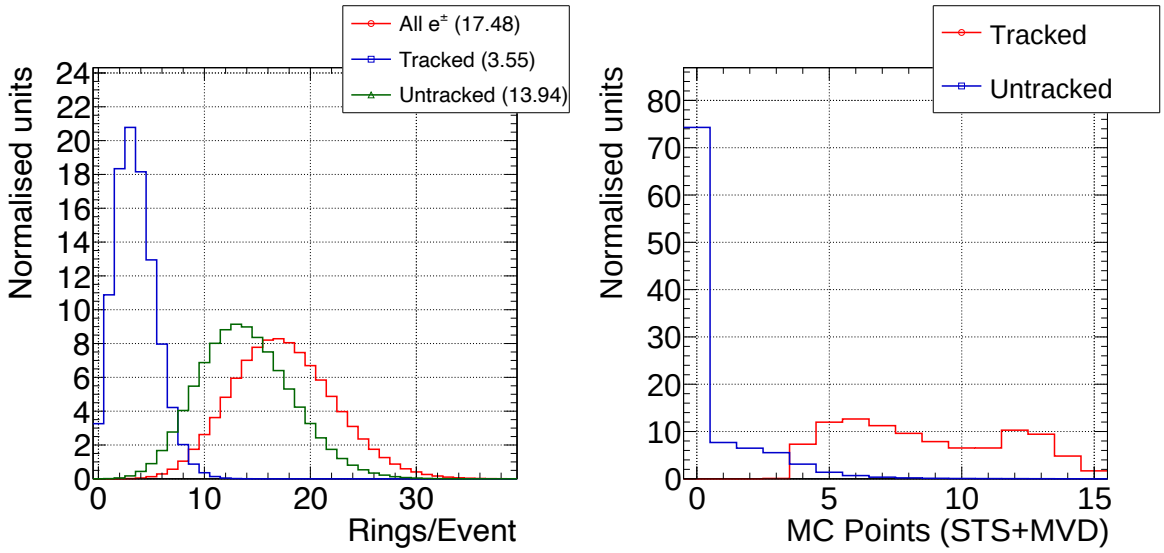

Figure 7.2: Left panel: Multiplicity of Cherenkov rings stemming from conversion with and without their corresponding track being reconstructed. Right panel: Number of MC points deposited by the conversion tracks in STS + MVD tracking system.

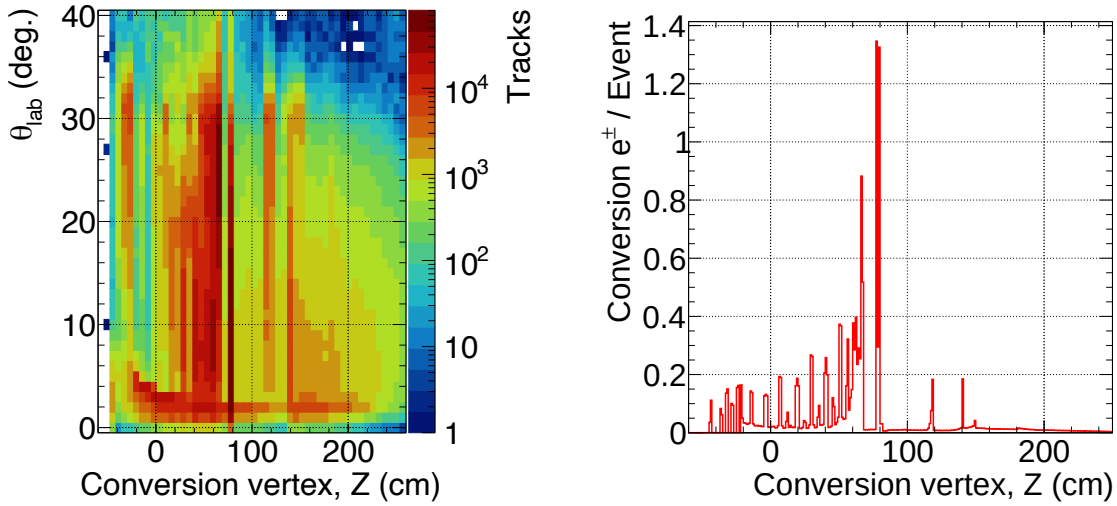

Figure 7.3: Left panel: Polar angle vs. vertex of pair production of the photons, where at least one of the electrons from the pair-production is untracked in the STS+MVD tracking system. Right panel: The Z-position of the photon conversion vertex, which produces at least one electron without a corresponding track candidate in STS.

fact that a significant number of conversion electrons only cause a low number of detector hits in STS / MVD can be understood by analyzing the conversion vertex of the photons in the detector material and the polar angle of the photons in the lab frame (see figure 7.3). It can be observed that the number of conversion points gradually increases towards the backward layers of the STS - partly due to the increasing thickness of the sensor layers (including cables) and

partly due to the additional conversion in the material surrounding the STS (such as readout electronics and exit window). The smaller fraction of the conversion electrons produced in the MVD and initial STS layers ($Z < 50\,\text{cm}$), are produced by photons that have a typical lower θ_{lab} angle. The combination of the downstream conversion vertex and the polar angle distributions of the photons (mother particle) makes these conversion electron (daughter particles) tracks to have a low probability of producing hits in STS.

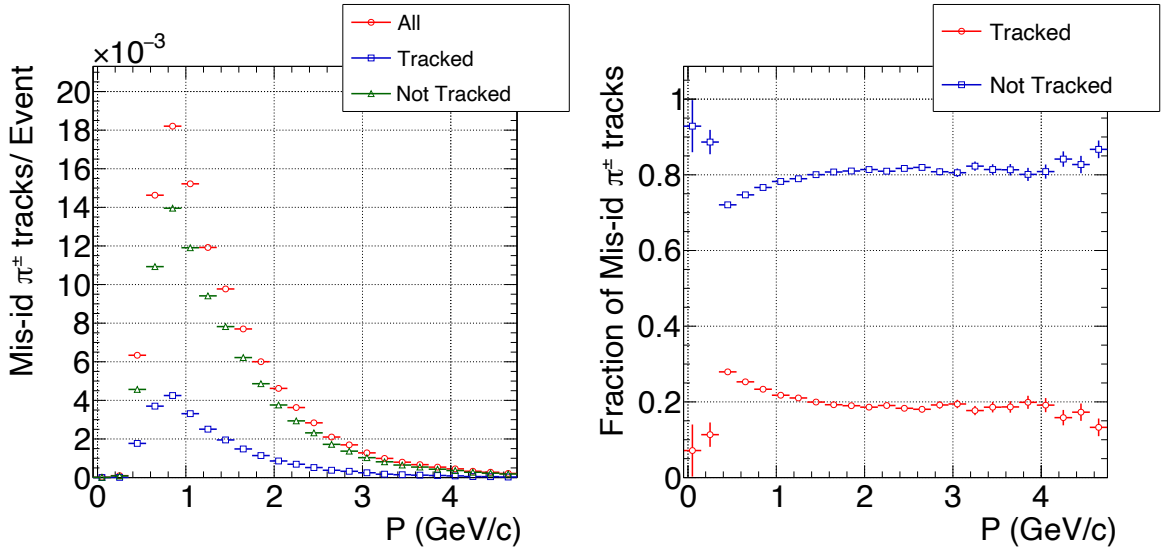

Figure 7.4: The number of misidentified charged pions per event is plotted as a function of the momentum of the pion tracks. Left panel: The pion tracks that are mismatched to the ring produced by a conversion electron, which has a corresponding reconstructed track in STS (blue curve (left)) and which do not have a corresponding reconstructed track in STS (green curve (left)) are shown. Right panel: The ratio of the number of pion tracks mismatched to conversion electrons (that have a corresponding reconstructed track (red) and do not have a corresponding reconstructed track (blue)) to the total number of misidentified pion tracks is shown as a function of momentum.

In the ring-track matching phase, the pions (especially sub-Cherenkov threshold pions) might be mismatched to the rings of the tracked or untracked conversion electrons. The figure 7.4 shows the extent of mismatch between the pions and the rings of tracked and untracked conversion electrons. The probability of mismatches between pions ($p < 4.7\,\text{GeV}/c$) and rings of untracked conversion electron is higher as compared to tracked electrons because of the abundance of untracked conversion electrons. The ratio of pions being mismatched to the rings of tracked versus untracked conversion electrons is 20:80 which equals the ratio of tracked/untracked electron rings (figure 7.2 (left)).

7.2 An approach to account for the conversion electrons

If track candidates are consistently matched to the closest RICH ring within a certain distance range, irrespective of any additional matching criteria, there may be instances where multiple tracks are assigned to the same ring. Here, a method of priority matching can be used (not

discussed in this thesis). Any track candidate that can be clearly identified as an electron in the downstream detectors (TRD, TOF) can also be considered as an electron in the RICH and should therefore be prioritized in the matching procedure to Cherenkov rings. These already assigned rings can then be removed prior to matching the remaining STS track candidates. The benefit (gain) of this approach is somewhat restricted by the electron identification performance of the downstream detectors. The method described above is effective as long as the conversion electron has a reconstructed track in STS/MVD.

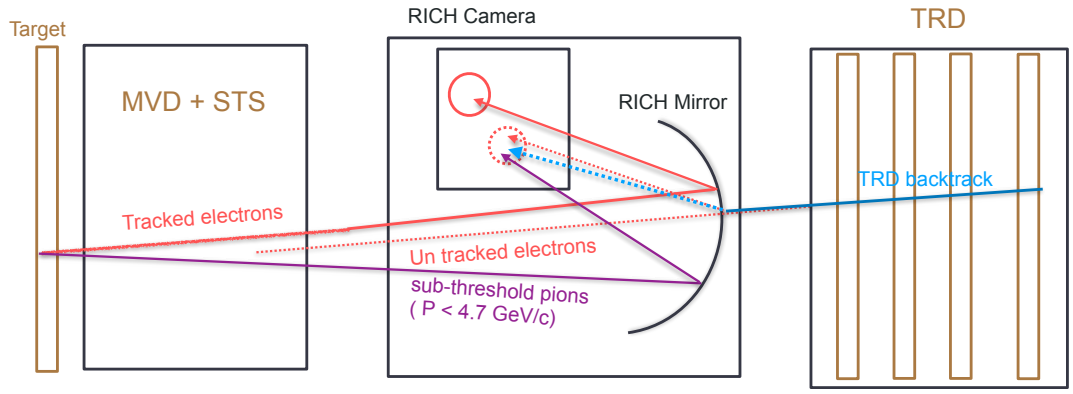

Figure 7.5: Schematic showing the untracked conversion electrons forming rings in RICH (dotted red line) and sub-threshold pions mismatched to the rings from these conversion tracks. These electrons are tracked in TRD and extrapolated back to RICH and matched to the closest ring (purple line).

However, the majority of the conversion tracks have no track candidate. Note that the primary leptons from the target are always expected to have an associated reconstructed track within STS. In this section, an advanced approach based on backtracking (discussed in section 6.6) is described, which aims to add track reference from TRD to those rings without any corresponding track candidate in STS. The method follows a two-step approach: in the first step, all the TRD hits are removed that could already be matched to STS tracks. All leftover hits in TRD now essentially have no correlated track candidate in STS and most likely contain the track traces from electrons produced by photon conversion after STS. In the second step, these leftover hits are combined to form tracks within the TRD detector, fitted using a linear model, and subsequently extrapolated back (upstream) onto the RICH mirror and thus projected onto the RICH camera. Then these tracks are matched to the closest ring and if the matching conditions are satisfied, the rings are flagged as stemming from electrons from photon conversion by assigning a conversion probability to the matched ring. This conversion probability will be used for further electron identification steps. A schematic showing the mismatch between the sub-threshold pions with the untracked electrons, with subsequent tracking of these electrons in TRD, is depicted in the figure 7.5.

In this method, the tracking capability of the TRD (simulated TRD-2D) is utilized along with its electron identification capability. Due to the non-availability of TRD-2D pads as components in the TRD MC geometry setup, the CA-based tracking utilizing solely TRD stations is not included in the current standard reconstruction scheme. Hence, for this study, an ideal track-

finder based on MC True information is used. Since, the track reconstruction efficiency for the CA tracker with STS + MVD is greater than 90%, with less than 2% fake tracks [137], this ideal tracker can be regarded as comparable to the CA tracker to be later used. Once the standard tracker with TRD-2D geometry and TRD track seeding for the CA trackers is available, this modular approach can be adopted.

7.3 Characteristics of the conversion electrons

The conversion electrons with rings in the RICH without any track candidate in the STS + MVD tracker are the tracks of interest. Henceforth, these tracks for this specific application of backtracking shall be referred to as **"signal electrons"**. The term "signal electrons" is used rather than simply "conversion electrons" in order to avoid including conversion electrons that may form after RICH and form hits in TRD but lack a ring in RICH. The number of hits

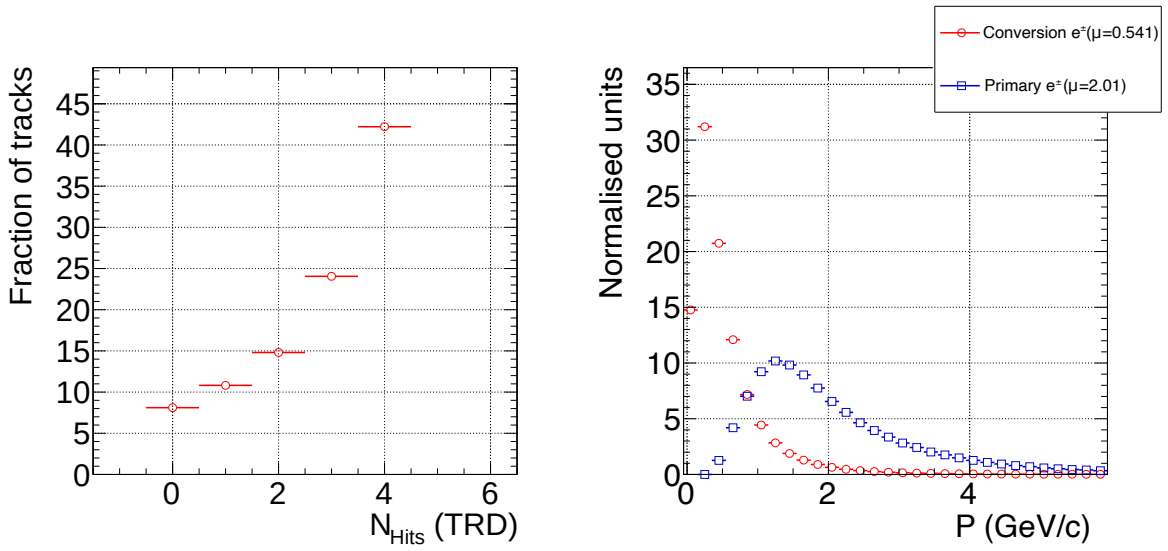

Figure 7.6: Left panel: Number of TRD hits and momentum distribution of signal electrons. Right panel: Comparison of momentum distribution for conversion electrons (signal + additional conversion electrons after RICH) (red) and primary electrons from ω-decay (blue).

produced by the signal electrons in the TRD is shown in the figure 7.6 (left). It can be observed that almost 80% of the signal tracks have at least two hits in the TRD. Since at least two hits are needed to form a track (best would be three or higher), a track is considered as accepted if $N_{\text{hits}} \geq 2$. Using only two hits to form tracks comes with the drawback of having more "fake" tracks due to combinatorics. This could, however, be mitigated by additionally requiring the track to feature a $\beta \approx 1$ based on time-of-flight measurement between RICH and TOF, after forward propagation of the TRD tracklet to TOF (This procedure is discussed in the next section). The momentum distribution of the signal electrons from photon conversion and from primary electrons stemming from ω-decays are shown in the figure 7.6 (right). Since the signal electrons stem from photon conversion, they feature smaller momenta compared to the primary electrons from the ω-decays. Because they have lower momenta, they produce fewer transition

photons. This is visible in the figure 7.7 (left). Using the naive Bayes classification, the TRD electron likelihood is calculated and shown for signal electrons in figure 7.7 (right). The electron likelihood is calculated by assuming track momenta of 0.6 GeV/c (figure 7.6 (right)), since the absence of STS hits prevents the determination of the momentum of each track. This likelihood distribution clearly demonstrates that relying solely on the electron reference in TRD to select the signal tracks (see figure 7.7 (right, red)) is not entirely advantageous, as the pions (green) possess comparable characteristics.

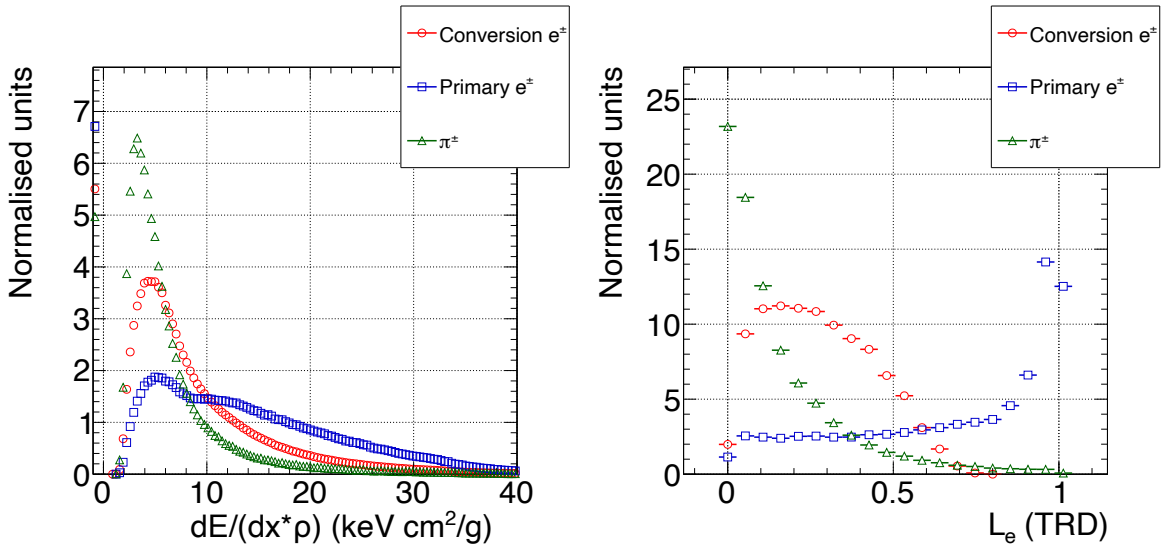

Figure 7.7: Energy loss in the TRD (left) and TRD electron likelihood for electrons from photon conversion (signal + additional conversion electrons after RICH), pions, and primary electrons (from ω-decay).

7.4 Proof of concept

To understand the potential of the backtracking strategy, a proof of concept simulation was performed with only these signal electrons in TRD, i.e., removing all STS-unmatched hits in TRD which are not part of the signal.[1] Thus, this simulation will demonstrate the expected gain from applying the backtracking method. This also helps in finding optimal values for different variables in the analysis for the further application. All found signal tracks are fitted by a linear model, and χ^2/NDF for the tracks are shown in the figure 7.8 (left). In this first implementation, the linear track fitting is done separately in X- and Y-coordinates. The tracks with $\chi^2/\mathrm{NDF}(X) \leq 1.0$ and $\chi^2/\mathrm{NDF}(Y) \leq 1.0$ are selected and matched to the closest ring in the RICH. The ring-track distances are shown in the figure 7.8 (right). The tracks are sharper along X compared to Y because the positional resolution in TRD2D along Y ($\sim$ 800 µm) is worse than along X ($\sim$ 100 µm). This information can be used to distinguish false matches, where the background tracks having complementary fit distance can be eliminated. In this first analysis, only a cut on the radial distance between ring and projected track coordinate

[1] First all the hits in TRD which are not matched to any STS hits should be removed. In the remaining hits, only hits that corresponds to the signal electrons are considered.

($\delta d < 5.0$) is applied. Having identified all Cherenkov rings without a corresponding STS track but with matching TRD backtrack and large TRD electron probability, these rings are removed prior to the final matching step (same as assigning $P_{conversion} = 1$). Now, as the final step,

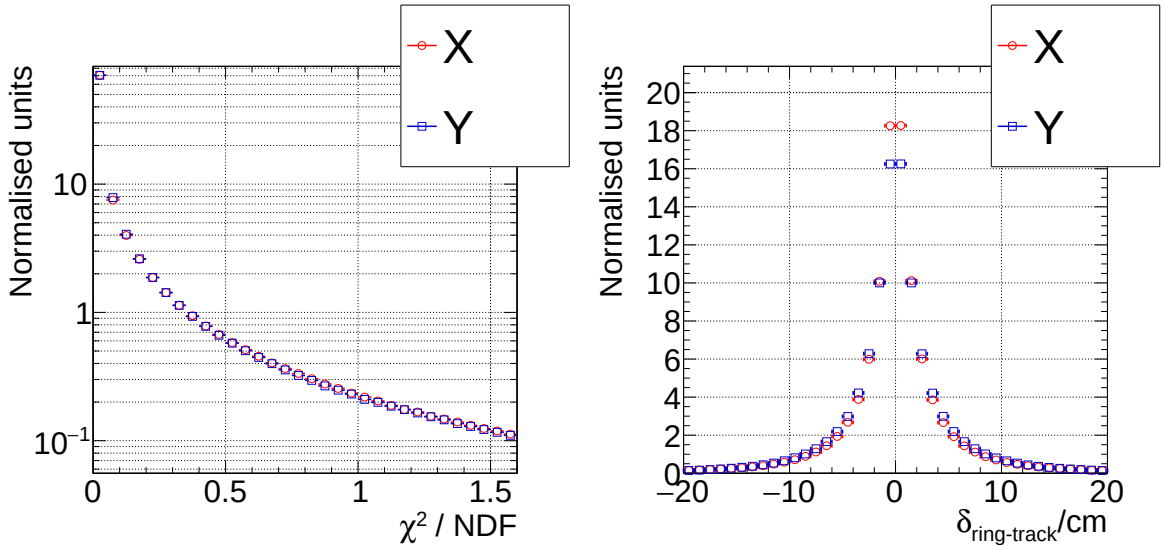

Figure 7.8: Left panel: χ^2/NDF for the fitted TRD tracklets. Right panel: Ring-backtrack matching distance in X and Y.

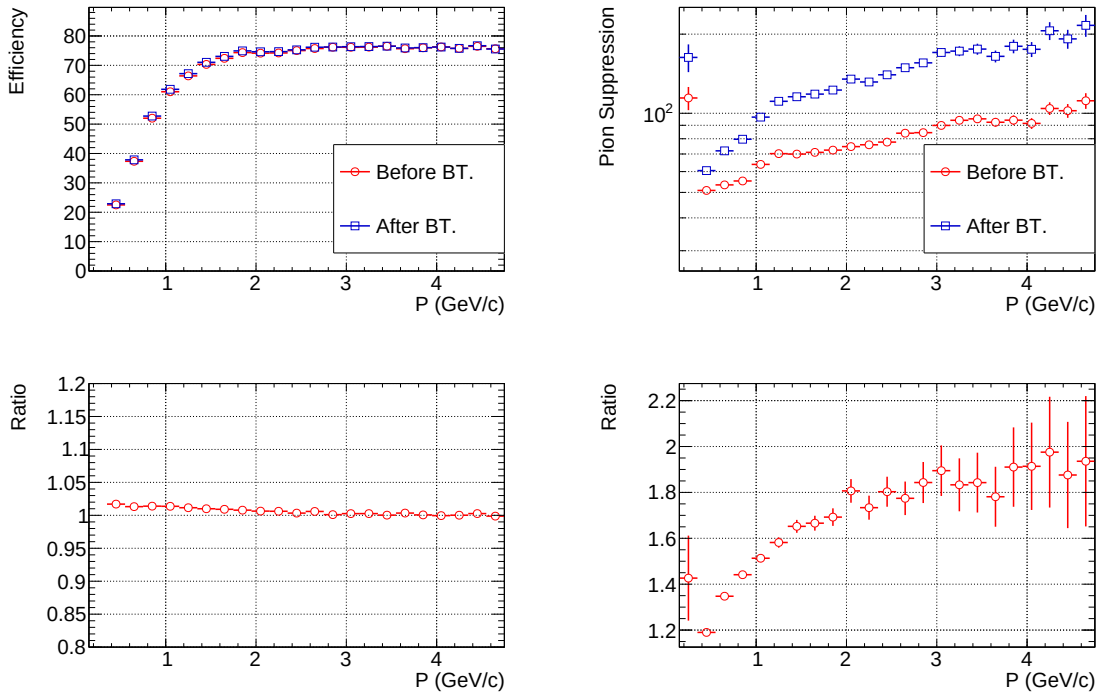

Figure 7.9: Electron detection efficiency (left) and pion suppression factor (right) with and without additional TRD backtracking.

the remaining rings are matched to the STS tracks in this procedure. The resulting efficiency of this approach for primary electrons and pion suppression factor are shown in the figure 7.9.

The definitions of both are

$$\text{Efficiency} = \frac{\text{Tracks identified as electrons}}{\text{Tracks having at least 7 hits in RICH}},$$

$$\pi^{\pm} \text{ suppression factor} = \frac{\text{Multiplicity of STS tracked } \pi^{\pm}}{\pi^{\pm} \text{ mis-id as } e^{\pm}}.$$

Since backtracked electrons fulfilling certain quality criteria almost always have a corresponding RICH ring in close vicinity, the chances of these tracks removing a random ring are very low. Hence, the measured efficiency for electrons does not deteriorate when using the backtracking technique. Only a negligible difference in the efficiency for primary electrons is observed. More drastically, a gain by a 40% - 80% in the pion suppression factor is observed over the full momentum range. This demonstrates the potential in this strategy.

7.5 General application of the method

As the efficacy of this strategy has been demonstrated, the approach is now applied to the complete data which is not limited to the TRD hits corresponding to signal electrons (conversion electrons), but encompasses all TRD hits. The first step in the method is to filter out the hits already matched to the STS tracks. The hits in TRD are matched to the STS tracks based on MC-ID, this is to prevent efficiency loss due to hit matching between the extrapolated STS tracks and TRD hits. The matched hits are removed, as hits from conversion electrons can be found in the remaining hits.

Figure 7.10 (left) shows all hits registered per event in the different layers of TRD. All layers have almost an equal number of hits (around 310 hits per event). After removing all TRD hits matched to STS tracks (using the embedded omega data sample), more than 50% of the original TRD hits remain, with fewer hits being removed in the TRD backward layers. This is caused by the material budget present in the initial layers, which facilitates the production of secondary charged particles (having no STS counterpart), which then produce additional hits in the latter TRD layers.

From all remaining hits, tracks comprising at least two hits are reconstructed. The multiplicity of backtracks per event is shown in figure 7.11 (left). It can be seen that there are almost 200 backtracks per event (most central, up to 40%) found. On extrapolating to RICH, it can be observed that 40% of the backtracks formed from TRD hits (that could not be correlated to STS tracks) have no track projection in the RICH (see figure 7.11 (left)). The remaining 60% of the tracks have projection to the RICH camera. In the next step, all backtrack candidates that point back to the RICH (extrapolated backtracks) are matched to the closest found ring in the RICH. The multiplicity of backtracks for which a ring could be found within 10 cm radial distance is shown in the figure 7.11 (right). From the figure 7.11 (right), it can be inferred that there are more than twice as many backtrack candidates pointing to the vicinity of a ring (distance less than 10 cm) as there are rings in total. Consequently, it will not be helpful to

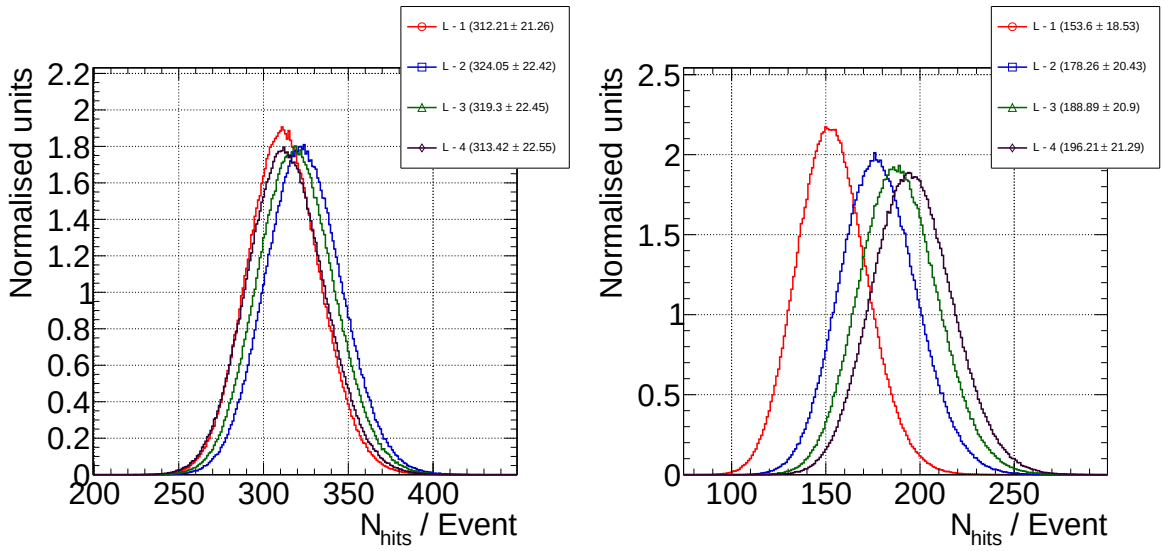

Figure 7.10: Left panel: Hit multiplicity per event registered in TRD in all four distinct TRD layers. Right panel: Hit multiplicity per event registered in TRD, after removing all hits that could be matched to STS tracks.

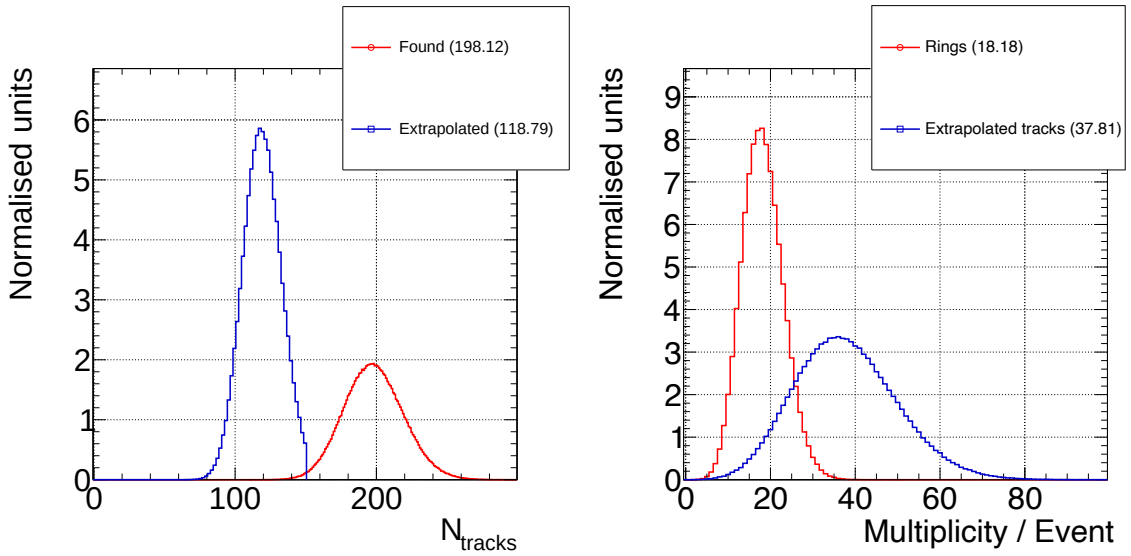

Figure 7.11: The distribution of TRD backtrack multiplicity per event is shown here. Left panel: The distributions of the number of backtracks reconstructed in TRD (found, red) and the number of TRD backtracks that have projection into the RICH camera (extrapolated, blue) per event. The figure indicates that almost 60% of the reconstructed TRD backtracks have projection in RICH (have RICH acceptance). Right panel: The distributions of the number of backtracks that have track projection in RICH at a distance less than 10 cm from a ring (extrapolated tracks, blue) and the total number of rings (rings, red) per event. The distributions indicate that there are almost twice as many backtrack projections as rings.

simply discard all rings in the vicinity of any backtrack projection, based solely on a minimum ring-track distance cut, as it could result in the reduction of rings of primary omega electrons.

The backtracks with RICH projections are located in the vicinity of any ring (distance less than 10 cm) composed of two components that are identified by the MC true information. The first

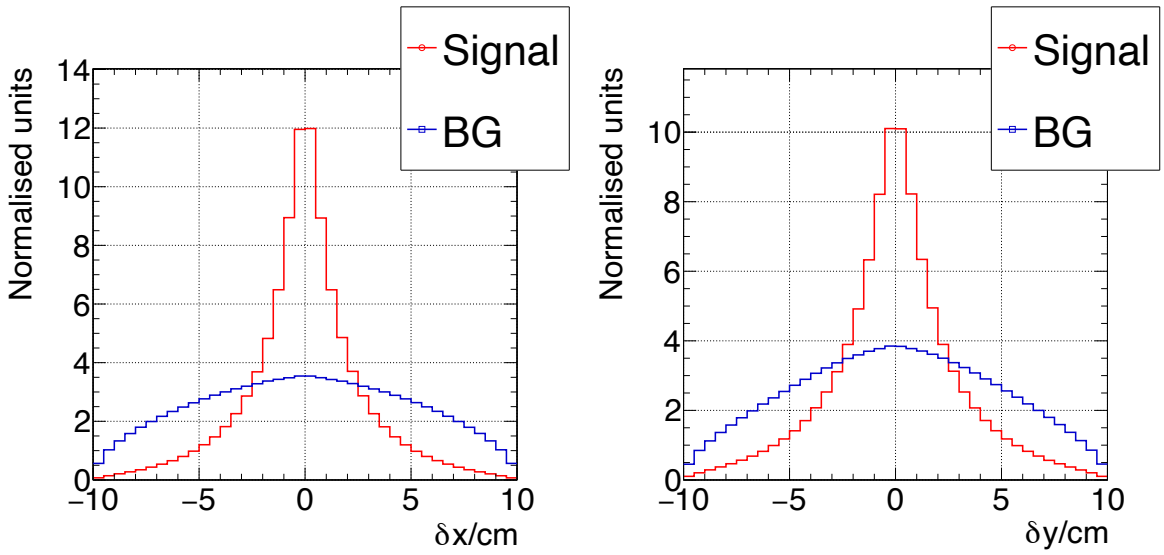

Figure 7.12: Ring-backtrack matching distance in X (left) and Y (right) for the TRD backtracks (tracks not seen in STS) formed by the conversion electrons having a ring in RICH (signal, red) and backtracks formed by other particles that do not have a ring in RICH (BG, blue).

is the TRD backtracks (tracks not seen in STS) formed by the conversion electrons (produced after STS) having a ring in RICH. This was previously denoted as **"signal tracks"**. The second component pertains to the TRD backtracks, which are formed by other particles (tracks that are not seen in STS) and have not produced a ring in RICH, but are present in the vicinity of the ring due to random projection. The backtracks with ring-backtrack distance less than 10 cm which itself did not produce that ring in RICH will be referred to as the **"background"** for the further investigation. With the initial distance cut, $d_{ring-backtrack}$ <10 cm, the differential ring-backtrack distance is shown in the figure 7.12. It is observed that the signal backtracks have a sharp ring-backtrack distribution, while the background without a ring reference has random projections, which form a broad distribution.

7.6 Background contribution

In order to understand the background backtracks, i.e., backtracks without any ring reference in RICH but are in proximity to the rings due to random projection, an analysis is performed by isolating particle species in the set of background tracks. The figure 7.13 shows the different particle species in the set of background backtracks (did not produce any ring), with projections in the vicinity of a ring ($d_{ring-backtrack} < 10$ cm). Electrons form the major background, with more than 10 projections per event. As it can be seen from figure 7.14a, the electron background is mostly from the photon conversions in the RICH mirror and exit window of RICH (250 cm $< Z_{vertex} <$ 350 cm). Moreover, there exists a contribution from photon conversion in the initial TRD layers, which results in the formation of tracks in the latter layers (400 cm $< Z_{vertex} <$ 550 cm). Next to electrons, the protons and pions make up the main background (more than 10 backtracks per event). From the figures 7.14b, 7.14d, it can be observed that the substantial

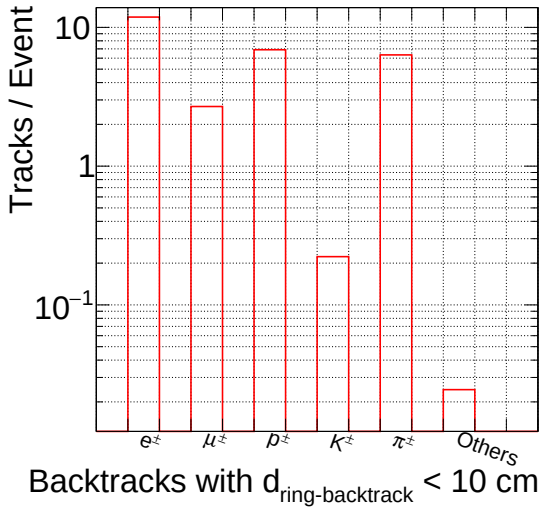

Figure 7.13: Different background contributions to the backtracks, with $d_{ring-backtrack}$ <10 cm.

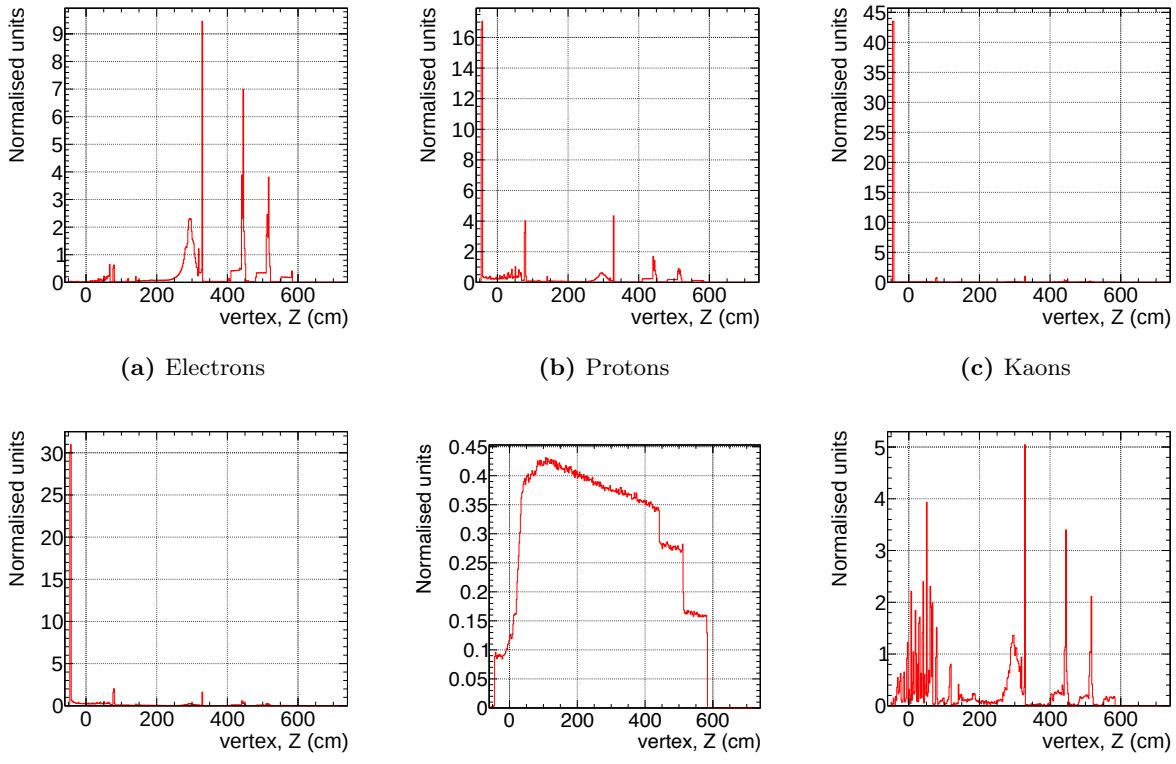

(a) Electrons **(b)** Protons **(c)** Kaons

(d) Pions **(e)** Muons **(f)** Others

Figure 7.14: Production vertex (Z-coordinate) of all the background tracks, with $d_{ring-backtrack}$ < 10 cm. The figures indicate that the substantial amount of hadron background arises from the target (the target is situated at $Z = -44$ cm).

portion of these backtracks originate from the target (or close to the target). Protons are partially produced by hadronic interaction in the detector material in STS, RICH, and TRD (initial layers). Although they are less significant, the kaons also form background backtracks,

but they are mainly produced in the target.

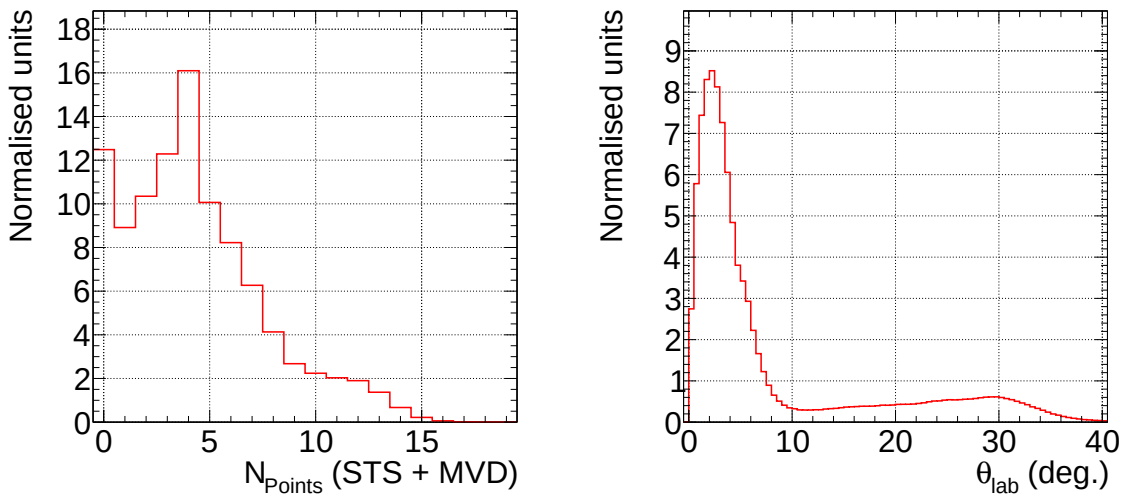

Figure 7.15: Left panel: Number of MC points in MVD + STS tracking system per back-tracked particle produced near the target ($Z_{vertex} < -40\,\text{cm}$). Right panel: Polar angle θ_{lab} (in degrees) of backtracks produced near the target ($Z_{vertex} < -40\,\text{cm}$).

The question then arises as to why the particles originating in the target (or close) do not have any tracks in STS. The characteristics of the backtracks produced near the target ($Z_{vertex} < -40\,\text{cm}$) are shown in the figure 7.15. It is evident from the figure 7.15 (left), 60% of the background backtracks produce less than 5 MC points. The insufficient number of MC points results in the non-trackability of these tracks. The lower number of MC points can be explained by the polar angle of the tracks in the lab frame (see figure 7.15 (right)). Here, most of the particles are emitted outside the CBM global acceptance ($\theta_{lab} \sim 2.5°$ to $25°$).

7.7 Additional variables for reducing background

In order to effectively reduce the number of backtrack candidates originating from background particles, potential supplementary parameters are explored along with the ring-backtrack distance to further improve the separation of conversion-induced Cherenkov rings. Therefore, in the end, all the parameters can be used to train an XGBoost model, whose output will provide a probability metric for each ring that would indicate whether the ring originated from a conversion electron that is not tracked in the STS. One possible option is to use the particle-ID capabilities of the TRD detector in order to identify electron backtracks in particular. As described in the section 7.3, the electron likelihood measure (using a naive Bayes condition) from TRD for the signal and background backtracks is derived and plotted in the figure 7.16 (left). As expected, the electron likelihood (L_e) for the signal backtracks (backtracks caused by a conversion electron, which also caused a ring in the RICH) is higher than those for the background (backtracks that should not point to a Cherenkov ring in the RICH, which mainly consists of hadrons). This

demonstrates the feasibility of utilizing electron likelihood as a separation parameter.

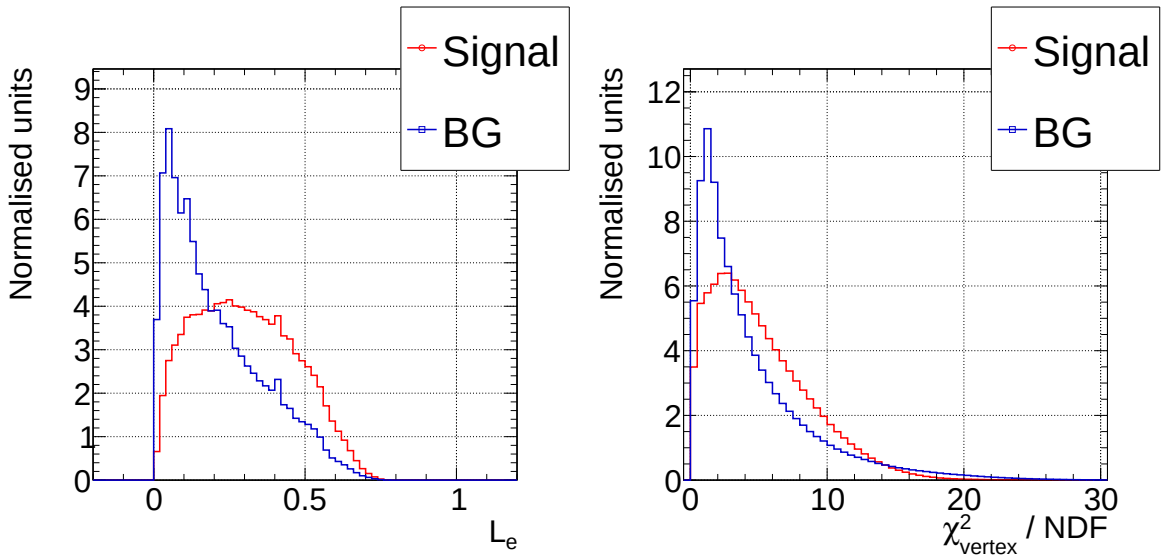

Figure 7.16: Additional parameters for selecting signal backtracks. Left panel: Electron likelihood derived from combining energy loss information from hits of the TRD backtrack (signal and background). Right panel: Goodness of track extrapolation to vertex measure, $\chi^2_{\text{vertex}}/\text{NDF}$, derived by assuming proton mass hypothesis and momentum of 0.6 GeV/c.

From the figures 7.13, 7.14, it is understood that hadrons contribute significantly to the background backtracks, and most of them originate in the target vertex. Utilizing this information, all the backtracks are extrapolated upstream to the vertex and the goodness of vertex fit measure, $\chi^2_{\text{vertex}}/\text{NDF}$, is derived and plotted in the figure 7.16 (right). In order to extrapolate tracks through the magnetic field, a proton mass hypothesis and a momentum of 0.3 GeV/c are assumed (based on the mean value of MC true momentum distribution).

The resultant $\chi^2_{\text{vertex}}/\text{NDF}$ distribution for the background has two contributions. First is from backtracks which originate from the vertex that manifests as a peak closer to zero ($\chi^2_{\text{vertex}}/\text{NDF} < 4.0$). The other is the contribution from the backtracks which have non-target vertices and therefore have large $\chi^2_{\text{vertex}}/\text{NDF}$ (> 15). The signal has a broad uni-modal $\chi^2_{\text{vertex}}/\text{NDF}$ distribution because of the different mass hypothesis and momentum assumptions.

The goodness of the track fit measure χ^2/NDF for the fitted TRD tracklets in both XZ and YZ plane is derived and plotted in the figure 7.17). The figure 7.17 hints that the difference between χ^2/NDF the distribution of signal and background backtracks, although weak, could be used for distinguishing them (using a XGBoost model).

The absolute position of the first hit (at the initial layer of TRD) of the TRD backtrack in polar coordinates is derived as radial position $R = \sqrt{x_{hit}^2 + y_{hit}^2}$ and polar angle $\theta = \tan^{-1}(\frac{y_{hit}}{x_{hit}})$ where (x_{hit}, y_{hit}) is the position coordinate of the first hit in backtrack. The derived absolute position distributions for signal and background are plotted in the figure 7.18. The distribution of radial distances between signal tracks and background exhibits distinguishable characterist-

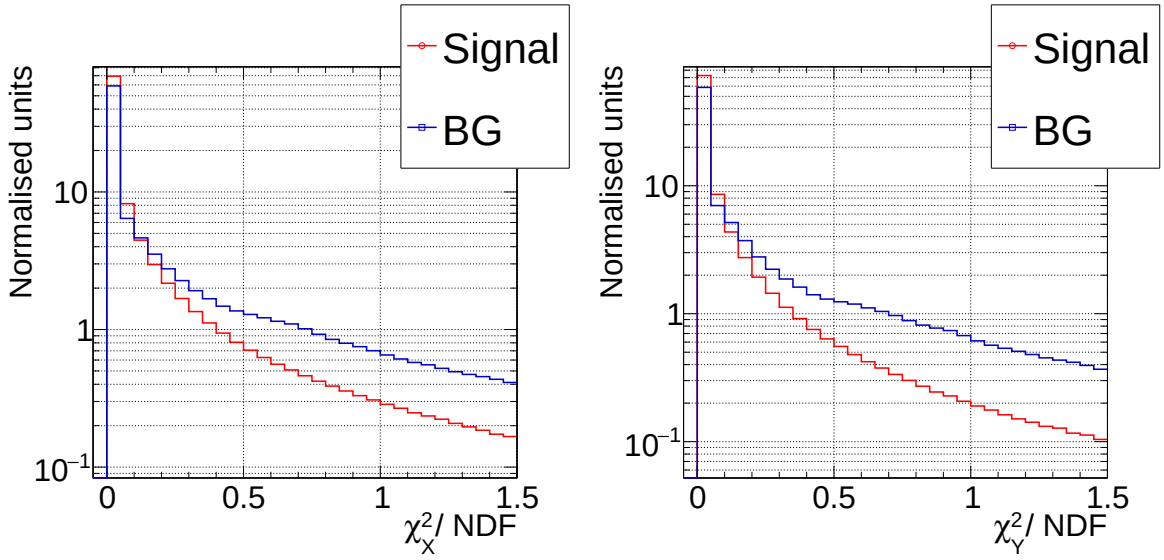

Figure 7.17: Goodness of track fit measure, χ^2/NDF for the fitted TRD tracklets in XZ plane and YZ plane for both signal and background backtracks.

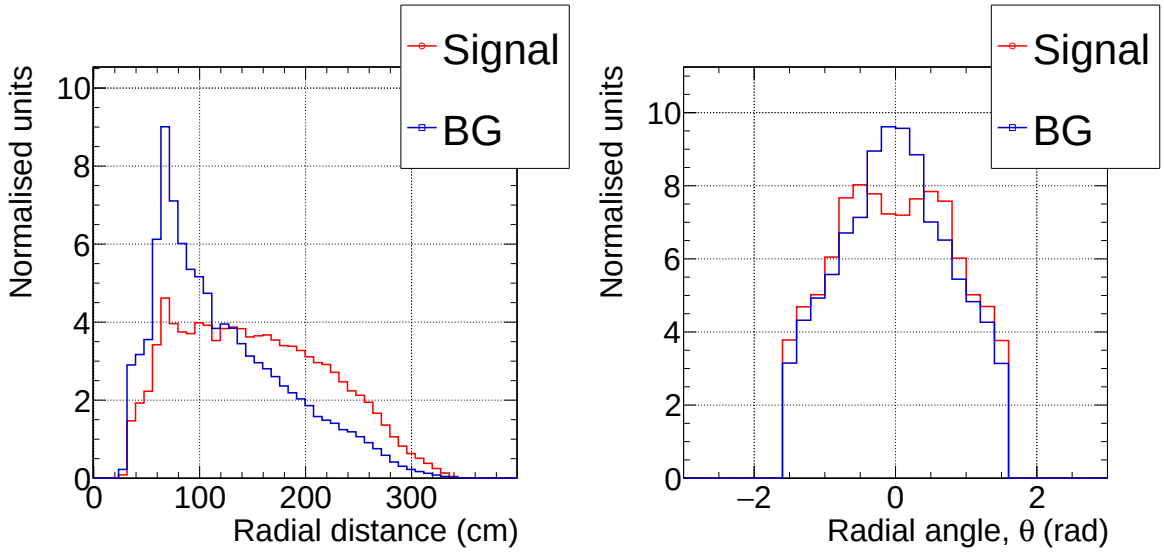

Figure 7.18: Absolute position of the first hit of backtracks for both signal and background in polar coordinates (radial distance (left) and polar angle (right)).

ics. Figure 7.18 (left) shows that the background tracks are closer to the beam pipe (smaller distance), while the signal tracks are spread out mostly in the inner parts of TRD. The distribution of the track polar angle (see figure 7.18 (right)) for signal resembles that of the background for angles greater than 0.8 rad, however, they exhibit different characteristics at lower angles. It is probably because the signal backtracks are electrons and positrons, which are deflected horizontally by the B-field more than the hadrons in the background backtracks sample. Thus, both the radial position (distance) and the polar angle can be used as additional variables for separating signals from the background.

7.8 RICH as secondary timer

A Time-of-Flight measurement between the RICH and TOF can be accomplished by extrapolating the TRD backtracks to the TOF. This facilitates the reduction of significant background hadrons (using velocity distribution), as well as the reduction of fake tracks due to combinatorics for TRD tracklets with two hits.

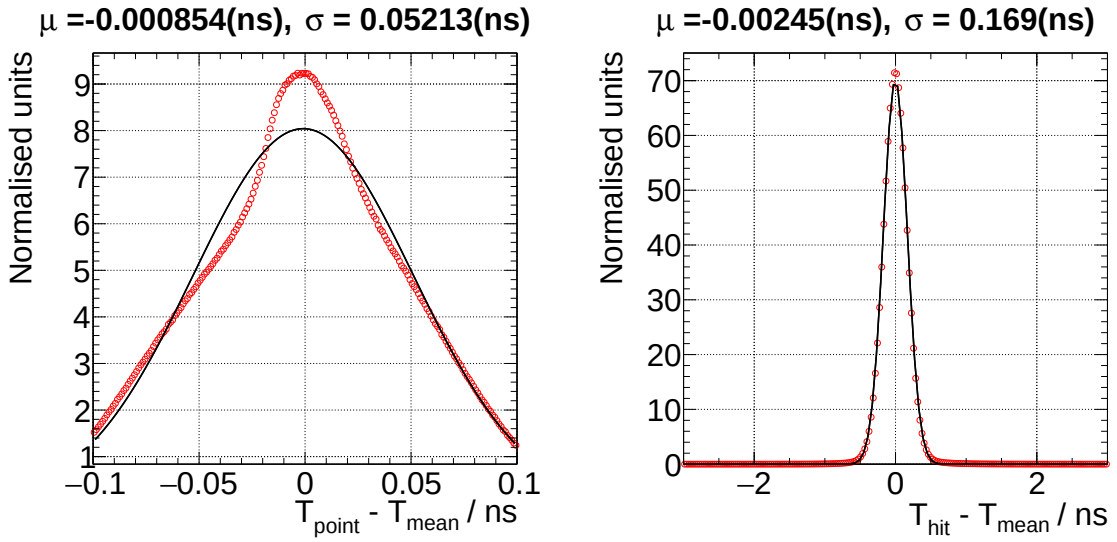

Figure 7.19: Left panel: Arrival time of all Cherenkov photons of a ring with respect to the mean arrival time. The resultant distribution is fitted with a Gaussian profile (black) and the σ of the distribution is estimated to be 52 ps. Right panel: Hit time deviation with respect to the mean time of the ring. The distribution is fitted with a Gaussian profile (black) and the σ of the distribution is estimated to be 169 ps.

The CBM TOF has a timing precision in the order of $\sigma \sim 60$ ps. A RICH hit time precision depends on the Transit Time Spread (TTS) of the photoelectrons in the MAPMT and the timing precision of the FEB. The TTS of the Hamamatsu H12700 MAPMTs is 350 ps FWHM [107]. Assuming a Gaussian distribution for the transit time, the standard deviation is hence $\sigma_{TTS} = 149$ ps. The timing precision of the FEB is found as $\sigma_{LE} \approx 22$ ps (see chapter 4, section 4.6). Therefore, the theoretical hit time spread should be $\sigma_{hit} = \sqrt{\sigma_{TTS}^2 + \sigma_{LE}^2} = 150$ ps[2]. These precision values are only feasible after very careful calibration, including walk correction of the timing signal; hence, for the safety margin in the simulation an additional 3% spread is assumed ($\sigma_{hit} = 155$ ps). Generation of Cherenkov photons in a medium is an immediate effect, with negligible timing uncertainty. The average time stamp of hits within a Cherenkov ring depends on the arrival time of all Cherenkov photons of that ring due to individual variations in the photon path length and the individual hit time spread from the measurement. The arrival time distribution of the Cherenkov photons within the same ring with respect to the ring time (average time of all hits in a ring) is given in figure 7.19 (left), which shows that the arrival time spread of Cherenkov photons in a ring is about 52 ps. The reconstructed hit time deviation

[2] the estimated single pixel timing precision in HADES is in the order of 192 ps [105].

to the mean time of the ring is plotted in the figure 7.19 (right). The mean reconstructed hit time spread within the ring is about 169 ps. This is because the arrival time of the Cherenkov photons is smeared with a Gaussian profile with a mean time of 155 ps to resemble the realistic timing precision. From the figure 7.19, it can be seen that the hit time spread is the dominating contribution to the ring mean time (t_{ring}). This exceptional timing resolution allows RICH to be used as a secondary timer.

For application of RICH timing information within the backtracking algorithm, the TRD tracklet is matched both to a Cherenkov ring in the RICH and to a hit in the TOF detector. The time and the position of the matched ring are found (t_{ring}, $\vec{r}_{\text{ring}}$) and the spatial distance between the Cherenkov ring and the interception point of the originating photon reflected on the mirror is measured, $d_{\text{ring-mirror}} = \|\vec{r}_{\text{mirror}} - \vec{r}_{\text{ring}}\|$. Next, the TOF hits are matched to the track, and the time and position of the attached most downstream TOF hit are measured (t_{TOF}, $\vec{r}_{\text{TOF}}$). Finally, the distance between the mirror and the TOF hit is measured $d_{\text{mirror-TOF}} = \|\vec{r}_{\text{TOF}} - \vec{r}_{\text{mirror}}\|$. The velocity fraction β is then given by

$$\beta = \frac{d_{\text{mirror-TOF}}}{t_{\text{TOF}} - t_{\text{ring}} + \frac{d_{\text{ring-mirror}}}{c}} / c \ . \tag{7.1}$$

The derived β for the signal and background backtracks are plotted in the figure 7.20. It can be seen that most of the signal tracks (being leptons) have $\beta \approx 1$. The hadronic component of the background backtracks has a broader distribution, with $\beta < 1$. Due to the abundance of (conversion) electrons also in the background sample, the background distribution also shows a peak at $\beta \approx 1$. [3] The estimated β^2 can thus be used as an additional parameter in discriminating electron/positron-induced backtracks from background tracks. As an alternative to utilizing RICH and TOF for time-of-flight computation, it is possible to assume that the tracks originate from the target. In this case, the T0 event time ($\sigma_{T0} \approx 60$ ps) could be used in conjunction with the TOF detector information to calculate a time of flight, providing a longer flight path and potentially better TOF precision. In this case, the estimation of the length of tracks under the influence of a magnetic field requires calculation of the momentum and charge of the tracks, which is not possible in this case. Using the T0 counter as a start time can be beneficial for the signal electrons that come from photon conversion after STS (not being affected by the magnetic field). Here, the backtracks can be seen as straight lines to the target because photons are not affected by the magnetic field. Regardless, the RICH-TOF timer acts as an independent measurement with the fewest assumptions and hence is used for further analysis.

[3] Both lepton peaks in the signal- and in the background distribution peak at beta slightly larger than one. This can be attributed to multiple factors, including the time difference between the track traveling to the mirror and Cherenkov photons reaching the mirror, $\sigma_T(TOF)$, and ring mean time assumption. Employing corrections to the time offsets could only improve the β estimation by shifting the distributions to a physical regime with a peak around one.

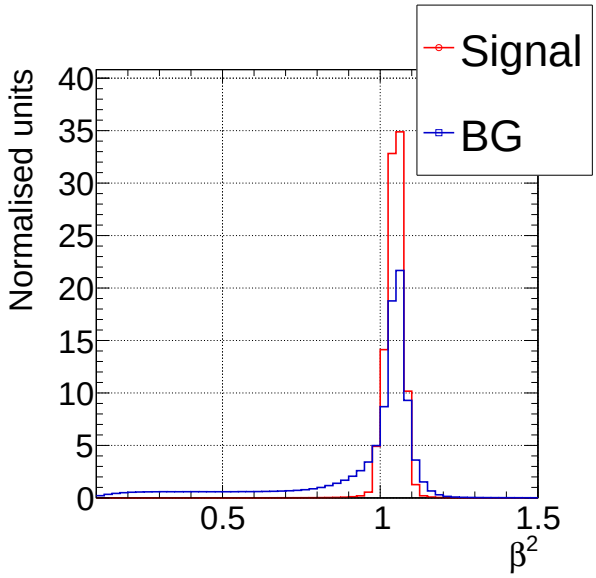

Figure 7.20: Velocity of the signal and background backtrack derived by using the RICH-TOF timer.

7.9 Machine Learning model for tagging the RICH rings

In the previous subchapters, the following variables have been identified to be effective in distinguishing signal from background in the set of backtracks: ring-backtrack distances $(\delta x, \delta y)$, absolute position of the TRD tracklet in polar coordinates (radial distance, radial angle), goodness of track-fit metrics (χ^2/NDF(X), χ^2/NDF(Y)), electron likelihood from TRD (L_e), goodness of vertex fit metric (χ^2_{vertex}/NDF), and velocity (β^2). The linear correlations between pairs of input

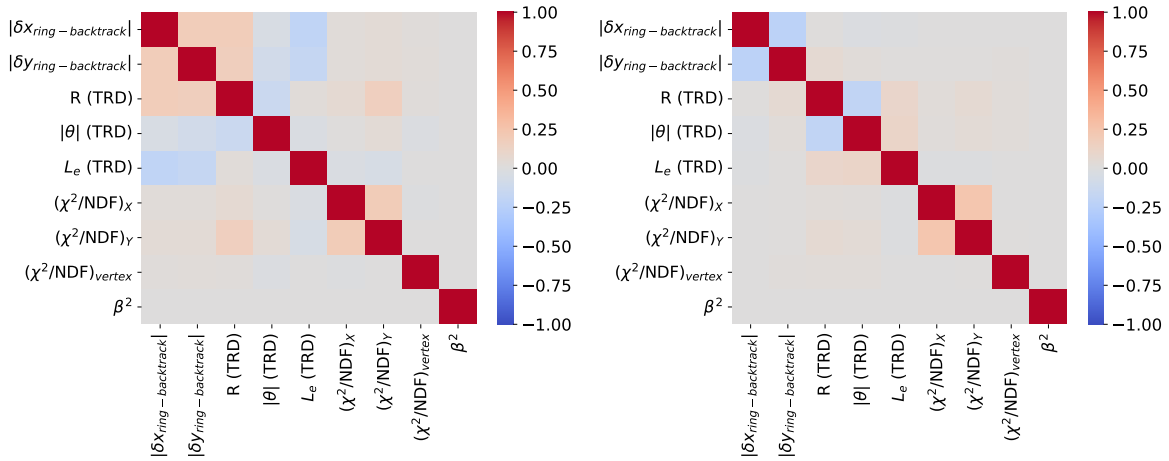

Figure 7.21: The Pearson correlation table depicts the linear correlation between various inputs to the ML model for separating signal and background backtracks. The left panel depicts the correlation matrix for signals, whereas the right panel depicts the background backtracks within the embedded omega sample. Here, R (TRD) is the radial position (distance), and θ (TRD) refers to the polar angle of the absolute position of the backtrack in TRD.

variables for signal and background backtracks are calculated by using the Pearson correlation metric, and plotted in figure 7.21. Absolute values of ring-backtrack distances $(\delta x, \delta y)$ and polar

angles of absolute position in TRD are used to calculate linear correlations because these are symmetric distributions. For the signal tracks, positive correlations are observed between the absolute ring-backtrack distances $(\delta x, \delta y)$. Similarly, a positive correlation is observed between absolute ring-backtrack distance in X and Y and the radial position in TRD. This can be attributed to the typical low momentum characteristics of the signals. Due to the residual magnetic field after STS, the low-momentum signal tracks are bent by larger angles, which results in a larger radial position in TRD. Furthermore, low-momentum tracks have a large spread in the ring-backtrack matching (as seen in chapter 6 section 6.6) due to multiple scattering, and hence they are positively correlated. The same argument follows for the negative correlation between ring-backtrack and electron likelihood, as low momentum signal tracks have less electron likelihood and a large spread in ring track distances. The velocity has the least correlation with all other variables for signal tracks. However, the linear correlation between the variables is weaker for the background tracks than for the signal tracks. As all the identified variables exhibit at least partial correlations with other variables, they can be utilized as inputs to a machine learning model.

In order to effectively use all the variables for efficient reduction of background, an XGBoost ML model is developed. A balanced dataset of 800×10^3 signal and background samples is used to train the model. All the hyperparameters of the model are optimized using a Bayesian optimization procedure. The results of the training dataset are shown in appendix A.4.2. The

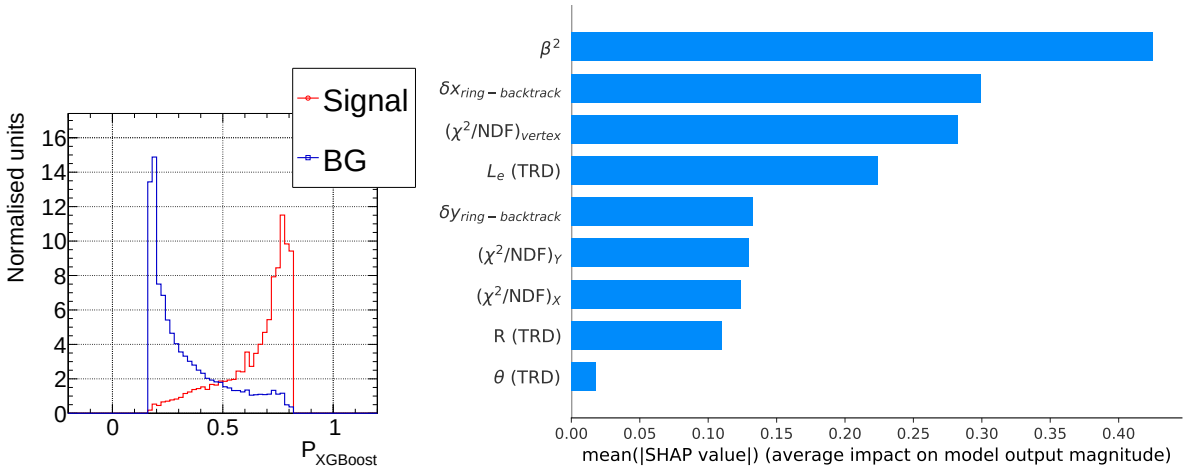

Figure 7.22: Left panel: Response from the XGBoost ML model for separating signal and background backtracks. Right panel: Relative input variable importance chart measured by the SHAP metric. Here, R (TRD) is the radial position (distance), and θ (TRD) refers to the polar angle of the absolute position of the backtrack in TRD.

trained model is tested on the full embedded omega dataset 5.2 and the response from the model is plotted in figure 7.22 (left). The model's output distribution ($P_{XGBoost}$) shows a clear distinction between the signal backtracks (caused by conversion electrons with corresponding rings in RICH) and the background backtracks (causing no rings in RICH).

The relative impact of different variables on the model performance is estimated using the SHAP metric and is plotted in figure 7.22 (right). As expected, velocity has the largest impact

on model prediction because it helps to reduce the substantial hadron background. Velocity as the most significant input is followed by the ring-backtrack distance along X $\delta x_{ring-backtrack}$. The influence of the $\delta x_{ring-backtrack}$ is higher than $\delta y_{ring-backtrack}$ because of the better ring-backtrack matching performance (see figure 7.12), which is the result of better spatial resolution of the hits in TRD along X compared to Y (see chapter 6, section 6.6). The χ^2_{vertex}/NDF feature has a larger influence as well, since distinguishable distributions are observed for the signal backtracks and background backtracks (see figure 7.16). As anticipated from the figure 7.18, the radial distance component of the absolute position of TRD tracks exhibits a greater influence in comparison to its corresponding polar angle. The goodness of TRD track fit measures, χ^2/NDF have an identical impact on the model performance. Since all input features have an impact on model performance, it is not necessary to further reduce the dimensions of the model.

The signal backtracks, and the electron component of the background backtracks stem from photon conversion in the detector material. The probability of pair production varies and is proportional to $\log E_\gamma$. Since most of the gammas arise from decays of π^0 mesons, their energy depends on the boost of the system. Hence, the probability of photon conversion depends on the collision energy. This might alter some of the distributions of observables used as input features in the proposed ML model. At the same time, the significant hadronic component of the background backtracks appears because they are not trackable by the STS+MVD tracking system (due to the topology of the CBM detector). Hence, here except for their multiplicity per event, the characteristics of the tracks (input features) are least influenced by the collision energy. Therefore, this trained model can be repurposed for systems with comparable collision energies. However, for very low collision energies, this model has to be retrained.

7.10 Including the XGBoost response into the RICH electron identifier models

From the previous section, it is understood that rings can be tagged with a probability metric that indicates whether the ring might belong to a conversion electron. In this case, the ring will have no correlated track candidate in STS and consequently should also not be considered in the standard track-to-ring matching procedure in order to avoid misidentification of arbitrary tracks as electrons. In this regard, the backtracking procedure described in previous sections is performed before matching any STS tracklets. This yields a set of backtrack projections for rings in RICH. The backtrack with the highest $P_{XGBoost}$ value will be chosen as the matched backtrack to that ring. Assuming the ring i has $N^k_{backtracks}$ backtrack projections, then the conversion probability for the ring is assigned as,

$$P^i_{conversion} = \max\ (P^{ik}_{XGBoost}), k = 0, ..., N^k_{backtracks}. \tag{7.2}$$

For rings without backtrack projections, a value of zero is assigned, since such rings have a very high probability of being caused by an electron originating directly from the target. Conversion probability is therefore added as an additional feature for a ring along with other ring features.

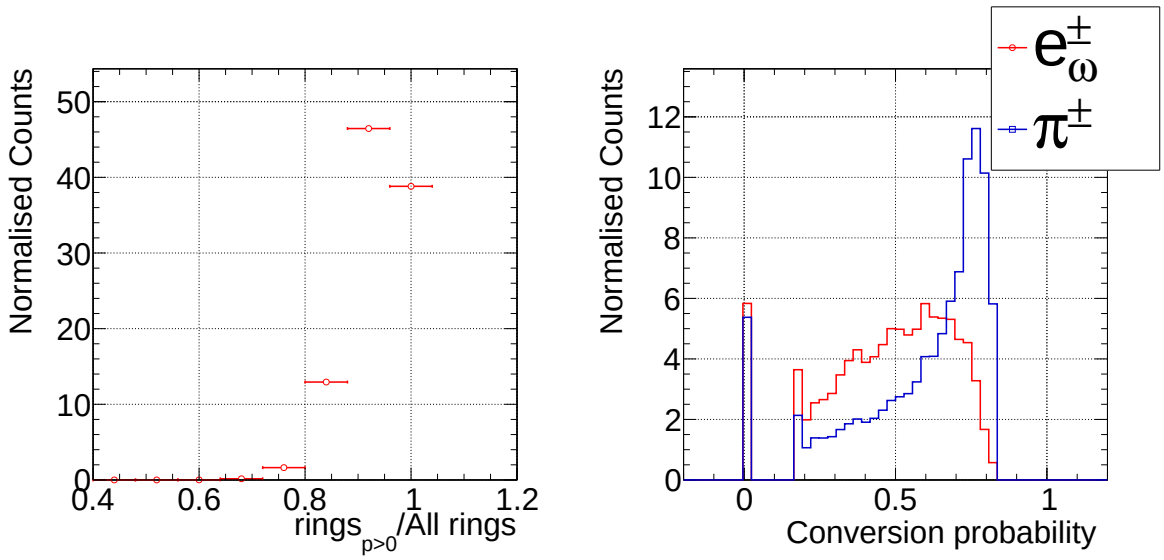

Figure 7.23: Left panel: Proportion of rings per event assigned with a conversion probability greater than zero. Right panel: Distributions of conversion probabilities assigned to rings that are matched to pions and primary electrons from omega decay.

Figure 7.23 (left) shows the proportion of rings per event that can be mapped using backtracks. It can be inferred from the figure 7.23 (left) that in almost 40% of all events, all rings in the RICH can be assigned a conversion probability value greater than zero, and in another almost 45% of all events, almost 90% of all rings have an associated conversion probability value greater than zero. It is evident that, consistently, more than 80% of all the rings are mapped with a conversion probability greater than zero for more than 95% of all events.

Subsequently, the STS tracks are matched with the rings using the closest distance method. The applied conversion probability distribution for the ring-matched ($\delta d < 10\,\text{cm}$) primary electrons and pions are shown in the figure 7.23 (right). It is apparent that the pions are matched to rings with a larger conversion probability compared to primary electrons. Therefore, these distinguishable characteristics can be used as additional information for the forward ML model for separating primary electrons and pions.

For the embedded omega dataset (see table 5.2), the linear correlations between the conversion probability metric and other input variables to the forward ML model for primary electrons and pions are calculated by using the Pearson correlation metric and plotted in the figure 7.24. The matching of both primary electrons and pions to a conversion ring is purely a random process. Furthermore, the conversion probability is determined independently without utilizing any of the ring parameters. Hence, the reason for correlations that arise between the conversion probability variable and other input features cannot be intuitively established. The figure 7.24 highlights the lack of strong correlation between the conversion probability and any other variable, allowing it to be used as an additional input parameter to the forward machine learning model.

As outlined in the preceding chapter 6, it is necessary to have two distinct XGBoost models (variant 2, variant 3) for the forward electron identifier. One for the STS tracks that are also

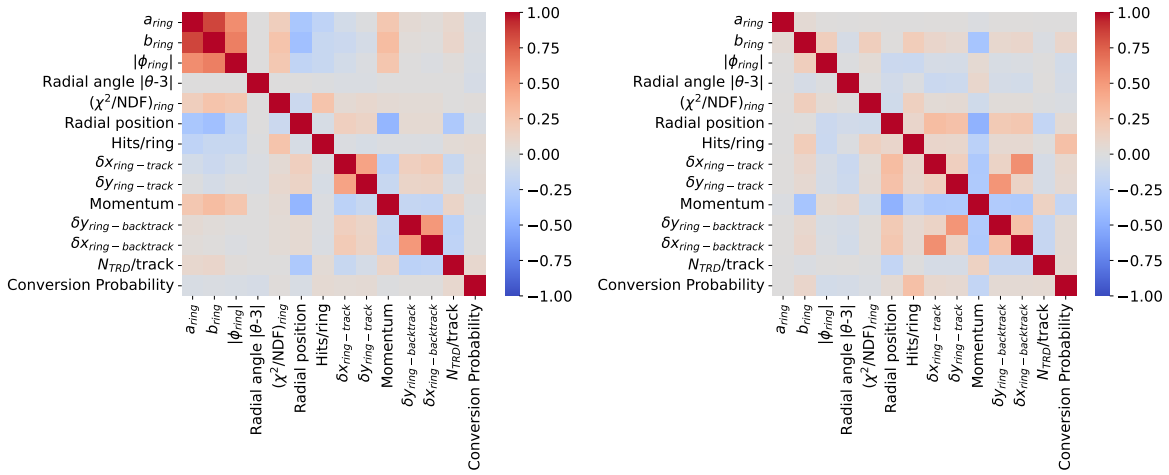

Figure 7.24: The Pearson correlation table depicts the linear correlation between various inputs to the upgraded ML model after inclusion of the conversion probability metric for both electrons (left panel) and pions (right panel) in the embedded omega sample.

detected in TRD (with at least 2 TRD hits), and one for the STS tracks that do not leave a trace in the TRD detector. In a similar manner, two XGBoost models are developed for STS tracks with and without associated hits in the TRD, and the conversion probability variable is incorporated into both models (variant 4, variant 5). The summary of the models trained with and without the conversion probability is shown in the table 7.1.

Table 7.1: Table displaying different variants of XGBoost developed in this chapter, with the input features used to train these models. The following input features are common for all models : $\{a_{ring},\ b_{ring},\ \phi_{ring}$, absolute ring position in polar co-ordinates (R, θ), hits/ring, ring-fit quality metric χ^2/NDF, Momentum$\}$ labelled "common input features". Note: δq represent the ring-track distance measure q, where $q = \{x,\ y,\ d\ (d = \sqrt{x^2 + y^2})\}$.

XGBoost model	Label	Input features				
		Common	δd (STS)	$\delta x, \delta y$ (STS)	$\delta x, \delta y$, N_{hits} (TRD)	P_{conv}
Variant 1	δd	✓	✓			
Variant 2	$\{\delta x, \delta y\}$	✓		✓		
Variant 3	$\{\delta x, \delta y\}$ $+\{\delta x_{BT}, \delta y_{BT}\}$	✓		✓	✓	
Variant 4	$\{\delta x, \delta y\}$ $+P_{conv}$	✓		✓		✓
Variant 5	$\{\delta x, \delta y\}$ $+\{\delta x_{BT}, \delta y_{BT}\}$ $+P_{conv}$	✓		✓	✓	✓

Both XGBoost models are trained using a balanced set of primary electrons and pions with uniform momentum distribution (see chapter 6, section 6.2) derived from the embedded electron sample (see table 5.2). All the hyperparameters of the model are optimized using the Bayesian

optimization method. The responses of the two upgraded XGBoost models (variant 4, variant 5) to the training data set can be found in the appendix A.4.3, A.4.4.

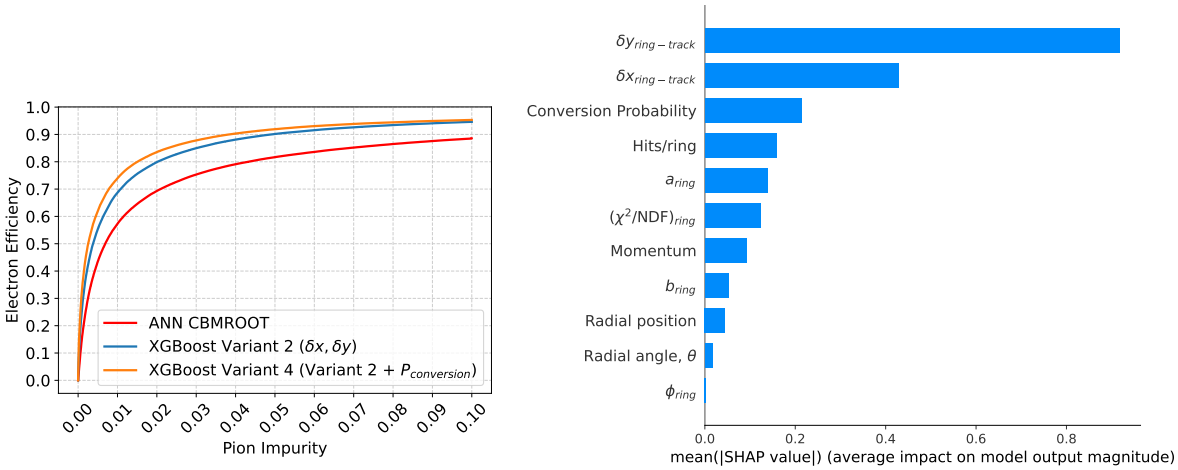

Figure 7.25: Response from the ML model with only RICH and including the conversion probability metric. Left panel: ROC curve depicting the reduced pion impurity for the same electron identification efficiency, resulting from the inclusion of the conversion probability metric. Right panel: Relative input variable importance chart measured by the SHAP metric.

The upgraded XGBoost model trained with the inclusion of the conversion probability for the STS tracks without associated hits in the TRD (variant 4) is tested on the embedded omega sample, and the results are plotted in figure 7.25. It is evident from the ROC response (see figure 7.25 (left)) that the inclusion of the conversion probability significantly enhances the performance of the model with regard to suppression of pions compared to the base XGBoost model trained with the same input features without the conversion probability (variant 2). The model enhanced with the inclusion of conversion probability outperforms the model without it by a significant 33% in terms of its pion suppression capability, while maintaining a comparable electron identification efficiency of 80%. The relative impact of different input features is calculated by using the SHAP metric and plotted in the figure 7.25 (right). It can be seen that, after the ring-track distance, the conversion probability has the most impact on model performance.

Another upgraded XGBoost model trained with TRD backtracking variables and conversion probability for the STS tracks with at least 2 associated TRD hits (variant 5) was tested on the embedded omega dataset 5.2, and the response from the model is plotted in the figure 7.26. It can be inferred from the ROC response curve that the XGBoost model that utilizes the conversion probability variable (variant 5) exhibits enhanced pion reduction capability for electron identification efficiencies above 40% compared to the model trained with the same input features as variant 5 but without the conversion probability (variant 3) trained without this feature. For 80% electron identification efficiency, the model trained with conversion probability (variant 5) outperforms the model trained without it (variant 3) by 20% in terms of pion reduction capability. The relative contribution of each of the input features to the model performance is calculated by using the SHAP metric and plotted in the figure 7.26 (right). It can be seen that, after the ring-track distances and ring-backtrack distances, the conversion probability has the

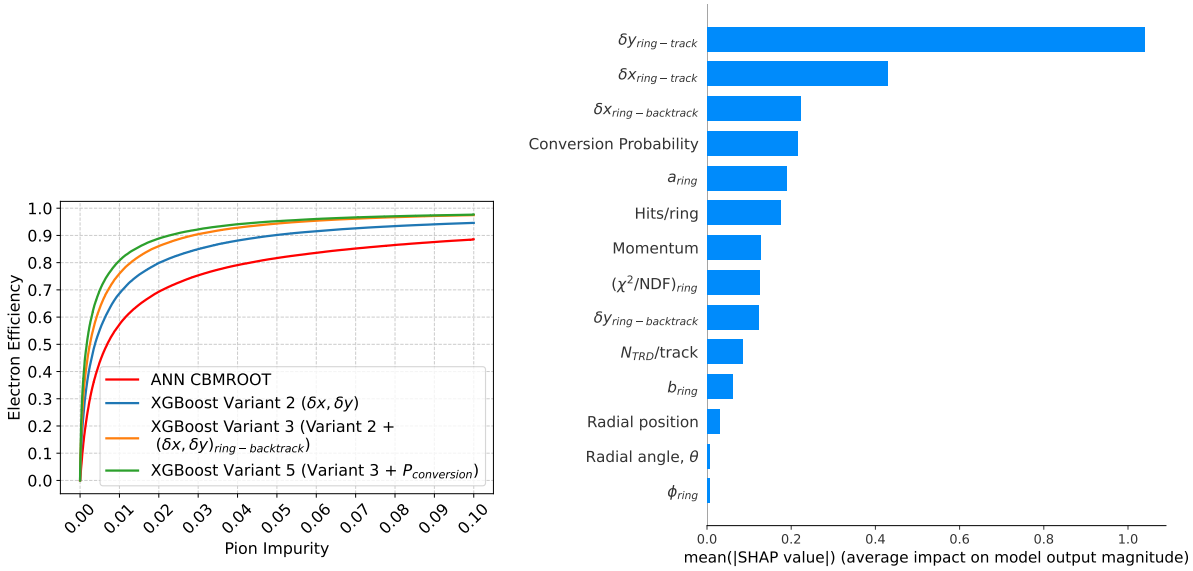

Figure 7.26: Response from the ML model with RICH, TRD distance measure, and conversion probability metric. Left panel: ROC curve depicting the reduced pion impurity for the same electron identification efficiency, resulting from the inclusion of the conversion probability metric. Right panel: Relative input variable importance chart measured by the SHAP metric.

most impact on model performance. The relative importance of a few of the ring parameters has decreased compared to the previous trained XGBoost models (Chapter 6, section 6.8). This is expected because by adding more variables with strong separation power, weaker features will have less relative impact.

8

Reconstruction of omega mesons

This chapter discusses the adoption of the XGBoost-based models that were developed in previous chapters into the CBMROOT framework. The response of the XGBoost models for the complete UrQMD dataset with embedded omega decays is explored. Furthermore, the application of the developed ML models to the reconstruction of omega mesons is presented. In the concluding sections, the enhanced performance of the developed XGBoost models in comparison to the conventional ANN in CBMROOT is exemplified.

8.1 Implementing XGBoost models into CBMROOT

The CBMROOT is a C++ based software architecture. Despite the availability of an XGBoost implementation in C/C++, the essential packages required for hyperparameter optimization are not widely available for C++. Therefore, for all development purposes, Python is used. Hence, the training and testing data is imported in a TTree format from the CBMROOT framework. The imported TTree is read out in a Python environment by using a compatible PyROOT package and is then converted into data frames (tabular data format for easy use with the ML model). The compiled data frames can then be used with the machine learning tools, such as PyTorch, TensorFlow, Keras, and XGBoost. The development of XGBoost models, using a Python framework, was discussed in the previous chapters. The trained and tested XGBoost models have to be implemented in the CBMROOT framework as part of the standard reconstruction routine. For this conversion, the Open Neural Network Exchange (ONNX) package is used. The ONNX package is used to convert developed models into a format that is compatible with different platforms [138]. All the XGBoost models developed are converted to ONNX format, and the converted model is then imported into CBMROOT-compatible FAIRSOFT-v18.

The conventional ANN used as standard in CBMROOT RICH reconstruction is trained based on the following observables: $\{a_{ring},\ b_{ring},\ \phi_{ring}$, absolute ring position in polar coordinates (R, θ), hits/ring, χ^2/NDF from ring fit, $\delta d_{ring-track}$, momentum$\}$. As described in the previous chapter, the conventional ANN model is replaced with different XGBoost models. The first variant is trained on the same input features, including the ring-track distance (δd). A first improvement is obtained by introducing differential ring-track distances ($\delta x, \delta y$) replacing the ring-track distance ($\delta d = \sqrt{\delta x^2 + \delta y^2}$), owing to the fact that the precision in track extrapolation is different for the vertical and horizontal planes (due to the magnetic field). In addition to the ring-track distance from STS track forward propagation, the local track-fit within the 4 layers of the TRD detector can be back propagated to the RICH, adding the ring-backtrack distance as another, independent observable. Therefore, the third variant of the XGBoost model is trained with the same parameters as the second, but adding the ring-backtrack distances and number of TRD hits in addition: $((\delta x, \delta y) + (\delta x_{BT}, \delta y_{BT}),\ N_{hits}\ (TRD))$. Following the implementation of the new conversion probability observable for the rings, the fourth XGBoost variant is trained with the same input features as the second variant, but now adding conversion probability as an additional parameter: $((\delta x, \delta y) + P_{conv})$. A fifth, final variant is trained with the same input features as the third, but again adding the additional conversion probability metric on top: $((\delta x, \delta y) + (\delta x_{BT}, \delta y_{BT}),\ N_{hits}\ (TRD) + P_{conv})$. A summary of the models is provided in the table 7.1. The response of the XGBoost models (as a measure of probability for the track to be an electron) to the embedded omega data sample for electrons and pions is shown in figure 8.1. Output of the XGBoost models ranges from 0 to 1. The output distribution shows a complementary behavior between electrons and pions for all models.

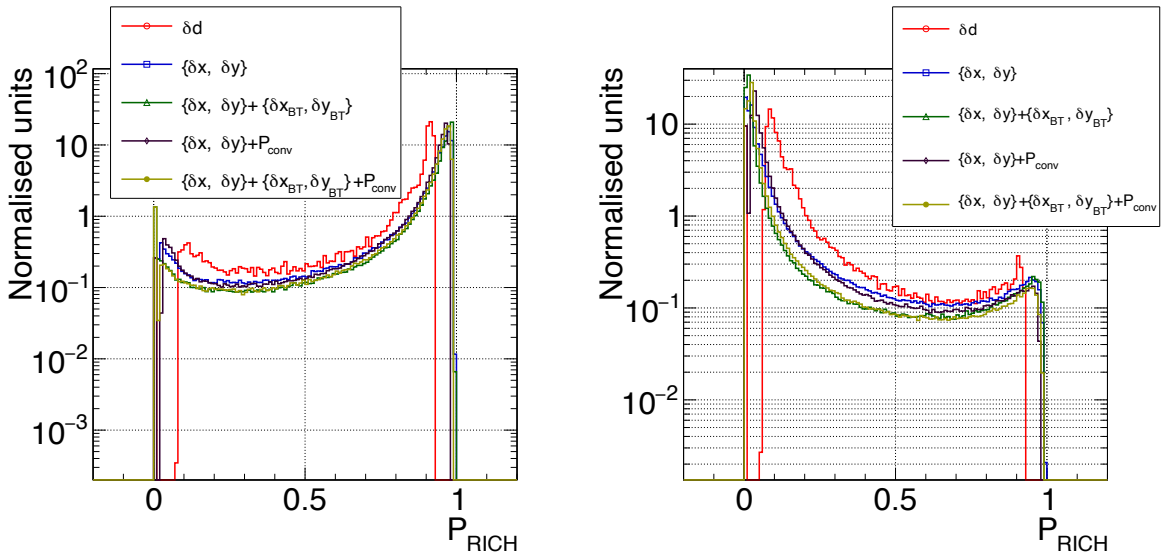

Figure 8.1: Left panel: Response from the different XGBoost models to primary electrons (left) and pions (right) in the embedded omega dataset (see table 5.2). Different lines represent the response from XGBoost models trained with different input features. The red line (δd) shows the upgrade of the ANN with XGBoost as reference, with the same input features as in the standard ANN. The blue line shows the response of the XGBoost model with differential ring-track distance δx, δy and the black line represents the response of the XGBoost model adding additional conversion probability P_{conv}. The green line represents the response of the XGBoost model with differential ring-track distances δx, δy and adding TRD backtracked ring-track distance δx_{BT}, δy_{BT} and number of hits in TRD, and the light-green line represents the XGBoost response with additional conversion probability P_{conv}.

8.2 Electron candidate selection for omega meson reconstruction

For the di-electron reconstruction with sufficient hadron suppression, the combination of RICH, TRD, and TOF is used for electron candidate selection. A track is accepted as TRD electron if the number of TRD hits is greater than 1 and if the electron likelihood is greater than 0.4 ($N_{hits}^{TRD} \geq 2,\ L_e(TRD) > 0.4$). Furthermore, a track is accepted as a TOF electron if the calculated squared mass is less than 0.1 $\mathrm{GeV^2/c^2}$ ($M^2 < 0.1$). For RICH electron identification, the electron identifiers based on conventional ANN and XGBoost models trained with different input features are used (see section 8.1). The purpose of this simulation is to understand the impact of different XGBoost-based electron identifiers on the final omega meson reconstruction. Different efficiency is achieved by imposing different cuts on the output of the ANN and XGBoost models ($P_{RICH} > P_{thr}$). In order to achieve this, track selection is made based on different RICH efficiency measures as defined in the equation,

$$E_{\mathrm{RICH}} = \frac{\text{Number of primary electrons identified as Electrons}}{\text{Number of tracks with } N_{hits}^{RICH} \geq 7}. \tag{8.1}$$

The efficiency of RICH is subsequently translated into global efficiency (RICH+TRD+TOF)

and the corresponding $\pi^{\pm}$ suppression factor is calculated using the equations,

$$\text{Efficiency} = \frac{\text{Number of primary electrons identified as Electrons}}{\text{Number of tracks with global acceptance}}, \tag{8.2}$$

$$\text{Global acceptance} = N_{hits}^{RICH} \geq 7 \;\&\; P_{RICH} > P_{Thr} \;\& \tag{8.3}$$

$$N_{hits}^{TRD} \geq 2 \;\&\; L_{e}^{TRD} \geq 0.4 \;\; \& \; N_{hits}^{TOF} \geq 1 \;\&\; M^2 \leq 0.1, \tag{8.4}$$

$$\text{Pion suppression} = \frac{\text{Total number of reconstructed pion tracks}}{\text{Pions mis-id as electrons}}. \tag{8.5}$$

The resulting pion suppression factors for different efficiencies are plotted in figure 8.2. From the

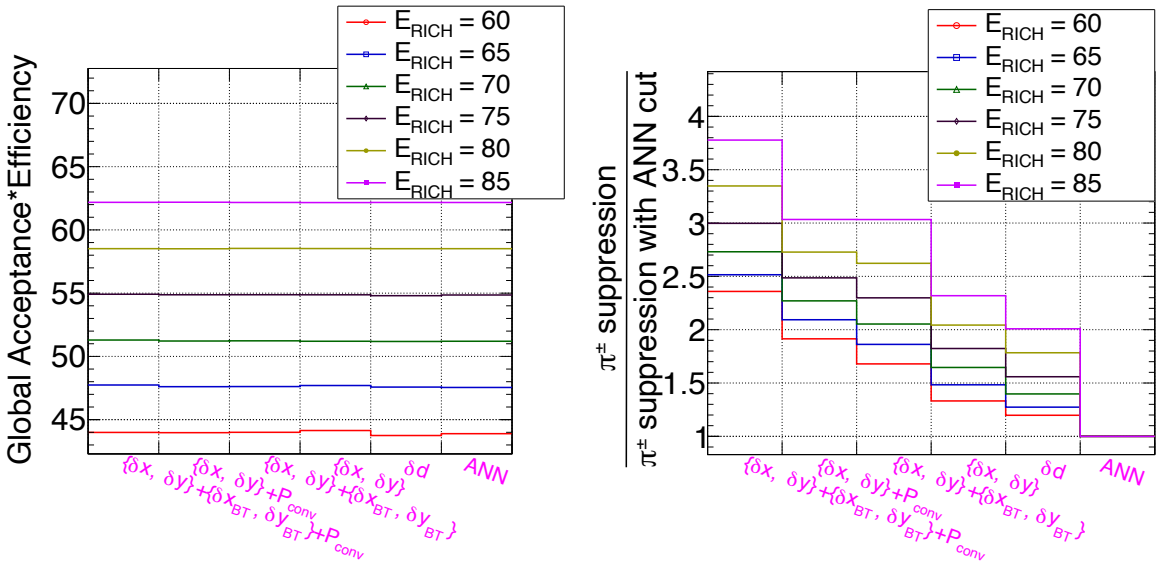

Figure 8.2: Left panel: Global acceptance × efficiency (reconstruction and identification) for primary electrons defined for different reconstruction efficiency in RICH. Right panel: Pion suppression obtained for different XGBoost models normalized with pion suppression with RICH ANN cut defined in the equation 8.2.

figure 8.2, it can be observed that the XGBoost-based identifiers perform better compared to the conventional ANN in terms of the pion suppression capability for the same electron identification efficiencies. Furthermore, it is evident that the XGBoost model (δd) trained with the same input features as the conventional ANN in CBMROOT has twofold pion rejection capability for 85% electron efficiency as compared to the conventional ANN. The XGBoost model (δd) exhibits a minimum of 30% greater performance than the conventional ANN in terms of $\pi^{\pm}$ suppression ability for all electron efficiencies. The XGBoost model trained with differential ring-track distance ($\delta x,\ \delta y$) has 10%-20% better pion rejection capability compared to the base XGBoost model (δd) for electron efficiencies. With the inclusion of the TRD-backtracked distance measures $((\delta x, \delta y) + (\delta x_{BT}, \delta y_{BT}))$ as additional input features, the XGBoost model performs better than the base XGBoost model (δd) by two folds for higher efficiencies and by at least 60% for the lower efficiencies. Furthermore, the models trained with the addition of the conversion probability metric (P_{conv}) have enhanced performances compared to the base models trained without it. The final improved variant of the XGBoost model trained with input features including the differential ring-track distances, TRD-backtracked ring-track distances, and the conversion probability $((\delta x, \delta y) + (\delta x_{BT}, \delta y_{BT}) + P_{conv})$ outperforms the base XGBoost

model (δd) by 50%-80% in terms of the pion rejection capability for higher electron identification efficiencies and outperforms the conventional ANN in CBMROOT by a factor of 3-3.8 times in terms of the pion rejection capability for higher electron efficiencies. All of the above models are further analyzed to determine their performance in the reconstruction of omega mesons.

8.3 Topological cuts on candidate tracks

The e^+, e^- candidates for the reconstruction of the omega mesons are selected based on the output of the different electron identifiers for RICH in combination with the TRD and TOF information (discussed in the section 8.2). A significant background in the selection of the omega electron sample is expected to stem from trackable electrons produced by photon conversion in the detector material. Hence, topological criteria are explored in addition to previously discussed machine learning based electron identification schemes for reducing background conversion electrons.

Electrons arising from off-vertex photon conversions can be partially eliminated, by checking a target-origin hypothesis during track fitting. This hypothesis is evaluated by first extrapolating the track to the collision vertex and then calculating the deviation of the extrapolated track projection from the collision vertex normalized to the corresponding variances in the vertex estimation. This normalized deviation is quantified by a goodness-of-fit measure χ^2_{vertex}. In order to find an optimal selection cut for the globally accepted tracks, χ^2_{vertex} for electrons explicitly stemming from omega mesons, for electrons stemming from other sources, and χ^2_{vertex} for all other particles (as reference) are calculated and plotted in figure 8.3 (left). It can be inferred from figure 8.3 (left), that the electrons from the omega decay exhibit a very similar distribution of χ^2_{vertex}, as observed for all particles. This is expected, since both the electrons from omega decays as well as most of the other particles originate from the collision vertex. However, the χ^2_{vertex} distribution for the other, non-omega electrons consists of two parts: a primary vertex contribution (lower values of χ^2_{vertex}), and an off-vertex contribution (higher values of χ^2_{vertex}) due to off-vertex photon conversion. Hence, in order to eliminate the off-vertex contribution, a criterion $\chi^2_{vertex} < 3$ is imposed during electron selection.

The objective of the χ^2_{vertex} cut is to eliminate off-vertex tracks. However, the resolution of the track fit parameters and the uncertainty in the determination of collision vertex lead to uncertainty in the χ^2_{vertex} fit. This can be observed in the broadness of the χ^2_{vertex} distribution in the figure 8.3 (left). Thus, it is safe to assume χ^2_{vertex} cut reduces off-target tracks. In order to further reduce the electron tracks stemming from photon conversion in the target, an opening angle cut is explored. Here, all combinatorial pairs of oppositely charged candidate tracks that survive the χ^2_{vertex} cut are identified. The opening angle of the selected pair of candidates is calculated from a positively charged track (E_1, $\vec{p_1}$) and a negatively charged track (E_2, $\vec{p_2}$) as,

$$\theta_{OA}(deg) = \frac{180}{\pi} \cos^{-1}\left(\frac{\vec{p_1}.\vec{p_2}}{|\vec{p_1}||\vec{p_2}|}\right). \tag{8.6}$$

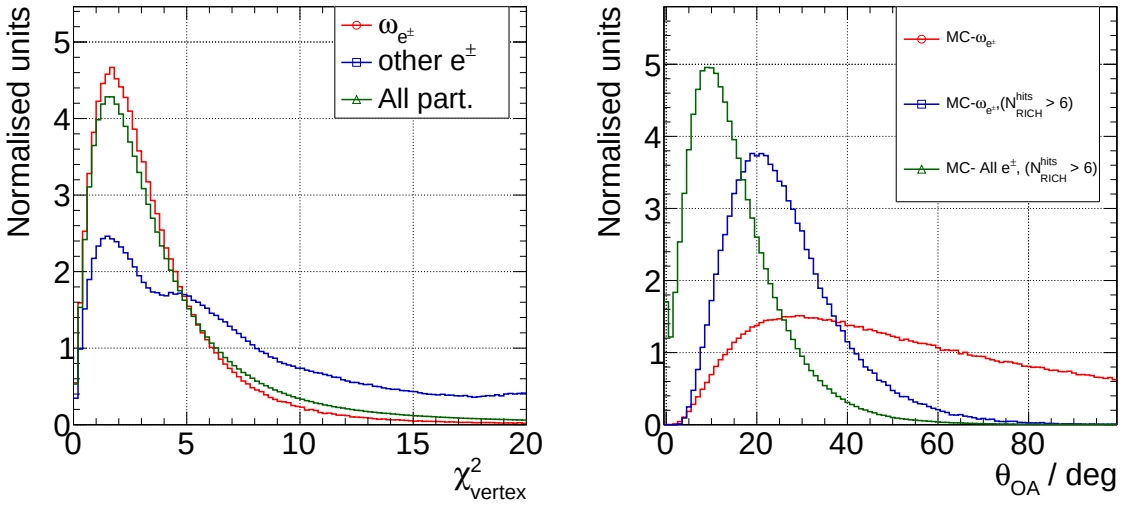

Figure 8.3: Left panel: χ^2_{vertex} derived by extrapolating the track to the primary vertex for electron tracks from omega decay (red), other UrQMD electrons (blue), and all particles (green). Right panel: Opening angle distribution derived for the pair of electrons matched by their true ID. All true pairs from omega decay (red), electrons from omega decay that have at least 7 hits in RICH (blue), and all electron pairs with at least 7 hits in RICH (green).

In order to derive an optimal opening angle cut, the opening angle for the pairs of true electrons from omega decays is plotted in figure 8.3 (right), together with the opening angle distribution for all (non-omega electron) tracks. It can be seen from the figure 8.3 (right), the opening angle of the electron pairs from all omega decays (red) is very broad spectrum. The omega particle undergoes a decay in the rest frame to e^+e^-, with the opening angle between them being 180 degree. In the boosted frame, the opening angle between them depends both on the energy of the omega particle and the omega decay orientation relative to the boost vector, leading to the broad opening angle distribution in the decay products. If the RICH acceptance condition ($N^{hits}_{RICH} > 6$) is applied (blue curve in the figure 8.3 (right)), the opening angle between the daughter electron tracks follows a Gaussian-like distribution with a tail towards a higher opening angle. By requiring both electrons to have hits in the RICH, the acceptance for large e^+e^- opening angles is significantly constrained, and it is reflected in the opening angle distributions (see figure 8.3 (right), red, blue). The opening angle distribution for all pair electrons (each pair from the same mother particle) exhibits a distinct Jacobian-like distribution (green curve in the figure 8.3 (right)) with a lower mean value than the electron pairs from omega decay, primarily due to the presence of electron pairs originating from the conversion electrons, which typically exhibit a lower opening angle. An opening angle cut of $\theta_{OA} > 20°$ is chosen here.

8.4 Omega meson signal reconstruction

The purpose of this work is to exclusively understand the impact of different electron identifiers. Hence, only two subsets of the candidate pairs that survived the previous selection criteria

(electron identification cuts and topological cuts) are used for the further analysis: pair electrons originating from the omega decay (using MC true identity and reconstructed momentum) and all non-electron pairs (where at least one track is falsely identified as electrons). It may appear that the previous exercise of topological cuts is redundant; however, this is not the case, as the topological cuts are an integral component of the standard di-electron reconstruction algorithm, which was utilized in this study to constrain the omega multiplicity. This allows for a thorough investigation of the impact of the electron identifiers within the confines of the conventional di-electron reconstruction scheme, which translates to understanding the impact on the reconstructable omega mesons.

In order to reconstruct the signal omega meson from the pair candidates, a twofold method is implemented. The first step involves finding the true omega signal and, consecutively, the non-electron background within the signal limits. A signal is derived by selecting the tracks that are electrons stemming from the omega decay. The invariant mass of the selected pair of candidates is calculated as,

$$M_{ee} = \sqrt{(E_1 + E_2)^2 + (\vec{p}_1 + \vec{p}_2)^2}, \tag{8.7}$$

where $E = \sqrt{\vec{p}^2 + M_e^2}$ and M_e is the rest mass of the electron. The derived invariant mass is filled in a histogram ($S(M_{ee})$). The entry into the histogram is weighted by a factor of Branching ratio($\omega \rightarrow e^+e^-$) $\times$ expected multiplicity of omega per event, in order to account for signal enrichment done by embedding one omega particle per event (see table 5.2). The weight factor w_{omega} for 8 AGeV central Au-Au collision is 7.36×10^{-5} (BR) $\times$ 0.270774 (Multiplicity). The resulting signal histogram comprises pairs matched by the identical omega particle and a combinatorial background as a result of the mixed matching of the tracks.

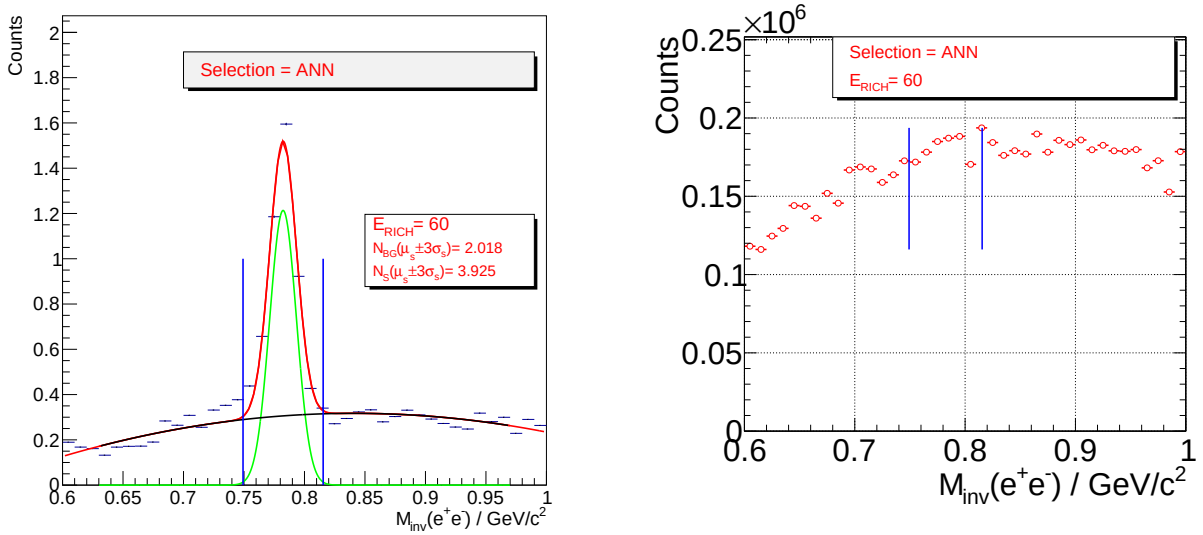

Figure 8.4: Example plots depicting the reconstructed ω signal (left panel) and reconstructed non-electron background (right panel) with signal selection criteria, where the electron candidates are selected using conventional ANN in CBMROOT for 60% RICH electron reconstruction efficiency.

A combination of a Gaussian profile (for signal) and a second-order polynomial (for combinatorial background) given in the equations,

$$f_{signal} = p_0 \times \exp(\frac{-(M_{ee} - p_1)^2}{2p_2^2}) \tag{8.8}$$

$$f_{background} = p_3 + p_4 \times M_{ee} + p_5 \times M_{ee}^2 \tag{8.9}$$

$$f_{total} = f_{signal} + f_{background} \tag{8.10}$$

is used to fit the histogram. Here, p_1 is the mean of the Gaussian (μ_s) and p_2 is its standard deviation (σ_s). The true signal contribution is then derived by,

$$S = \sum_{\mu_s - 3\sigma_s}^{\mu_s + 3\sigma_s} S(M_{ee}) - \int_{\mu_s - 3\sigma_s}^{\mu_s + 3\sigma_s} f_{background}. \tag{8.11}$$

The sum refers to the total number of entries in the bins within the integral limits.

The figure 8.4 (left) shows the invariant mass spectrum of the signal derived by using the ANN as the base electron identifier for 60% RICH electron reconstruction efficiency (selected by imposing a cut on the output of the ANN). The blue lines represent the data, and the red line depicts the fit function described in the equation 8.10. The black line depicts the combinatorial background contribution, and the green line depicts the final extracted signal. The same exercise is repeated for the different electron identification efficiencies (by varying the cut on the output of the ANN) and using different identifiers with the XGBoost base model instead of the conventional ANN in CBMROOT described in the section 8.1. The results are included in the appendix A.5.1, A.5.2, A.5.3, A.5.5, A.5.4, A.5.6.

8.5 Signal to background ratio estimation

Similar to the signal, background tracks that meet the omega candidate selection criteria are selected. A pair of unlike charged tracks is considered as background if at least one of them is non-electron. The invariant mass of the background tracks is calculated by using the equation 8.7, and histogrammed ($B(M_{ee})$). It is important to note that this histogram is not weighted, unlike the one done for electrons from omega decay. The figure 8.4 (right) shows the invariant mass spectrum of the background derived by using the ANN as the base electron identifier for 60% RICH electron reconstruction efficiency (selected by imposing a cut on output of the ANN). The red lines represent the data, and the blue lines represent the signal limits derived for the same RICH efficiency and underlying electron identifier. Contribution from the non-electron background is derived from the background distribution $B(M_{ee})$ as,

$$\text{Background} = \int_{\mu_s - 3\sigma_s}^{\mu_s + 3\sigma_s} B(M_{ee}) dM_{ee}. \tag{8.12}$$

Here, μ_s and σ_s are the mean and standard deviation derived for the signal estimation (see previous section 8.4). Similarly, the same exercise is repeated for the different electron identification efficiencies (by varying the cut on the output of the ANN) and using different identifiers with the XGBoost base model instead of the conventional ANN in CBMROOT described in the section 8.1. The derived invariant mass spectrum of the background for different electron identifiers is included in the appendix A.5.7, A.5.8, A.5.9, A.5.11, A.5.10, A.5.12.

The contribution of signal and background for different underlying electron identifiers for different RICH electron efficiencies is computed. The signal to background ratio for different identifiers is calculated and further normalized to the signal to background ratio derived by using ANN. The result is plotted in the figure 8.5. As expected, all XGBoost-based electron identifiers have superior performance when compared to ANN in CBMROOT. The XGBoost model (variant 1), which was trained using the same input feature as ANN (as indicated by δd), exhibits a performance enhancement of at least 50% in comparison to ANN for RICH electron efficiency of 60%. For the RICH efficiencies higher than 75%, the normalized S/B ratio obtained by using the XGBoost model (variant 1) trained with the same input features as ANN is two times higher than the ANN model. Compared to the δd model (variant 1), the XGBoost model trained with the differential distance $\delta x, \delta y$ (variant 2) has at least 10% improved S/B performance for higher RICH efficiencies.

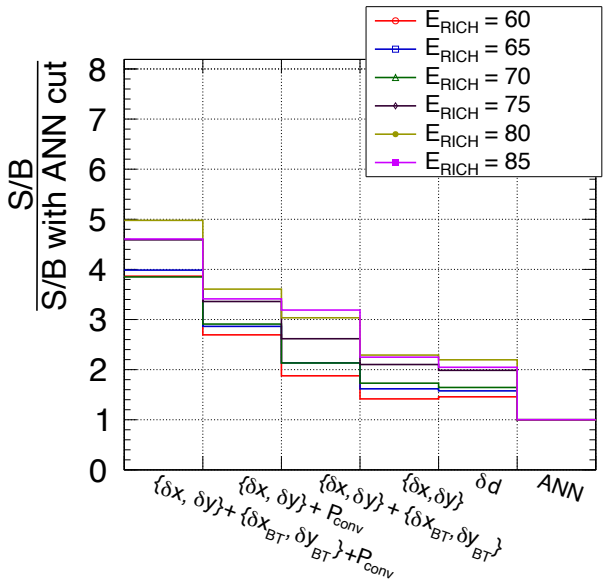

Figure 8.5: The signal to non-electron background ratio within $\mu_s \pm 3\sigma_s$ limits for the different electron track selection methods, normalized to the signal to non-electron background ratio derived with the electron selection using ANN cut.

The inclusion of the TRD backtracked ring-track reference $(\delta x_{BT}, \delta y_{BT})$ (variant 3) resulted in a 50% increase in the S/B ratio compared to the base XGBoost model (δd) (variant 1), and the S/B ratio was three times higher compared to the ANN in CBMROOT for higher RICH efficiencies. The additional conversion probability metric for the ring (P_{conv}) (variant 4) has greatly enhanced the S/B ratio as compared to the base XGBoost model (δd) (variant 1) by a factor of two, and has 350% higher S/B compared to the ANN model for the higher RICH efficiencies.

The final improved XGBoost model (variant 5), which is trained with differential forward ring-track distances ($\delta x, \delta y$), TRD backtracked ring-track reference ($\delta x_{BT}, \delta y_{BT}$, $N_{hits}(TRD)$), and conversion probability metric for the ring (P_{conv}) outperforms the base XGBoost model (δd) (variant 1) by at least two times for lower RICH efficiencies and at least 2.5 times for higher RICH efficiencies. For the lower RICH efficiencies, the aforementioned model outperforms the ANN in CBMROOT by at least four times, and by at least five times for the higher RICH efficiencies in terms of the signal to background ratio. The figure 8.5 demonstrated the effectiveness of the additional variables introduced in this thesis for the di-electron reconstruction.

8.6 S/B ratio at the maximum significance

At present, the performance of various electron identifiers, including conventional ANN and XGBoost variants, has been compared in terms of their performance at various electron identification efficiencies.

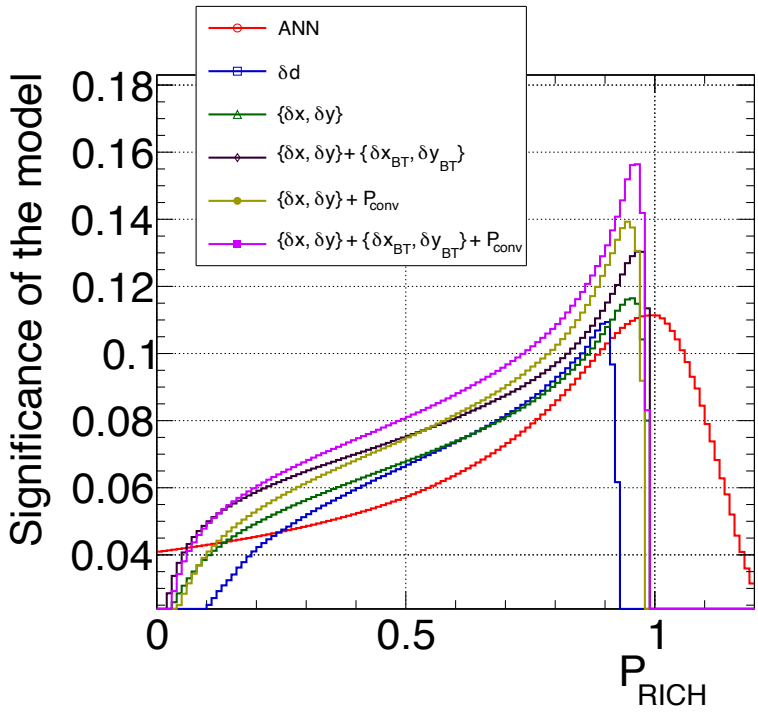

Figure 8.6: Significance for different electron identifiers (conventional ANN and different variants of XGBoost models) calculated for different output threshold (P_{rich}). The plot indicates that each model has an output threshold for which there is a maximum significance.[1]

Following that, the response of different models is compared at the point of maximum significance. The significance at different thresholds of the output of the model is defined as $\frac{N_e \times w_{omega}}{\sqrt{N_e \times w_{omega} + N_\pi}}$. Here, N_e is the number of primary electrons (from omega decay) correctly iden-

[1]Note: The output of the ANN (single-layer perceptron) is essentially the sum of the responses of all intermediate neurons, and as a result, it extends beyond ±1.

tified, and it is weighted by the w_{omega} (7.36×10^{-5} (Branching ratio) $\times 0.270774$ (Multiplicity), defined in section 8.4), N_{π} is the number of pions misidentified as electrons. The significance of the various electron identifiers calculated for different output thresholds is depicted in the figure 8.6. It is evident from the figure 8.6 that for each electron identifier, there exists a threshold setting $P_{thr}^{max-sig}$ at which the model exhibits its maximum significance.

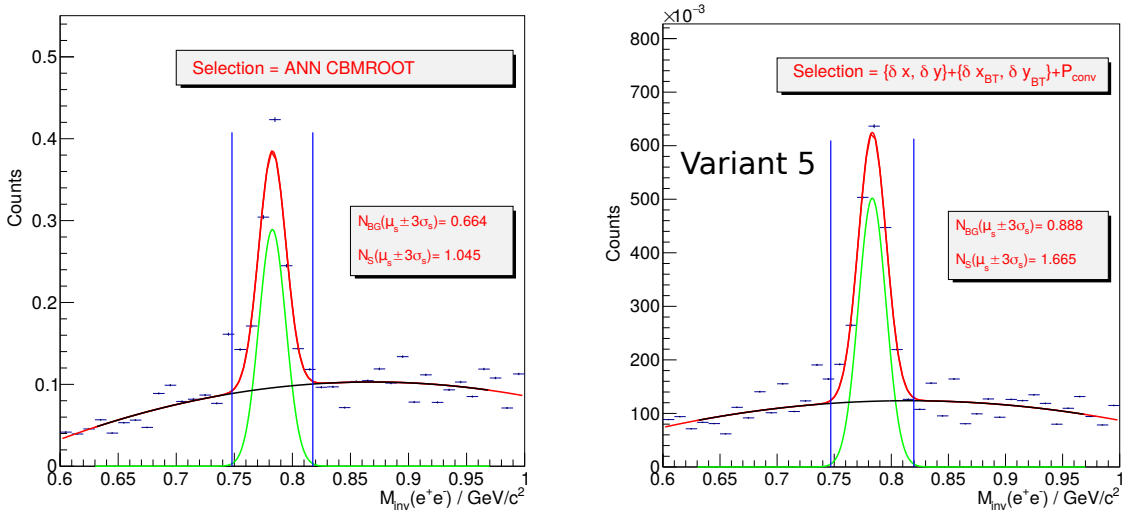

(a) Conventional ANN

(b) XGBoost variant 5 - $(\delta x,\ \delta y) + (\delta x_{BT}, \delta y_{BT} + N_{hits}^{TRD}) + P_{conv}$

Figure 8.7: The figure depicts the signal ω reconstructed (invariant mass) with electron candidates selected using ANN and XGBoost variant-5 at the point of maximum significance.

Similar to the previous section (see section 8.4), the invariant mass of omega mesons (signal) is calculated, and non-electron background contributions are estimated (for the same topological and TRD+TOF electron identification cuts) using conventional ANN and different XGBoost variants as underlying RICH electron identifiers by setting a threshold for its maximum significance $P_{thr}^{max-sig}$. Figure 8.7 depicts the invariant mass distributions of the ω mesons that were obtained using ANN and an advanced variant of the XGBoost that employs backtracking variables (variant 5) as electron identifiers. The other results are included in the appendix A.5.13, A.5.14.

Finally, the signal to non-electron background ratio for different electron identifiers is estimated and normalized to the value of the signal to non-electron background calculated using conventional ANN. The results are shown in the figure 8.8. Different XGBoost variants display superior performance compared to the conventional ANN. The XGBoost models, variant 1 (indicated by δd) which was trained using the same input feature as ANN and variant 2 which was trained with the differential distances $\delta x, \delta y$ show similar performance, and are at least 25% better in comparison to ANN. The XGBoost variant 3 trained with the TRD backtracked ring-track reference $(\delta x_{BT}, \delta y_{BT})$ and TRD hit multiplicity shows 80% improvement compared to the conventional ANN, and it is at least 45% better compared to XGBoost variant 1 (trained with same input feature as ANN) in terms of S/B performance. The additional conversion probability metric

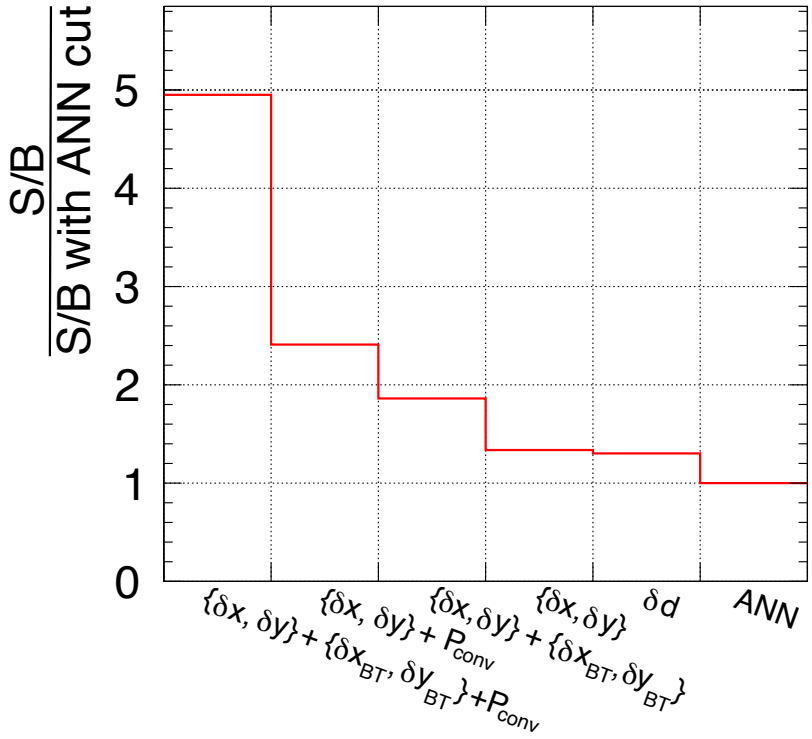

Figure 8.8: The signal to non-electron background ratio within $\mu_s \pm 3\sigma_s$ limits for the different electron track selection methods at their maximum significance, normalized to the signal to non-electron background ratio derived with the electron selection using ANN at its maximum significance.

for the ring (P_{conv}) (variant 4) has greatly enhanced the S/B ratio as compared to the base XGBoost model (δd) (variant 1) by a factor of approximately two.

The most significant enhancement is shown by the final improved XGBoost model (variant 5), which is trained with differential forward ring-track distances ($\delta x, \delta y$), TRD ring-backtracked reference ($\delta x_{BT}, \delta y_{BT}$, $N_{hits}(TRD)$), and conversion probability metric for the ring (P_{conv}). This model outperforms the base XGBoost model (δd) (variant 1) by at least 3.5 times and by a factor of 5 compared to the conventional ANN at the point of maximum significance. The figure 8.8 further illustrates the significant impact of the novel techniques developed in this thesis for the final di-electron reconstruction.

9

Summary and Outlook

One of the primary objectives of the CBM experiment is to measure the di-lepton spectral function in heavy ion collisions at energies around 2 GeV to 5 GeV center of mass energies. Since di-leptons are unaffected by the strong interactions, they serve as penetrating probes in order to understand the QCD phase produced in the initial stages of heavy-ion collisions. The CBM experiment is designed for dedicated measurements of both di-electrons and di-muons. The focus of this thesis pertains to the measurement of di-electrons. In CBM, the Ring Imaging Cherenkov detector (RICH) is used for identification of electrons in combination with the Transition Radiation Detector (TRD) and Time-of-Flight (TOF) detector. Here, the readout electronics (called DIRICH) of RICH are crucial in order to fully exploit the capability of the RICH detector. A detailed evaluation of the performance qualification of the MAPMT (photon sensor)-DIRICH readout chain has been conducted, and the resulting findings are summarized in this chapter. CBMROOT, a software framework based on ROOT, is used to simulate the operational behavior of the RICH and other sub-detectors of the CBM experiment. At present, the reconstruction and identification algorithms for electron tracks have been decoupled for RICH, TRD, and TOF. A comprehensive optimization of the current standalone reconstruction scheme for RICH has been performed, and a novel reconstruction scheme that utilizes the information from the TRD and TOF detectors was implemented and evaluated for enhanced identification efficiency of the electron tracks. The improved electron reconstruction scheme was used to reconstruct omega mesons through its $\omega \rightarrow e^+e^-$ decay.

9.1 Performance and quality testing of CBM RICH front-end electronics

Using a dedicated lab test setup, different measurements on the DIRICH readout chain (which will be used in the upcoming CBM RICH detector) were carried out in order to qualify the readout chain for the CBM RICH detector, and several quantitative results were obtained. The neighboring channel charge sharing crosstalk for single photon detection with H12700 MAPMTs connected to DIRICH FEB modules was measured to be less than 2%. This crosstalk probability was found to be independent of the applied discrimination threshold in the range of 30 mV to 70 mV, which is well below the average single-photon signal amplitude. A dedicated test using simultaneous incident photons from a pulsed laser source was performed to check the compatibility of the readout chain to handle high photon occupancy, as it is expected in CBM.

The large occupancy was confirmed to cause significant additional capacitive crosstalk hits (parasitic crosstalk due to the use of a common dynode system), with almost 88% additional crosstalk hits for 18 simultaneous signal hits per MAPMT (on the higher side of occupancy). However, these capacitive crosstalk hits were found to have low ToT characteristics ($\leq$ 3 ns), well separated from ToT values for real photon hits. Hence, these additional hits can be easily removed by imposing a simple ToT cut on registered hits. Though the overall data rate does increase due to additional crosstalk hits (at least as long as no additional ToT condition was implemented on the DIRICH FEB itself), the data after applying a ToT cut will be rather clean. In the expected maximum MAPMT occupancy range of up to $\sim$ 28%, an optimal ToT cut of 3 ns is found to be sufficient.

The lab setup was also used to perform a successful high rate test of the DIRICH front-end electronic readout chain. Apart from the well-understood data transfer limitations imposed by the lab setup, it is found that an individual DIRICH FEB channel can handle at least up to 2.2 MHz input rate. However, the size of the individual channel buffers and the main DIRICH FEB buffer are currently subject to certain limitations. A test of data quality at a large input rate was performed using a pulsed laser as a signal source and an LED driven with low direct current as an uncorrelated background source. A collimator used in combination with the laser provided a realistic ring-like hit pattern on the MAPMT for this test. Even at very high uncorrelated background hit rates, the data purity of the signal hits of interest is maintained (if appropriate time cuts are applied during data analysis), and the data is still transmitted reliably. Analog signal propagation and digitization show no impairment even under the highest tested rate conditions.

In addition to the high rate and high occupancy measurement, a dedicated measurement was made to characterize the capability of DIRICH FEB to distinguish simultaneous hits in time. It was found that the leading edge timing precision to distinguish both hits in the same DIRICH FEB was about 22 ps and in different DIRICH FEBs was about 36 ps, hence proving the DIRICH FEB was not the limiting factor in resolving simultaneous hits as compared to MAPMTs (the transit time spread of H12700 MAPMTs is 149 ps RMS). Using the identical setup, the DIRICH FEB's capability to distinguish simultaneous double photon hits (within the same pixel) from single photon hits by utilizing ToT information was evaluated. It was found that the ToT has a strong correlation with the width of the input pulse but a weak correlation with the amplitude of the signal. Hence, presently, the DIRICH FEB is found not suitable to resolve single photon hits from double photon hits.

The new iteration of the power module to be used in the CBM RICH was tested for its noise-emitting characteristics by observing the noise bandwidth measure of DIRICH FEBs on the same backplane, powered by the new module and using DC/DC converters in combination with a single input supply voltage of 18 V to 32 V. Using an additional copper shielding covering the DC/DC circuit part, the new power module produces noise comparable to powering via externally regulated low-voltage supplies, as previously used in HADES. The observed average noise half-bandwidth was less than 10 mV which is far below the intended operation input

threshold regime (50 mV to 70 mV). These results were confirmed with the larger (six fully equipped backplanes) mRICH setup.

The measurements described above not only proved valuable for the final qualification of the DIRICH readout chain for CBM RICH but also served to define optimal operating parameters for later routine operation. As an outlook, the developed lab setup can now also be used to derive a parametrization of capacitive crosstalk probability as a function of distance from the initiating photon hit and as a function of occupancy. This will help to implement crosstalk in a more realistic way into the CBMROOT simulation framework.

9.2 Di-electron reconstruction

Besides the hardware qualification measurements, a significant software restructuring was performed in reference to the reconstruction and identification of the electron tracks. It has been observed that the STS tracks that are projected to the RICH camera (to be matched to a ring) exhibit a systematic deviation in the ring-track distances. In order to rectify this inefficiency, data-driven track extrapolation and systematic ring-track distance correction methods were implemented. The corrected inefficiencies increased the efficiency of the projection of electron tracks in the vicinity of the rings ($d < 1$ cm) by 5%, without any changes in the amount of projection of pion tracks. As an outlook, the use of the extrapolation methodology has to be revisited to fix the inefficiencies. This could involve changing the energy loss function to include the Bethe-Bloch and Bremsstrahlung phenomena (attempted by Martin, et al., in [65]).

9.2.1 Upgraded machine learning models for electron identification

The electron identification using the RICH detector is done after the initial closest distance-based track matching. A candidate for the ring-track has the parameters that include the features of the ring and the momentum of the track. An artificial neural network (ANN) which is a single-layer perceptron, was conventionally used for electron identification. In this thesis, the conventional ANN has been replaced by the XGBoost-based ML model (variant 1). A new concept for training machine learning models was introduced, where the input features were derived by setting a uniform momentum distribution for electrons and pions. This allows the utilization of the trained models across collision energies and centralities. On applying the upgraded model to the UrQMD 8 AGeV central Au-Au collisions with embedded $\omega \rightarrow e^+e^-$, an increase in pion discrimination performance of up to 100% for higher electron identification efficiencies (85%) is seen by replacing the conventional ANN with the XGBoost model. Furthermore, the ring-track distance (δd) was found to be the relatively important variable for the model for XGBoost model performance. Therefore, in order to benefit from the information, the ring-track absolute distance ($\delta d = \sqrt{\delta x^2 + \delta y^2}$) is assessed differentially in X (δx) and Y (δy). Consequently, a new XGBoost model is trained with the classical input features with the inclusion of differential ring-track distances ($\delta x,\ \delta y$) (variant 2) replacing absolute ring-track distance (δd). The upgraded

XGBoost model ($\delta x,\ \delta y$) has an improved pion rejection performance of up to 20% in higher efficiencies (85%) compared to the XGBoost model trained with absolute distance (δd).

The next big venture was to exploit the tracking capabilities of the TRD (especially TRD-2D), a method labeled "backtracking" has been implemented. This involves fitting the global track in TRD and subsequently extrapolating tracklets back to the RICH. As a result, it provides a supplementary track-pointing vector for the ring in addition to the forward track-pointing vector from STS. A new variant of the XGBoost model (variant 3) was trained with all the features of variant 2 along with the ring-backtrack differential distances ($\delta x_{ring-backtrack}$, $\delta y_{ring-backtrack}$), and number of hits per TRD tracklet (N_{hits}^{TRD}). It was observed that the upgraded XGBoost model (variant 3) outperforms the conventional ANN by up to 200% in terms of pion rejection capability for an 85% electron identification efficiency.

9.2.2 Backtracking conversion electrons

It has been observed that the primary source of misidentification of pions was due to their mismatch with the rings of electrons that stem from the photon conversion in the detector material, which are often not reconstructed in the tracking stations. Furthermore, the unreconstructed electrons were found to be produced from the photon conversion in the downstream stations of STS and the exit window of STS, as they produce fewer hits in the tracking stations. Therefore, in order to provide a track reference for these electron rings, a novel version of the backtracking method was employed. The concept was to track these electrons in the TRD layers, fit them, and extrapolate them back to the RICH. Due to the higher/larger acceptance of the TRD subdetector for such tracks, the TRD backtracking approach has large potential for improving the electron ID process. The extrapolated tracks were then matched to the closest ring, and the ring was assigned a probability metric that indicates that this particular ring is stemming from an STS-untracked conversion electron. A machine learning model based on XGBoost was employed to identify these conversion electrons in TRD. The output of the XGBoost model provides the probability that a particular ring originates from an STS-untracked conversion electron. This procedure should be performed prior to matching the STS tracklets to the rings. The derived conversion probability was then added to the ring alongside the other standard parameters (like the radius and number of hits).

The incorporation of the derived conversion probability metric results in the emergence of two additional variants of the XGBoost model for electron identification. The summary of the different models is shown in the table 9.1. XGBoost model variant 4, which trained on the additional conversion probability metric, outperforms the model trained without it, XGBoost model variant 2 (all the other features are the same) in terms of pion rejection capability by at least 46% at a lower electron identification efficiency of 60%. Variant 5 of the XGBoost model was the most efficient model; along with common input features, it was additionally trained using differential ring-STS track distances, differential ring-TRD backtracked references, and the conversion probability metric. It has been observed that this model possesses a far better

Table 9.1: Table displaying different variants of XGBoost developed in this thesis, with the input features used to train these models. The following input features are common for all models: $\{a_{ring},\ b_{ring},\ \phi_{ring}$, absolute ring position in polar coordinates (R, θ), hits/ring, ring-fit quality metric χ^2/NDF, Momentum$\}$ labeled "common input features". Note: δq represent the ring-track distance measure 'q', where q=x, y, d (d = $\sqrt{x^2+y^2}$).

XGBoost model	Label	Input features				
		Common	δd (STS)	$\delta x, \delta y$ (STS)	$\delta x, \delta y$, N_{hits} (TRD)	P_{conv}
Variant 1	δd	✓	✓			
Variant 2	$\{\delta x, \delta y\}$	✓		✓		
Variant 3	$\{\delta x, \delta y\}$ $+\{\delta x_{BT}, \delta y_{BT}\}$	✓		✓	✓	
Variant 4	$\{\delta x, \delta y\}$ $+P_{conv}$	✓		✓		✓
Variant 5	$\{\delta x, \delta y\}$ $+\{\delta x_{BT}, \delta y_{BT}\}$ $+P_{conv}$	✓		✓	✓	✓

pion rejection capability by a factor of up to 3.6 times superior to the conventional ANN at an electron efficiency of 85%.

9.2.3 Reconstruction of omega meson

The impact of these models was studied on the reconstruction of omega mesons through their e^+e^- decay channel. In addition to the RICH electron identifier, for the selection of candidate tracks, both topological cuts and electron identification cuts from TOF and TRD are utilized.

Table 9.2: The table below displays the calculated signal to non-electron background ratio when using different variants of XGBoost models normalized to the conventional ANN previously used as standard. The signal to non-electron background ratio is shown for the electron identification efficiencies of 60% and 85% in RICH, and the point of maximum significance for all the models.

XGBoost model	Label	$\frac{\text{Signal/Non-electron background}}{\text{Signal/Non-electron background with ANN}}$		
		$E_{RICH} = 60\%$	$E_{RICH} = 85\%$	Max. Significance
Variant 1	δd	1.45	2.05	1.23
Variant 2	$\{\delta x, \delta y\}$	1.42	2.26	1.30
Variant 3	$\{\delta x, \delta y\}$ $+\{\delta x_{BT}, \delta y_{BT}\}$	1.90	3.21	1.8
Variant 4	$\{\delta x, \delta y\}$ $+P_{conv}$	2.67	3.41	2.4
Variant 5	$\{\delta x, \delta y\}$ $+\{\delta x_{BT}, \delta y_{BT}\}$ $+P_{conv}$	3.84	4.62	4.92

All the variants of the XGBoost models developed in the course of the thesis outperform the conventional ANN in terms of reconstruction of omega mesons (see table 9.2). The final version of the XGBoost model, which encompasses all the advancements, outperforms the conventional ANN and other versions of the XGBoost, demonstrating the significant impact of the modifications in the electron reconstruction scheme for CBM RICH.

9.2.4 Outlook

This dissertation exploits the tracking capabilities of the TRD and employs the TOF timer to reduce the background in backtracking the untracked electrons stemming from photon conversion in the material after STS and also to provide the secondary ring-backtrack distance measures. However, the electron identification capabilities of the TRD and TOF are used as a cut-based selection for the final omega meson reconstruction. As a prospective outlook, it is feasible to develop a global electron identifier that utilizes not only the tracking capabilities but also the electron identification features of the TRD and TOF. Further, the global electron classifier (RICH+TRD+TOF) could make additional use of the energy loss measurement from stations of STS for better hadron-electron separation. Since employing all the sub-detectors for electron identification will involve numerous features, a machine learning model can be adopted for the application. As proposed in this thesis, the concept of training machine learning models with features derived from uniform momentum distribution can be employed, thereby enabling the utilization of the trained models across collision energies and centralities.

In order to reduce the background contribution arising from tracked electrons resulting from photon conversion, topological cuts are used for track selection. This underscores the possibility of implementing machine learning models for electron candidate pair selection, based on the electron identification features, opening angle of the pairs, collision vertex-fit measures, and sub-detector hit multiplicities. Furthermore, the pair selection ML model can be optimized for selecting different parts of low-mass vector mesons. This approach might result in developing an ideal/adaptable machine learning model by utilizing two oppositely charged track features as inputs and identifying the type of low-mass vector meson as output (ρ, ω, ϕ), with the possibility of including (J/ψ).

10

Additional applications

In this chapter, potential supplementary applications that resulted from the implementation of diverse methodologies derived from this thesis are reviewed. Sections of this chapter are published in the following reports/papers,

- P.Subramani, et al., *RICH timing precision and its possible applications*, CBM Progress report 2023 [136].

10.1 Particle Identification via time of flight using the RICH ring time

The CBM TOF has a timing precision in the order of $\sigma \sim 60\,\text{ps}$, which is used for the identification of hadrons ($\pi/K, K/p$ separations) [75]. As reference time T0, the TOF will use the time measured by the CBM BMON detector, which is designed to have a timing precision of $\sigma < 50\,\text{ps}$ [139]. The TRB3 based padiX discriminator with GET4 ASIC is under consideration for the BMON readout system, which is inspired by HADES. As the CBM RICH possesses excellent timing precision, it may prove appealing to utilize its ring time as supplementary time of flight measurement in CBM. All the while, the CBM RICH uses TRB3 based DIRICH readout electronics with excellent timing precision (described in section 4.6). This section focuses on the potential use of the RICH ring times in conjunction with the TOF detector time to enhance the particle ID. Hereby, the time information of the RICH is always extracted for each ring individually and correlated to tracks at a distance of less than 2 cm. The time and the position of the matched ring is found (t_{ring}, $\vec{r}_{\text{ring}}$) and the distance between ring and its origin on the mirror is measured, $d_{\text{ring-mirror}} = \|\vec{r}_{\text{mirror}} - \vec{r}_{\text{ring}}\|$. Next, the TOF hits are matched to the track and the time and position of the farthest attached TOF is measured (t_{TOF}, $\vec{r}_{\text{TOF}}$). Finally, the distance between the mirror and TOF hit is measured $d_{\text{mirror-TOF}} = \|\vec{r}_{\text{TOF}} - \vec{r}_{\text{mirror}}\|$.

The velocity fraction is then given by

$$\beta = \frac{d_{\text{mirror-TOF}}}{t_{\text{TOF}} - t_{\text{ring}} + \frac{d_{\text{ring-mirror}}}{c}} / c \; . \tag{10.1}$$

The distribution of β as a function of momentum is shown in figure 10.1. Visibly, protons are clearly separable from electrons and pions. However, the separation is much weaker for high momentum electrons and pions. An electron/pion separation might only be possible at low

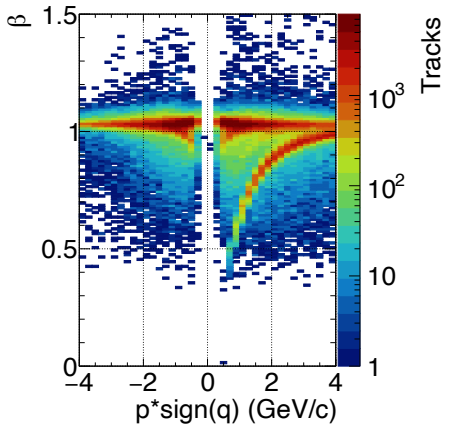

Figure 10.1: β vs momentum spectrum using RICH ring times and TOF matched hits to derive β.

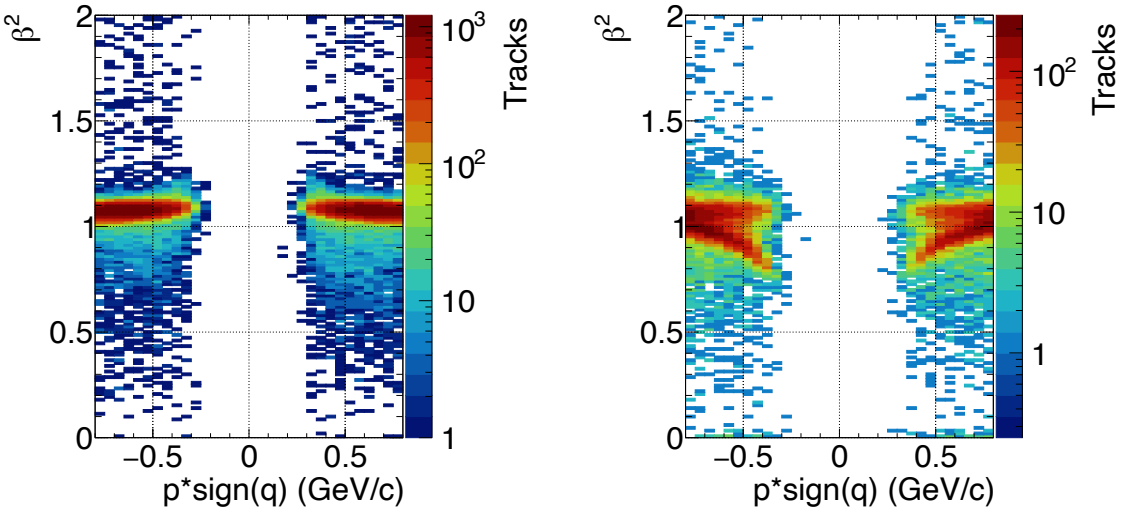

Figure 10.2: β^2 vs momentum spectrum for lower momenta using RICH ring times and TOF matched hits. Displayed separately for electrons (left) and pions (right)

momenta, as shown in figure 10.2.

10.2 Removing track fragments in Di-electron analysis

The selection of a di-electron candidate necessitates the tracking of both e^+ and e^- tracks in the STS+MVD tracker and their global identification with RICH+TRD+TOF detectors. Often, one of the pair electron tracks originating from the target are not tracked in the STS+MVD, while their partner track is tracked and globally identified. This contribution is called "Track fragment", and it is the major combinatorial background to the complete di-electron reconstruction [140]. These tracks often leave traces in the STS+MVD tracker, but they are often not reconstructed because the hits are low and/or not consecutive for good track reconstruction. The major contributors for the track fragments are due to conversion electrons. Number of MC points deposited by the conversion track fragments are shown in the figure 10.3.

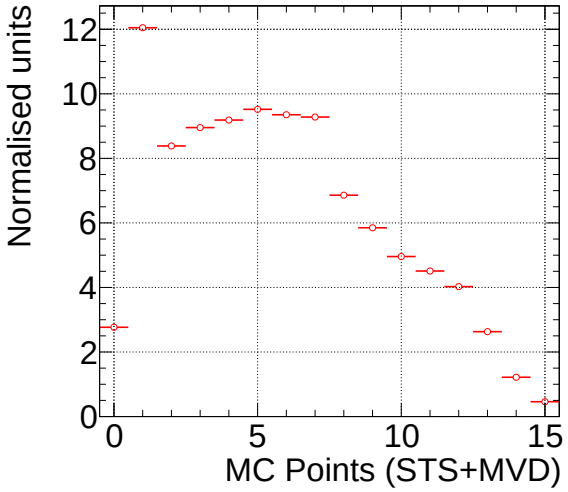

Figure 10.3: Distribution of number of MC points deposited by the track fragments. The plot shows that almost 80% of all track fragments have at least 3 MC points in the STS+MVD tracker.

In this section, a possible application of backtracking approach to remove these conversion electrons is discussed. Similar to TRD backtracking, the first step is to remove the all hits in the STS+MVD tracker which are already part of the reconstructed tracks. The leftover hits must contain the hits formed by the track fragments. The next step is to filter all the global electron tracks from the target which survive initial candidate selection criteria. A cone of search window around the candidate track is formed with a smaller opening angle. Assuming the track fragment has the similar momentum to the partner track, a track following hit finder can be performed and hits can be added to the fragment track. If a valid track fragment is found for the partner global track (based on multiplicity and topological cuts), then the partner global track can be eliminated from further analysis, thereby reducing the combinatorial background from these tracks.

10.3 Reconstructing low-momentum primary electrons

The second element of the backtracking strategy is the development of TRD-seeded track finding method based on CA (cellular automata) algorithm. This is done to find secondary electron tracks (mainly stemming from the photon conversion in the detector materials) that are not tracked by the STS+MVD tracking systems. An additional advantage of the method is the possibility of tracking the electrons from the omega decay which are not tracked by the STS+MVD tracking system. This could be possible, especially for tracks with low transverse momentum (smaller emission angle).

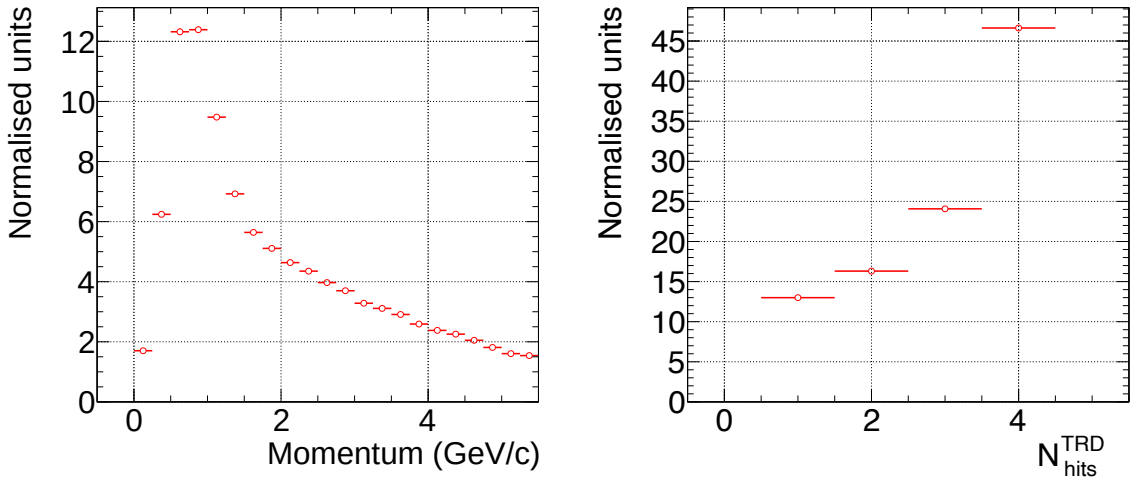

Figure 10.4: Figures depicting the characteristics of the untracked primary electrons stemming from the decay of the omega meson. The true momentum distribution of the untracked primary electrons with at least 1 hit in the TRD is shown in the left plot. The right plot depicts the distribution of the number of reconstructed hits produced in the TRD by the untracked primary electrons (with at least 1 hit in TRD).

In order to demonstrate the use case of this argument, a proof-of-concept simulation was performed, and the results were plotted in the figure 10.4. The figure 10.4 (left) shows MCTrue momentum distribution of the untracked primary electrons stemming from the decay of the omega mesons, which has at least one hit in TRD, indicating that electrons with lower momenta ($P < 1.2\,\mathrm{GeV/c}$) are the major portion of the tracks not reconstructed in STS+MVD. Furthermore, the figure 10.4 (right) shows the number of hits in TRD produced by these untracked primary electrons (with at-least 1 hit in TRD). This indicates that a few untracked primary electron tracks can be reconstructable in the TRD-seeded track finder approach.

A

Additional figures

This appendix contains all additional figures referenced in this thesis but not considered important enough to be included in the main text.

A.1 Additional figures for Chapter 4

A.1.1 Calibration of filter with ToT cut

The procedure described in section 4.5.2 is repeated for finding the transmission probability of the ND filters by imposing a ToT cut of < 3 ns on the registered hits (shown in the figure A.1 and tabulated in Table A.1), thus reducing the probability of crosstalk even in low multiplicities (< 3 hits). The derived transmittance T is used for finding the expected number of hits without filter in section 4.5.

Table A.1: Transmission probability of the ND filters

Filter Number	Transmission probability (T)	Neutral density (ND $= \log_{10} \frac{1}{T}$)
1	0.052153 ± 0.000374	1.282730 ± 0.003116
2	0.013485 ± 0.00038	1.870318 ± 0.012304

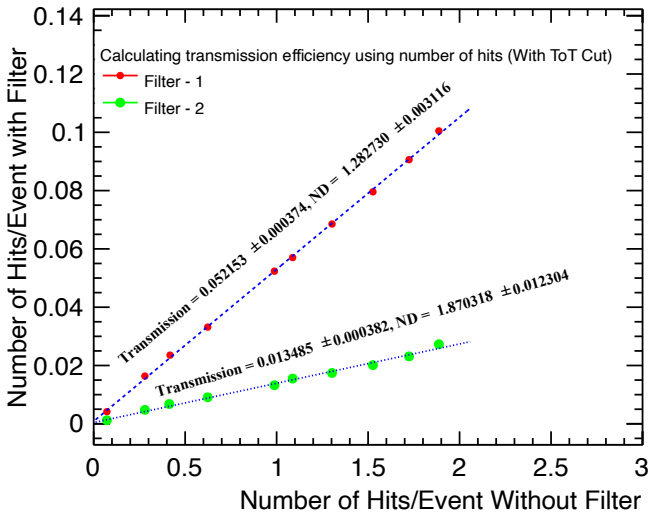

Figure A.1: Estimation of the transmission probability of ND filters with cut on ToT (> 3 ns) on the registered hits.

A.1.2 Simulation of the double photons

The contribution of double photons is determined through a Monte Carlo simulation. This is done by throwing N random numbers corresponding to the (number of hits registered in a MAPMT) into an 8 $\times$ 8 matrix. The probability of finding two values in a single index is found, and considered to be the probability of double photon hits. The non-homogeneous illumination of MAPMT, might result in producing double photons often in some regions. Therefore, the values in the derived matrix are weighted according to homogeneity of illumination. 3×10^6 events are simulated and plotted in figure A.2.

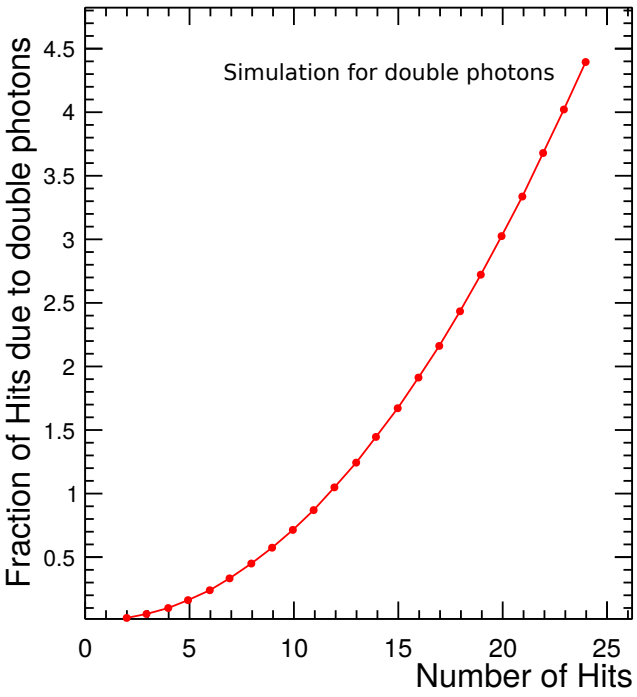

Figure A.2: Simulation result for the double photon contribution as a function of hit multiplicity.

A.1.3 Scaler rate vs. rate at DAQ for different threshold values

A test is performed to check the high rate behavior of the DIRICH FEB for different noise discrimination thresholds. Since the scaler rate is calculated after the threshold is set, the possibility of any behavior change is not expected and figure A.3 affirms the assumption.

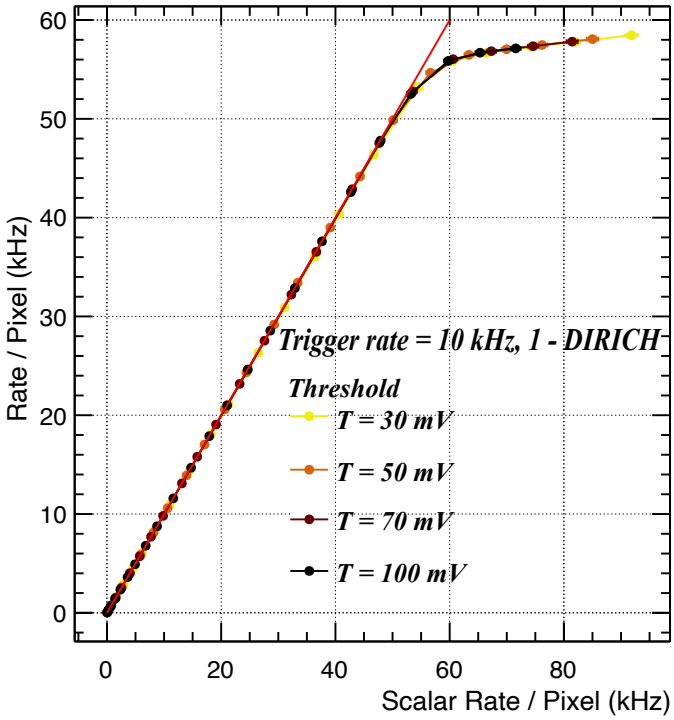

Figure A.3: scaler rate vs. rate at DAQ for different threshold values.

A.1.4 Median noise bandwidth

To avoid the outlier bias of finding the average and maximum noise bandwidth for each channel in the DIRICH FEB, the median half noise bandwidth for each channel is found (plotted in the figure A.4). The results indicate, the derived median noise bandwidth is in quite an agreement with the average half noise bandwidth.

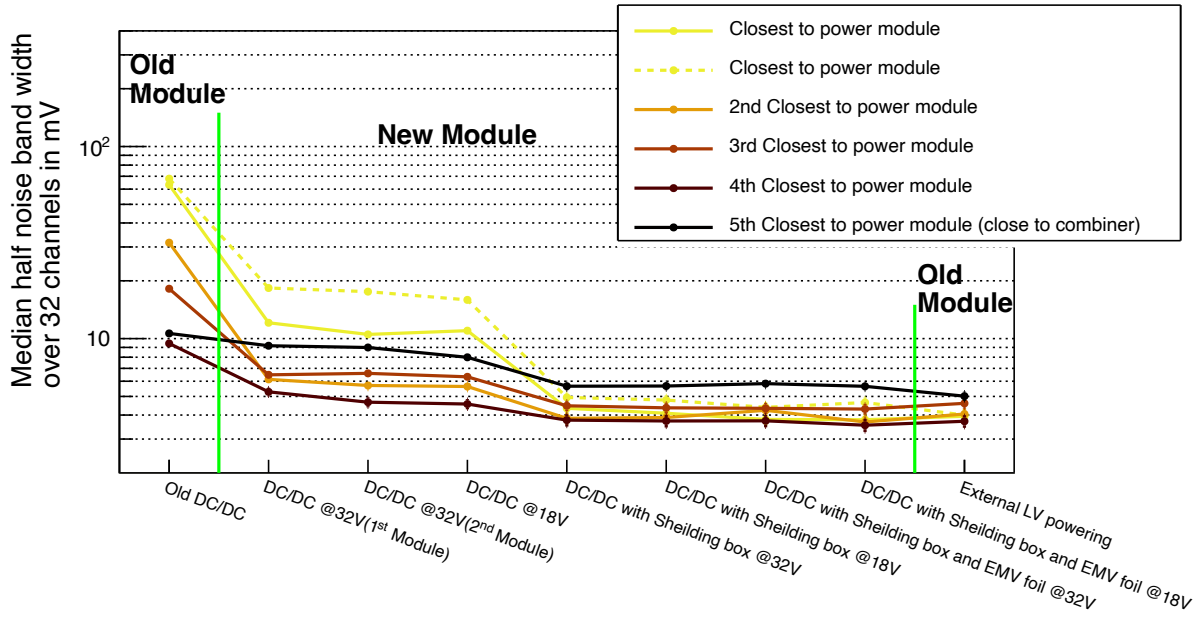

Figure A.4: The median half noise bandwidth over 32 channels for different iterations of power modules for different configurations.

A.1.5 Direct comparison of noise bandwidth due to two power modules at mRICH

The average half noise bandwidth induced on DIRICH FEB by the operation of old and new power modules on the same backplane (derived by performing independent scans) are compared and the values for each DIRICH FEB are shown in figure A.5. The measured noise levels are consistent with each other, and further the noise bandwidth is lower at the center of the backplane for both the cases.

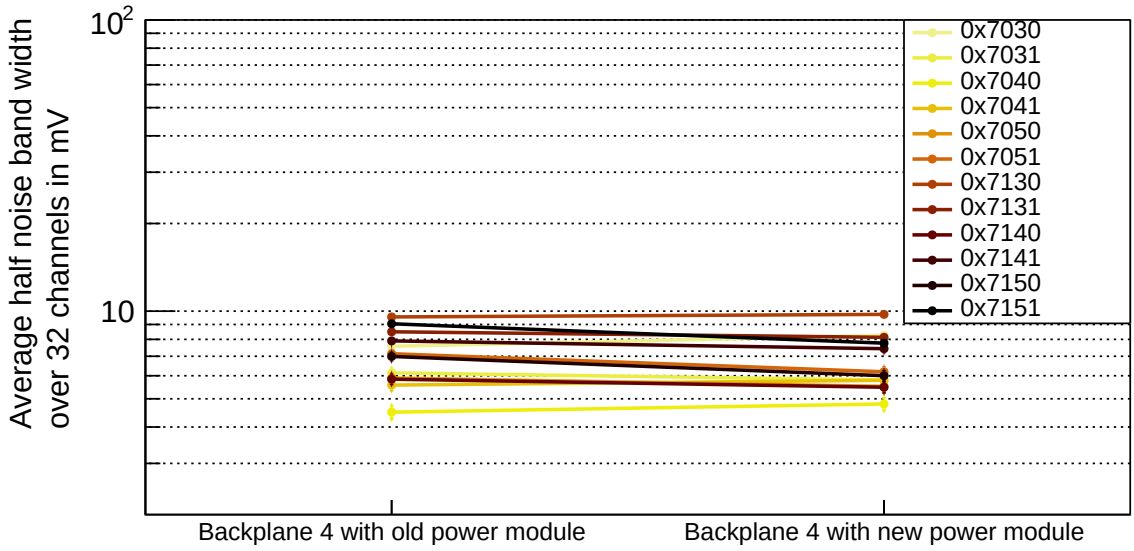

Figure A.5: Direct comparison of the noise bandwidth of the DIRICH FEBs due to two different power modules. Backplane 4—Center left at the mRICH setup (see figures 4.22, 4.25).

A.1.6 Effect of change in power module to time over threshold measurement

The overall timing performance of DIRICH should be unaffected by any changes to the power module. In order to verify that a setup as shown in the figure 4.5 with the laser is tuned to have less than two hits per event is used. The ToT of the hits is measured, and the measurement is repeated by changing the power module. The change in the DC / DC converter has a negligible effect on the overall timing precision of the DIRICH FEB (see figure A.6).

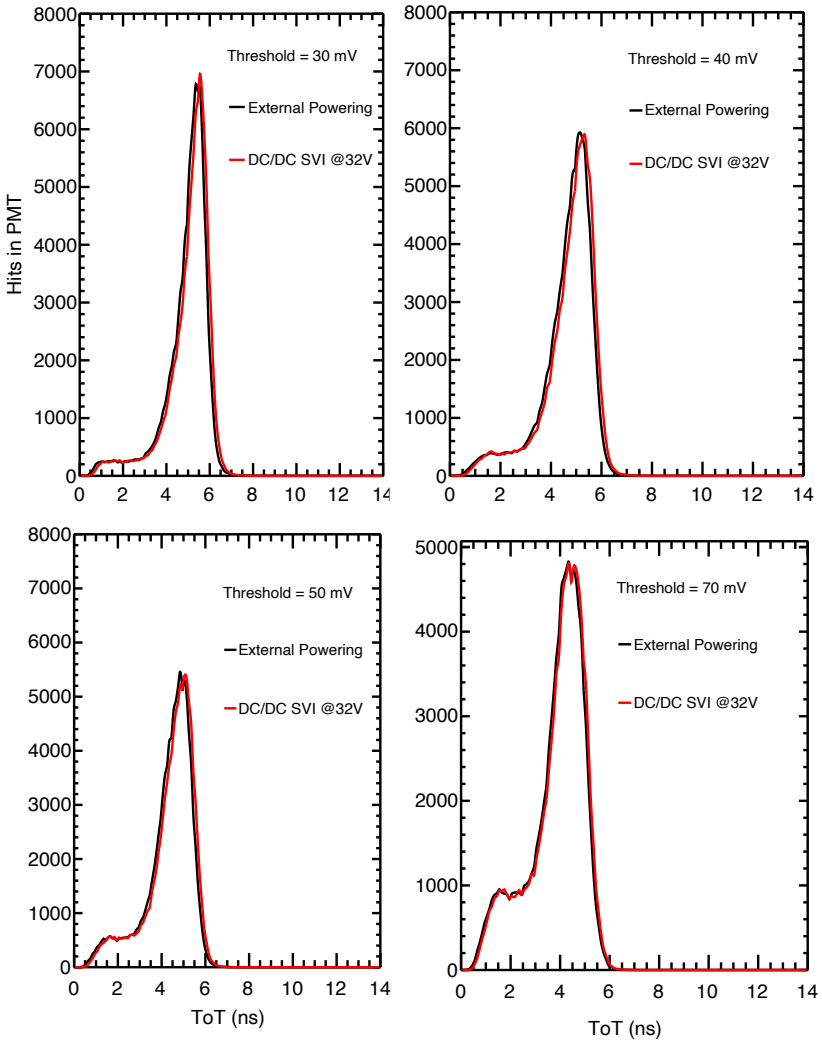

Figure A.6: Time over threshold spectra for different thresholds with the external powering and new DC / DC @ 32 V.

A.2 Additional figures for Chapter 5

A.2.1 Y component of the ring-track distance for different extrapolation layers

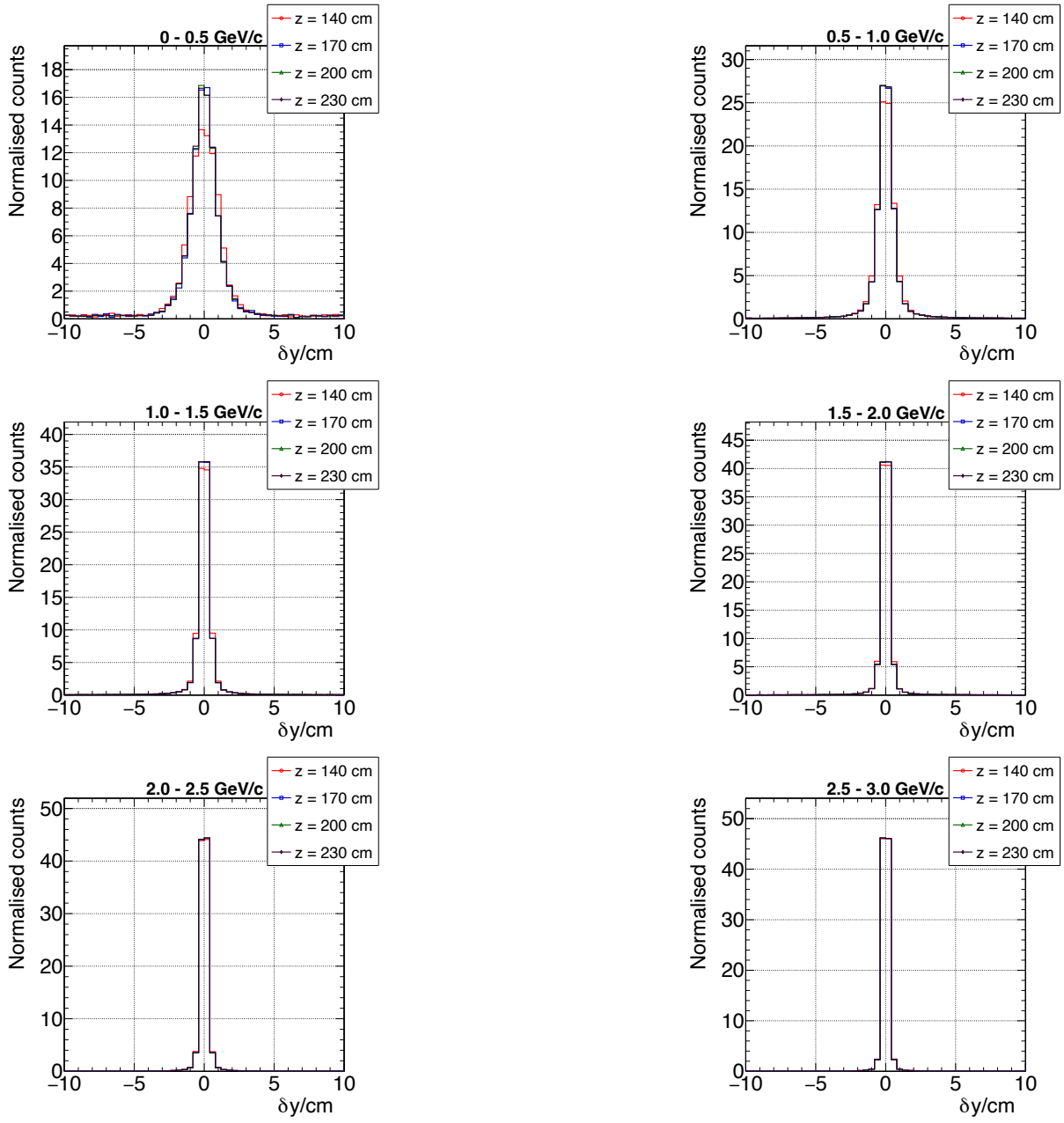

Figure A.7: Y component of the ring-track distance δy for different momenta of the electrons extrapolated to RICH at selected extrapolation layers.

A.2.2 Ring-track absolute distance for positrons

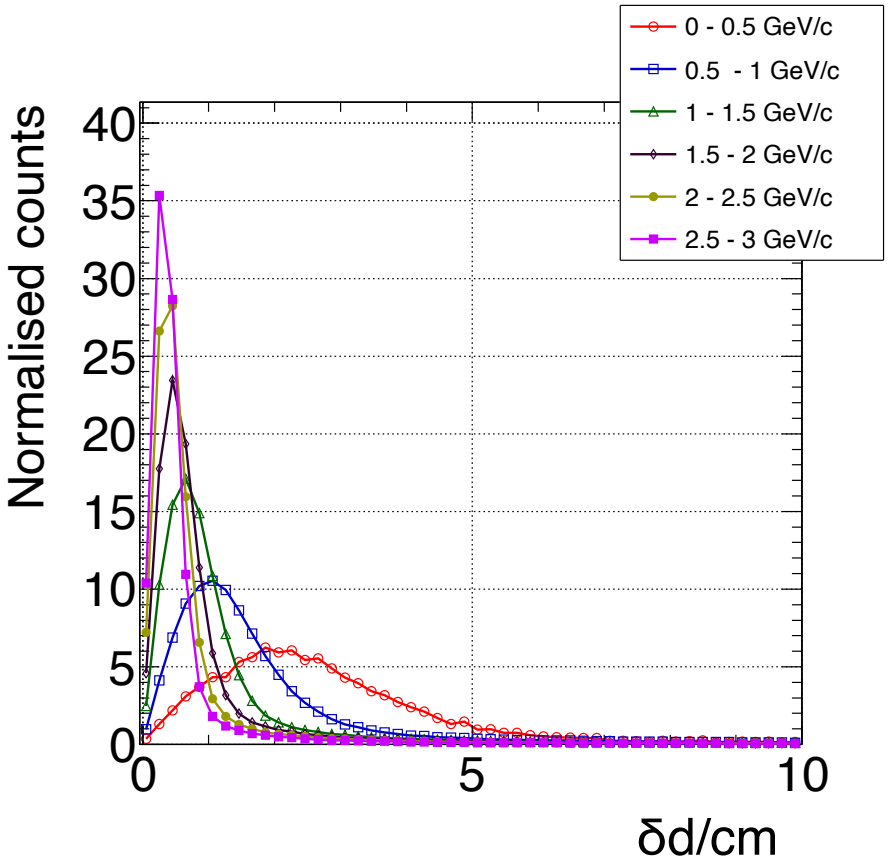

Figure A.8: Absolute ring-track distance at the photo-detector plane for electrons of different momenta.

A.2.3 Ring-track distance in X after applying corrections

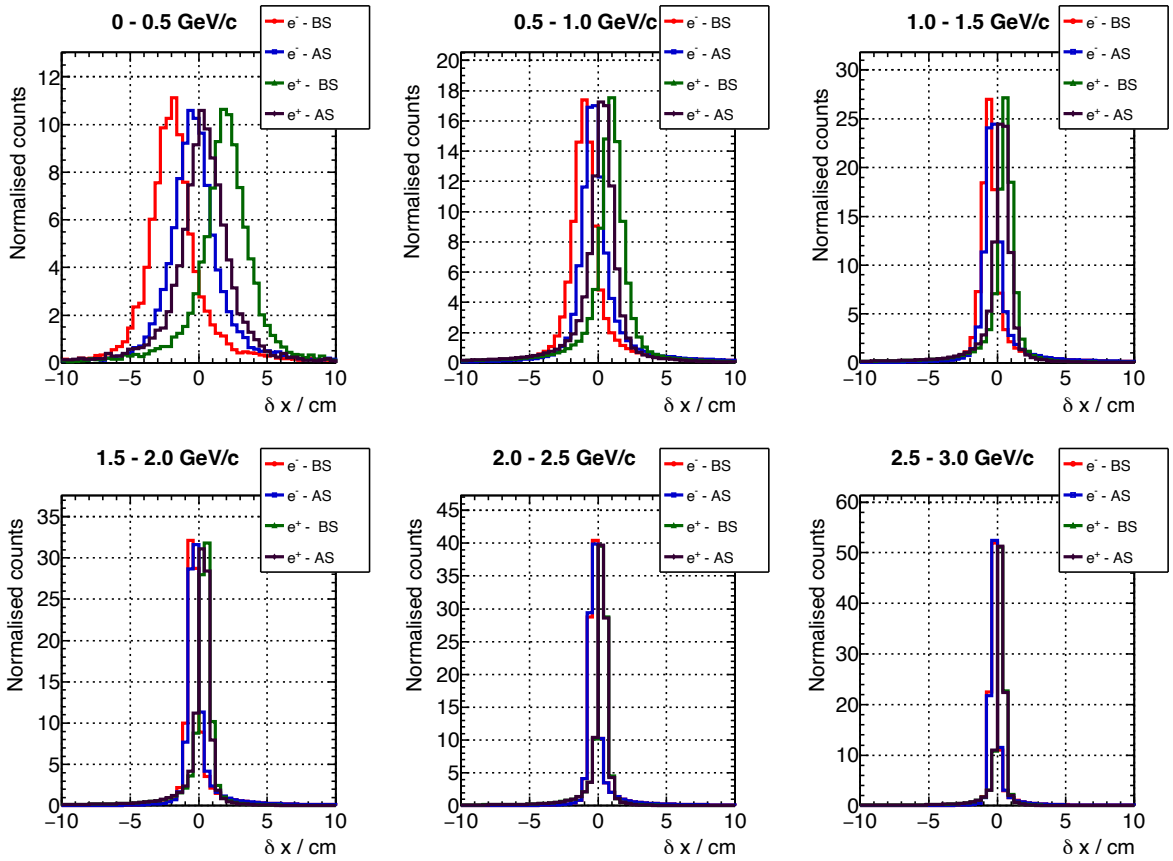

Figure A.9: Ring-track distance in X (δx) distance for electrons and positrons at different momenta before (BS) and after (AS) correction.

A.2.4 Ring-track distance in Y after applying corrections

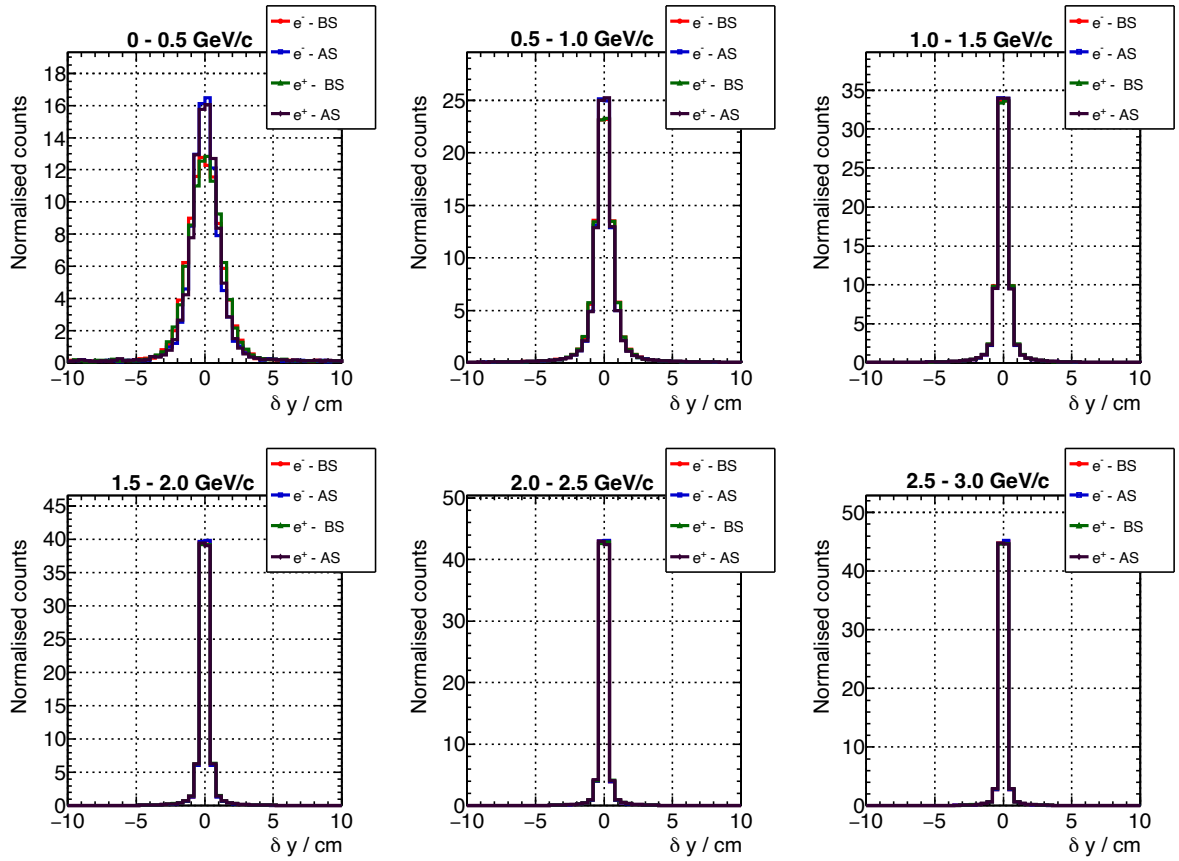

Figure A.10: Ring-track distance in Y (δy) distance for electrons and positrons at different momenta before (BS) and after (AS) correction.

A.3 Additional figures for Chapter 6

A.3.1 Response from XGBoost model for the training sample with inclusion of differential distance measure

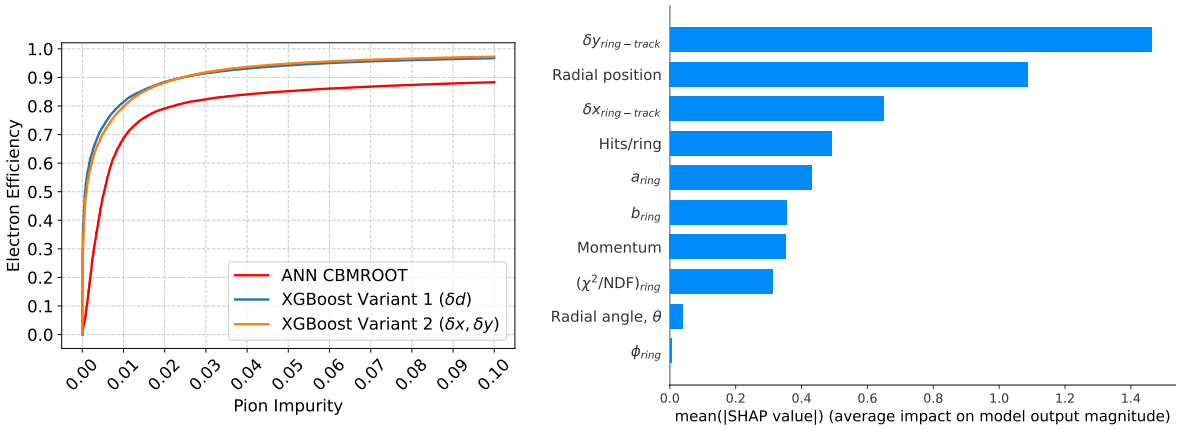

Figure A.11: Response from the ML models for the training sample. Left panel: ROC curve depicting the pion impurity for different electron identification efficiencies. Right panel: Relative input variable importance chart measured by the SHAP metric.

A.3.2 Transformation of input features

Additional variable transformations, such as scaling distances with momentum, were tried as inputs to the XGBoost model, but they did not improve the performance for the embedded omega sample. Since the momentum itself is given as an input feature for training the model, the trained model could have learned the relation, which may be the reason for this. Another aspect of the variable transformation involves normalizing the differential distance with the expected width for different momentum and XY position in the camera plane. However, given that the momentum and XY position in the camera are provided as inputs to the XGBoost/ANN model, it is anticipated that the model will derive these relative widths while training (similar to normalizing with momentum). Therefore, the relative distance measures are not used as additional input variables for training the XGBoost/ANN model.

A.3.3 Ring-backtrack fit performance for positrons

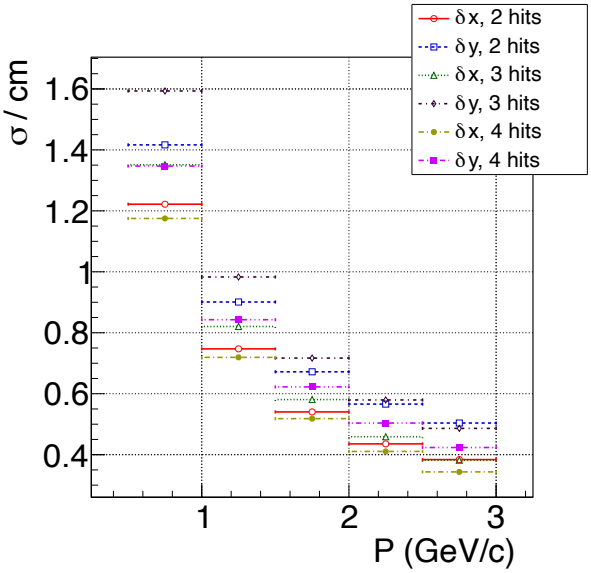

Figure A.12: The performance of the ring track matching using TRD-2D for e^+.

A.3.4 Response from XGBoost model for the training sample with inclusion of TRD backtracked variables

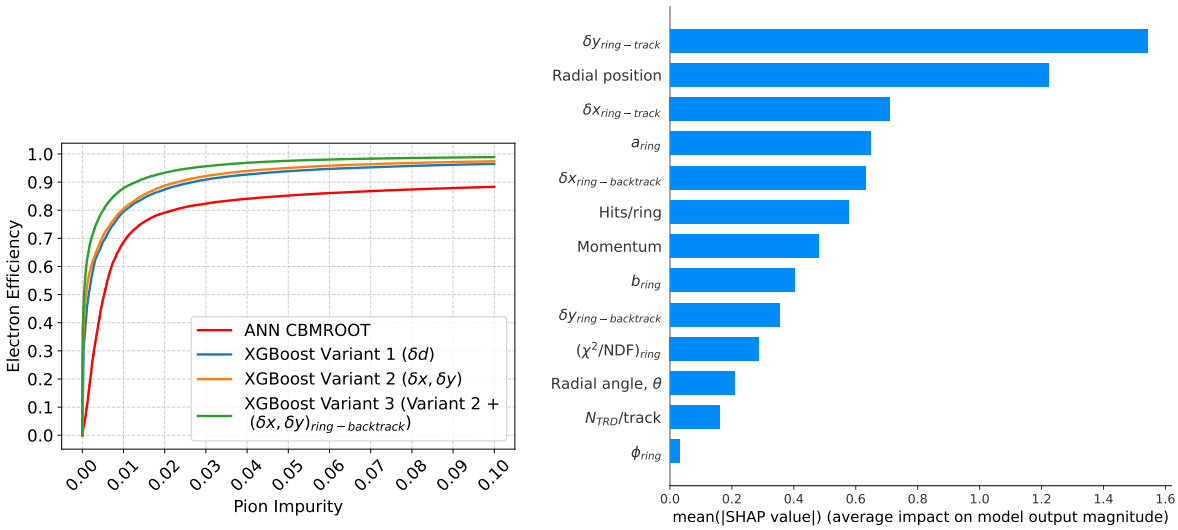

Figure A.13: Response from the ML model for training sample with inclusion of TRD backtracking variables Left panel: ROC curve depicting the reduced pion impurity for same electron identification efficiency. Right panel: Relative input variable importance chart measured by the SHAP metric.

A.3.5 Addressing missing values in the data

Fill the missing data with dummy values, and re-training the model is only advisable if the variables with data missing possess the least significance and exhibit a low correlation with

other input variables. This is because any nonphysical data can be used to fill the missing data, potentially reducing the impact of data changes on the ML inference. For example, if the $\delta x_{ring-backtrack}$ has lower importance, then one can use $\delta x_{ring-backtrack}$ >10 cm for all tracks without TRD acceptance. However, this is not the case for all three backtracking variables in this instance. Here the variables possess greater importance for the ML inference. For example, if $\delta x_{ring-backtrack}$ >10 cm is filled for tracks without TRD acceptance, there is a possibility that the model will consistently classify these tracks as pions. Nevertheless, it is possible to try different combinations of nonphysical TRD hits and backtracking distances to compare model performance, which may not guarantee the expected performance which is achieved for the TRD tracks with acceptance (figure 6.17). Therefore, in this thesis, the option of using two different models for two scenarios involving acceptance of the TRD tracks is used.

A.4 Additional figures for Chapter 7

A.4.1 Angular acceptance as a function of conversion vertex for conversion electrons

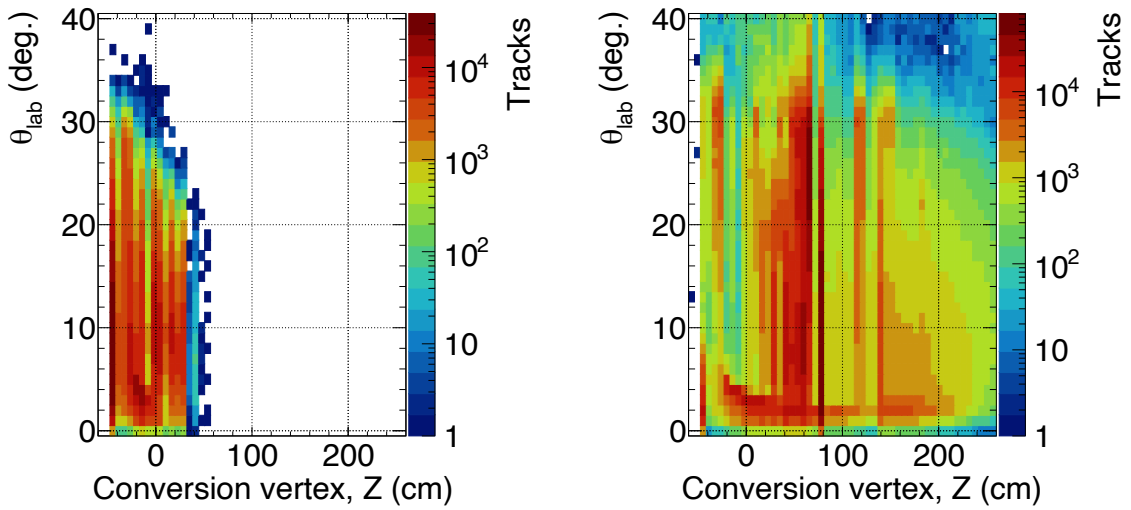

Figure A.14: Acceptance polar angle as function of conversion vertex for tracked conversion electrons (left) and untracked conversion electrons (right).

A.4.2 Response from XGBoost model trained for deriving conversion probability for the ring

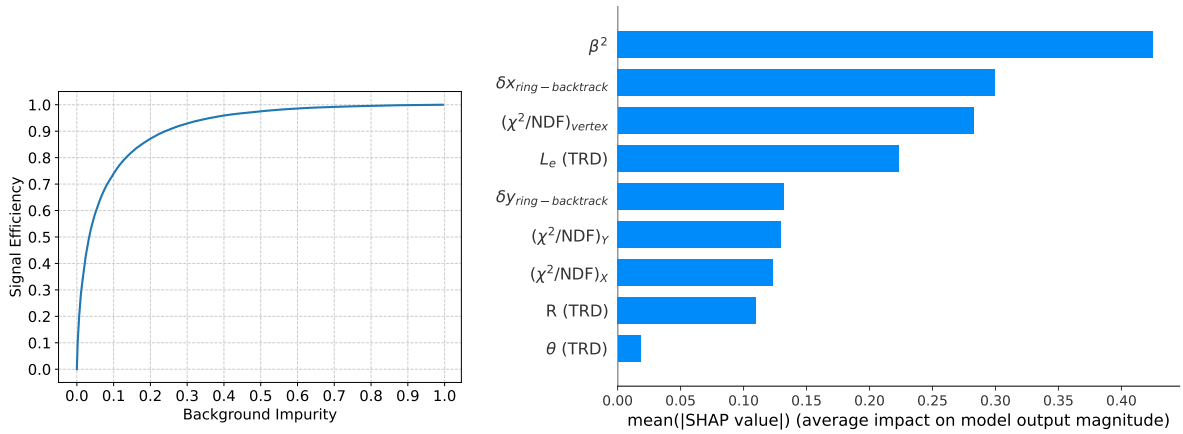

Figure A.15: Response from the ML model for the training sample. Left panel: ROC curve depicting the background backtracks impurity for different signal efficiency. Right panel: Relative input variable importance chart measured by the SHAP metric.

A.4.3 Response from the XGBoost model for the training sample with inclusion of differential distance measure and conversion probability

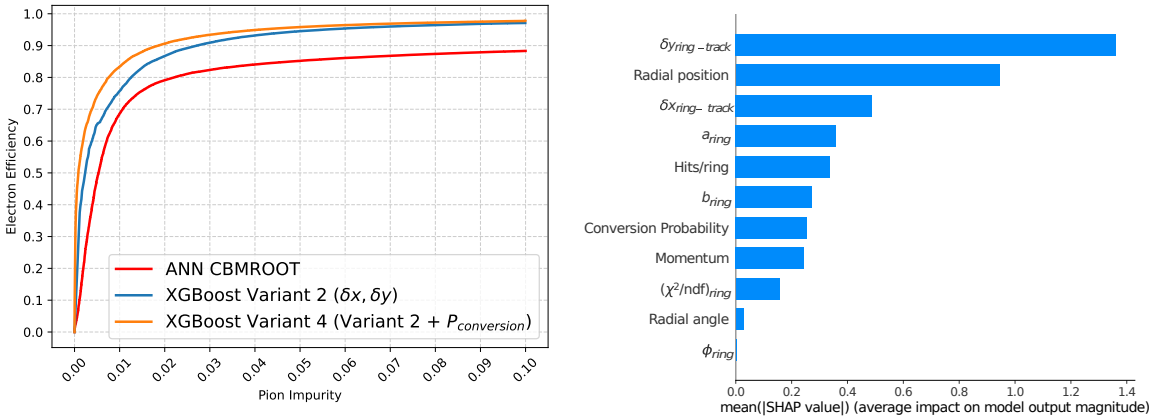

Figure A.16: Response from the ML models after including the conversion probability metric to the RICH standalone input features for the training sample. Left panel: ROC curve depicting the pion impurity for different electron identification efficiency. Right panel: Relative input variable importance chart measured by the SHAP metric.

A.4.4 Response from the upgraded XGBoost model for the training sample with inclusion of TRD backtracked ring-track distances and conversion probability

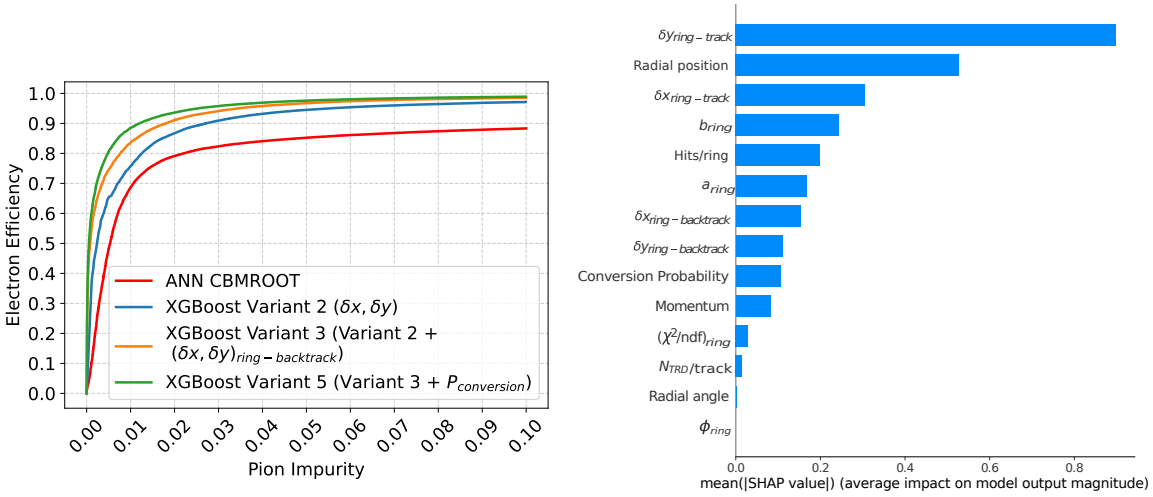

Figure A.17: Response from the ML model for the training sample. Left panel: ROC curve depicting the pion impurity for different electron identification efficiency. Right panel: Relative input variable importance chart measured by the SHAP metric.

A.5 Additional figures for Chapter 8

A.5.1 Omega meson signal estimation using ANN in CBMROOT as electron identifier

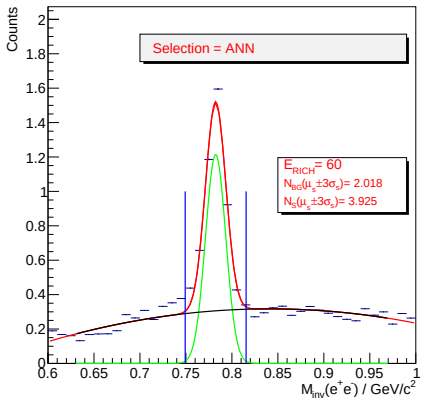

(a) Efficiency = 60%

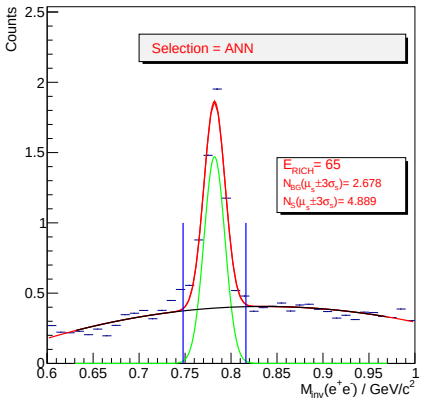

(b) Efficiency = 65%

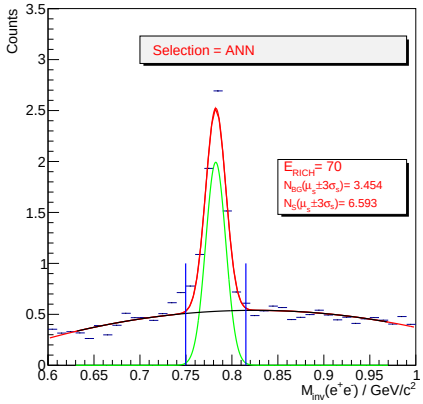

(c) Efficiency = 70%

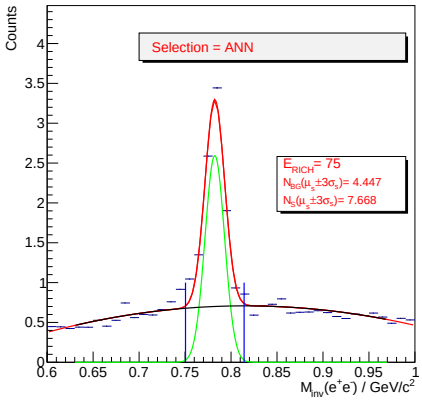

(d) Efficiency = 75%

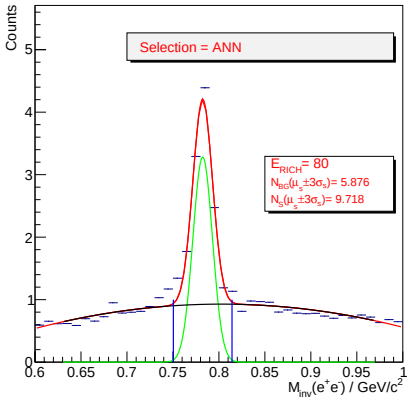

(e) Efficiency = 80%

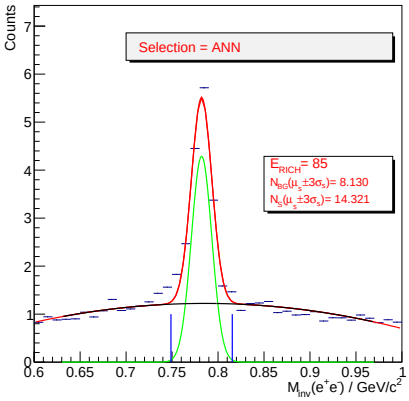

(f) Efficiency = 85%

Figure A.18: The figure depicts signal ω reconstructed with electron candidates selected using ANN in CBMROOT for different RICH electron reconstruction efficiencies.

A.5.2 Omega meson signal estimation using XGBoost model variant 1 as electron identifier

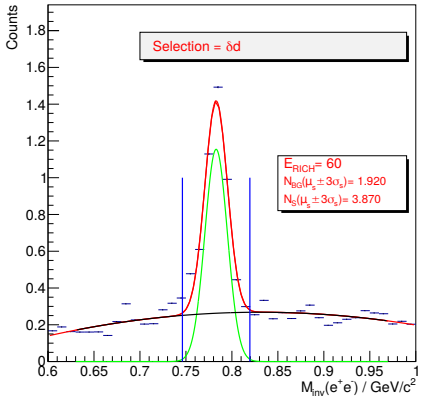

(a) Efficiency = 60%

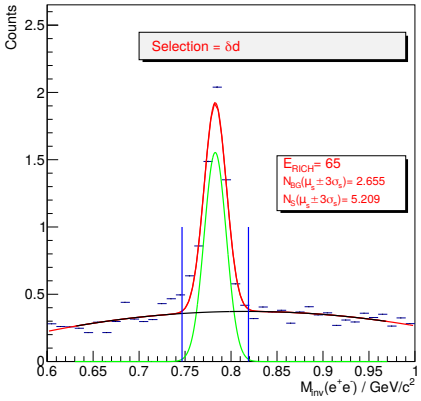

(b) Efficiency = 65%

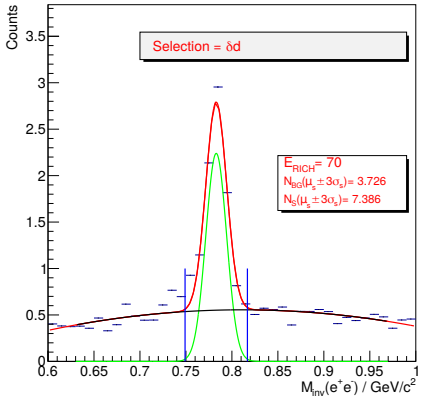

(c) Efficiency = 70%

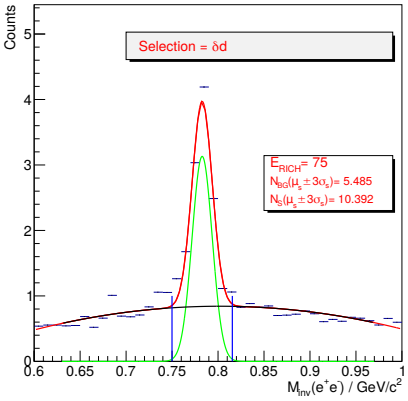

(d) Efficiency = 75%

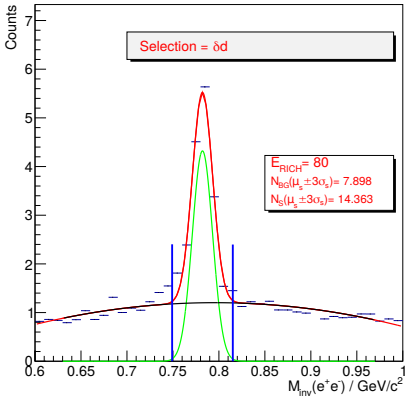

(e) Efficiency = 80%

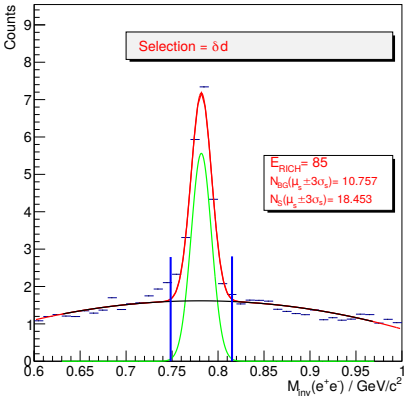

(f) Efficiency = 85%

Figure A.19: The figure depicts signal ω reconstructed with electron candidates selected with XGBoost model (δd) trained with same input features as ANN cut for different RICH electron reconstruction efficiencies.

A.5.3 Omega meson signal estimation using XGBoost model variant 2 as electron identifier

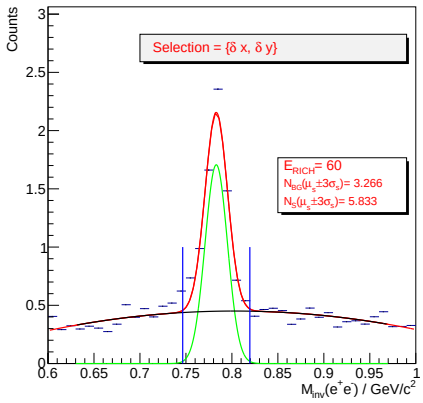

(a) Efficiency = 60%

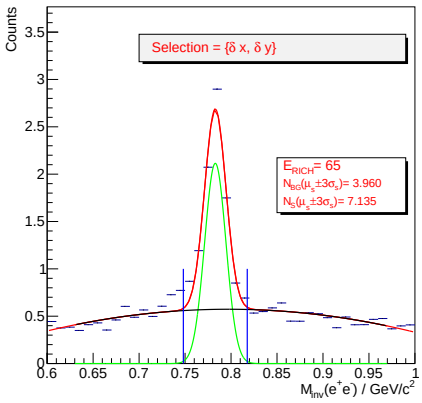

(b) Efficiency = 65%

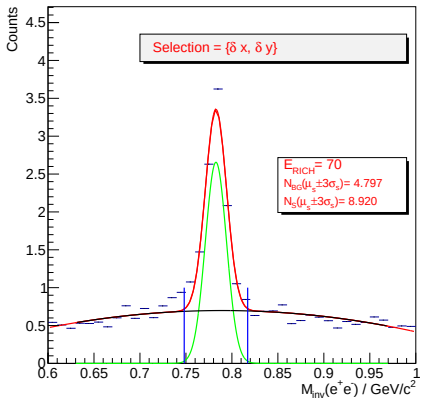

(c) Efficiency = 70%

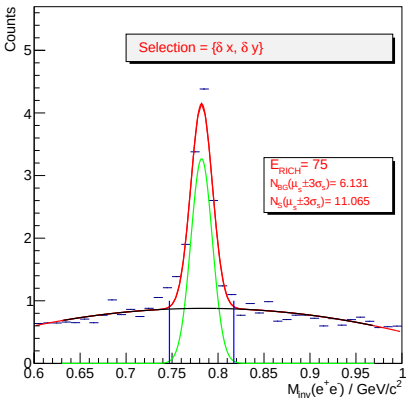

(d) Efficiency = 75%

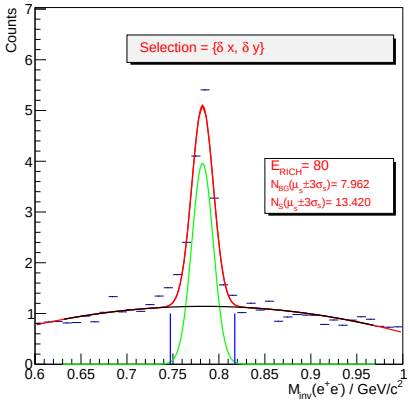

(e) Efficiency = 80%

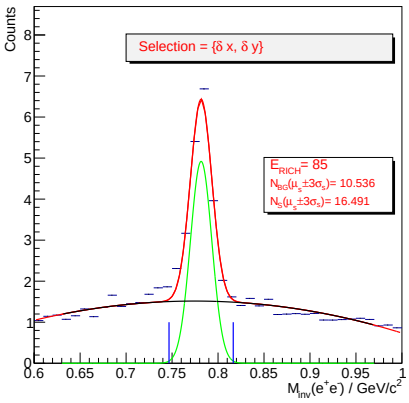

(f) Efficiency = 85%

Figure A.20: The figure depicts signal ω reconstructed with electron candidates selected using XGBoost model trained with features including the differential ring-track distances $(\delta x, \delta y)$. Different subplots represent the reconstruction of signal for different RICH electron reconstruction efficiencies.

A.5.4 Omega meson signal estimation using XGBoost model variant 3 as electron identifier

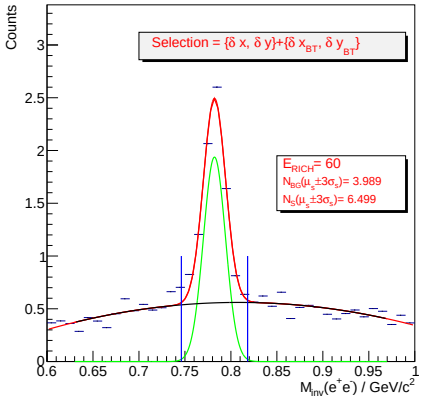

(a) Efficiency = 60%

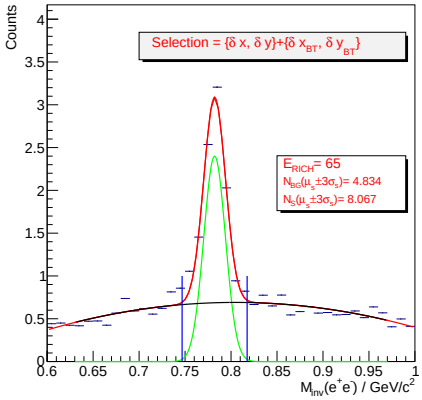

(b) Efficiency = 65%

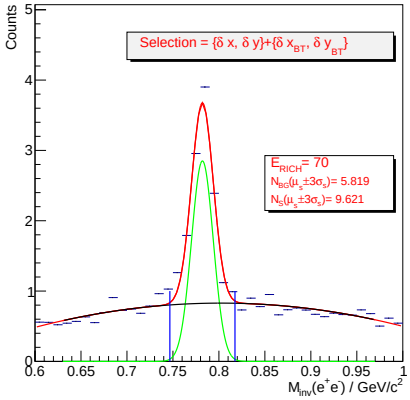

(c) Efficiency = 70%

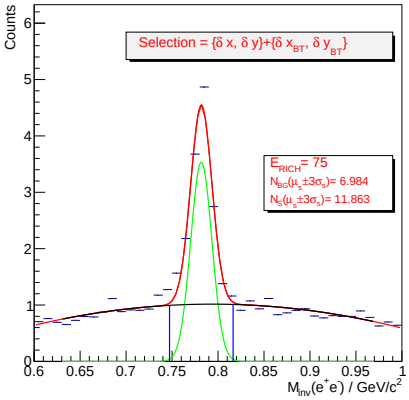

(d) Efficiency = 75%

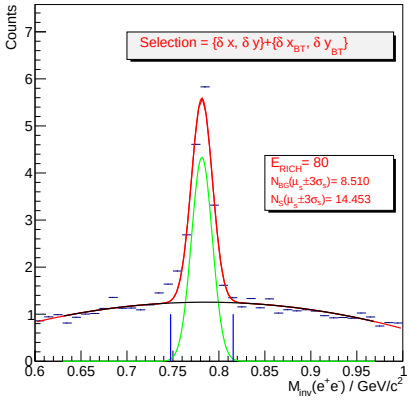

(e) Efficiency = 80%

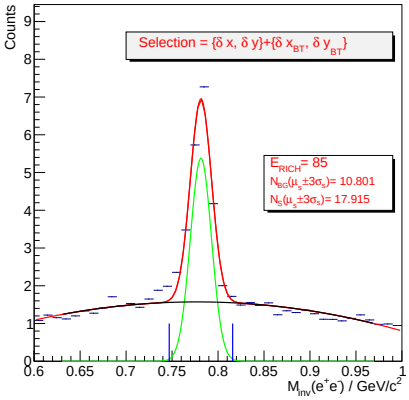

(f) Efficiency = 85%

Figure A.21: The figure depicts the signal ω reconstructed with electron candidates selected using the XGBoost model trained with features including the differential ring-track distance $(\delta x, \delta y)$, and TRD backtracked ring-track reference $(\delta x_{BT}, \delta y_{BT})$. Different subplots represent the reconstruction of signal for different RICH electron reconstruction efficiencies.

A.5.5 Omega meson signal estimation using XGBoost model variant 4 as electron identifier

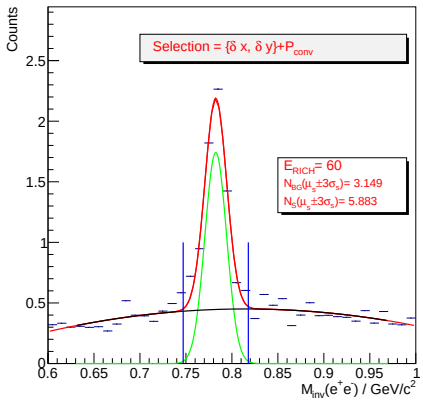

(a) Efficiency = 60%

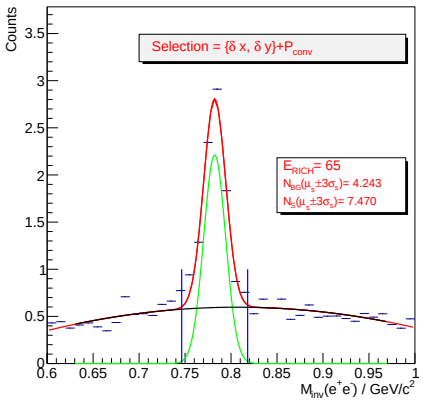

(b) Efficiency = 65%

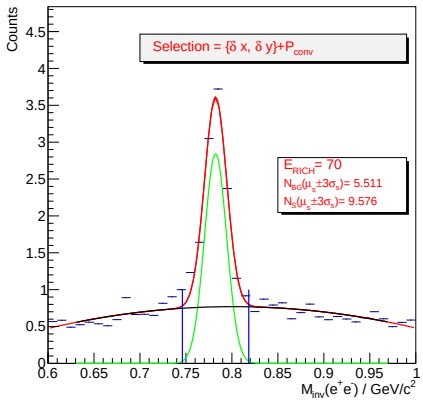

(c) Efficiency = 70%

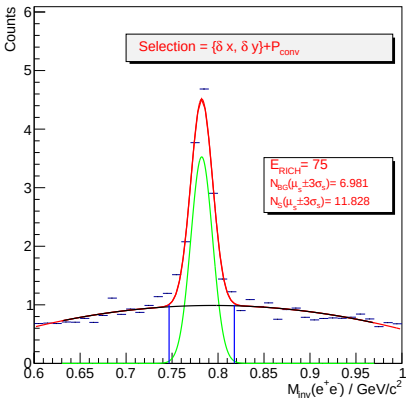

(d) Efficiency = 75%

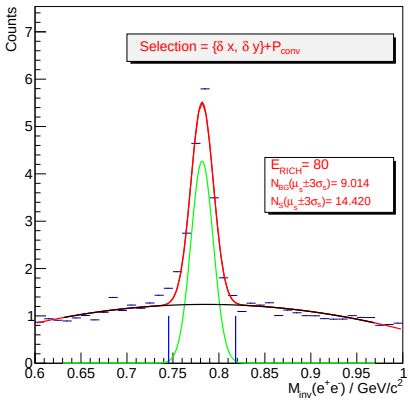

(e) Efficiency = 80%

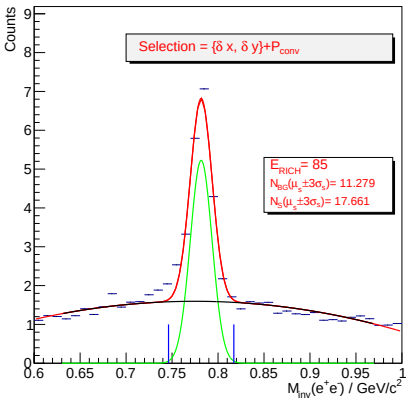

(f) Efficiency = 85%

Figure A.22: The figure depicts the signal ω reconstructed with electron candidates selected using the XGBoost model trained with features including the differential ring-track distance, and the conversion probability. Different subplots represent the reconstruction of signal for different RICH electron reconstruction efficiencies.

A.5.6 Omega meson signal estimation using XGBoost model variant 5 as electron identifier

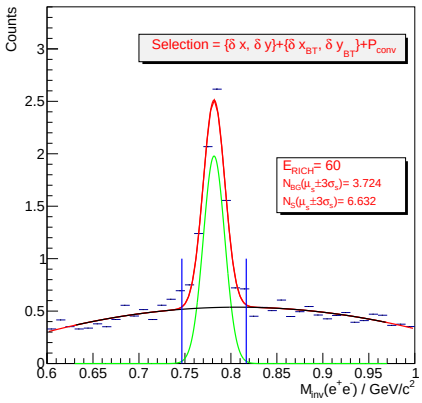

(a) Efficiency = 60%

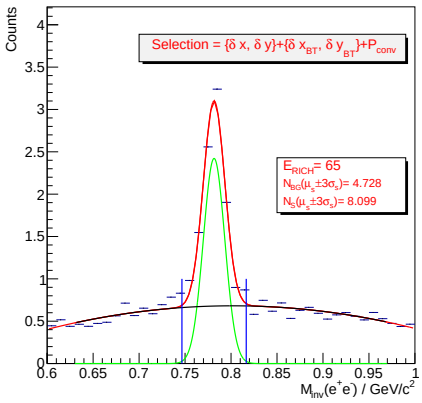

(b) Efficiency = 65%

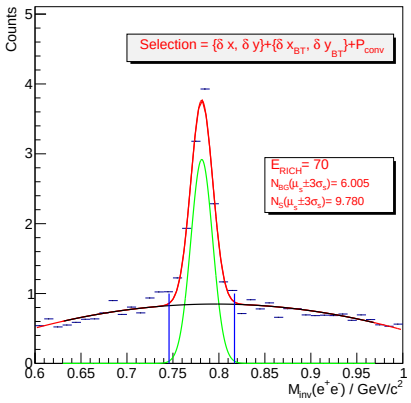

(c) Efficiency = 70%

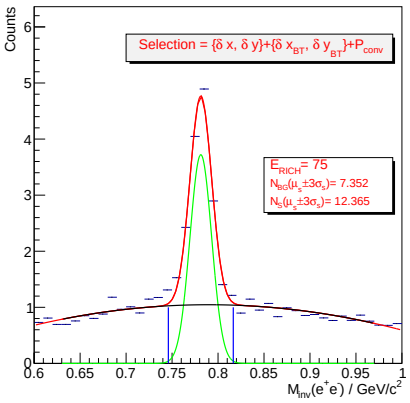

(d) Efficiency = 75%

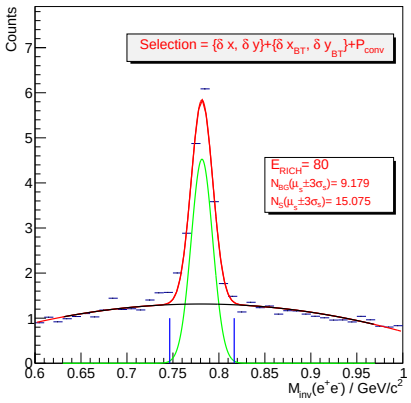

(e) Efficiency = 80%

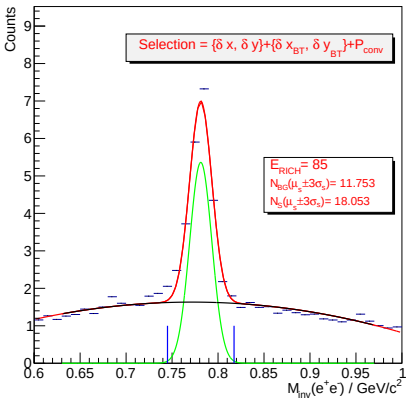

(f) Efficiency = 85%

Figure A.23: The figure depicts the signal ω reconstructed with electron candidates selected using the XGBoost model trained with features including the differential ring-track distance $(\delta x, \delta y)$, TRD backtracked ring-track reference $(\delta x_{BT}, \delta y_{BT})$, and conversion probability for the rings (P_{conv}). Different subplots represent the reconstruction of signal for different RICH electron reconstruction efficiencies.

A.5.7 Non-electron background estimation using ANN in CBMROOT as electron identifier

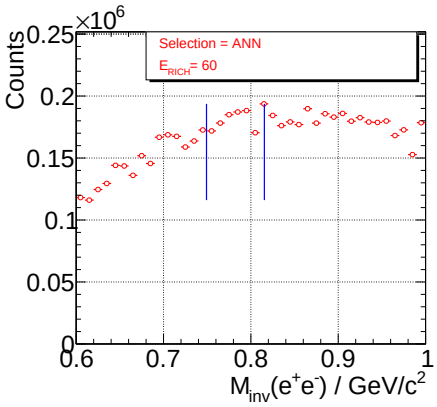

(a) Efficiency = 60%

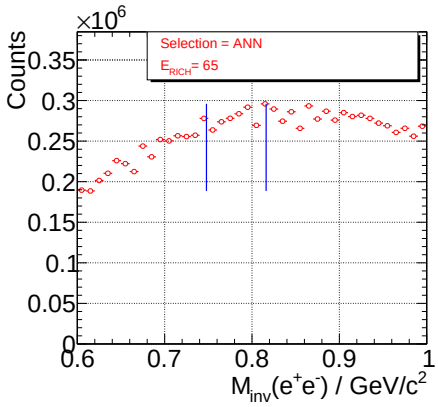

(b) Efficiency = 65%

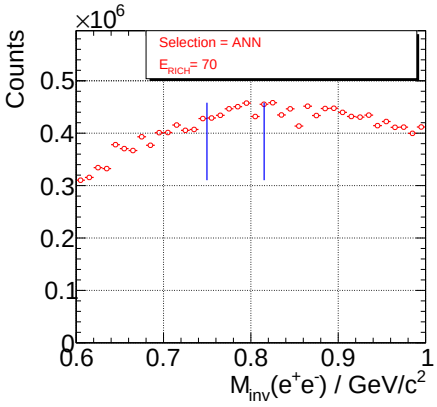

(c) Efficiency = 70%

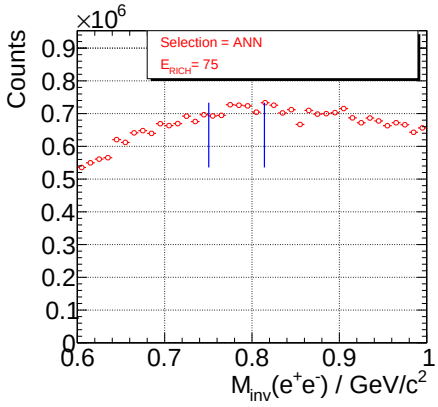

(d) Efficiency = 75%

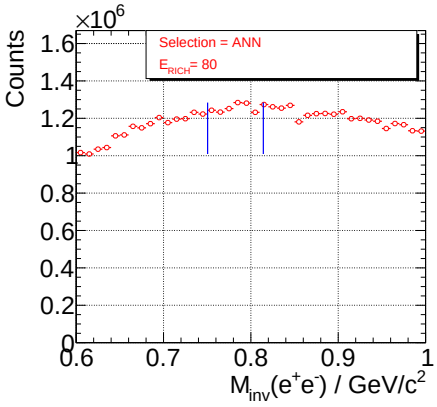

(e) Efficiency = 80%

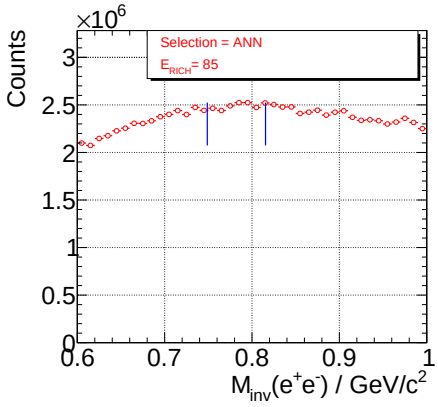

(f) Efficiency = 85%

Figure A.24: The figure depicts non-electron background reconstructed with signal selection criteria, with electron candidates selected using ANN in CBMROOT for different RICH electron reconstruction efficiencies.

A.5.8 Non-electron background estimation using XGBoost model variant 1 as electron identifier

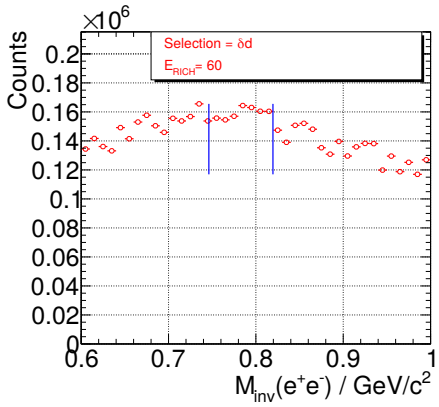

(a) Efficiency = 60%

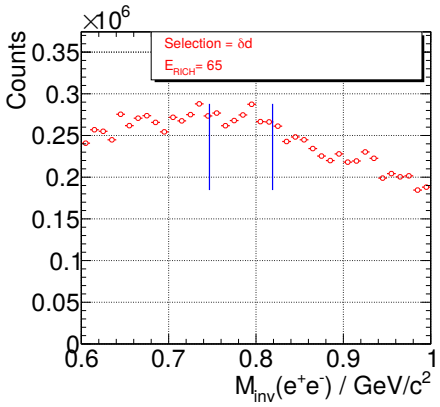

(b) Efficiency = 65%

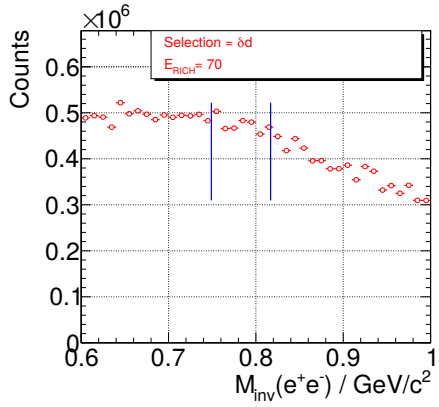

(c) Efficiency = 70%

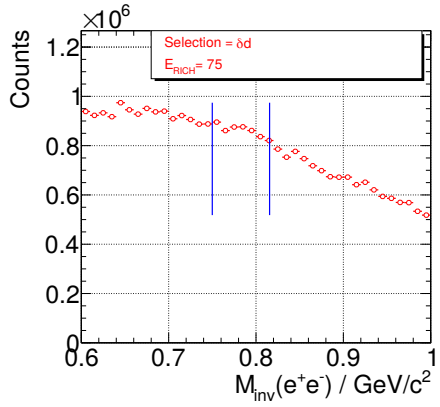

(d) Efficiency = 75%

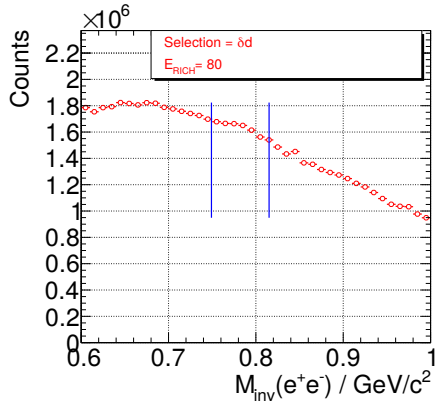

(e) Efficiency = 80%

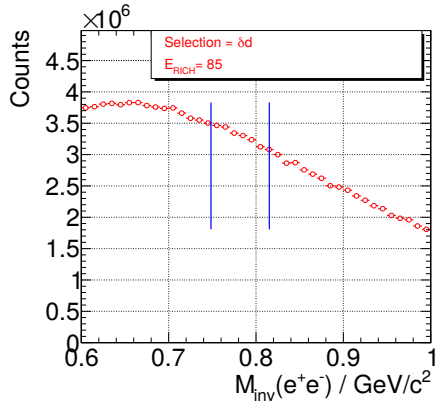

(f) Efficiency = 85%

Figure A.25: The figure depicts non-electron background reconstructed with signal selection criteria, with electron candidates selected with a XGBoost model (δd) trained with same input features as ANN cut for different RICH electron reconstruction efficiencies.

A.5.9 Non-electron background estimation using XGBoost model variant 2 as electron identifier

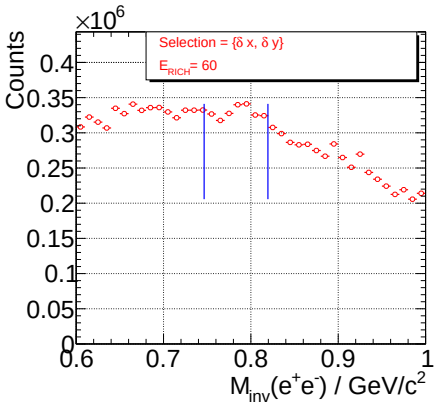

(a) Efficiency = 60%

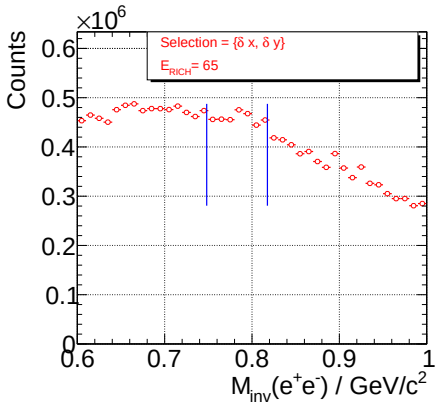

(b) Efficiency = 65%

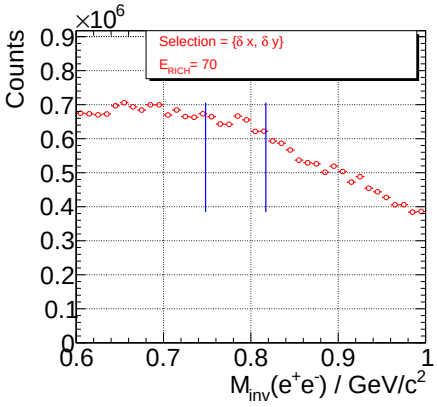

(c) Efficiency = 70%

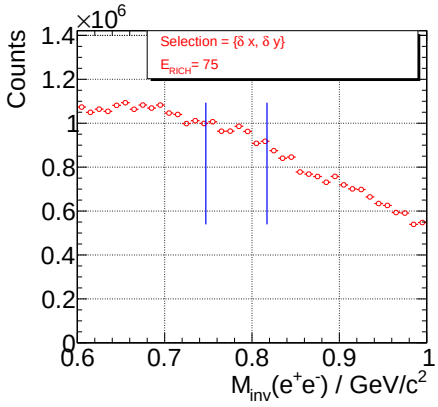

(d) Efficiency = 75%

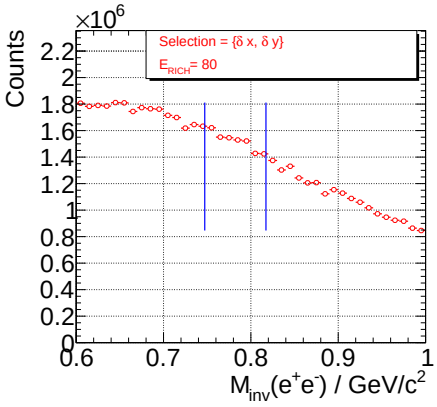

(e) Efficiency = 80%

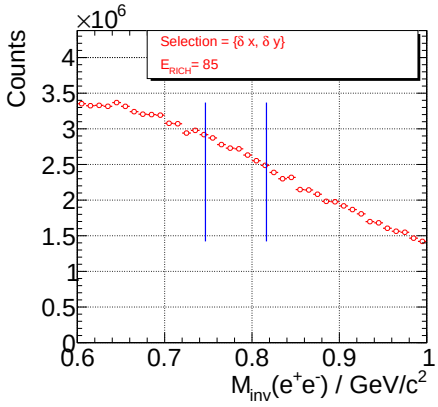

(f) Efficiency = 85%

Figure A.26: The figure depicts non-electron background reconstructed with signal selection criteria, with electron candidates selected using a XGBoost model trained with features including the differential ring-track distances $(\delta x, \delta y)$. Different subplots represent the reconstruction status for different RICH electron reconstruction efficiencies.

A.5.10 Non-electron background estimation using XGBoost model variant 3 as electron identifier

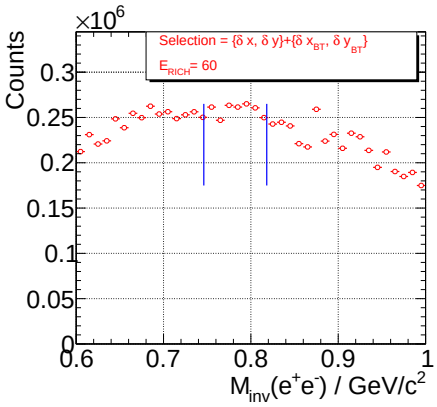

(a) Efficiency = 60%

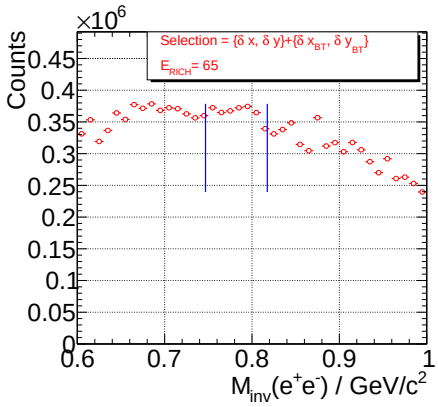

(b) Efficiency = 65%

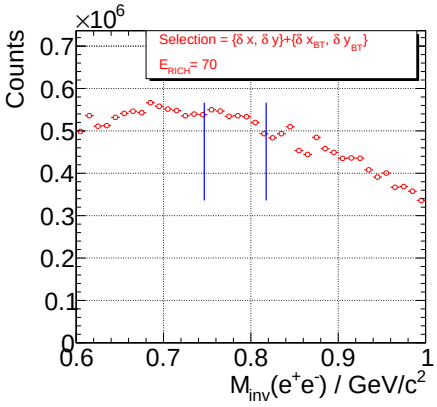

(c) Efficiency = 70%

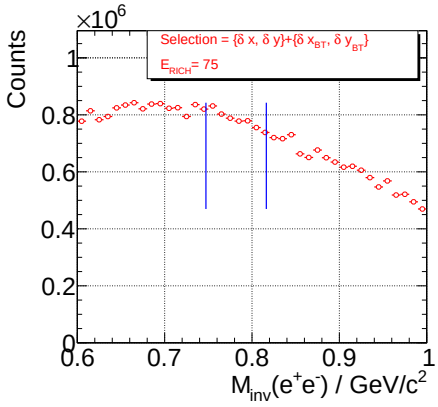

(d) Efficiency = 75%

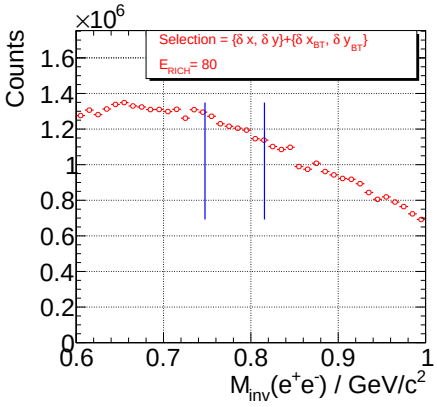

(e) Efficiency = 80%

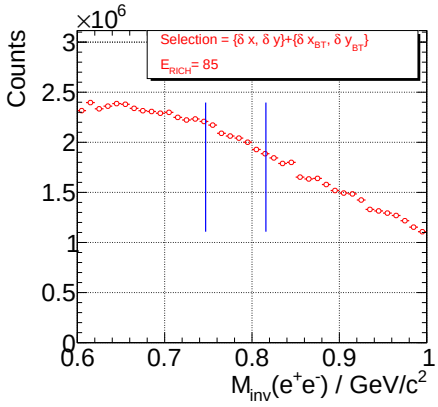

(f) Efficiency = 85%

Figure A.27: The figure depicts the non-electron background reconstructed with signal selection criteria with electron candidates selected using the XGBoost model trained with features including the differential ring-track distance $(\delta x, \delta y)$, and TRD backtracked ring-track reference $(\delta x_{BT}, \delta y_{BT})$. Different subplots represent the reconstruction status for different RICH electron reconstruction efficiencies.

A.5.11 Non-electron background estimation using XGBoost model variant 4 as electron identifier

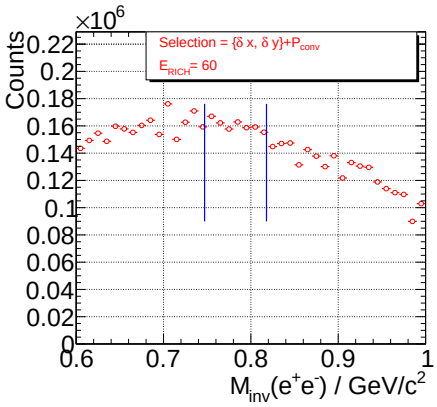

(a) Efficiency = 60%

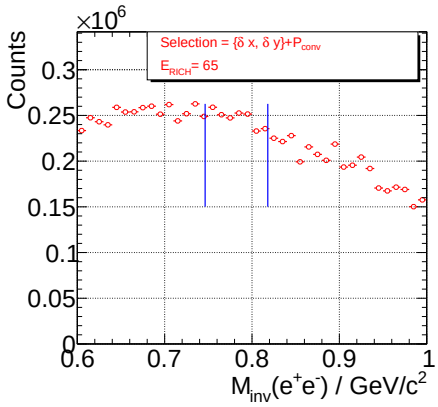

(b) Efficiency = 65%

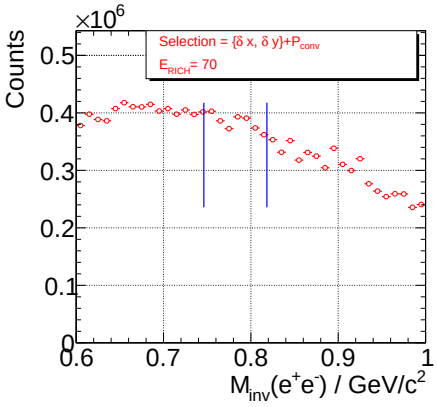

(c) Efficiency = 70%

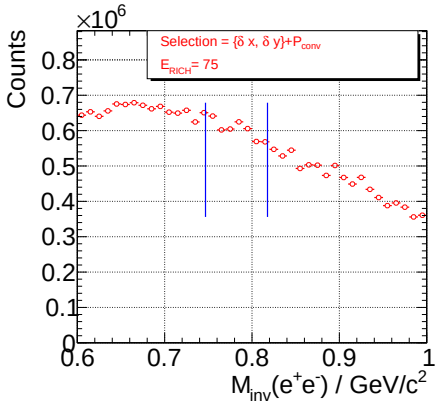

(d) Efficiency = 75%

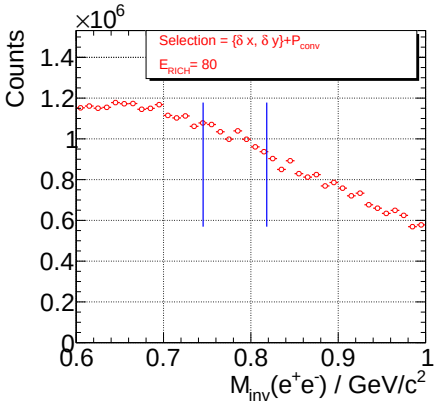

(e) Efficiency = 80%

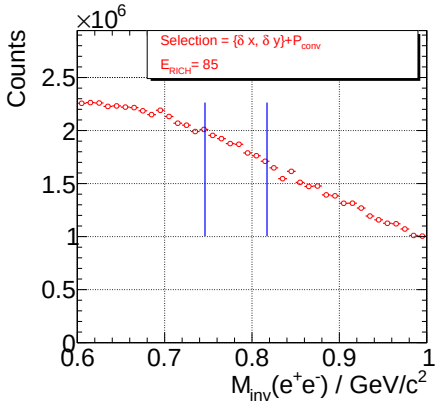

(f) Efficiency = 85%

Figure A.28: The figure depicts the non-electron background reconstructed with signal selection criteria with electron candidates selected using the XGBoost model trained with features including the differential ring-track distance and the conversion probability. Different subplots represent the reconstruction status for different RICH electron reconstruction efficiencies.

A.5.12 Non-electron background estimation using XGBoost model variant 5 as electron identifier

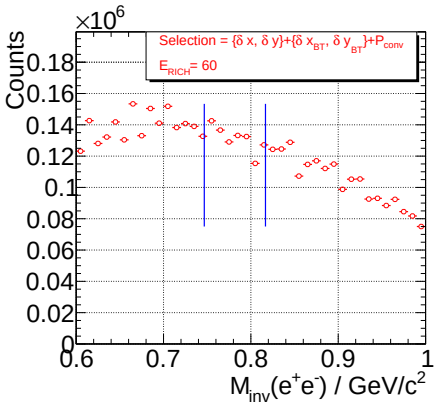

(a) Efficiency = 60%

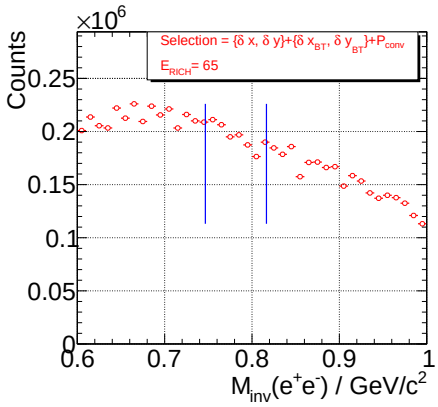

(b) Efficiency = 65%

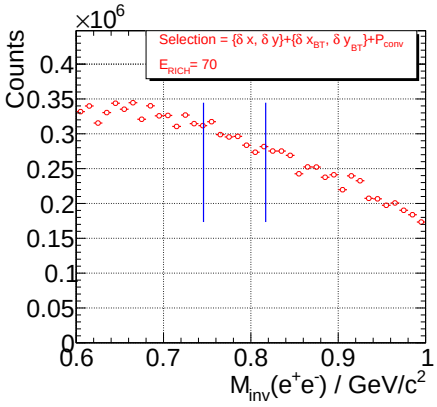

(c) Efficiency = 70%

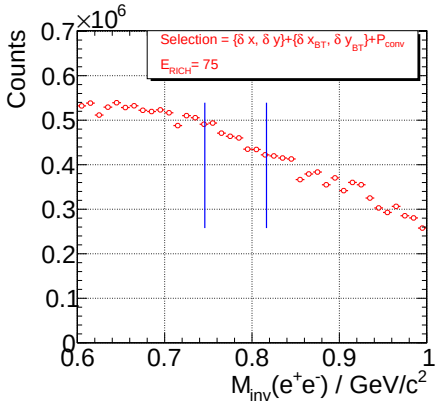

(d) Efficiency = 75%

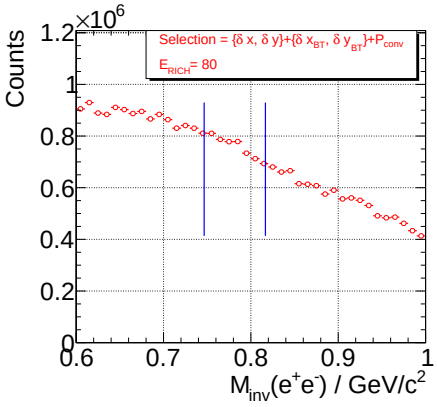

(e) Efficiency = 80%

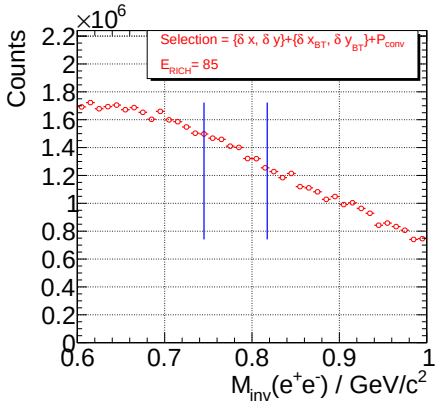

(f) Efficiency = 85%

Figure A.29: The figure depicts the non-electron background reconstructed with signal selection criteria with electron candidates selected using the XGBoost model trained with features including the differential ring-track distance $(\delta x, \delta y)$, TRD back-tracked ring-track reference $(\delta x_{BT}, \delta y_{BT})$, and conversion probability for the rings (P_{conv}). Different subplots represent the reconstruction status for different RICH electron reconstruction efficiencies.

A.5.13 Omega meson signal estimation using conventional ANN and XGBoost variants as electron identifiers at the point of maximum significance

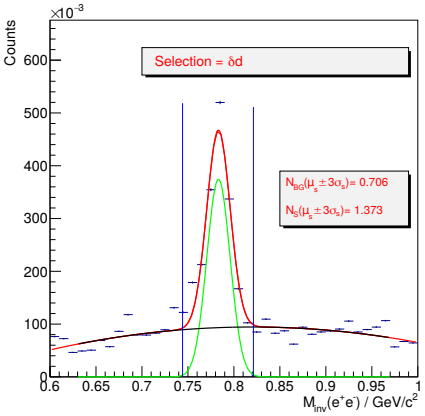

(a) XGBoost variant 1 - δd

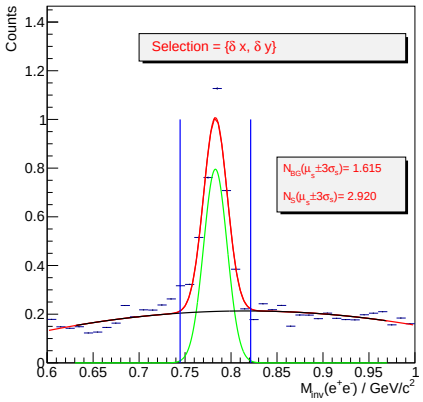

(b) XGBoost variant 2 - $(\delta x,\ \delta y)$

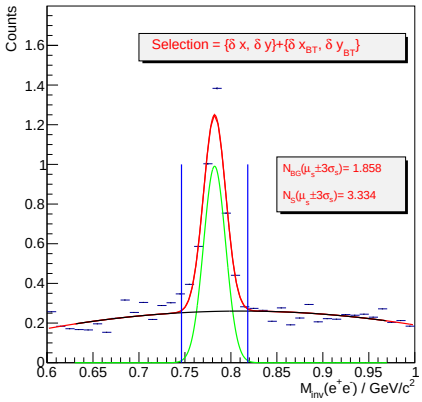

(c) XGBoost variant 3 - $(\delta x,\ \delta y)\ +$ $(\delta x_{BT}, \delta y_{BT} + N_{hits}^{TRD}$

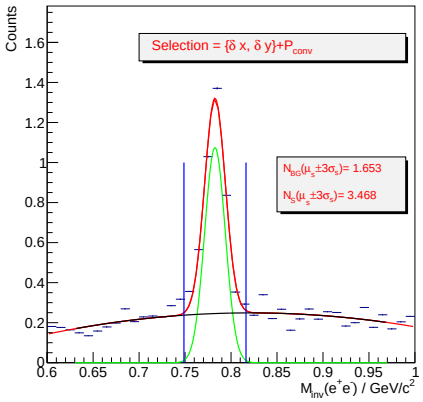

(d) XGBoost variant 4 - $(\delta x,\ \delta y) + P_{conv}$

Figure A.30: The figure depicts the signal ω reconstructed with electron candidates selected using different electron identifiers at the point of maximum significance. Different subplots represent the reconstruction of signal for different electron identifiers.

A.5.14 Non-electron background using conventional ANN and XGBoost variants as electron identifiers at the point of maximum significance

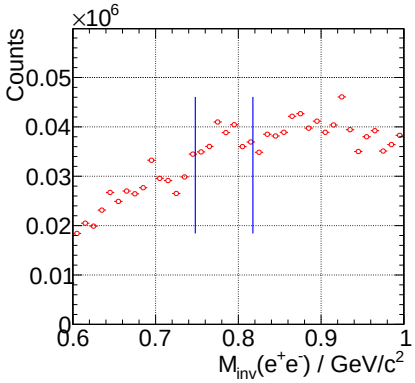

(a) Conventional ANN

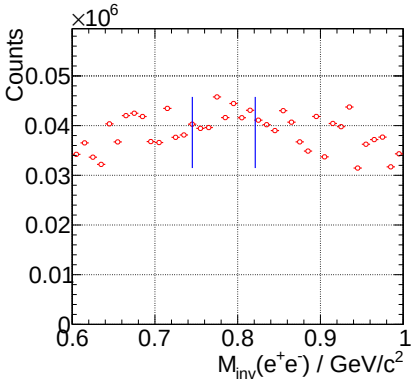

(b) XGBoost variant 1 - δd

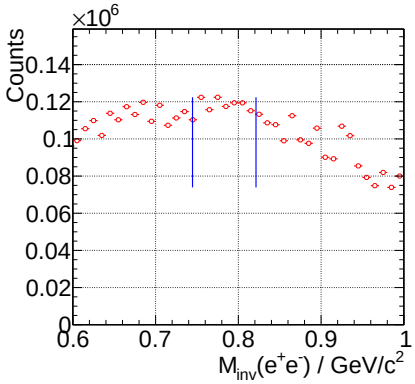

(c) XGBoost variant 2 - (δx, δy)

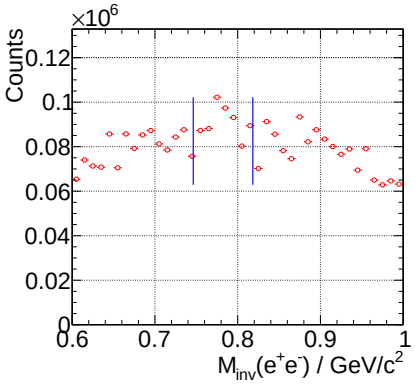

(d) XGBoost variant 3 - (δx, δy) + ($\delta x_{BT}, \delta y_{BT} + N_{hits}^{TRD}$)

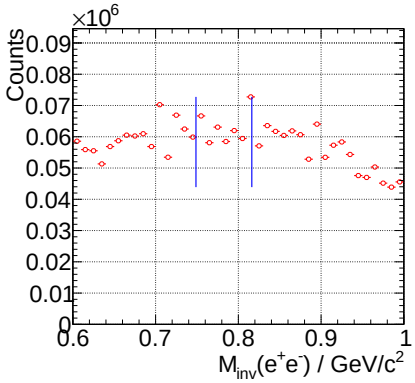

(e) XGBoost variant 4 - (δx, δy) + P_{conv}

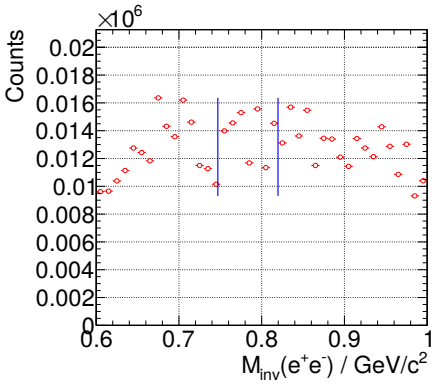

(f) XGBoost variant 5- (δx, δy) + ($\delta x_{BT}, \delta y_{BT} + N_{hits}^{TRD}$) + P_{conv}

Figure A.31: The figure depicts the non-electron background reconstructed with signal selection criteria, with electron candidates selected using different electron identifiers at the point of maximum significance. Different subplots represent the reconstruction status for different electron identifiers.

References

[1] W. N. Cottingham and D. A. Greenwood. *An Introduction to the Standard Model of Particle Physics*. 2nd ed. Cambridge University Press, 2007.

[2] Cliff Burgess and Guy Moore. *The Standard Model: A Primer*. Cambridge University Press, 2006.

[3] David J Griffiths. *Introduction to elementary particles; 2nd rev. version*. Physics textbook. New York, NY: Wiley, 2008. URL: https://cds.cern.ch/record/111880.

[4] David Tong. *David Tong, Lectures on Particle physics (CERN)*. URL: http://www.damtp.cam.ac.uk/user/tong/particle.html.

[5] Stefan Scherer and Matthias R. Schindler. *A Chiral Perturbation Theory Primer*. 2005. arXiv: hep-ph/0505265 [hep-ph]. URL: https://arxiv.org/abs/hep-ph/0505265.

[6] Michelangelo L Mangano. 'Introduction to QCD'. In: *CERN-OPEN-2000-255* (2000). DOI: 10.5170/CERN-1999-004.53. URL: https://cds.cern.ch/record/454171.

[7] David J. Gross. 'Asymptotic Freedom, Confinement and QCD'. In: *History of Original Ideas and Basic Discoveries in Particle Physics*. Ed. by Harvey B. Newman and Thomas Ypsilantis. Boston, MA: Springer US, 1996, pp. 75–99. DOI: 10.1007/978-1-4613-1147-8_7. URL: https://doi.org/10.1007/978-1-4613-1147-8_7.

[8] Frank Wilczek. 'Nobel Lecture: Asymptotic freedom: From paradox to paradigm'. In: *Rev. Mod. Phys.* 77 (3 2005), pp. 857–870. DOI: 10.1103/RevModPhys.77.857. URL: https://link.aps.org/doi/10.1103/RevModPhys.77.857.

[9] Yi-Bo Yang et al. 'Proton Mass Decomposition from the QCD Energy Momentum Tensor'. In: *Phys. Rev. Lett.* 121 (21 Nov. 2018), p. 212001. DOI: 10.1103/PhysRevLett.121.212001. URL: https://link.aps.org/doi/10.1103/PhysRevLett.121.212001.

[10] Kohsuke Yagi, Tetsuo Hatsuda and Yasuo Miake. *Quark-Gluon Plasma*. Cambridge University Press, 2005.

[11] *ALICE at LHC website*. URL: https://alice.cern/.

[12] *STAR at RHIC website*. URL: https://www.bnl.gov/rhic/star.php.

[13] *NA61 at SPS website*. URL: https://shine.web.cern.ch/.

[14] *HADES at SIS18 website*. URL: https://hades.gsi.de/.

[15] Michael Strickland. *Hydrodynamization and resummed viscous hydrodynamics*. 2024. arXiv: 2402.09571 [nucl-th]. URL: https://arxiv.org/abs/2402.09571.

[16] Marin, A et al. Gonzalez, V. Basu, S. 'Extraction of the specific shear viscosity of quark-gluon plasma from two-particle transverse momentum correlations'. In: *Eur. Phys. J. C* 81 (2021), p. 465. DOI: https://doi.org/10.1140/epjc/s10052-021-09260-z.

[17] ALICE Collaboration. 'Correlated Event-by-Event Fluctuations of Flow Harmonics in Pb-Pb Collisions at $\sqrt{s_{NN}} = 2.76$ TeV'. In: *Phys. Rev. Lett.* 117 (18 Oct. 2016), p. 182301. DOI: 10.1103/PhysRevLett.117.182301. URL: https://link.aps.org/doi/10.1103/PhysRevLett.117.182301.

[18] Y. Aoki et al. 'The order of the quantum chromodynamics transition predicted by the standard model of particle physics'. In: *Nature* 443.7112 (Oct. 2006), pp. 675–678. ISSN: 1476-4687. DOI: 10.1038/nature05120. URL: https://doi.org/10.1038/nature05120.

[19] V. A. Goy et al. 'Sign problem in finite density lattice QCD'. In: *Progress of Theoretical and Experimental Physics* 2017.3 (Mar. 2017), p. 031D01. ISSN: 2050-3911. DOI: 10.1093/ptep/ptx018. eprint: https://academic.oup.com/ptep/article-pdf/2017/3/031D01/11150731/ptx018.pdf. URL: https://doi.org/10.1093/ptep/ptx018.

[20] *The 39th International Symposium on Lattice Field Theory*. https://pos.sissa.it/430/.

[21] Masashi Kaneta. 'Thermal and Chemical Freeze-out in Heavy Ion Collisions'. PhD thesis. Hiroshima U., 1999.

[22] Anton Andronic et al. 'Decoding the phase structure of QCD via particle production at high energy'. In: *Nature* 561.7723 (Sept. 2018), pp. 321–330. ISSN: 1476-4687. DOI: 10.1038/s41586-018-0491-6. URL: https://doi.org/10.1038/s41586-018-0491-6.

[23] *The CBM Physics Book*. DOI: https://doi.org/10.1007/978-3-642-13293-3.

[24] Jean-Yves Ollitrault. 'Anisotropy as a signature of transverse collective flow'. In: *Phys. Rev. D* 46 (1 July 1992), pp. 229–245. DOI: 10.1103/PhysRevD.46.229. URL: https://link.aps.org/doi/10.1103/PhysRevD.46.229.

[25] R. Averbeck. 'Heavy-flavor production in heavy-ion collisions and implications for the properties of hot QCD matter'. In: *Progress in Particle and Nuclear Physics* 70 (2013), pp. 159–209. ISSN: 0146-6410. DOI: https://doi.org/10.1016/j.ppnp.2013.01.001. URL: https://www.sciencedirect.com/science/article/pii/S0146641013000021.

[26] Masayuki Asakawa and Masakiyo Kitazawa. 'Fluctuations of conserved charges in relativistic heavy ion collisions: An introduction'. In: *Progress in Particle and Nuclear Physics* 90 (2016), pp. 299–342. ISSN: 0146-6410. DOI: https://doi.org/10.1016/j.ppnp.2016.04.002. URL: https://www.sciencedirect.com/science/article/pii/S0146641016300023.

[27] E. L. Feinberg. 'Direct production of photons and dileptons in thermodynamical models of multiple hadron production'. In: *Il Nuovo Cimento A (1965-1970)* 34.3 (Aug. 1976), pp. 391–412. ISSN: 1826-9869. DOI: 10.1007/BF02783618. URL: https://doi.org/10.1007/BF02783618.

[28] L. D. McLerran and T. Toimela. 'Photon and dilepton emission from the quark-gluon plasma: Some general considerations'. In: *Phys. Rev. D* 31 (3 Feb. 1985), pp. 545–563. DOI: 10.1103/PhysRevD.31.545. URL: https://link.aps.org/doi/10.1103/PhysRevD.31.545.

[29] R. Rapp, G. Chanfray and J. Wambach. 'Rho meson propagation and dilepton enhancement in hot hadronic matter'. In: *Nuclear Physics A* 617.4 (1997), pp. 472–495. ISSN: 0375-9474. DOI: https://doi.org/10.1016/S0375-9474(97)00137-1. URL: https://www.sciencedirect.com/science/article/pii/S0375947497001371.

[30] R. Rapp and J. Wambach. *Chiral Symmetry Restoration and Dileptons in Relativistic Heavy-Ion Collisions*. 1999. arXiv: hep-ph/9909229 [hep-ph]. URL: https://arxiv.org/abs/hep-ph/9909229.

[31] Ralf Rapp and Charles Gale. 'ρ properties in a hot meson gas'. In: *Phys. Rev. C* 60 (2 July 1999), p. 024903. DOI: 10.1103/PhysRevC.60.024903. URL: https://link.aps.org/doi/10.1103/PhysRevC.60.024903.

[32] Karl-Heinz Kampert. '"Electromagnetic Probes of Hot and Dense Nuclear Matter"'. In: *"Hot and Dense Nuclear Matter"*. Ed. by Walter Greiner, Horst Stöcker and André Gallmann. "Boston, MA": "Springer US", 1994, "23–37". ISBN: "978-1-4615-2516-5". DOI: "10.1007/978-1-4615-2516-5_3". URL: https://doi.org/10.1007/978-1-4615-2516-5_3.

[33] R. Rapp and H. van Hees. 'Thermal electromagnetic radiation in heavy-ion collisions'. In: *The European Physical Journal A* 52.8 (Aug. 2016), p. 257. ISSN: 1434-601X. DOI: 10.1140/epja/i2016-16257-0. URL: https://doi.org/10.1140/epja/i2016-16257-0.

[34] H.Arthur Weldon. 'Thermal phase space'. In: *Annals of Physics* 214.1 (1992), pp. 152–159. ISSN: 0003-4916. DOI: https://doi.org/10.1016/0003-4916(92)90065-T. URL: https://www.sciencedirect.com/science/article/pii/000349169290065T.

[35] Tetyana Galatyuk. 'Di-electron spectroscopy in HADES and CBM : from p + p and n + p collisions at GSI to Au + Au collisions at FAIR'. Doctoral thesis. Universitätsbibliothek Johann Christian Senckenberg, 2009, p. 166.

[36] I. Niculescu et al. 'Experimental Verification of Quark-Hadron Duality'. In: *Phys. Rev. Lett.* 85 (6 Aug. 2000), pp. 1186–1189. DOI: 10.1103/PhysRevLett.85.1186. URL: https://link.aps.org/doi/10.1103/PhysRevLett.85.1186.

[37] J.J. Sakurai. *Currents and Mesons*. The University of Chicago Press, 1969.

[38] M. Herrmann, B.L. Friman and W. Nörenberg. 'Properties of ρ-mesons in nuclear matter'. In: *Nuclear Physics A* 560.1 (1993), pp. 411–436. ISSN: 0375-9474. DOI: https://doi.org/10.1016/0375-9474(93)90105-7. URL: https://www.sciencedirect.com/science/article/pii/0375947493901057.

[39] G. Chanfray, M. Ericson and M. Oertel. 'In-medium modification of the isovector pion–nucleon amplitude'. In: *Physics Letters B* 563.1 (2003), pp. 61–67. ISSN: 0370-2693. DOI: https://doi.org/10.1016/S0370-2693(03)00596-3. URL: https://www.sciencedirect.com/science/article/pii/S0370269303005963.

[40] Bengt Friman. 'Vector meson propagation in dense matter'. In: *APCTP Workshop on Astro-Hadron Physics: Properties of Hadrons in Matter*. Oct. 1997, pp. 337–354. arXiv: nucl-th/9801053.

[41] K Nakamura and (Particle Data Group). 'Review of Particle Physics'. In: *Journal of Physics G: Nuclear and Particle Physics* 37.7A (July 2010), p. 075021. DOI: 10.1088/0954-3899/37/7A/075021. URL: https://dx.doi.org/10.1088/0954-3899/37/7A/075021.

[42] *Tetyana Galatyuk, Measuring the Temperature of the Hot-Dense Fireball, CBM Students seminar*. https://indico.gsi.de/event/12138/ (CBM Internal).

[43] The HADES Collaboration. 'Probing dense baryon-rich matter with virtual photons'. In: *Nature Physics* 15.10 (Oct. 2019), pp. 1040–1045. ISSN: 1745-2481. DOI: 10.1038/s41567-019-0583-8. URL: https://doi.org/10.1038/s41567-019-0583-8.

[44] G Agakichiev et al. 'Systematic study of low-mass electron pair production in p–Be and p–Au collisions at 450 GeV/c'. In: *The European Physical Journal C - Particles and Fields* 4.2 (June 1998), pp. 231–247. ISSN: 1434-6052. DOI: 10.1007/PL00021659. URL: https://doi.org/10.1007/PL00021659.

[45] Yang, Chi. 'Dielectrons and Direct Virutal Photons at RHIC-STAR'. In: *EPJ Web Conf.* 235 (2020), p. 02002. DOI: 10.1051/epjconf/202023502002. URL: https://doi.org/10.1051/epjconf/202023502002.

[46] *Event mixing, ALICE O2 documentation*. https://aliceo2group.github.io/analysis-framework/docs/advanced-specifics/eventMixing.html.

[47] *FAIR website*. https://fair-center.eu/.

[48] *Super Fragment Separator*. https://www.gsi.de/work/gesamtprojektleitung_fair/super_frs.

[49] Herlert, Alexander. 'The NUSTAR program at FAIR - Overview and present status of the project'. In: *EPJ Web of Conferences* "71" (2014), "00064". DOI: "10.1051/epjconf/20147100064". URL: https://doi.org/10.1051/epjconf/20147100064.

[50] *Technical Report for the Design, Construction and Commissioning of the Active Target for FAIR (ACTAF) for the R3B experiment*. https://edms.cern.ch/document/1816116/2.

[51] *Technical Proposal for the ILIMA Project*. https://fair-center.eu/fileadmin/FAIR/experiments/NUSTAR/Pdf/ILIMA_tp_20050120-printed.pdf.

[52] *The APPA collaboration website*. https://fair-center.eu/user/experiments/appa.

[53] *The SPARC experiment website*. https://www.gsi.de/work/forschung/appamml/atomphysik/ap_und_fair/sparc/einleitung.

[54] Th. Stöhlker et al. 'APPA at FAIR: From fundamental to applied research'. In: *Nuclear Instruments and Methods in Physics Research Section B: Beam Interactions with Materials and Atoms* 365 (2015). Swift Heavy Ions in Matter, 18 – 21 May, 2015, Darmstadt, Germany, pp. 680–685. ISSN: 0168-583X. DOI: https://doi.org/10.1016/j.nimb.2015.07.077.

[55] K. Schoenberg et al. 'High-energy-density-science capabilities at the Facility for Antiproton and Ion Research'. In: *Physics of Plasmas* 27.4 (Apr. 2020), p. 043103. ISSN: 1070-664X. DOI: 10.1063/1.5134846. eprint: https://pubs.aip.org/aip/pop/article-pdf/doi/10.1063/1.5134846/15926936/043103_1_online.pdf. URL: https://doi.org/10.1063/1.5134846.

[56] Johan Messchendorp. 'The $\bar{\text{P}}$ANDA Experiment at FAIR — Subatomic Physics with Antiprotons'. In: *Proceedings of the 14th International Conference on Meson-Nucleon Physics and the Structure of the Nucleon (MENU2016)*. DOI: 10.7566/JPSCP.13.010016.

[57] PANDA Collaboration. *Physics Performance Report for PANDA: Strong Interaction Studies with Antiprotons*. 2009. arXiv: 0903.3905 [hep-ex].

[58] *PANDA physics program*. https://panda.gsi.de/article/panda-physics.

[59] *Physics Opportunities with Proton Beams at SIS100*. URL: https://indico.gsi.de/event/18475/overview.

[60] I. C. Arsene et al. 'Dynamical phase trajectories for relativistic nuclear collisions'. In: *Phys. Rev. C* 75 (3 Mar. 2007), p. 034902. DOI: 10.1103/PhysRevC.75.034902. URL: https://link.aps.org/doi/10.1103/PhysRevC.75.034902.

[61] HADES Collaboration. 'Measurement of global polarization of Λ hyperons in few-GeV heavy-ion collisions'. In: *Physics Letters B* 835 (2022), p. 137506. ISSN: 0370-2693. DOI: https://doi.org/10.1016/j.physletb.2022.137506. URL: https://www.sciencedirect.com/science/article/pii/S0370269322006402.

[62] Ilya Selyuzhenkov and (for the STAR Collaboration). 'Global polarization measurement in Au+Au collisions'. In: *Journal of Physics G: Nuclear and Particle Physics* 32.12 (Nov. 2006), S557. DOI: 10.1088/0954-3899/32/12/S76. URL: https://dx.doi.org/10.1088/0954-3899/32/12/S76.

[63] Iouri Vassiliev et al. 'Hypernuclei Program at the CBM Experiment'. In: *Proceedings of the 12th International Conference on Hypernuclear and Strange Particle Physics (HYP2015)*. DOI: 10.7566/JPSCP.17.092001. eprint: https://journals.jps.jp/doi/pdf/10.7566/JPSCP.17.092001. URL: https://journals.jps.jp/doi/abs/10.7566/JPSCP.17.092001.

[64] T.Galyutuk. *Interaction rates at different experiments*. URL: https://github.com/tgalatyuk/interaction_rate_facilities/.

[65] Peter Senger and Volker Friese. *CBM Progress Report 2022*. Tech. rep. CBM PR 2022. Darmstadt, 2022, p. 226. DOI: 10.15120/GSI-2023-00384. URL: https://repository.gsi.de/record/336786.

[66] Peter Senger and Volker Friese. *CBM Progress Report 2022*. Tech. rep. CBM PR 2022. Darmstadt, 2022, p. 226. DOI: 10.15120/GSI-2023-00384. URL: https://repository.gsi.de/record/336786.

[67] Alexander Malakhov and Alexey Shabunov, eds. *Technical Design Report for the CBM Superconducting Dipole Magnet*. Darmstadt: GSI, 2013, 80 S. URL: https://repository.gsi.de/record/109025.

[68] J. Stroth and M. Deveaux. *Technical Design Report for the CBM: Micro Vertex Detector (MVD)*. Tech. rep. URL: https://repository.gsi.de/record/246516.

[69] Johann Heuser et al., eds. *[GSI Report 2013-4] Technical Design Report for the CBM Silicon Tracking System (STS)*. Darmstadt: GSI, 2013, 167 p. URL: https://repository.gsi.de/record/54798.

[70] Subhasis Chattopadhyay et al., eds. *Technical Design Report for the CBM : Muon Chambers (MuCh)*. Darmstadt: GSI, 2015, 190 S. URL: https://repository.gsi.de/record/161297.

[71] Arindam Sen. 'Development Of Resistive Plate Chamber For The CBM Experiment At FAIR And Other Application Of Radiation Detector'. PhD thesis. Bose Institute, India, 2023.

[72] Christoph Blume, C. Bergmann and D. Emschermann. *The Transition Radiation Detector of the CBM Experiment at FAIR : Technical Design Report for the CBM Transition Radiation Detector (TRD)*. Tech. rep. FAIR Technical Design Report. Darmstadt: CBM Collaboration, 2018, 165 p. DOI: 10.15120/GSI-2018-01091. URL: https://repository.gsi.de/record/217478.

[73] V. L. Ginzburg and I. M. Frank. 'Radiation of a uniformly moving electron due to its transition from one medium into another'. In: *J. Phys. (USSR)* 9 (1945), pp. 353–362.

[74] Alexandru Bercuci and Mihai Petrovici. *An Enhanced Tracking Device For the Inner Region of the TRD wall*. https://niham.nipne.ro/main_280221.pdf.

[75] Norbert Herrmann, ed. *Technical Design Report for the CBM Time-of-Flight System (TOF)*. Darmstadt: GSI, 2014, 182 S. URL: https://repository.gsi.de/record/109024.

[76] Otari Javakhishvili. *FSD hardware and readout, CBM Collaboration meeting 03-2023 (CBM Internal)*. https://indico.gsi.de/event/19018/contributions/78551/.

[77] Petr Chaloupka. *FSD, CBM Collaboration meeting 03-2023 (CBM Internal)*. https://indico.gsi.de/event/19018/contributions/78304/.

[78] *The CBM DAQ system*. https://www.cbm.gsi.de/detectors/daq.html.

[79] J. Cuveland et al. *Technical Design Report for the CBM Online Systems – Part I DAQ and FLES Entry Stage*. Nov. 2022.

[80] Volker Friese and Ilya Selyuzhenkov. *CBM Progress Report 2018*. Tech. rep. CBM Progress Report 2018. Darmstadt: CBM Collaboration, 2019, 220 p. DOI: 10.15120/GSI-2019-01018. URL: https://repository.gsi.de/record/220128.

[81] P. A. Čerenkov. 'Visible Radiation Produced by Electrons Moving in a Medium with Velocities Exceeding that of Light'. In: *Phys. Rev.* 52 (4 Aug. 1937), pp. 378–379. DOI: 10.1103/PhysRev.52.378. URL: https://link.aps.org/doi/10.1103/PhysRev.52.378.

[82] L. Rosenfeld. 'Čerenkov radiation and its applications: J. V. Jelley, (Pergamon Press, London, 1958. x – 304 pages. 65s. net).' In: *Nuclear Physics* 15 (1960), p. 530. ISSN: 0029-5582. DOI: https://doi.org/10.1016/0029-5582(60)90351-5. URL: https://www.sciencedirect.com/science/article/pii/0029558260903515.

[83] I. M. Frank and I. E. Tamm. 'Coherent visible radiation of fast electrons passing through matter'. In: *Compt. Rend. Acad. Sci. URSS* 14.3 (1937). Ed. by V. L. Ginzburg, B. M. Bolotovsky and I. M. Dremin, pp. 109–114. DOI: 10.3367/UFNr.0093.196710o.0388.

[84] 'The COMPASS RICH project'. In: *Nuclear Instruments and Methods in Physics Research Section A: Accelerators, Spectrometers, Detectors and Associated Equipment* 433.1 (1999), pp. 207–211. ISSN: 0168-9002. DOI: https://doi.org/10.1016/S0168-9002(99)00297-1. URL: https://www.sciencedirect.com/science/article/pii/S0168900299002971.

[85] S. Gambetta. 'The LHCb RICH detectors: Operations and performance'. In: *Nuclear Instruments and Methods in Physics Research Section A: Accelerators, Spectrometers, Detectors and Associated Equipment* 952 (2020). 10th International Workshop on Ring Imaging Cherenkov Detectors (RICH 2018), p. 161882. ISSN: 0168-9002. DOI: https://doi.org/10.1016/j.nima.2019.02.009. URL: https://www.sciencedirect.com/science/article/pii/S0168900219301846.

[86] *C. Feier-Reisen, 42nd CBM Collaboration Meeting*. https://indico.gsi.de/event/17147/ (CBM Internal).

[87] Ievgenii Kres. 'Optimization of the CBM-RICH detector geometry and its use for the reconstruction of neutral mesons using conversion method'. PhD thesis. Wuppertal U., 2019.

[88] *The FAIRSOFT Repository*. https://github.com/FairRootGroup/FairSoft.

[89] *The FAIRROOT Repository*. https://github.com/FairRootGroup/FairRoot.

[90] S.A. Bass et al. 'Microscopic models for ultrarelativistic heavy ion collisions'. In: *Progress in Particle and Nuclear Physics* 41 (1998), pp. 255–369. ISSN: 0146-6410. DOI: https://doi.org/10.1016/S0146-6410(98)00058-1. URL: https://www.sciencedirect.com/science/article/pii/S0146641098000581.

[91] I. Fröhlich et al. 'Pluto: A Monte Carlo Simulation Tool for Hadronic Physics'. In: *PoS* ACAT (2007), p. 076. DOI: 10.22323/1.050.0076. arXiv: 0708.2382 [nucl-ex].

[92] R Brun et al. *GEANT 3: user's guide Geant 3.10, Geant 3.11; rev. version*. Geneva: CERN, 1987. URL: https://cds.cern.ch/record/1119728.

[93] et al. S. Agostinelli. 'Geant4—a simulation toolkit'. In: *Nuclear Instruments and Methods in Physics Research Section A: Accelerators, Spectrometers, Detectors and Associated Equipment* 506.3 (2003), pp. 250–303. ISSN: 0168-9002. DOI: https://doi.org/10.1016/S0168-9002(03)01368-8. URL: https://www.sciencedirect.com/science/article/pii/S0168900203013688.

[94] M. Becker et al. 'Qualification of DIRICH readout chain'. In: *Nuclear Instruments and Methods in Physics Research Section A: Accelerators, Spectrometers, Detectors and Associated Equipment* 1056 (2023), p. 168570. ISSN: 0168-9002. DOI: https://doi.org/10.1016/j.nima.2023.168570. URL: https://www.sciencedirect.com/science/article/pii/S0168900223005600.

[95] M. Becker et al. 'Status of the development of the RICH detector for CBM including a mRICH prototype in mCBM'. In: *Nuclear Instruments and Methods in Physics Research Section A: Accelerators, Spectrometers, Detectors and Associated Equipment* 1059 (2024), p. 168832. ISSN: 0168-9002. DOI: https://doi.org/10.1016/j.nima.2023.168832. URL: https://www.sciencedirect.com/science/article/pii/S0168900223008239.

[96] Peter Senger and Volker Friese. *CBM Progress Report 2020*. Tech. rep. CBM Progress Report 2020. Darmstadt: CBM Collaboration, 2021, 235 p. DOI: 10.15120/GSI-2021-00421. URL: https://repository.gsi.de/record/237432.

[97] Peter Senger and Volker Friese. *CBM Progress Report 2021*. Tech. rep. CBM Progress Report 2021. Darmstadt: CBM Collaboration, 2022, 239 p. DOI: 10.15120/GSI-2022-00599. URL: https://repository.gsi.de/record/246663.

[98] J. Michel et al. 'Electronics for the RICH detectors of the HADES and CBM experiments'. In: *Journal of Instrumentation* 12.01 (Jan. 2017). DOI: 10.1088/1748-0221/12/01/C01072.

[99] J. Adamczewski-Musch et al. 'Status of the CBM and HADES RICH projects at FAIR'. In: *Nuclear Instruments and Methods in Physics Research Section A: Accelerators, Spectrometers, Detectors and Associated Equipment* 952 (2020), p. 161970. ISSN: 0168-9002. DOI: https://doi.org/10.1016/j.nima.2019.03.025. URL: https://www.sciencedirect.com/science/article/pii/S0168900219303249.

[100] S.Lebedev. 'Status RICH simulations'. 36th CBM Collaboration meeting 2020 (CBM Internal).

[101] *CBM Progress Report 2017*. Tech. rep. CBM Progress Report 2017. Darmstadt, 2018, p. 146. DOI: 10.15120/GSI-2018-00485.

[102] Sascha Reinecke. 'Characterisation of photon sensors for the CBM-RICH and its use for the reconstruction of neutral mesons via conversion'. PhD thesis. Bergischen Universität Wuppertal, 2016. URL: https://repository.gsi.de/record/206473.

[103] *Nominal values of the ND filters, Thor labs*. URL: https://www.thorlabs.com/newgrouppage9.cfm?objectgroup_id=5011.

[104] Adrian Amatus Weber. 'Development of readout electronics for the RICH detector in the HADES and CBM experiments - HADES RICH upgrade, mRICH detector construction and analysis'. PhD thesis. Justus-Liebig-Universität Gießen, 2021. DOI: http://dx.doi.org/10.22029/jlupub-288.

[105] Jörg Förtsch. 'Upgrade of the HADES RICH photon detector and first performance analyses'. PhD thesis. Bergischen Universität Wuppertal, 2021. DOI: https://doi.org/10.25926/69gp-b484.

[106] *CBM Progress Report 2023*. Tech. rep. CBM Progress Report 2023. CCBY4. CBM, 2024, 240 p. DOI: 10.15120/GSI-2024-00765. URL: https://repository.gsi.de/record/352779.

[107] *Hamamatsu, H12700 SERIES*. URL: https://www.hamamatsu.com/content/dam/hamamatsu-photonics/sites/documents/99_SALES_LIBRARY/etd/H12700_H14220_TPMH1379E.pdf.

[108] Léo Grinsztajn, Edouard Oyallon and Gaël Varoquaux. *Why do tree-based models still outperform deep learning on tabular data?* 2022. arXiv: 2207.08815 [cs.LG]. URL: https://arxiv.org/abs/2207.08815.

[109] Henrik Schiller. 'Application of Machine Learning to Particle Identification for Dielectron Analysis in CBM'. MA thesis. University of Münster, 2022.

[110] Pavish Subramani for CBM Collaboration. 'Machine learning application for electron identification in CBM'. FAIR next generation scientists - 8th Edition Workshop.

[111] P.Subramani et al. *Using TRD-2D tracking for an improved ring-track matching*. Tech. rep. CBM progress report, 2023.

[112] Xiaoyao Liang. 'Chapter 1 - Theoretical basis'. In: *Ascend AI Processor Architecture and Programming*. Ed. by Xiaoyao Liang. Elsevier, 2020, pp. 1–40. ISBN: 978-0-12-823488-4. DOI: https://doi.org/10.1016/B978-0-12-823488-4.00001-1. URL: https://www.sciencedirect.com/science/article/pii/B9780128234884000011.

[113] Fionn Murtagh. 'Multilayer perceptrons for classification and regression'. In: *Neurocomputing* 2.5 (1991), pp. 183–197. ISSN: 0925-2312. DOI: https://doi.org/10.1016/0925-2312(91)90023-5. URL: https://www.sciencedirect.com/science/article/pii/0925231291900235.

[114] Sreerama Murthy and Steven Salzberg. 'Decision tree induction: how effective is the greedy heuristic?' In: *Proceedings of the First International Conference on Knowledge Discovery and Data Mining*. KDD'95. Montréal, Québec, Canada: AAAI Press, 1995, pp. 222–227.

[115] Anqi Mao, Mehryar Mohri and Yutao Zhong. *Cross-Entropy Loss Functions: Theoretical Analysis and Applications*. 2023. arXiv: 2304.07288 [cs.LG]. URL: https://arxiv.org/abs/2304.07288.

[116] David H. Wolpert. 'Stacked generalization'. In: *Neural Networks* 5.2 (1992), pp. 241–259. ISSN: 0893-6080. DOI: https://doi.org/10.1016/S0893-6080(05)80023-1. URL: https://www.sciencedirect.com/science/article/pii/S0893608005800231.

[117] Leo Breiman. 'Bagging predictors'. In: *Machine learning* 24 (1996), pp. 123–140.

[118] Robert E. Schapire and Yoav Freund. *Boosting: Foundations and Algorithms*. The MIT Press, May 2012. ISBN: 9780262301183. DOI: 10.7551/mitpress/8291.001.0001. eprint: https://direct.mit.edu/book-pdf/2280056/book_9780262301183.pdf. URL: https://doi.org/10.7551/mitpress/8291.001.0001.

[119] Leo Breiman. 'Random Forests'. In: *Machine Learning* 45.1 (Oct. 2001), pp. 5–32. ISSN: 1573-0565. DOI: 10.1023/A:1010933404324. URL: https://doi.org/10.1023/A:1010933404324.

[120] Fariha Sohil, Muhammed Sohail and Javid Shabbir. 'An introduction to statistical learning with applications in R: by Gareth James, Daniela Witten, Trevor Hastie, and Robert Tibshirani, New York, Springer Science and Business Media, 2013'. In: *Statistical Theory and Related Fields* 6 (Sept. 2021), pp. 1–1. DOI: 10.1080/24754269.2021.1980261.

[121] Kilian Weinberger. *Machine Learning for Intelligent Systems- Lecture series*. https://www.cs.cornell.edu/courses/cs4780/2018fa/lectures/lecturenote19.html.

[122] Tianqi Chen and Carlos Guestrin. 'XGBoost: A Scalable Tree Boosting System'. In: *Proceedings of the 22nd ACM SIGKDD International Conference on Knowledge Discovery and Data Mining*. Vol. 11. ACM, Aug. 2016, pp. 785–794. DOI: 10.1145/2939672.2939785. URL: http://dx.doi.org/10.1145/2939672.2939785.

[123] *ELI5 documentation*. https://fair-center.eu/.

[124] Marco Tulio Ribeiro, Sameer Singh and Carlos Guestrin. '"Why Should I Trust You?": Explaining the Predictions of Any Classifier'. In: *Proceedings of the 22nd ACM SIGKDD International Conference on Knowledge Discovery and Data Mining*. KDD '16. San Francisco, California, USA: Association for Computing Machinery, 2016, pp. 1135–1144. ISBN: 9781450342322. DOI: 10.1145/2939672.2939778. URL: https://doi.org/10.1145/2939672.2939778.

[125] Avanti Shrikumar, Peyton Greenside and Anshul Kundaje. *Learning Important Features Through Propagating Activation Differences*. 2019. arXiv: 1704.02685 [cs.CV]. URL: https://arxiv.org/abs/1704.02685.

[126] Sebastian Bach et al. 'On Pixel-Wise Explanations for Non-Linear Classifier Decisions by Layer-Wise Relevance Propagation'. In: *PLOS ONE* 10.7 (July 2015), pp. 1–46. DOI: 10.1371/journal.pone.0130140. URL: https://doi.org/10.1371/journal.pone.0130140.

[127] Scott M. Lundberg and Su-In Lee. 'A unified approach to interpreting model predictions'. In: *Proceedings of the 31st International Conference on Neural Information Processing Systems*. NIPS'17. Long Beach, California, USA: Curran Associates Inc., 2017, pp. 4768–4777. ISBN: 9781510860964.

[128] Meng Li et al. 'Shapley value: from cooperative game to explainable artificial intelligence'. In: *Autonomous Intelligent Systems* 4.1 (Feb. 2024), p. 2. ISSN: 2730-616X. DOI: 10.1007/s43684-023-00060-8. URL: https://doi.org/10.1007/s43684-023-00060-8.

[129] *XGBoost Documentation*. URL: https://xgboost.readthedocs.io/en/stable/.

[130] Thomas Bartz-Beielstein and Martin Zaefferer. 'Hyperparameter Tuning Approaches'. In: *Hyperparameter Tuning for Machine and Deep Learning with R: A Practical Guide*. Ed. by Eva Bartz et al. Singapore: Springer Nature Singapore, 2023, pp. 71–119. ISBN: 978-981-19-5170-1. DOI: 10.1007/978-981-19-5170-1_4. URL: https://doi.org/10.1007/978-981-19-5170-1_4.

[131] Tanay Agrawal. 'Hyperparameter Optimization Using Scikit-Learn'. In: *Hyperparameter Optimization in Machine Learning: Make Your Machine Learning and Deep Learning Models More Efficient*. Berkeley, CA: Apress, 2021, pp. 31–51. ISBN: 978-1-4842-6579-6. DOI: 10.1007/978-1-4842-6579-6_2. URL: https://doi.org/10.1007/978-1-4842-6579-6_2.

[132] Fernando Nogueira. *Bayesian Optimization: Open source constrained global optimization tool for Python*. 2014. URL: https://github.com/bayesian-optimization/BayesianOptimization.

[133] Nicolas Schilling, Martin Wistuba and Lars Schmidt-Thieme. 'Scalable Hyperparameter Optimization with Products of Gaussian Process Experts'. In: *Machine Learning and Knowledge Discovery in Databases*. Ed. by Paolo Frasconi et al. Cham: Springer International Publishing, 2016, pp. 33–48. ISBN: 978-3-319-46128-1.

[134] Mikhail Lifshits. 'Lectures on Gaussian Processes'. In: *Lectures on Gaussian Processes*. Berlin, Heidelberg: Springer Berlin Heidelberg, 2012, pp. 1–117. ISBN: 978-3-642-24939-6. DOI: 10.1007/978-3-642-24939-6_1. URL: https://doi.org/10.1007/978-3-642-24939-6_1.

[135] Daniel Berrar. 'Cross-Validation'. In: *Encyclopedia of Bioinformatics and Computational Biology*. Ed. by Shoba Ranganathan et al. Oxford: Academic Press, 2019, pp. 542–545. ISBN: 978-0-12-811432-2. DOI: https://doi.org/10.1016/B978-0-12-809633-8.20349-X.

[136] P. Subramani et al. *RICH timing precision and its possible applications*. Tech. rep. CBM progress report, 2023.

[137] Valentina Akishina. 'Four-dimensional event reconstruction in the CBM experiment'. Doctoral thesis. Universitätsbibliothek Johann Christian Senckenberg, 2017, p. 181.

[138] Open Neural Network Exchange. *Open Neural Network Exchange 1.18.0 documentation*. https://onnx.ai/onnx/intro/index.html.

[139] A. Rost. *Status of the diamond based BMON system for CBM*. 42nd CBM Collaboration meeting 2023 (CBM Internal).

[140] Adrian Meyer-Ahrens. *Status of e+e- analysis with papa, CBM Collaboration meeting 03-2023 (CBM Internal)*. https://indico.gsi.de/event/16428/contributions/70285/ (CBM Internal).

List of Figures

List of Tables

Acknowledgments

I am reminded of the words penned over two millennia ago by the Tamil saint Thiruvalluvar:

காலத்தி னாற்செய்த நன்றி சிறிதெனினும்
ஞாலத்தின் மாணப் பெரிது.

Even a modest act of assistance, when rendered in times of need, surpasses the earth in its excellence.

As a young individual hailing from a farming family in the hilly regions of southern India, I received numerous such acts of kindness, which enabled me to undertake and complete this dissertation at a world-class particle physics laboratory in Germany. I extend my heartfelt gratitude to all those whose support has made the completion of this thesis possible.

First and foremost, I express my profound gratitude to Prof. Karl-Heinz Kampert for granting me the opportunity to conduct research within the distinguished CBM experiment, as part of the esteemed Astro-/Particle Physics group at Wuppertal. His wisdom, incessant support, and steadfast guidance have been invaluable throughout my research journey. Notably, he has always addressed my inquiries and requests with affirmative and insightful responses, for which I am sincerely appreciative.

I extend my deepest gratitude to Dr. Christian Pauly for his unwavering support throughout my doctoral studies. He has consistently been attentive to my inquiries and adept at resolving my challenges. His encouragement and recognition of even the smallest achievements have been remarkable, akin to the nurturing care of a devoted mentor. I am also deeply appreciative of his meticulous proofreading of this thesis.

I express my sincere gratitude to Dr. Jörg Förtsch, for his steady support over the past four years. His consistent assistance, day and night, has been crucial. Our brainstorming sessions and discussions across various fields have profoundly influenced the progression of this thesis. Whenever I present a preliminary idea, Christian refines it into a coherent form, and Jörg meticulously hones it into a polished concept. I thank again for all his suggestions and for proofreading this thesis.

I express my gratitude to Prof. Claudia Höhne for her invaluable feedback during our various meetings. Her insights have been enlightening and have greatly influenced the development of the concepts presented in this thesis. I extend my gratitude to Prof. Tetyana Galatyuk for providing platforms to showcase my work in the CBM collaboration. Her guidance has been instrumental in my continued dedication to dilepton physics. I extend my gratitude to Prof. Anton Andronic for refereeing this thesis. I express my humble gratitude to Prof. Raghunath Sahoo for introducing me to the field of Quark-Gluon Plasma physics and for his mentorship throughout my research journey. I would like to thank Dr. Suman Deb for sharing and engaging me in reading interesting papers about QGP physics.

I gratefully thank the members of the CBM/HADES group, for their support and collaboration. I am deeply appreciative of Dr. Jesús Peña Rodrigues, Simon Neuhaus, Sukyung Kim, Athira Sreejith, Abhishek Deshmukh, and Dennis Pfeifer for their substantial assistance and kindness throughout the course of this thesis work. I would also like to thank Athira for her help in editing multiple images included in this thesis. I am forever thankful to Tetiana Povar for her thoughtful conversations and consistent moral support. I am grateful to the other members of the Astro-/Particle Physics group for their engaging discussions and valuable insights. I extend my thanks to Dr. Simon Lebedev for introducing me to the software framework, Martin Beyer for his innovative viewpoints, and other members of the Giessen RICH group. I extend my gratitude to Dr. Ramesh and Mr. Venkatachalam for their guidance, which has been instrumental in shaping my academic journey.

எழுமை எழுபிறப்பும் உள்ளுவர் தங்கண்
விழுமந் துடைத்தவர் நட்பு

Friendship of those who wiped the tears of sorrow from their eyes on earth, will remain in the memory of the wise through all seven worlds, in seven-fold birth.

I graciously thank Adrian Meyer-Ahrens for always being a call away and for having pleasant discussions, both in professional and personal life. I extend my thanks to Cornelius Feier-Riesen for his refreshing conversations and wise counsel through turbulent times. I express my sincere gratitude to the other members of the CBM ECR team for placing your faith in me to represent our team to the collaboration board. I thank my friends who played a significant role in shaping my time in Germany. I am especially thankful to Vivek and Swetha for providing me with shelter during my first week, Karthick and Anitha for their generous hospitality, Lakshmi and Prabha for their delightful meals and cheerful presence, Naveen and Devi for their warm and heartfelt welcome, Shivani for her kind and encouraging words, and Lokesh for his motivation and assistance. I would also like to express my sincerest gratitude to my childhood friends Bala and Sanjith for their confidence in me. I extend my thanks to my friends Ragul, Anand, Sriram, Radhakrishnan, Pranesh, Nikhil, Siva, and all friends from my village for their care and support. I also thank friends from The Nilgiris residing in Germany for providing me with motivation and encouragement during my visits.

தந்தை மகற்காற்று நன்றி அவையத்து
முந்தி இருப்பச் செயல்

The greatest deed a father/parent can do for their child is to ensure they excel among the learned.

I owe who I was, who I am, and who I will become to the sacrifice and hard work of my mother - Saraswathi, my late father - Subramani, my aunt - Saibaby, and my brother - Abinesh. I am forever grateful for the unconditional love, care, nurturing, and freedom I have received from them every day. Dedicating this thesis to you is but a small token of my deep respect and love. I also extend my gratitude to the members of my extended family for their love and enduring support, especially my late uncles — Natarajan, Harichandran, and Venkatesan - whose guidance and influence paved the way for my career in research.

Last but certainly not least, I extend my heartfelt gratitude to my fiancée, Pooja, for her trust, patience, and love. Enduring days without calls has been difficult, yet the inspiration you provide has made my time spent on research truly worthwhile.

Declaration of Authorship

English

I hereby declare that the thesis submitted is my own unaided work. All direct or indirect sources used are acknowledged as references.

This thesis was not previously presented to another examination board and has not been published.

Deutsch

Hiermit versichere ich, die vorliegende Arbeit selbstständig und unter ausschließlicher Verwendung der angegebenen Literatur und Hilfsmittel erstellt zu haben.

Die Arbeit wurde bisher in gleicher oder ähnlicher Form keiner anderen Prüfungsbehörde vorgelegt und auch nicht veröffentlicht.

Wuppertal, den _____ _____

(Pavish Subramani)